The evolution of galaxies and AGN

HILL, MICHAEL,DAVID

ON

THE EVOLUTION OF GALAXIES AND AGN

Michael David Hill

A thesis presented in accordance with the regulations for admittance to the degree of Doctor of Philosophy.

Department of Physics
University of Durham
United Kingdom

September 2010

Declaration

The work described in this thesis was undertaken between 2007 and 2010 while the author was a research student under the supervision of Prof. Tom Shanks in the Department of Physics at the University of Durham. This work has not been submitted for any other degree at the University of Durham nor any other University.

Some of the work contained in Chapters 2 and 3 of this thesis appears in

- **Hill M. D. & Shanks T.**, *The contribution of AGN to the sub-mm population*, 2010, Mon. Not. R. Astron. Soc., in press (arXiv:1007.1659)

Some of the work contained in Chapter 4 appears in

- **Hill M. D. & Shanks T.**, *Extending PLE models into the mid-IR, far-IR and sub-mm*, 2010, accepted for publication in Mon. Not. R. Astron. Soc. (arXiv:1007.3126)

The evolution of galaxies and AGN

Michael D. Hill

Abstract

This thesis presents a study of some current questions regarding the evolution of galaxies and AGN. We first argue that the bright submillimetre number counts may be dominated by obscured AGN rather than ultraluminous starbursts. Through statistical analyses of the ECDFS and WHDF, we show that $N_{\rm H} > 10^{22}$ cm^{-2} AGN are typically bright at 870μm, with less absorbed AGN being much weaker sub-mm emitters. Overall, X-ray-detected AGN contribute 1.5 ± 0.1 Jy deg^{-2} to the sub-mm background, $\approx 3\%$ of the total, in agreement with the prediction of an AGN model which also fits the bright sub-mm counts. When Compton-thick, X-ray-undetected sources are included, this non-unified model predicts a total AGN contribution to the sub-mm background of 25–40%. The measured dependences of sub-mm flux on X-ray flux, luminosity and column density all agree well with model predictions. We therefore suggest that sub-mm galaxies may contain the absorbed AGN population which has long been sought to explain the X-ray background.

Moving to shorter wavelengths, we find that AGN may continue to dominate the source counts down to $\lambda \approx 200\mu$m. Below this, dusty star-forming galaxies are shown to fit the observed number counts and colours reasonably well. Below $\lambda \approx 5\mu$m starlight takes over from dust as the main source of flux. These conclusions are supported by the good fit to the observations of phenomenological models assuming pure luminosity evolution.

Finally, using a new survey of $z \approx 3$ Lyman-break galaxies (LBGs), we find evidence for the supernova-driven feedback which is thought to be an essential ingredient of galaxy evolution. By cross-correlating LBG positions with Lyα absorption in quasar sightlines, we find (a) that the intergalactic medium shows excess neutral hydrogen within 4 h^{-1} Mpc of LBG positions, consistent with their lying in overdense regions, but also (b) that a Lyα transmission spike may exist extending out to $\approx 1.5\ h^{-1}$ Mpc around LBGs, indicating that galactic winds from LBGs may have ionised the IGM within this radius.

Acknowledgements

I am grateful first and foremost to my supervisor, Prof. Tom Shanks, for three years of unwavering guidance through the world of scientific research. His knowledge of and enthusiasm for all things astronomical and cosmological has been endlessly valuable, and working with him has been a source of inspiration and entertainment in equal measure. Mostly, though, I am grateful for the support and kindness that he and his wife Kath unreservedly show to all of Tom's students.

I would like to acknowledge others in the department whose advice or assistance I benefited from over the years – particularly Dr. Nigel Metcalfe, whose expertise in galaxy surveys has been extremely valuable, Prof. Ian Smail who was enormously helpful and obliging in the work I did with submillimetre galaxies, and Drs. Rich Bielby and Neil Crighton for their involvement with the LBG project. For assistance with technical problems I could never have solved alone, I thank Alan Lotts and Dr. Peter Draper. I also gratefully acknowledge three years of generous financial support from the Science and Technology Facilities Council.

I'm thankful to those fellow postgrads and postdocs with whom I shared an office, a pint or a consolatory discussion about how, actually, all of our supervisors expect too much of us and don't understand our terrible hardships: Owen Parry, Dr. Rich Bielby, Dr. Tim Rawle, Dr. Matt Middleton, Dr. Neil Crighton, Utane Sawangwit, Dr. Dave Wake, Andy Goulding, Adam Ingram, Dr. Stephen Fine, Julie Wardlow, Joe Whitbourn and many others who have made the years pass faster and ensured I take away memories that don't just involve galactic spectral energy distributions.

This thesis marks for me not only the end of three years of postgraduate study, but also the culmination of twenty uninterrupted years of education. This academic career would not have been possible without the ceaseless support of my parents, although they did tend to be in some far-flung corner of the world on many of the occasions when I most needed advice. I thank them and the rest of my family for their constant encouragement, whatever I decided to do.

My final word of acknowledgement goes to the person who deserves the most thanks of all. I am eternally grateful for her inexhaustible support, her unending reassurance, her friendship and her love. She is the person without whom I could never have accomplished this thesis, and therefore the person to whom it is dedicated.

For my fiancée,

Tamara

We shall not cease from our exploration
And the end of all our exploring
Will be to arrive where we started
And know the place for the first time

T. S. Eliot, *Four Quartets*, 1942

Contents

List of Figures

List of Tables

I

Introduction

The process by which galaxies formed and evolved into the systems we see today remains one of the most important questions in modern astronomy. We do not currently have a comprehensive picture of how and when most of the stellar content of the universe was assembled.

It is thought that galaxies were formed in regions of overdensity in the underlying dark matter distribution of the universe (e.g. Quinn, Salmon & Zurek, 1986; Frenk et al., 1990), which is itself a manifestation of the primordial density fluctuations imprinted during inflation (Guth, 1981; Linde, 1982). Gravitational interactions in the dark matter amplify the initial fluctuations, giving rise to a universe with a highly inhomogeneous matter distribution. The baryonic matter of the universe is drawn into the massive dark matter halos, whereupon it cools and forms stars (e.g. Abel, Bryan & Norman, 2001).

This broad outline can explain how most matter in the universe came to be concentrated into comparatively dense, tightly bound structures, rather than being uniformly distributed, and lays the foundation for why these structures should be luminous. However, our picture of how the earliest galactic systems evolved into the diverse range of structures we see today is far from complete. The epoch at which galaxies assemble the majority of their mass, the relative importance of galaxy mergers and secular evolution, the role of feedback from supernovae and/or active nuclei and the establishment of the Hubble sequence are among many outstanding issues in our understanding of galaxy evolution.

This Introduction aims to provide a brief overview of the historical background to the study of galaxies and their evolution, as well as a look in somewhat greater depth at Lyman-break galaxies, submillimetre galaxies and active galactic nuclei, all of which play a key role in current galaxy evolution studies, and on which this thesis largely

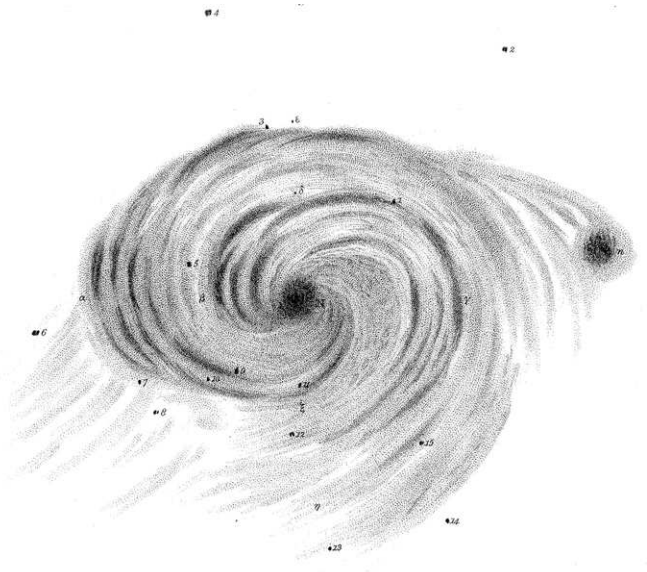

FIGURE 1.1: *A sketch of M51, the first known spiral nebula, produced by the Earl of Rosse in 1849. Thought at the time to be part of the Milky Way, it in fact lies 7 Mpc away. This may be the first observational image of a spiral galaxy ever published. Image: Rosse (1850)*

focusses.

1.1 Historical Background

1.1.1 The origins of extragalactic astronomy

The earliest observations of distant galaxies, beyond the immediate neighbourhood of the Milky Way, were made by the Earl of Rosse in the 1840s (Fig. 1.1), however mainstream opinion at the time held that these were not extragalactic sources but gaseous nebulae within our own galaxy. It was not until 1920, when astronomy's 'Great Debate' took place (Curtis, 1921; Shapley, 1921), that the idea of these so-called *spiral nebulae* as separate distant galaxies, or 'island universes', was taken seriously.

The implications of this idea were enormous: the universe would have to be vast in scale for such large systems to appear so small from the Earth. For many astronomers at the time, the implied distances were utterly implausible. The question, though, was to be resolved just a few years later by Edwin Hubble, whose observations of Cepheid variables in spiral nebulae confirmed that the nebulae were at such great distances that they were unquestionably separate galaxies (Hubble, 1926). Hubble's work proved historic for a second reason. As well as measuring the distances to the galaxies, he determined

their velocities and found that the two were linked: galaxies at greater distances have greater recessional velocities. The universe, he discovered, is expanding. With these seminal discoveries, extragalactic astronomy was born.

1.1.2 Galaxies as evolving systems

The Hertzsprung-Russell (HR) diagram, which plots the colour or temperature of a star against its absolute magnitude or luminosity, was developed many years before Hubble's groundbreaking discoveries (Hertzsprung, 1911; Russell, 1913). However, it was not known at the time that the distribution of stars on the plot represented an evolutionary sequence.

The idea that stellar evolution drove the phenomenology of the HR diagram was considered from early times (Strömgren, 1933), but could not be conclusively determined. Work in this area was hindered, in no small part, because it was not until the end of the 1930s that the nuclear fusion processes by which stars produce their luminous output were discovered (Bethe, 1939). By the 1960s, however, the importance of understanding the effects of stellar evolution in distant galaxies was clearly acknowledged (Sandage, 1961; Tinsley, 1968), even if just as a correction to apply when making cosmological measurements.

Sandage (1961) defined the evolution correction — the change in apparent magnitude of a galaxy — as:

$$\Delta m = -2.5 \log \int_{t_0-\tau}^{t_0} \frac{\mathrm{d}L}{\mathrm{d}t} \mathrm{d}t \tag{1.1}$$

where $\mathrm{d}L/\mathrm{d}t$ is the rate of change in the galaxy's luminosity due to stellar evolution, t_0 is the present epoch and τ is the light travel time (i.e., the observed radiation was emitted at a time $t_0 - \tau$). Sandage noted, however, that with contemporary knowledge of stellar evolution it was not possible to properly constrain $\mathrm{d}L/\mathrm{d}t$ and therefore solve the equation.

Soon it was realised that $\mathrm{d}L/\mathrm{d}t$ could be approximated even without a detailed model of stellar evolution using the technique of *evolutionary population synthesis*. Rather than attempting to determine the evolution of the individual stars making up a galaxy, this method is concerned with *galaxy evolution* as a whole. The evolutionary term $\mathrm{d}L/\mathrm{d}t$ was found to be dependent primarily on the galaxy's initial mass function (IMF; the distri-

bution of stellar masses in galaxy), since its luminosity is dominated by massive main sequence stars (Tinsley, 1978). Tinsley therefore showed that the luminosity evolution of galaxies could be parametrised in terms only of the power-law slope of the IMF, according to Eqn. 1.2.

$$\frac{\mathrm{d}M}{\mathrm{d}(\ln t)} = 1.2 - 0.25x \tag{1.2}$$

where M is absolute magnitude and $x + 1$ is the slope of the IMF. By combining this approach with prescriptions for the star-formation rate (Bruzual, 1983; Bruzual & Charlot, 1993) and chemical composition (Arimoto & Yoshii, 1987), it became possible to create usable models of galaxy evolution.

Today, the IMF of galaxies remains one of the most important parameters in any galaxy evolution model, yet it is still not well constrained. Although the Salpeter (1955) IMF, which sets $x = 1.35$, is most widely used by astronomers, many other models invoke alternative IMFs to explain observations. Metcalfe et al. (2001, 2006) find that in pure luminosity evolution models of late-type spiral galaxies, the Salpeter IMF overpredicts the number of high-redshift sources which should be detectable in the NIR (see also Chapter 4 and Hill & Shanks, 2010b), preferring instead a steep-sloped $x = 3$ IMF for these objects. In this dwarf-dominated IMF there are fewer stars at the very bright high-mass end, reducing a galaxy's surface brightness.

Conversely, in some semi-analytic models of galaxy evolution within the Λ-cold dark matter (ΛCDM) paradigm a very shallow, or 'top-heavy', IMF is invoked for starburst galaxies to match observations in the far-infrared and submillimetre (Baugh et al., 2005; Lacey et al., 2008). The resulting giant-dominated starburst galaxies fit well the observations of galaxies in the far-infrared and submillimetre, however a poor fit is achieved for the NIR redshift distributions so well matched by an $x = 3$ model (Gonzalez-Perez et al., 2009).

1.1.3 Observing and modelling galaxy evolution

The development through the 1980s and early 1990s of galaxy evolution models based on population synthesis methods parallelled an increase in the availability of observational data. Larger telescopes and the development of CCD imaging meant observers could reliably probe increasingly faint magnitudes. Of particular interest was how the number

of galaxies varied as a function of apparent magnitude (Shanks et al., 1984; Butcher & Oemler, 1985; Koo, 1986; Heydon-Dumbleton et al., 1989; Maddox et al., 1990; Metcalfe et al., 1991, 1995) and redshift (Kirshner et al., 1978; Peterson et al., 1986; Metcalfe et al., 1989; Koo & Kron, 1987; Cowie et al., 1991; Dressler & Gunn, 1992).

The observed $n(m)$ and $n(z)$ relations provided key tests of galaxy evolution models. Shanks et al. (1984) showed that the source counts in the B band showed clear evidence for evolution, rising too steeply at faint magnitudes be consistent with no-evolution models (see also Koo, 1981). Little evolution was initially observed in redder wavebands, but Metcalfe et al. (1991) showed that the R band counts in fact exhibited only marginally less evolution than the bluer bands. Also of interest were the colour distributions of galaxies, with several studies revealing a trend for galaxies at fainter magnitudes to have bluer colours (Kron, 1980; Tyson 1988; Lilly et al., 1991; Metcalfe et al., 1991); this was also interpreted as strong evidence for galaxy evolution (Shanks et al., 1984).

With the discovery that the galaxy population showed evidence for significant evolution, searches began in earnest for populations of galaxies at high redshifts (e.g. Partridge, 1974; Davis & Wilkinson, 1974), which could better constrain this evolution. It was expected from gravitational collapse arguments (e.g. Eggen, Lynden-Bell & Sandage, 1962) that young galaxies in the throes of forming most of their stars would undergo a highly luminous phase, and from upper limits on the optical background (Dube, Wickes & Wilkinson, 1979) it was inferred that this luminous phase must occur at $z \geq 5$ (Koo & Kron, 1980). Additionally, predictions of the population synthesis models described above were shown to agree well with observations if a high redshift of galaxy formation was assumed in the models.

At the same time, however, theoretical frameworks for galaxy formation and evolution were being developed (White & Rees, 1978; Davis et al., 1985; White & Frenk, 1991; Bower, 1991; Cole, 1991), which modelled galaxy evolution *ab initio* as a hierarchical process, driven by the merging of many smaller systems over long timescales, and such models tended to favour a slow build-up of mass and therefore predicted very few massive galaxies at $z > 1$.

Therefore, the question of the very *existence* of massive galactic systems at $z > 1$, when the universe was less than half its current age, became a pressing one. Early surveys, which mainly attempted to identify these 'primeval' galaxies by searching for Lyman alpha (Lyα) emission, were unsuccessful (for a review, see Pritchet, 1994). As recently as 1995 astronomers knew of not a single 'normal' galaxy with a confirmed red-

shift above unity (Giavalisco, 2002), although radio-loud sources at high-redshift had been known about for many years (Schmidt, 1965; Spinrad, 1982; Lilly, 1988; Rawlings, Eales & Warren, 1990; Chambers et al., 1990) thanks to strong, easily detectable emission lines in these objects (for a review, see McCarthy, 1993).

In the mid-1990s a great leap in the redshift frontier for detecting normal galaxies was made thanks to two crucial developments: the use of the Lyman-break technique to preselect $z > 2$ galaxy candidates by their optical colours (Steidel & Hamilton, 1993; Steidel et al., 1996), and the advent of new bolometers on ground-based telescopes sensitive to electromagnetic radiation at submillimetre wavelengths ($300\mu\text{m} < \lambda < 1000\mu\text{m}$), where high-redshift objects dominate the bright sources (Smail et al., 1997; Barger et al., 1998; Hughes et al., 1998). These new techniques/instruments have resulted in the detection of large galaxy populations at $z \gtrsim 2$.

It has since been shown that, despite the intuitive expectation that merger-driven galaxy evolution should yield few massive high-z galaxies, the existence of these established galaxy populations at $z > 2$ is consistent with hierarchical evolution models when AGN feedback (Bower et al., 2006) and/or cold gas accretion (Dekel et al., 2009; Kang et al., 2010) are taken into account. Further observational studies of high-redshift galaxies are vital to constraining models of galaxy evolution; such studies are the focus of this thesis. In the following sections, we review the Lyman-break and submillimetre galaxy populations which have proven so valuable to our understanding of the high-z universe.

1.2 Lyman-break galaxies

The Lyman-break technique, which in the 1990s revolutionised studies of the high-redshift universe, exploits the presence of the Lyman break, a continuum discontinuity at 912Å, in the spectra of star-forming galaxies. The break arises in the atmospheres of stars in the galaxy itself, in the interstellar medium (ISM) permeating the galaxy, and in intervening clouds of neutral hydrogen. A neutral hydrogen atom in the ground state has an ionisation potential of 13.6 eV, and can therefore be ionised by a photon with $\lambda = h/(13.6\,\text{eV}) = 912$Å. Therefore, as a result of the ubiquity of neutral hydrogen in young galaxies (Heckman, 2000) and in the intergalactic medium at high redshift (Steidel et al., 1995, 1999; Madau, 1995), photons with $\lambda \leq 912$Å (i.e. energies greater than 13.6 eV) tend to be absorbed before reaching the Earth, producing a break in the ultraviolet spectrum.

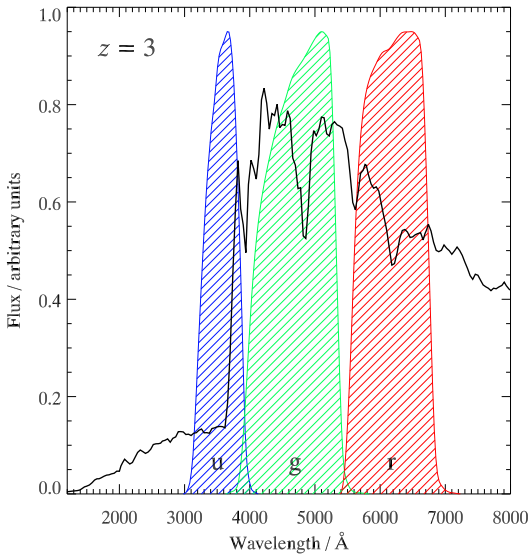

FIGURE 1.2: *The Lyman-break technique. At $z = 3$, the Lyman break in the SED of a typical star-forming galaxy (modelled here using the code of Bruzual & Charlot, 2003) lies between the u and g filters. Very little flux is detected in the u band, and the galaxy is said to have 'dropped out' of u. The extremely red $u - g$ colour allows for photometric selection of LBGs.*

The absorption of ultraviolet light by O_3 in the Earth's atmosphere initially made detecting this feature in low-redshift objects impossible (it has since been achieved using the *GALEX* satellite; Burgarella et al., 2006), however for galaxies at $z \geq 2$ the Lyman break is shifted to optical wavelengths, where deep imaging with ground-based telescopes is easily achievable. Candidate Lyman-break galaxies (LBGs) can be selected from broadband colours, because an LBG will exhibit a very red colour across two filters which bracket the Lyman break (Fig. 1.2).

It was realised some 30 years ago that high-z targets could be identified in this way (Meier, 1976), but until the 1990s no surveys were carried out to exploit it. It was the LBG survey of Steidel et al. (1996) which first followed up a significant number of colour-selected $z \approx 3$ galaxy candidates with spectroscopic observations. This work confirmed beyond doubt for the first time the existence of a large population of normal, star-forming galaxies at $z > 3$.

Madau et al. (1996) also used this method to identify high-redshift galaxies. Using Hubble Deep Field (HDF) data, these authors identified relatively small samples of LBGs at $z \approx 2.75$ and $z \approx 4$. Using the comoving space densities and average luminosities of

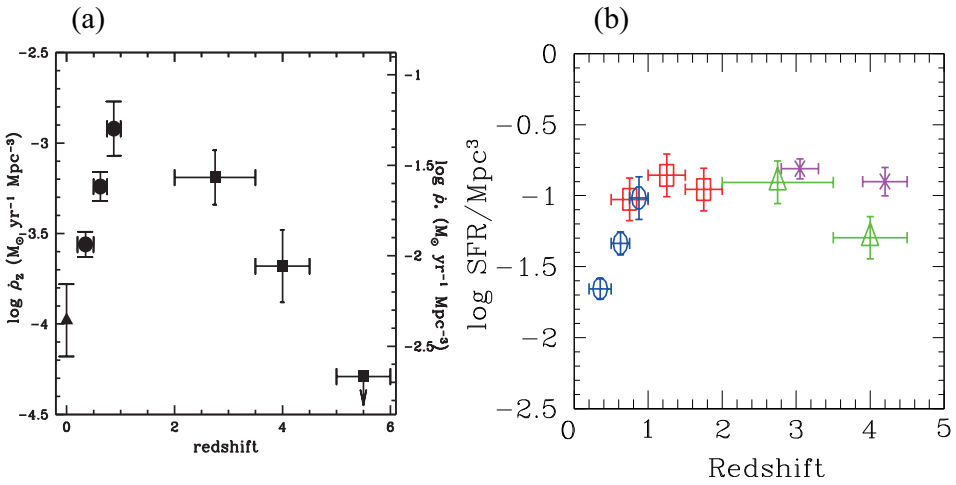

FIGURE 1.3: *'Madau plots' showing measurements of the cosmic SFR density against redshift.* (a) *The original data, which indicated a peak at* $z \approx 1$–2 *(figure: Madau, 1997).* (b) *The plot presented by Steidel et al. (1999), with dust extinction taken into account. The importance of correcting for dust attenuation is clear.*

these samples and the sample of Steidel et al. (1996), as well as measurements of local star-forming galaxies, they deduced that the star formation rate density ($\dot{\rho}_*$ / $\mathrm{M}_\odot$ yr^{-1} Mpc^{-3}) of galaxies peaked at $z \approx 1$–2 and then fell off rapidly at higher redshifts (the 'Madau plot', Fig. 1.3*a*)[1]. The implication was that most of the star formation (and metal enrichment, on which their paper mainly focusses) occurred around $z \approx 1.5$, and not at earlier times as the monolithic collapse models had predicted. This discovery of a peak in the cosmic SFR history at these relatively late times was shown instead by Baugh et al. (1998) to be in good agreement with the hierarchical galaxy formation scenario, in which this peak had long been predicted to occur at $z \approx 1$ (White & Frenk, 1991; Lacey et al., 1993; Cole et al., 1994).

However, Madau et al. noted that the calculated $\dot{\rho}_*$ values at high redshift would increase markedly if the LBGs were significantly obscured by dust. Following their groundbreaking 1996 paper, Steidel et al. (1999) presented a survey of $z \approx 4$ LBGs, this time including estimates of the implied SFR density at high-z. Importantly, they included dust attenuation corrections in their estimates and showed that there was in fact no evidence of a fall-off at $z > 2$ (Fig. 1.3*b*). A similar undertaking by Rowan-Robinson

[1]A cosmology with $H_0 = 50$ km s^{-1} Mpc^{-1} and $q_0 = 0.5$ is assumed in Fig. 1.3; in a standard ΛCDM cosmology with $H_0 = 70$ km s^{-1} Mpc^{-1} and $\Omega_m = 0.3$ the amplitude of the low-z increase in $\dot{\rho}_*$ would not be as great.

(1999) produced consistent results. This author also showed that, as a result of these dust corrections, the hierarchical evolution models of Cole et al. (1994) now significantly underpredicted $\dot{\rho}_*$ at $z \gtrsim 1.5$, whereas simpler luminosity evolution models could provide a good fit. More recently, however, it has been shown that hierarchical formation models are able to reproduce the observed SFR density at high-z (Lacey et al., 2010), even as observations have continued to show that $\dot{\rho}_*$ remains high out to very high redshifts (Yüksel et al., 2008).

1.2.1 Properties of LBGs

From the outset, it was noted that LBGs are 'normal' galaxies — that is, they appear to have similar properties to the star-forming galaxies we see at low redshift (Steidel et al., 1996). This initial conclusion has not changed in the intervening years even as many observers have carried out follow-up observations of LBGs in different wavebands and redshift ranges.

LBGs are found to have comparable luminosities to (but more compact sizes than) local spirals (Lowenthal et al., 1997), and their extinction-corrected UV continua and emission lines suggest fairly moderate star-formation rates of ≈30–90 $M_\odot$ yr^{-1} (Steidel et al., 1996; Lowenthal et al., 1997; Pettini et al., 2001; Magdis et al., 2010)[2], comparable to local and low-z starburst galaxies (Sargsyan & Weedman, 2009). Dust extinction in most LBGs is found to be fairly modest, with $E(B-V) \approx 0.3$ (Steidel et al., 1999).

To better constrain the masses of LBGs, Magdis et al. (2008) surveyed a sample of $z \approx 3$ LBGs in the mid-infrared in order to observe the rest-frame near-infrared, since this regime provides better stellar mass constraints than the rest-frame UV/optical on which most previous surveys focussed. They found that LBGs typically have stellar masses of $\sim 10^{10}$–10^{11} $M_\odot$ (similar to earlier results found by e.g. Pettini et al., 2001; Shapley et al., 2001), again comparable to local star-forming galaxies.

The most prominent spectral feature of LBGs, other than the presence of the Lyman break, is the Lyman alpha line, which may be seen in either emission or absorption (e.g. Steidel et al., 2003; Bielby et al., 2010) and which arises as a result of on-going star-formation. Lyα emission in LBGs is typically not as strong as is observed in Lyman alpha emitters (LAEs), and the relationship between these two classes of galaxy has been the subject of much investigation, with recent work by Lai et al. (2008) suggesting that LAEs

[2]These are total star-formation rates, calculated initially for high-mass stars and then extrapolated assuming a Salpeter IMF.

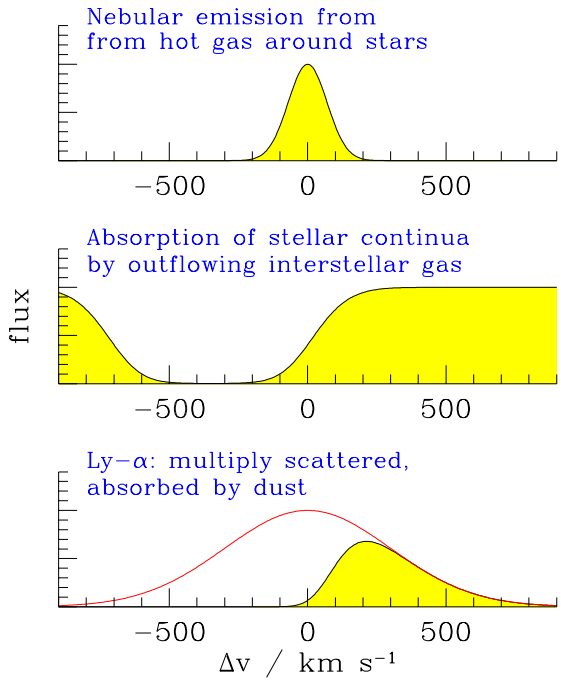

FIGURE 1.4: *The source of velocity offsets in LBG spectral features. The nebular emission lines represent the intrinsic redshift of the galaxy; ISM absorption lines are detected in gas which is flowing out of the galaxy toward the observer, resulting in a measurement which is blueshifted relative to the nebular lines. Lyα emission is seen having been scattered off the inner edge of the outflowing shell on the far side of the galaxy, yielding a systematically higher redshift. Figure: Adelberger et al. (2003)*

may form the low mass end of the LBG population.

How the strength of the Lyα line in LBGs correlates with other properties has been the subject of several studies. Results have generally indicated that the Lyα emission is weaker in younger LBGs with higher SFRs (Shapley et al., 2001; Kornei et al., 2010), likely because such LBGs are also dustier (Adelberger & Steidel, 2000; Reddy et al., 2006a; Kornei et al., 2010; Pentericci et al., 2010), which efficiently quenches Lyα emission.

Pettini et al. (2001) surveyed $z \approx 3$ LBGs at near-infrared wavelengths, enabling them to build a picture of these high-z galaxies in the rest-frame optical, where all traditional surveys of low-redshift galaxies have been carried out. They conclude that LBGs are highly metal enriched, with higher metallicities than any other objects at comparable redshift, save for quasars. However, they also suggest that many of these metals will be lost from the galaxies due to galactic superwinds expelling interstellar material into the intergalactic medium. These winds, which may prove highly consequential to galaxy

evolution, are discussed next.

1.2.2 Galactic outflows

One of the key results from spectroscopic observations of LBGs has been that different apparent redshifts are measured for the nebular emission lines, the silicon and carbon absorption lines associated with the interstellar medium (ISM), and the Lyα emission from star-forming regions. The nebular emission lines are generally taken to represent the intrinsic redshift of the galaxy, relative to which the ISM lines are normally blueshifted and the Lyα line redshifted (Pettini et al., 2001; Adelberger et al., 2003).

This is indicative of a shell of outflowing material, thought to be driven from LBGs by galactic winds (Heckman et al., 2000; Pettini et al., 2001). The ISM absorption lines are observed principally in the outflowing front which lies between us and the galaxy, yielding a systematically lower redshift for these lines. The effluxing shell has a high optical depth to Lyα photons, so Lyα photons emitted from the galaxy toward the Earth are mostly absorbed. The only Lyα photons we detect are those which have been resonantly scattered off the back of the redshifted outflowing shell of material behind the galaxy, giving a systematically higher redshift than the intrinsic galaxy redshift (see Fig. 1.4).

Supernova-driven galactic winds are thought to be extremely important to the evolution of galaxies and the intergalactic medium (IGM) which separates them. Observations have shown that the high-redshift IGM is enriched with metals (e.g. Songaila & Cowie, 1996; Ellison et al., 2000; Schaye et al., 2000; Songaila, 2001; Pettini et al., 2003; Pieri, Schaye & Aguirre, 2006), and it is expected that the origin of these metals lies within galaxies. Galactic-scale 'superwinds' are thought to be the only viable process by which these metals can be transferred to the IGM.

A single supernova explosion creates a bubble of heated, metal-enriched, outflowing material, but is unlikely to be able to expel material out of a galaxy entirely. However, the combination of many supernovae produces overlapping, super-heated bubbles with high-velocity outflowing winds (Heckman et al., 1990; Lehnert & Heckman, 1996), able to drive galactic outflows on a large scale. Wilman et al. (2005) have shown that galaxies may influence the IGM on scales exceeding 100 kpc.

These superwinds have been modelled in hydrodynamical simulations, which demonstrate well how supernova-driven outflows heat and enrich the surrounding IGM (Fig. 1.5). These simulations have suggested that outflows play a crucial role in quenching star-formation, which is otherwise over-predicted (Davé et al., 2001; Springel & Hern-

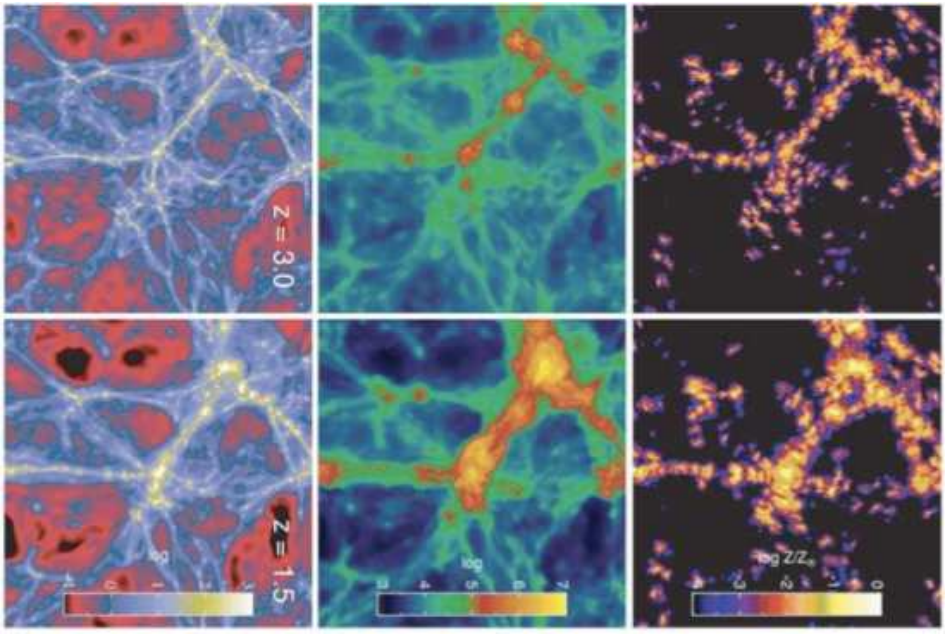

FIGURE 1.5: *Simulated heating and enrichment of the IGM by galaxies. Left to right, the images show matter density, temperature and metallicity; the top row shows snapsnots at $z = 3.0$, the bottom row at $z = 1.5$. As the matter distribution has condensed and galaxies have formed, bubbles have been created around this structure by large-scale galactic winds, in which the IGM is heated and metal-enriched. Figure adapted from Oppenheimer & Davé (2006)*

quist, 2003). Springel & Hernquist (2003) also show that galactic outflows can explain the low fraction of baryonic matter located in stars, while Erb et al. (2006) show that an outflow model can explain the observed mass-metallicity relation (Tremonti et al., 2004). Simulations by Oppenheimer & Davé (2006) have shown that the winds are likely to be momentum-driven, with greater outflow velocities in galaxies with higher star-formation rates.

Adelberger et al. (2003) cross-correlated $z \approx 3$ LBG positions with Lyα absorption features in QSO sightlines to measure the effect LBGs have on their environment. They detected a significant increase in neutral hydrogen within 5 h^{-1} Mpc of LBGs, consistent with these galaxies lying in regions of overdensity in the underlying dark matter distribution; however, at $\lesssim 1\ h^{-1}$ Mpc from LBG positions they measured a decrease in the amount of neutral hydrogen. It was suggested that high-velocity galactic winds had created an envelope from which the H I had been expelled. Further observations by Adelberger et al. (2005), however, failed to detect this decrease in neutral hydrogen. Crighton et al. (2010) also found no evidence for this effect, but noted that redshift mea-

surement errors and intrinsic LBG velocity dispersions could substantially smooth out any detectable hydrogen transmission spike.

In summary, simulations strongly suggest that feedback associated with supernova-driven galactic outflows is a vital component of galaxy evolution, and considerable observational evidence exists to indicate that such outflows occur. However, more observational evidence regarding the nature and extent of these large-scale, high-velocity outflows is essential to better understand the relationship between galaxies and the IGM and to further constrain theoretical models.

1.3 The submillimetre population

Contemporaneous with the first major LBG surveys was the advent of a new ground-based bolometer sensitive to radiation in the submillimetre (sub-mm) regime, opening a new window on the high-redshift universe. Blank-field surveys with this instrument, the Submillimetre Common-User Bolometer Array (SCUBA; Holland et al., 1999) on the Atacama Pathfinder Experiment (APEX) telescope, revealed a population of bright galaxies at $\lambda = 850\mu$m (Smail et al., 1997; Barger et al, 1998; Hughes et al., 1998), which did not appear to have bright optical counterparts.

Bright sub-mm galaxies lie at high redshifts, with an $n(z)$ distribution peaking at $z \approx 2$ (Chapman et al., 2005). Observations at 850μm favour high-z detections because of the strong negative k-correction at this wavelength for typical extragalactic source spectral energy distributions. In the rest frame, 850μm lies on the long-wavelength tail of the blackbody emission associated with cool dust (Fig. 1.6*a*); as redshift increases, the observed 850μm band samples the SED at points increasingly high up the blackbody curve, where the flux from the object is much greater, yielding a strongly negative k-correction. This is balanced somewhat by the $1/d_L^2$ dependence of the received flux, where d_L is the luminosity distance to the source, which acts to reduce the apparent brightness of the object. The result of these competing processes is that sources of a given luminosity will have roughly the same observed 850μm flux across the range $1 < z < 10$ (Fig. 1.6*b*).

1.3.1 Dust emission

Emission in the far-infrared and sub-mm regimes arises from dust emission. Several components of dust in galaxies and AGN have been identified, including water ice, sili-

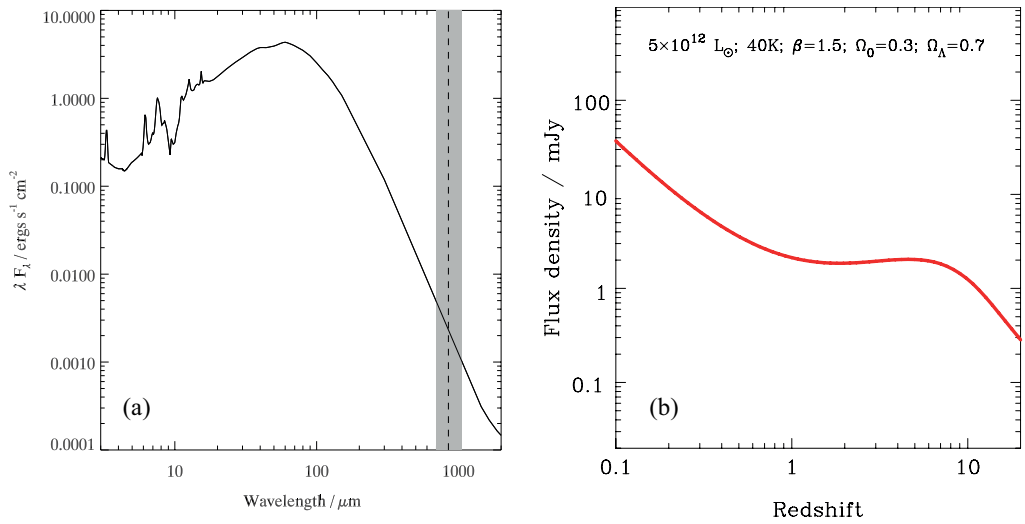

FIGURE 1.6: (a) *The rest-frame mid-IR–sub-mm SED of the starburst galaxy M82. The wavelength range of the SCUBA 850μm filter is shown by the grey region. In the rest-frame the sub-mm band samples the long-wavelength tail of the dust emission peak, but as the SED is redshifted it observes increasingly further up the blackbody curve; this is the origin of the strong negative 850μm k-correction.* (b) *The observed 850μm flux of a fixed-luminosity source at increasing redshift. Due to the strong k-correction, the apparent flux remains the same from $z = 1$ to $z = 10$. Panel* (b) *adapted from Blain et al. (2002).*

con carbide and ammonia (Stein & Soifer, 1983), as well as long hydrocarbon molecules responsible for several prominent mid-infrared emission lines (Leger & Puget, 1984), however by far the largest fraction is made up of graphite and silicate grains (Stein & Soifer, 1983; Draine & Lee, 1984). These grains, less than 1μm in diameter, are stochastically heated by absorbing energetic UV/optical radiation emitted from stars and active nuclei. The dust then cools by reradiating this energy at longer, infrared wavelengths.

The wavelength at which this re-emission peaks depends on the temperature of the dust grains, according to Wein's displacement law, $\lambda_{\rm max} \propto 1/T$. In regions where the radiation field is strongest, close to stars or a nuclear source, the dust can reach high temperatures. A maximum is set by the sublimation temperatures of silicates and graphite; 1000 K and 1500 K, respectively. FIR/sub-mm emission, however, is associated with cool dust at $T \approx 20$–60 K, lying further from the sources of radiation (or shielded from it). Dust temperatures measured for bright sub-mm sources are generally $T \approx 30$–40 K (Chapman et al., 2005; Pope et al., 2006; Coppin et al., 2008b; Elbaz et al., 2010)

1.3.2 Properties of submillimetre sources

A major challenge in discerning the nature of sub-mm sources has been the difficulty in measuring counterparts. Sub-mm bright sources are typically optically faint, so deep imaging is required to detect them in optical bands. The wide, 15–20″ beam of sub-mm instruments means positional uncertainties are very high, and since optical observations can reach sub-arcsecond resolutions, any sub-mm source is likely to have many possible faint optical counterparts.

By exploiting the radio-FIR correlation measured for local star-forming galaxies (Condon, 1992), it is possible to use radio observations to pin down the position of a sub-mm source with greater accuracy. The assumption is that a radio source lying within the positional error of a sub-mm source can be reliably taken as its counterpart. However, robust radio counterparts are typically measured for only around half of sub-mm galaxies (Ivison et al., 2002; Borys et al., 2004; Wardlow et al., 2010). Mid-IR imaging can be used to find additional sub-mm source counterparts, however the increase is fairly modest (Wardlow et al., 2010). Nevertheless, these multiwavelength matching procedures are crucial to determining precise positions for sub-mm sources enabling them to be studied further. This of course introduces a selection effect into most studies of sub-mm galaxies, with analyses being based on the radio-detected subset of the sub-mm population. Statistical methods, which avoid the need to identify counterparts, can offer a way around this problem: this is the subject of Chapter 2.

Notwithstanding the limitations described above, much is now known about the sub-mm population. These are high-redshift sources with extremely high bolometric luminosities ($\gtrsim 10^{12}$ $L_\odot$), comparable to local ultraluminous infrared galaxies (ULIRGs) or high-redshift quasars. While such ultraluminous galaxies are quite rare in the local universe (Soifer & Neugebauer, 1991), bright sub-mm galaxies appear to be far more commonplace at $z \approx 2$ (Blain et al., 2002). The number counts of sub-mm galaxies show evidence for strong evolution in this population (Smail et al., 1997; Coppin et al., 2008a). Sub-mm sources are rich in gas (e.g. Greve et al., 2005) and dust (e.g. Santini et al., 2010), with the high dust masses responsible for their optical faintness.

These sources are known to host both AGN and starburst activity (e.g. Alexander et al., 2005). Many authors have suggested that the star-formation component signficantly dominates the bolometric output of the galaxies, with extremely high implied star-formation rates on the order of 100–1000 $M_\odot$ yr^{-1} (Coppin et al., 2006). However,

the contribution made by the active nucleus to the total power output is yet unclear. Observations of sub-mm galaxies in the X-ray and mid-IR have yielded estimates of 8–30% (Alexander et al., 2005; Pope et al., 2008), however a major caveat to these results remains: if the AGN is very heavily obscured — in particular if it is Compton-thick[3] — then current measurements of its bolometric contribution will be substantially underestimated. This is discussed further in Chapter 3.

Sub-mm observations of high-redshift QSOs have suggested that a dichotomy may exist between obscured and unobscured quasars, with the former being preferentially brighter in the sub-mm than the latter. Page et al. (2004) measured sub-mm fluxes for two matched-luminosity samples of QSOs, one unobscured ($N_{\rm H} < 10^{22}$ cm^{-2}) and one obscured ($N_{\rm H} > 10^{22}$ cm^{-2}), finding that the high-z obscured sources showed higher fluxes. Subsequent works have also suggested that more obscured AGN may be brighter in the sub-mm (e.g. Priddey et al., 2007; Martínez-Sansigre et al., 2009; Rigopoulou et al., 2009; Hill & Shanks, 2010a). This has important implications for our understanding of active galactic nuclei, which are discussed next.

1.4 Active galactic nuclei

It is now well accepted that most, or perhaps all, massive galaxies host at their centre a supermassive black hole (Kormendy & Richstone, 1995; Magorrian et al., 1998). Exactly how these black holes (BHs) form and evolve is not entirely clear, but observations showing that the BH mass correlates strongly with the velocity dispersion of the galactic bulge (the M–σ relation; Gebhardt et al., 2000) indicate that the process of BH and galaxy formation are interlinked.

In a minority ($\sim$ a few per cent; Huchra & Burg, 1992) of local galaxies, the supermassive black hole is not in a quiescent state, but is instead actively accreting matter. As the matter is drawn gravitationally toward the BH, conservation of angular momentum causes it to form a flattened rotating disc, called the accretion disc. The gravitational potential of the infalling matter is converted into radiative energy, resulting in a luminous output from the central core, which in this state is termed an active galactic nucleus (AGN). Since the masses involved are so great, the energy output from the accretion process is extremely high: the brightest active galactic nuclei are the most luminous objects in the universe.

[3] a neutral hydrogen column density of $N_{\rm H} \gtrsim 10^{24}$ cm^{-2}

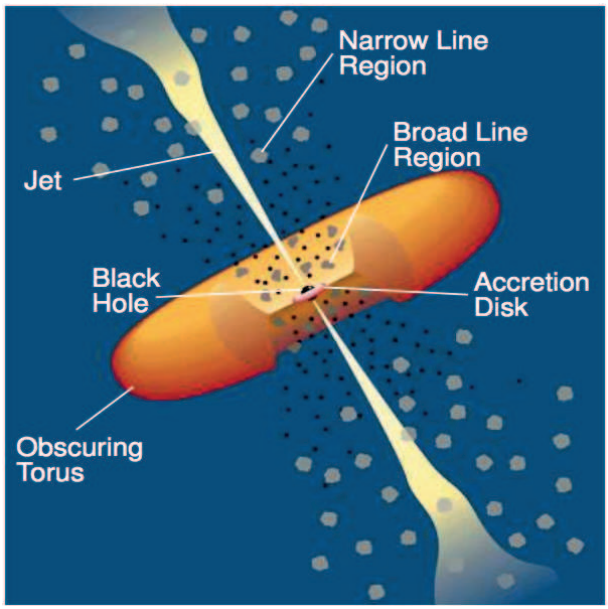

FIGURE 1.7: *The unified AGN model with key components, as described in the text, indicated. The figure is an illustrative guide only and is not to scale. Original figure: Urry & Padovani (1995).*

Studies of AGN date to the work of Seyfert (1943), who first identified such objects from the optical emission lines in their spectra, leading to their being called Seyfert galaxies. Khachikian & Weedman (1974) later showed that Seyferts could be divided into two distinct classes: Seyfert 1s, whose spectra include both broad (several $\times\ 10^3$ km s^{-1}) and narrow ($< 10^3$ km s^{-1}) emission lines, and Seyfert 2s, in which only the narrow lines are observed. A similar distinction exists in quasi-stellar objects (QSOs; quasars[4]), with type 1 quasars and type 2 quasars defined analogously to the Seyfert classes. The distinction between QSOs and Seyferts lies in their luminosity, with quasars being the more luminous. LINERs are an additional AGN class, falling below Seyferts on the luminosity scale.

1.4.1 AGN unification

The standard model for AGN today is the 'unified model' (Antonucci, 1993). In this paradigm, the broad-line and narrow-line classes of AGN/quasars do not represent different types of object; they arise solely from orientation effects. For a given luminosity,

[4]Traditionally, the term *quasar* applies only to those very luminous AGN which are radio-loud, being a contraction of *quasi-stellar radio source*, however in the current usage it has come to refer to any quasi-stellar object, particularly when the radio properties are not under consideration. The terms radio-quiet and radio-loud quasar, though incompatible with the original usage, are widespread as a result.

therefore, no *intrinsic* difference between the type 1 and type 2 sources is though to exist.

The model invokes an optically and geometrically thick torus of dust which encircles the central nucleus. Crucially, the toroidal geometry of the dust means that an observer with a side-on perspective will see only the outer edge of the torus and not the nuclear region within it, while a face-on observer will have an unobstructed view of the core (Fig. 1.7). These different inclinations result in the type 2 and type 1 classifications, respectively, with the different observed spectral features arising because the gas in different parts of the AGN orbits the BH at different velocities.

The high velocity material forms what is called the broad-line region (BLR; Fig. 1.7) and lies in the circumnuclear region relatively close to the central black hole, resulting in high velocities which cause Doppler broadening of the emission lines. The gas here is photoionised by the central source, and must be fairly dense as forbidden transition lines (which occur only in low-density gas) are collisionally suppressed (Ferland & Peterson, 1989; Ferland et al., 1992). The BLR likely consists of a large number of small gas clouds (e.g. Dietrich et al., 1999) contained within a compact region on the scale of just several light-days (Peterson & Wandel, 1999).

The narrow-line region (NLR; Fig. 1.7) is many orders of magnitude larger than the BLR, reaching kpc scales[5] (Crenshaw et al., 2000; Tadhunter et al., 2001; Holt, Tadhunter & Morganati, 2003). However, the density of gas in the NLR is several orders of magnitude below that of the BLR (Koski, 1978), and since emissivity goes as the square of density, it is therefore unsurprising that in spite of its small relative size the BLR, when visible, can dominate the observed spectrum of an AGN. The rarefied nature of the NLR gives rise to forbidden transitions, such as the prominent [OIII] $\lambda\lambda$ 4959 5007 lines (e.g. Kaiser et al., 1999; Baskin & Laor, 2005; Liu et al., 2010).

The unified AGN model therefore represents a remarkably elegant way of reconciling the different observed populations of AGN. In essence, it states that AGN fall into two basic categories: obscured and unobscured, with the division dependent upon whether or not the AGN is viewed through the obscuring torus. Support for such a model may be found from X-ray observations: while the classical division between type 1 and 2 AGN is made based on optical emission lines, it is clear also that the unified model predicts that in other wavebands, such as the X-ray where AGN emit strongly, there should be a discernible difference between the two classes due to different levels of obscuration. X-ray surveys have shown that this trend exists, with type 2s generally exhibiting higher

[5]For comparison with the BLR, 1 kpc $\sim 10^6$ light-days

obscuring column densities than type 1s (e.g. Tajer et al., 2007; Stalin et al., 2010).

1.4.2 Non-unified schemes

In §1.3 it was noted that recent sub-mm surveys of obscured and unobscured AGN have revealed a preference for more obscured AGN to show greater sub-mm emission. This trend has been detected in samples of QSOs with matched luminosities (Page et al., 2004): the unified AGN model predicts no intrinsic difference between such populations, with the apparent differences expected to arise purely as a result of inclination effects.

Sub-mm radiation, however, is insensitive to such effects. Electromagnetic radiation at these long wavelengths is not absorbed by interstellar material, and should therefore escape from galaxies isotropically. Different sub-mm fluxes for obscured and unobscured AGN are therefore difficult to reconcile with the unified AGN model.

An alternative model to the unified scheme suggests that obscured AGN represent an earlier phase in the life cycle of AGN, preceding the unobscured phase (Fabian et al., 1999). This is discussed further in Chapter 3, where we also compare observational measurements of X-ray sources in the sub-mm to both unified and non-unified models.

1.4.3 X-ray properties of AGN

As noted above, AGN emit strongly at X-ray energies. Indeed, AGN are thought to be responsible for almost the entire cosmic X-ray background (e.g. Gilli, Comastri & Hasinger, 2007). X-ray emission is produced in the central nuclear region of the AGN, where the infall of matter onto the supermassive BH generates a high flux of ultraviolet photons (Shakura & Sunyaev, 1973). Inverse Compton scattering of these photons by hot electrons in the accretion disc results in an up-scatter to X-ray energies (Haardt & Maraschi, 1991, 1993).

There are two primary mechanisms by which these X-rays may then prevented from escaping from the source and reaching the observer. The first is photoelectric absorption, which occurs when X-rays excite or ionise the inner (K-shell) electrons of atoms in the obscuring medium; this can occur in elements up to Ni (Turner & Miller, 2009). The likelihood of photoelectric absorption events *decreases* with increasing X-ray energy. The second is Compton down-scattering, the inelastic scattering of X-rays by electrons, which acts to reduce the X-ray energy. The fractional energy loss is given by $\Delta E/E \approx 2E/m_{\rm e}c^2$ (Turner & Miller, 2009), so the efficiency of this mechanism *increases* with increasing en-

ergy.

Both processes occur more frequently in sources with higher column densities of obscuring gas, with Compton scattering only occurring significantly when the column density exceeds the inverse of the Thomson cross-section; such sources are called Compton-thick. In Compton-thin AGN, therefore, photoelectric absorption is the only noteworthy process by which X-rays are obscured, and thus such sources can always be observed at energies above a few keV ('hard X-rays'). In Compton-thick AGN, however, the down-scattering means that X-ray emission is suppressed at high energies as well, making these sources extremely hard to detect in the X-ray.

The potential to observe X-rays from Compton-thick AGN does remain, by virtue of the Compton reflection component (e.g. Matt et al., 1996, 2000). These Compton-scattered X-rays have a hard continuum with a peak at 20–30 keV — the flux falls off at lower energies due to absorption, at higher energies due to Compton scattering (Comastri, 2004). Since the measured X-ray background also shows a hard continuum with a similar peak at this energy, it has been suggested that the Compton reflection emission from obscured AGN may be a crucial aspect of fitting the X-ray background (e.g. Fabian et al., 1990).

1.5 This thesis

This thesis presents recent results regarding the evolution of galaxies and AGN, with a focus on sources at high redshifts ($z \gtrsim 2$). In Chapter 2 we present observational analyses of the link between X-ray-detected AGN and sub-mm sources. Investigations of the AGN contribution to sub-mm galaxies are important to understanding the star-formation and accretion histories of the universe. In Chapter 3 we employ a model of obscured AGN to estimate the contribution made by the X-ray-undetected population, missing from our X-ray sample. We use the observational results from Chapter 2 to test and constrain our AGN model.

In Chapter 4 we investigate the applicability of pure luminosity evolution models, known to describe well observations of galaxies in the optical and near-infrared, at mid-IR, far-IR and sub-mm wavelengths. Where the galaxy model breaks down, we once again investigate the possible AGN contribution, using the same obscured AGN model as in Chapter 3.

Chapter 5 presents initial results of a deep sub-mm survey of the William Herschel

Deep Field. Using statistical techniques we find an indication that obscured AGN may be brighter in the sub-mm than unobscured AGN, consistent with our results in Chapters 2–3 as well as other published findings.

As discussed in this Introduction, the two most effective methods of high-redshift source detection are sub-mm observations and the Lyman-break technique. With Chapters 2–5 focussing on the former, in Chapters 6–7 we explore the latter.

Chapter 6 presents the results of a large survey we have undertaken of $z \approx 3$ LBGs. We describe the analysis of 5 new fields in which a spectroscopic survey has been carried out using the VIMOS spectrograph, resulting in > 1000 new LBGs with confirmed redshifts. This sample represents the second half of a larger survey, the first half of which was presented by Bielby et al. (2010). In Chapter 7 we combine the two samples, yielding a catalogue of > 2000 LBGs, in order to analyse the clustering and supernova-driven feedback of these high-z galaxies.

A cosmology with $H_0 = 70$ km s^{-1} Mpc^{-1}, $\Omega_m = 0.3$ and $\Omega_\lambda = 0.7$ is assumed unless otherwise stated.

II

The contribution of AGN to the sub-mm population

2.1 Introduction

It is now more than a decade since the first blank field surveys with the SCUBA instrument (Holland et al., 1999) on the James Clerk Maxwell Telescope revealed the existence of large numbers of highly luminous sources for which a significant fraction (often the majority) of the total bolometric output is in the far-infrared and submillimetre wavelength regimes (e.g. Smail et al., 1997; Barger et al, 1998; Hughes et al., 1998). These bright objects were quickly found to lie at high redshifts and to be heavily obscured by dust (for a review see Blain et al., 2002). There is now evidence that they host considerable star formation as well as concurrent AGN activity (Alexander et al., 2005). Although many authors have concluded that the former process dominates the bolometric luminosity of sub-mm galaxies, the contribution of AGN nevertheless remains unclear.

Obscured quasars are the primary candidates to explain the "missing" hard X-ray background (e.g. Worsley et al., 2005). Since these highly absorbed sources are likely to be dust-rich objects, they would be expected to have substantial luminosities in the infrared where the reprocessed light is emitted. The wavelength regime in which this emission peaks will depend upon the typical temperature of the obscuring dust. If it is cool enough, sub-mm galaxies are viable candidates for this long-sought obscured quasar population. Obscured AGN models have been shown to give a reasonable fit to the bright end of the sub-mm source counts (Gunn & Shanks, 1999), while star-forming galaxies are expected make the dominant contribution at fainter fluxes (Busswell &

Shanks, 2001).

Many authors have presented sub-mm and millimetre observations of high-z QSOs (e.g. Andreani et al., 1993; Chini & Krügel, 1994; McMahon et al., 1994; Omont et al., 1996, 2001, 2003; Hughes et al., 1997; Priddey et al., 2003; Rawlings et al., 2004; Petric et al., 2006; Coppin et al., 2008a; Martinez-Sansigre et al., 2009), however the issue of whether the active nucleus is ultimately responsible for the high luminosities at long wavelengths remains a largely open question. Observational analyses are often unable to exclude either a starburst-dominated or an AGN-dominated system (e.g. Priddey & McMahon, 2001; Petric et al., 2006).

One of the key tenets of the unified AGN model (Antonucci, 1993) is that the nucleus is surrounded by dust with a toroidal geometry, such that different viewing angles provide access to different regions, thus giving rise to the separate classifications of narrow- and broad-line AGN. This dust is irradiated by the active nucleus and since the luminosities of these sources are very high the surrounding dust can be heated to high temperatures. If the sub-mm emission results from dust irradiated by the AGN instead of star-formation, it must lie far enough from the central engine to maintain a cool (~ 30K) temperature. Simple torus models have shown that this is possible – the extent of the dusty torus can reach the kiloparsec scale, and dust at these large radii can be cool enough to produce sub-mm/millimetre emission consistent with observed spectra (Granato & Danese, 1994; Andreani et al., 1999; Kuraszkiewicz et al., 2003).

As noted in Chapter 1, recent sub-mm observations of AGN have somewhat called into question the unified AGN model, with studies such as that by Page et al. (2004) indicating that more X-ray absorbed AGN may be much brighter in the sub-mm than unabsorbed AGN. Such a dichotomy is not easily explained by the unified model, since sub-mm emission is not absorbed by dust or gas and so should not be affected by viewing angle. Instead, absorbed and unabsorbed AGN may form an evolutionary sequence (Fabian, 1999).

This chapter presents work which exploits the unprecedented combination of depth and width in the sub-mm and X-ray data of the Extended *Chandra* Deep Field South to present new tests of predictions of models for the AGN contribution to the sub-mm number counts and background. We shall mainly be using cross-correlation and stacking techniques which avoid the need to identify individual sub-mm sources with individual X-ray or optical sources. Such identifications are always difficult when the sub-mm resolution is poor and here we restrict ourselves to statistical measurements of the properties

of sub-mm sources near X-ray and optical sources.

The first most basic test of such models is that AGN X-ray sources should cross-correlate on the sky with sub-mm sources. Previous results have been ambiguous – Almaini et al. (2003) measured a positive correlation out to large angular separation ($\theta \approx 2'$), while Borys et al. (2004) found that although a large fraction of sub-mm sources had coincident X-ray sources ($\theta < 7''$), there was no correlation out to larger separations.

The X-ray and sub-mm data can also test unified versus non-unified pictures for the AGN absorption (Page et al., 2004). The most heavily absorbed AGN may only be detected via the host galaxy at optical/IR wavelengths; we shall therefore also look for cross-correlations between sub-mm sources and normal, high redshift galaxies and compare any excess to AGN model predictions.

2.2 Data

In this work we have made use of multiwavelength data from the Extended *Chandra* Deep Field South (ECDFS), which covers $\approx 30 \times 30$ arcmin^2. The ECDFS comprises four contiguous fields, each with ≈ 250ks *Chandra* exposures, arranged in a 2×2 grid centred on the 1Ms *Chandra* Deep Field South (CDFS). We use the X-ray point source catalogue presented by Lehmer et al. (2005), who detect 762 X-ray point sources in the ECDFS. They give accurate positional measurements with a median uncertainty of $0''.35$ and provide soft band (0.5–2keV), hard band (2–8keV) and full band (0.5–8keV) fluxes.

Chandra's increased off-axis PSF means that the sensitivity in each of the four ECDFS frames is worst around the edges – this includes the centre of the ECDFS where the four individual frames meet. This central area was covered by the original CDFS observations; we therefore combine the catalogue of Lehmer et al. (2005) with the CDFS catalogue of Giacconi et al. (2002). We match sources to avoid duplication and include only those CDFS sources with soft-band fluxes of $S_{0.5-2.0} \geq 1 \times 10^{-16}$ergs s^{-1} cm^{-2}, such that the depth of the central region is the same as that of the extended field. This yields a final ECDFS catalogue of 852 X-ray sources.

We make use of a sample of X-ray sources with confirmed spectroscopic redshifts. These are taken from a survey of the central CDFS area by Tozzi et al. (2006) and a wider survey of the full ECDFS by Treister et al. (2009). Objects from Treister et al.'s catalogue lying within 3″ of an object in Tozzi et al.'s catalogue are excluded. This yielded a spectroscopic redshift sample of 277 X-ray sources. We also supplement this with 114

photometric redshifts from Tozzi et al.'s (2006) catalogue.

The ECDFS was observed at 870μm with the Large APEX Bolometer Camera (LABOCA; Siringo et al., 2009) on the APEX telescope (Güsten et al., 2006) as part of the LABOCA ECDFS Sub-mm Survey (LESS; Weiß et al., 2009)[1]. With ≈ 200 hrs total on-source integration time these observations reached a uniform noise level of 1.2 mJy beam^{-1} over the full $30' \times 30'$ area. We make use of the resulting beam-smoothed sub-mm map as well as the catalogue of 126 sources detected at $\geq 3.7\sigma$ (Weiß et al., 2009).

At 24μm and 70μm we use public imaging from the Far-Infrared Deep Extragalactic Legacy Survey (FIDEL; Dickinson et al., 2007) using the Multiband Imaging Photometer for Spitzer (MIPS; Rieke et al., 2004). The SExtractor source extraction software was used to obtain source lists from these images.

The ECDFS is one of four fields observed in the optical/near-IR as part of the Multiwavelength Survey by Yale-Chile (MUSYC). We make use of their publicly released BVR-selected catalogue (Gawiser et al., 2006) which has ∼85,000 objects and reaches a depth of $R < 26.4$.

2.3 Methodology

2.3.1 Statistical techniques

We perform statistical analyses of ECDFS sources in the X-ray, sub-mm, optical and infrared, making use of the angular two-point correlation function, $w(\theta)$, defined according to Eqn. 2.1.

$$w(\theta) = \frac{\mathrm{DD}}{\mathrm{DR}} - 1 \tag{2.1}$$

where DD and DR are the number of data–data and data–random pairs, respectively, at a given angular separation θ.

This function determines the significance of any overlap between two populations (that is, how many objects in one population coincide with an object in the other) by measuring the number of pairs of objects across the two datasets at a given angular separation; these are data–data pairs. The same measurement is made after substituting one dataset for a set of randomly distributed sources, to find the numbers of data–random

[1]ESO programme IDs 078.F-9028(A), 079.F-9500(A), 080.A-3023(A) and 081.F-9500(A)

pairs. The correlation function compares the number of data–data pairs at a given separation to the number of data–random pairs, in order to measure whether any excess exists.

We also use another formulation of the correlation function, which is equivalent to a stacking analysis. Here, we cross-correlate the objects in a source list with each individual pixel of a flux map in order to measure the excess of flux associated with the objects in the list. We find the average pixel value within annuli of increasing radius, having subtracted the mean flux. In this case $w(\theta)$ is defined as:

$$w(\theta) = \frac{\sum_{i=1}^{n_\theta}(f_i(\theta) - \bar{f})}{n_\theta} \tag{2.2}$$

where n_θ is the number of pixels in a given θ-bin, f_i is the value of the $i^{\rm th}$ pixel in that bin and $\bar{f}$ is the average pixel value. In both cross correlation techniques we make use of the NPT cross-correlation software of Gray et al. (2004).

2.3.2 Error analysis and simulations

We measure the uncertainties on our cross-correlation results using jackknife errors, dividing the field into a 3×3 grid and measuring the correlation function with each of the regions excluded in turn. This provides nine separate measurements of $w(\theta)$, from which we find the jackknife error as the standard deviation of the nine results multiplied by $\sqrt{N-1} = \sqrt{8}$. This method is intended to give a truer estimate of the error than simple Poisson statistics. In Fig. 2.1 we compare a set of jackknife and Poisson errors and find that the two are comparable out to $\theta \sim 30''$, suggesting that Poisson statistics can be used fairly reliably at low separations. At higher angular separations, where the number of pairs becomes large, Poisson statistics underpredict the error.

Our primary cross-correlation result, presented in the next section, shows a significant cross-correlation between X-ray and sub-mm sources. As a further test of this result we will perform simple simulations to measure the likelihood of it arising by chance, by replacing the real sub-mm source list by simulated catalogues which have the same number of sources, and repeating the cross correlation analysis using the simulated catalogues.

The real submillimetre sources are not uniformly distributed across the field and

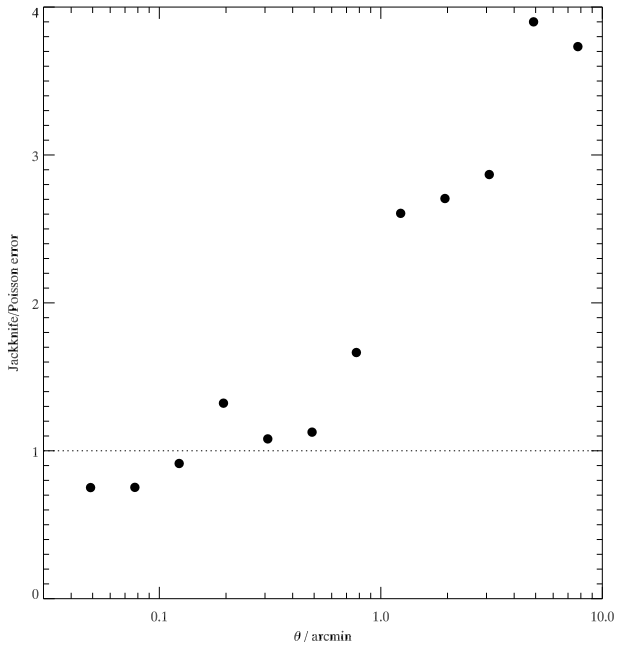

FIGURE 2.1: *A comparison of jackknife errors and Poisson errors, showing that at $\theta \leq 30''$ the two are fairly comparable but that at greater separations the Poisson error may be an underprediction of the true uncertainty.*

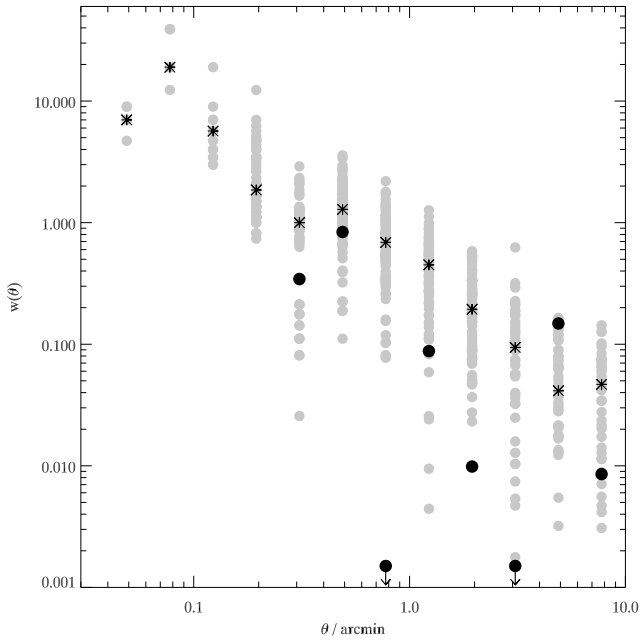

FIGURE 2.2: *Autocorrelation of the 126 submillimetre sources (black circles) compared to that of 100 simulated catalogues of 126 sources (grey circles). The median value of the simulated catalogue autocorrelation is marked at each angular separation as a black asterisk. The clustering of the simulated catalogues is comparable to that of the real sources.*

therefore it is necessary, in order to ensure a robust test, that the simulated catalogues show the same level of clustering as the real catalogue. This is achieved by randomly placing 60 cluster centres around which 3 associated objects are placed with some clustering length, and then diluting this source list with a further 60 randomly located objects. This results in 240 sources, of which 126 are selected at random to appear in the final simulated catalogue such that it has the same size as the true submillimetre source list. The number of cluster centres, associated objects and random sources were chosen *a posteriori* in order to best match the clustering characteristics of the real submillimetre objects. Figure 2.2 shows the autocorrelation of the real submillimetre sources compared to that of 100 simulated catalogues; the simulated catalogues are seen to reproduce the clustering of the real sources well.

2.4 Cross-correlation with X-ray sources

Fig. 2.3 shows the result of our cross-correlation (Eqn. 2.1) of 852 *Chandra* X-ray sources with 126 LABOCA sub-mm sources; there is a significant positive correlation. *Chandra* sources are known to be dominated by AGN at the X-ray fluxes where these sources are selected; starbursts do not make a comparable contribution until $S_{0.5-2.0} \sim 10^{-17}$ergs s^{-1} cm^{-2} (Bauer et al., 2004), some $10\times$ fainter than the limit of the ECDFS data. Therefore, this result appears to suggest a strong AGN contribution to the sub-mm population.

Other authors have also presented cross-correlations of X-ray and sub-mm sources, as shown in Fig. 2.3. Almaini et al. (2003) cross-correlated *Chandra* X-ray sources in the ELAIS N2 field with 17 SCUBA 850μm sources and measured an extended correlation which they attributed to the two populations tracing the same large-scale structure. However, Borys et al. (2004) tested this result in the *Hubble* Deep Field North (HDFN) and did not detect any large-scale correlation.

Of the 19 SCUBA sources in the HDFN, Borys et al. (2004) report that 8 have an X-ray source within 7″; these pairs were excluded from their cross-correlation analysis, but if included would yield a positive peak in the correlation function at low separation. This is in line with our analysis, which shows a strong peak at $\theta \lesssim 10''$ but no evidence for the strong clustering at larger separations detected by Almaini et al. (2003).

We find 30 X-ray sources in the ECDFS which lie within 10″ of a sub-mm source, while a random distribution of sources would give only 7.5 such pairs (see Table 2.1). Assuming Poisson statistics, the detection of 30 pairs therefore represents an 8.2σ excess,

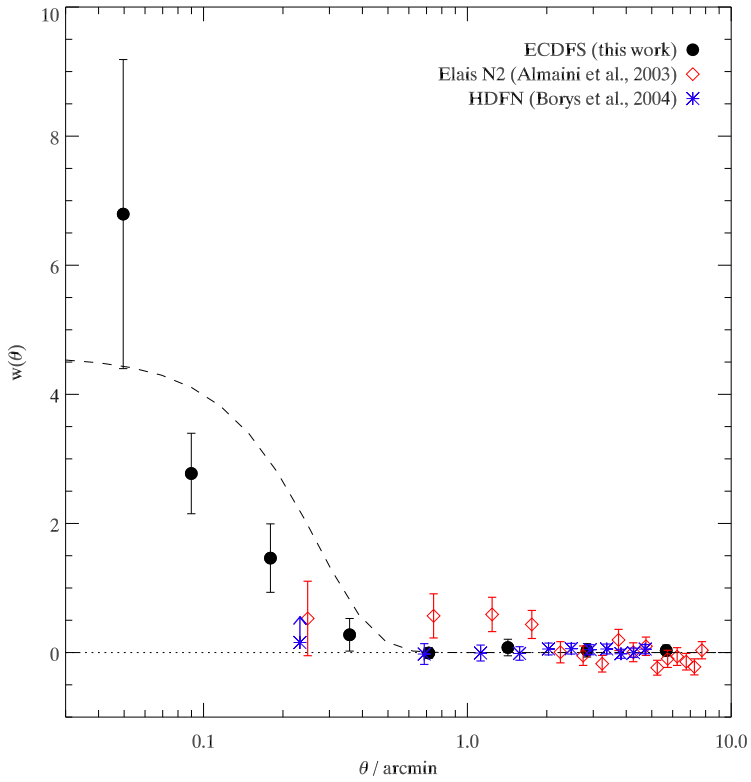

FIGURE 2.3: *Cross-correlation of sub-mm sources with X-ray sources showing a strong correlation between the two populations. An approximation of the LABOCA beam profile is indicated by the black dashed line; the correlation peak lies within the beam profile, showing no positive correlation out to larger separations. This is indicative of the detection of source counterparts rather than associated objects tracing the same structure. For comparison we show previous results by other authors: Almaini et al. (2003) detect an extended correlation at large separations, in contrast to our results and those of Borys et al. (2004). Borys et al. excluded pairs at low separation from their analysis, so we show the first point as a lower limit.*

and indicates that roughly a quarter of the 126 sub-mm sources have an X-ray source — likely an AGN — within the radius of the LABOCA beam. In 300 simulations we found no detections of a comparable correlation, suggesting that it is unlikely this result could have been achieved by chance.

2.4.1 X-ray flux dependence

In a non-unified AGN model absorbed and unabsorbed sources are intrinsically different, perhaps representing two stages of an evolutionary sequence, rather than differing purely due to orientation effects. In the absorbed phase the AGN is enshrouded by gas and dust; the unabsorbed phase occurs after this obscuring material has dissipated. Therefore, it is more absorbed AGN which are expected to be preferentially submillimetre-bright.

Models of X-ray number counts have shown that at bright fluxes unabsorbed AGN make the dominant contribution while absorbed AGN dominate at fainter source counts (e.g. Gunn, 1999; Gilli, Comastri & Hasinger, 2007). Based on these models, we divide the *Chandra* sources at a soft-band (0.5–2 keV) flux of $S_{0.5-2.0} = 1.5 \times 10^{-15}$ ergs s^{-1} cm^{-2}, yielding 685 faint X-ray sources and 167 bright sources.

In Fig. 2.4*a* we see that it appears certain that the faint X-ray sources show a significant correlation with sub-mm sources, while it appears that the bright X-ray sources are less — or not at all — correlated. In Table 2.1, alongside the data for the full X-ray sample, we show the numbers of detected and expected X-ray-sub-mm pairs for faint and bright sources. We confirm the strong significance of the correlation for the faint sources. Out to $\theta \leq 20''$ we find 58 pairs of sub-mm and faint X-ray sources compared to an expectation of 23.8, a 7.0σ excess assuming Poisson statistics, which we have determined to be reliable at these separations (§2.3.2). Any excess for the bright X-ray sources is less significant, although the statistics become poorer and the possibility that the bright and faint X-ray sources are drawn from the same population cannot be ruled out. Nevertheless, it appears certain that the strong cross-correlation found in Fig. 2.3 originates mostly in the fainter X-ray sources.

This result is in line with observations by Barger et al. (2001), who presented submillimetre observations of 135 X-ray sources in the *Chandra* Deep Field North. They found that the brightest X-ray sources were weaker submillimetre emitters than fainter X-ray sources.

Figs. 2.4*b* and *c* show the equivalent correlations between X-ray sources and the 24

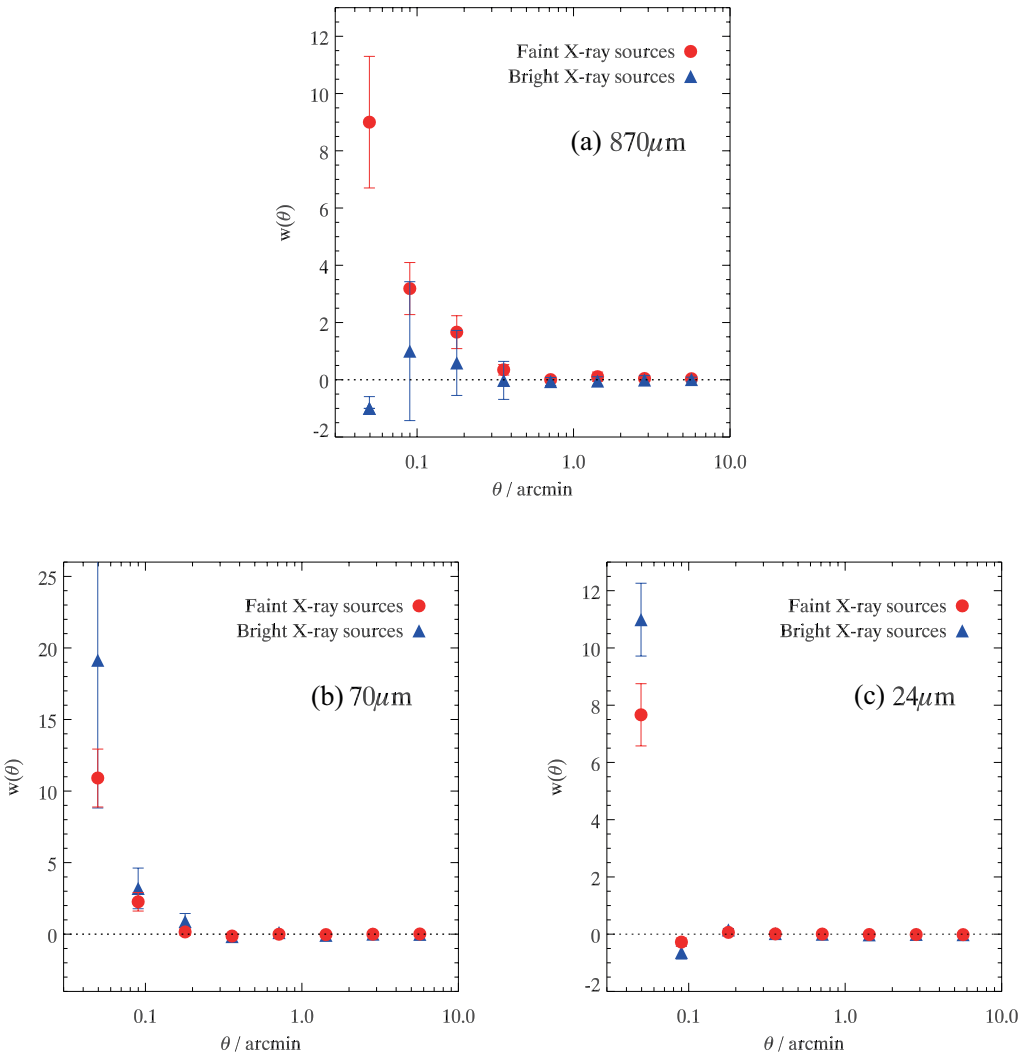

FIGURE 2.4: *Cross-correlation of* (a) *sub-mm,* (b) *70μm and* (c) *24μm sources with X-ray sources, with jackknife errors. Red circles represent the correlations for faint X-ray sources ($S_{0.5-2.0} < 1.5 \times 10^{-15} ergs\ s^{-1}\ cm^{-2}$), blue triangles show that for bright sources. At 24μm and 70μm, bright X-ray sources show a stronger correlation, but at 870μm this trend appears to be reversed. Note that the vertical scale is different for the central panel.*

TABLE 2.1: *Detected and expected numbers of X-ray–submillimetre pairs at separations of $\theta < 30''$ for all X-ray sources in the ECDFS and separately for those with bright and faint X-ray fluxes. The "expected" number of pairs is that which would arise from a random distribution of sources, while the detected number is that found from the real X-ray sources. In the first two bins we find 58 faint X-ray–submillimetre pairs, compared to an expectation of 23.8 pairs — a 7.0σ excess assuming Poisson statistics, which we have shown to be reliable at these angular separations. The bright sources show a far less significant excess, with 9 pairs in the first two bins compared to an expected 5.5.*

θ / arcsec	All X-ray sources		Faint X-ray sources		Bright X-ray sources	
	Detected	Expected	Detected	Expected	Detected	Expected
$0-10$	30	7.5	27	6.0	3	1.3
$10-20$	37	22.0	31	17.8	6	4.2
$20-30$	40	37.4	34	30.0	6	7.4

and 70 micron sources in the ECDFS. Here, strong correlations are seen split broadly evenly between the faint and bright sources. If anything, the brighter X-ray sources may show a stronger correlation than the fainter ones, contrary to the tentative indication in the sub-mm. One possible explanation would be the different k-corrections in these wavebands – at 870μm there is a strong negative k-correction, increasing the detection of high-redshift sources, while at 24μm and 70μm the k-correction is positive, favouring lower redshifts. This could account for the different results in Fig. 2.4. To test this, we cross-correlate the 24μm and 70μm sources with bright and faint X-ray sources in the redshift catalogue, imposing redshift cuts of $z > 0.5$ and $z > 1$; we find that the results are not affected.

Different dust temperatures might explain any difference in the sub-mm and 24–70μm properties of the bright and faint X-ray populations. If the faint sources include the more absorbed AGN, it may be that more absorbed sources have cooler dust temperatures — this idea is discussed further in §2.6. Any temperature difference between bright and faint flux X-ray sources is unlikely to be driven by warmer dust in more luminous sources, since Lutz et al. (2010) have shown that $L_X > 10^{44}$ ergs s^{-1} X-ray sources

have brighter sub-mm fluxes. We therefore next directly consider the luminosity dependence of the sub-mm properties of the ECDFS X-ray sources to test Lutz et al.'s result.

2.4.2 L_X dependence

Fig. 2.5 shows our sub-mm stacking analysis (Eqn. 2.2) for high- and low-luminosity X-ray sources, divided at $L_X = 10^{44}$ ergs s^{-1}. Here we focus on a stacking analysis to be consistent with Lutz et al. (2010). We find a clear difference between the low and high L_X sources in the sense that the high-L_X sources are brighter in the sub-mm, confirming the result of Lutz et al. In this analysis we have used a catalogue of 277 X-ray sources with confirmed spectroscopic redshifts, combining sources in the catalogues of Tozzi et al. (2006) and Treister et al. (2009).

Thus high-luminosity X-ray sources are stronger sub-mm sources than low-luminosity X-ray sources, whereas in Fig. 2.4 we found that fainter flux X-ray sources were significant sub-mm emitters. To make the comparison with Fig. 2.5 easier, in Fig. 2.6*a* we show the stacked sub-mm flux around faint and bright X-ray sources. This again shows that the faint-flux sources are at least as powerful sub-mm sources as the bright.

However, the comparison between the flux and luminosity results could be affected by the incompleteness of the spectroscopic redshift (spec-z) sample used to produce the L_X result. In Figs. 2.6*b* and *c* we show the equivalent results for the spec-z and photometric samples. Comparing Fig. 2.6*b* to Fig. 2.6*a*, it seems that the spec-z sample looks more similar to the L_X result in Fig. 2.5, with the brighter flux sources appearing more sub-mm bright than their fainter counterparts. Therefore, the spec-z sample may not be a representative subset of the X-ray sources in terms of the sources' sub-mm properties.

Comparing Figs. 2.6*a* and *b* suggests that there is a population of *Chandra* sources in the full ECDFS catalogue which have faint X-ray fluxes but are bright at 870μm, which are missing from the spec-z sample. If these faint sources also have lower X-ray luminosities, it would cast some doubt on the idea that sub-mm emission arises from high-luminosity sources only. We therefore next consider the differences between the spectroscopic sample and the full catalogue.

2.4.3 Incompleteness of the spectroscopic sample

We have seen that there is some indication of a difference between the sub-mm properties of X-ray sources in the full catalogue and of those in the spec-z subset, and we therefore

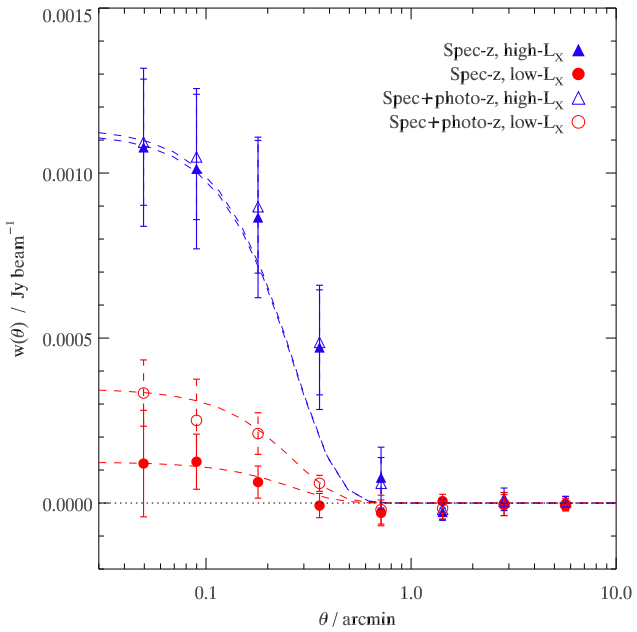

FIGURE 2.5: *Sub-mm stacking analysis of X-ray sources divided into high-luminosity ($L_X > 10^{44}$ ergs s^{-1}; blue triangles) and low-luminosity ($L_X < 10^{44}$ ergs s^{-1}; red circles). We show the results for the spec-z sample only (solid), and for the sample with photo-z also included (open). Sources are correlated with sub-mm pixel values to measure the excess of sub-mm flux associated with these sources. It is clear that the more X-ray luminous sources are brighter at 870μm. We again show the LABOCA beam profile, normalised to the data; the correlations are consistent with the beam profile, suggesting the detection of source counterparts rather than associated objects. The uncertainties shown are jackknife errors.*

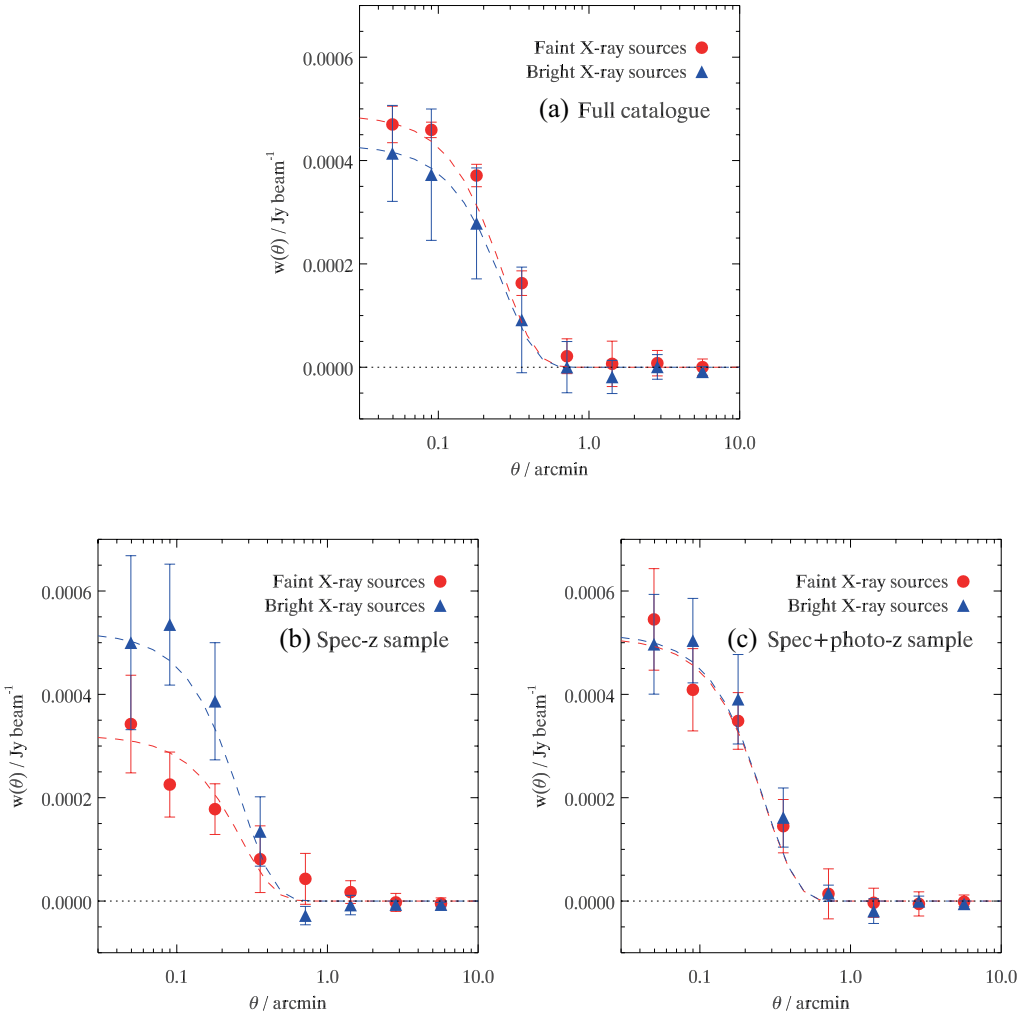

FIGURE 2.6: *Stacking analysis showing the average excess of sub-mm flux associated with faint ($S_{0.5-2.0} < 1.5 \times 10^{-15}$ ergs s^{-1} cm^{-2}) and bright X-ray sources in* (a) *the full ECDFS catalogue,* (b) *the spectroscopic sample and* (c) *the combined spec-z and photo-z sample. In the full catalogue, the faint sources show a higher stacked flux than the bright, but in the spec-z subset the bright sources dominate in the sub-mm, suggesting this sample is not representative of the full catalogue. The combined redshift sample is better representative of the full catalogue. We show the LABOCA beam profile (dashed/dash-dot line for faint/bright sources); the correlations are consistent with these lines, which again suggests the detection of source counterparts rather than associated objects. The uncertainties shown are jackknife errors.*

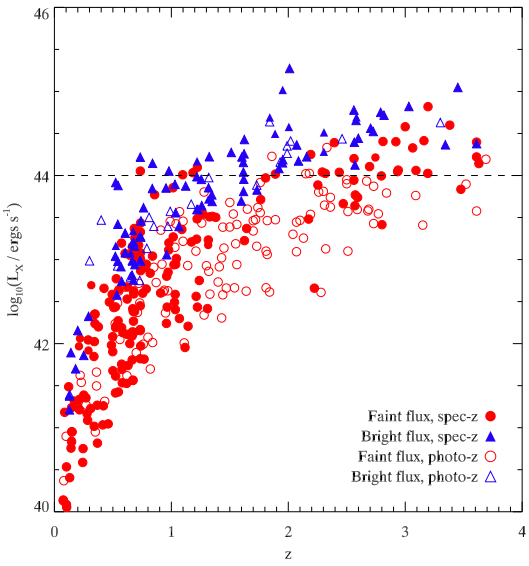

FIGURE 2.7: *X-ray luminosity as a function of redshift for ECDFS sources in the spec-z sample (filled points) and photo-z sample (open points). Faint X-ray sources are shown as red circles, bright X-ray sources as blue triangles. The line at $L_{\rm X} = 10^{44}$ ergs s^{-1} shows the luminosity limit which has been found to separate submm-bright and submm-faint sources. There is a notable deficiency of faint-flux spec-z sources in the range $1.3 < z < 2.5$.*

attempt to identify ways in which the latter is unrepresentative of the former. We first find that the spec-z sample is missing faint-flux, low-luminosity X-ray sources at high redshifts, with a particularly significant dearth of faint X-ray sources in the range $1.3 < z < 2.5$ (Fig. 2.7).

In this redshift range the spec-z sample consists almost entirely of bright X-ray sources, whereas the full sample would be expected to also include faint sources here. Submillimetre-bright objects are known to lie at high-redshift, with an $n(z)$ peaking at $z \approx 2$ (Chapman et al., 2005), so the deficiency of faint-flux, low-luminosity sources in this redshift range in the spec-z sample could be significant.

The upper panel of Fig. 2.8 highlights another aspect of the difference between the full and spec-z samples. There is an appreciable difference in the hardness of the sources in the full catalogue and the spec-z subset, with the latter significantly undersampling the harder sources.[2] A Kolmogorov–Smirnov (KS) test indicates a 0.26% likelihood that the two distributions are drawn from the same population, falling to 0.1% if the spikes

[2]Hardness ratio is defined as $HR = (H - S)/(H + S)$, where H and S represent the photon counts in the hard (2–8 keV) and soft (0.5–2 keV) bands, respectively

at $HR = \pm 1$ are excluded from the test. Since the difference between Figs. 2.6*a* and *b* may indicate that there exists a population of faint X-ray, submillimetre-bright sources without measured spectroscopic redshifts, the indication found here that the sources missing from the spec-z sample may typically be high-redshift, absorbed AGN provides an interesting suggestion that such sources are bright at 870μm.

We previously limited our redshift catalogue to only include secure spectroscopic redshifts measured by Tozzi et al. (2006) and Treister et al. (2009). We now add to the 277 spec-z sources 114 sources with photometric redshifts, also presented in Tozzi et al.'s catalogue. The distribution of hardness ratios for the photo-z sources is shown in the lower panel of Fig. 2.8 and it is clear that they better represent the overall distribution than the spec-z sources do. When added to the spec-z sample to give a combined redshift catalogue of 391 objects, a KS test yields a 2.3% likelihood that the redshift catalogue and the full catalogue sample the same population. Though still small, this probability is an order of magnitude greater than found previously. Additionally, Fig. 2.7 shows that the combined redshift catalogue does not exhibit the same deficiency of faint-flux, low-luminosity sources in the $1.3 < z < 2.5$ range. In Fig. 2.6*c*, we show that, having included these extra photo-z sources, the sub-mm stacking analysis for faint-flux objects now better resembles that found with the full sample.

However, while the sub-mm contribution from faint-flux X-ray sources has increased, Fig. 2.5 shows that this does not yield a substantial increase in the contribution from the X-ray sources with low intrinsic luminosities, which remains significantly below that of the high-luminosity sources. This suggests that the reduced sub-mm contribution found for faint-flux sources in the spec-z sample (Fig. 2.6*b*) was not simply the result of undersampling the low-luminosity X-ray sources. Instead, we continue to find that high-luminosity sources dominate the AGN sub-mm contribution.

This means that many of these high-luminosity sources must also be faint in X-ray flux. There is of course no necessary contradiction here, since these sources are expected to lie at high redshift. If there is also a preference for more absorbed AGN to be sub-mm bright, this would compound the effect, with absorption making the high-luminosity sources appear fainter still in X-ray flux. Of course, the full redshift sample still has less than half the total number of X-ray sources, so it remains conceivable that the sub-mm contribution of the low-L_X population could rise if these were to be included in Fig. 2.5.

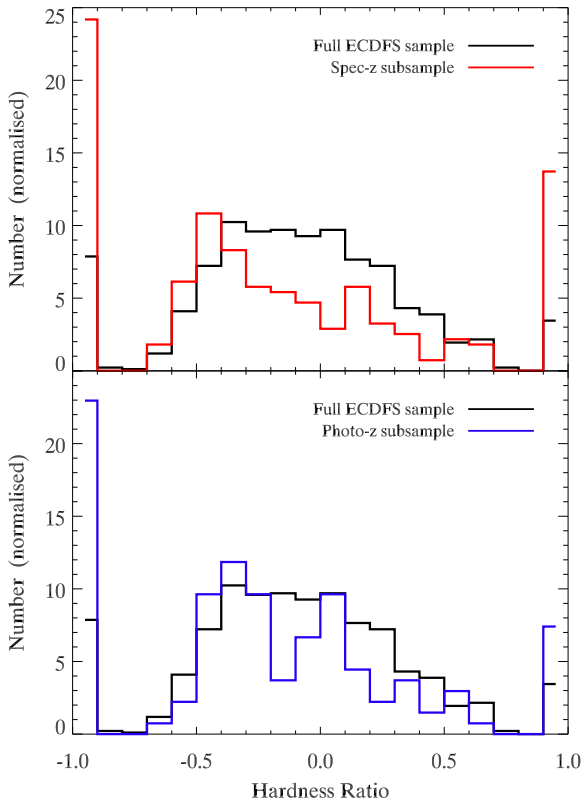

FIGURE 2.8: *The hardness ratio distribution of sources in the full ECDFS X-ray catalogue compared to those in the spec-z sample (top panel) and photo-z sample (bottom panel), all normalised to the same total number of sources. The spec-z subset significantly undersamples the harder sources in the ECDFS, while the photo-z sample contains relatively more hard sources and is better representative.*

2.4.4 Hardness ratio dependence

We now make a more direct test of the hypothesis that absorbed X-ray sources are strong sub-mm emitters by performing the sub-mm stacking analysis and cross-correlation for X-ray sources divided by hardness ratio. The stacking analysis is shown in Fig. 2.9*a* and although the significance is marginal, if anything it is the harder sources which contribute more than the softer ones. Our standard cross-correlation method (Eqn. 2.1) gives a similar result.

The division between 'harder' and 'softer' sources in Fig. 2.9*a* is at $HR = -0.4$, which corresponds to a hydrogen column density of $N_H = 10^{22}$ cm^{-2} at $z = 1$, assuming a power-law spectrum with $\Gamma = -2$. This column density is an appropriate place to divide the sample, since a non-unified AGN model (Chapter 3) predicts that $N_H > 10^{22}$ cm^{-2} sources are typically more sub-mm bright, while in the unified AGN model we should find that $N_H < 10^{22}$ cm^{-2} and $N_H > 10^{22}$ cm^{-2} sources have the same average sub-mm flux.[3]

Therefore, the finding that the stacked fluxes of the harder and softer sources are similar in Fig. 2.9*a* appears to be supportive of the unified AGN model. However, this analysis does not take into account the effect of redshift on hardness ratio. As Fig. 2.10 shows, at $z \geq 2$ our soft, $HR < -0.4$ population will include very absorbed ($\log(N_H/\mathrm{cm}^{-2}) = 22$–$23$) sources. It is therefore not certain that the sub-mm correlation measured for $HR < -0.4$ X-ray sources in Fig. 2.9*a* arises from the low-column, less absorbed population; it could instead be due to highly absorbed AGN at high-redshift. To break the degeneracy between redshift and column we must use the X-ray sources with known redshifts.

We divide the X-ray redshift sample (using both spec-z and photo-z) into four bins: $z = 0.25$–0.75, 0.75–1.5, 1.5–2.5 and 2.5–3.5. In each bin sources are split into hard and soft, with the divisions made at $HR = -0.25$, -0.37, -0.45 and -0.47, these being the hardness ratios corresponding to $N_H = 10^{22}$ cm^{-2} for $z = 0.5$, 1.0, 2.0 and 3.0, respectively (Fig. 2.10). This gives us a sample of $N_H < 10^{22}$ cm^{-2} sources and $N_H > 10^{22}$ cm^{-2} sources.

The sub-mm stacking analyses for these absorbed and unabsorbed samples are shown in Fig. 2.9*b*. There is now a stronger indication that the more absorbed sources are brighter in the sub-mm. Comparing the two panels of Fig. 2.9, it appears that some of

[3]This fiducial column of $N_H = 10^{22}$ cm^{-2} is also consistent with the result of Page et al. (2004), who find that quasars more absorbed than this limit dominate the sub-mm contribution.

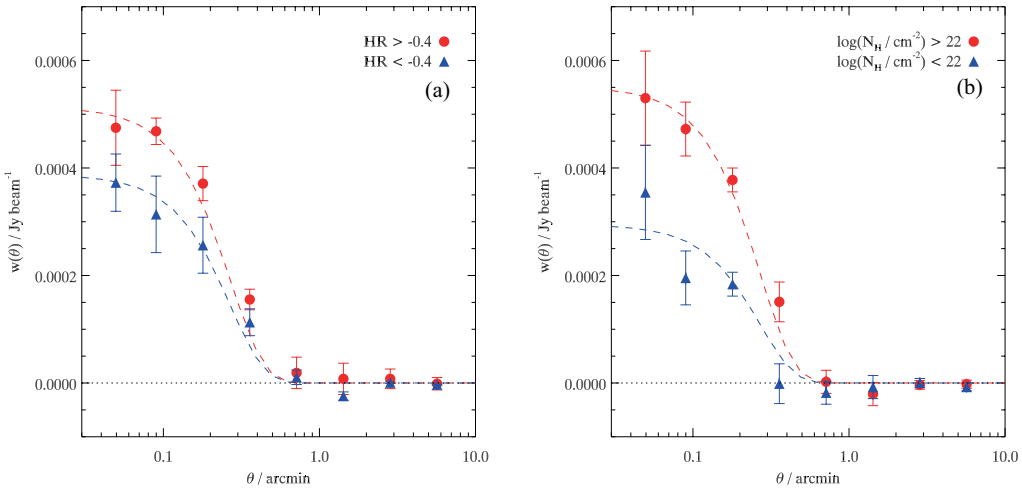

FIGURE 2.9: *Sub-mm stacking analyses for ECDFS X-ray sources.* (a) *X-ray sources are divided into hard (red circles) and soft (blue triangles) sources at a hardness ratio of* -0.4. (b) *X-ray sources are divided into absorbed (red circles) and unabsorbed (blue triangles) at a column density of* $N_H = 10^{22}$ *cm*$^{-2}$*; this is done by combining hardness ratio and redshift information, as described in the text. Jackknife errors are shown.*

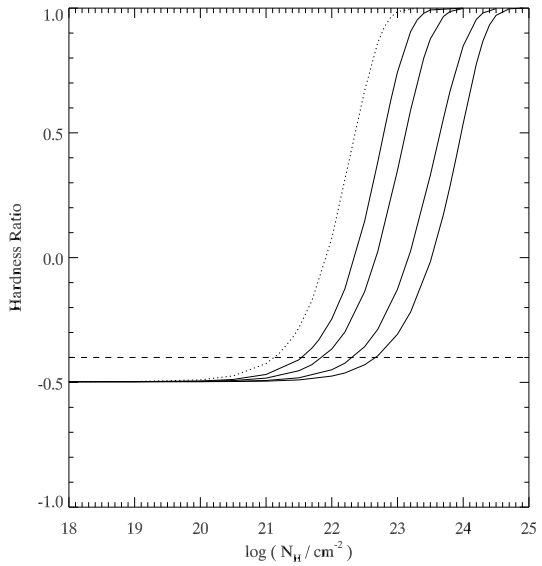

FIGURE 2.10: *Hardness ratio vs. hydrogen column density for AGN at different redshifts, generated with the* Chandra *PIMMS tools assuming a power-law spectrum with* $\Gamma = -2$. *The dotted line on the left represents* $z = 0$*; moving right, the next four lines are for* $z = 0.5$*, 1.0, 2.0 and 3.0. The dashed line at* $HR = -0.4$ *shows where we divide the sample for the analysis in Fig. 2.9*a.

the sub-mm flux associated with the softer X-ray sources does arise from the absorbed, $N_H > 10^{22}$ cm^{-2} population.

Lutz et al. (2010) also investigated how sub-mm flux depends on column density for ECDFS X-ray sources and found average stacked fluxes for the $N_H < 10^{22}$ cm^{-2} and $N_H > 10^{22}$ cm^{-2} populations which are in good agreement our measurements in Fig. 2.9*b*.

We have also cross-correlated the absorbed and unabsorbed X-ray source samples with the sub-mm sources using the correlation function in Eqn. 2.1. We detect 12 X-ray–sub-mm pairs within a separation of $\theta < 15''$ for the more absorbed sources, compared to 3.3 expected pairs from a random distribution, representing a 4.7σ excess. For the less absorbed sources, we expect 1.3 pairs and detect 2, so find no significant excess.

2.4.5 Summary

Summarising the results so far, we have found evidence that *Chandra* X-ray sources and LABOCA 870μm sources in the ECDFS are strongly spatially correlated. This $> 8\sigma$ result represents the most significant detection of a cross-correlation between X-ray and sub-mm sources found to date.

We have explored the possible dependence of this cross-correlation on X-ray flux, X-ray luminosity, hardness ratio and column density. Our results have shown marginal indications that fainter ($S_{0.5-2.0} < 1.5 \times 10^{-15}$ ergs s^{-1} cm^{-2}) or harder ($HR > -0.4$) X-ray sources correlate more strongly with the sub-mm, and a stronger suggestion that more absorbed ($N_H > 10^{22}$ cm^{-2}) X-ray sources are preferentially sub-mm bright. The strongest dependence appears to be on X-ray luminosity, with $L_X > 10^{44}$ ergs s^{-1} sources being significantly brighter in the sub-mm. In Chapter 3 we compare these results to the predictions of an AGN model.

2.5 Cross-correlation with optical populations

2.5.1 Cross-correlation of optical galaxies and sub-mm sources

We next cross-correlate ECDFS sub-mm sources with optical sources from the MUSYC BVR-selected catalogue. We divide the optical sources into four populations according to their $B-R$ and $R-I$ colours, intended to correspond to low-z red, high-z red, low-z blue and high-z blue galaxies, where high-z refers to $z > 0.5$ sources. The catalogue has

a depth of $R < 26$ and is therefore expected to contain significant numbers of $z > 0.5$ galaxies. In Table 2.2 we show the colour criteria used to divide the galaxies into the four populations and the resulting number of sources in group.

The selection criteria were defined using well established galaxy evolution models (Metcalfe et al., 2001, 2006). The criteria are marked in Fig. 2.11 along with the BRI colour-redshift tracks predicted by the models and data from the deep GOODS-North survey (Giavalisco et al., 2004) in which the looping features predicted by the models are clearly visible.

Of the four galaxy populations, we find that only the high-z red galaxies cross-correlate strongly with sub-mm sources. The high-z red galaxies also have the brightest stacked sub-mm flux – this is clear from Fig. 2.12*a* which shows the 870μm stacking analyses for all four populations. In the other two panels we show the corresponding stacking analyses at 70μm and 24μm. Here again the high-z red galaxies are the brightest population, indeed in these wavebands they are the only sources to show any significant flux.

The stacked average fluxes at 24μm, 70μm and 870μm are summarised in Table 2.3 for all four optical galaxy populations as well as for the X-ray sources. These stacked fluxes are derived directly from the data shown in Fig. 2.12 (for optical galaxies) and Fig. 2.6*a* (for X-ray sources). We fit Gaussian beam profiles to the data, with the FWHM of the Gaussians set equal to the appropriate beamsize: 27″ for the smoothed LABOCA map (Weiß et al., 2009) and 18″ and 6″ for *Spitzer* MIPS 70μm and 24μm data (Rieke et

TABLE 2.2: *Selection criteria used to divide sources in the MUSYC BVR-selected galaxy catalogue into four populations, based on PLE galaxy evolution models presented by Metcalfe et al. (2001, 2006). An additional cut of $R < 26$ was made for all four populations. The final column shows the number of sources in each group.*

Population	Selection criteria	Number
High-z red galaxies	$(R-I) > 0.5$; $(B-R) < 2.86(R-I) - 0.23$	12,109
Low-z red galaxies	$(B-R) > 1.2$; $(B-R) > 2.86(R-I) - 0.23$	6,621
High-z blue galaxies	$(R-I) < 0.5$; $(B-R) < 0.6$	23,552
Low-z blue galaxies	$(R-I) < 0.5$; $(B-R) < 1.2$; $(B-R) > 0.6$	15,023

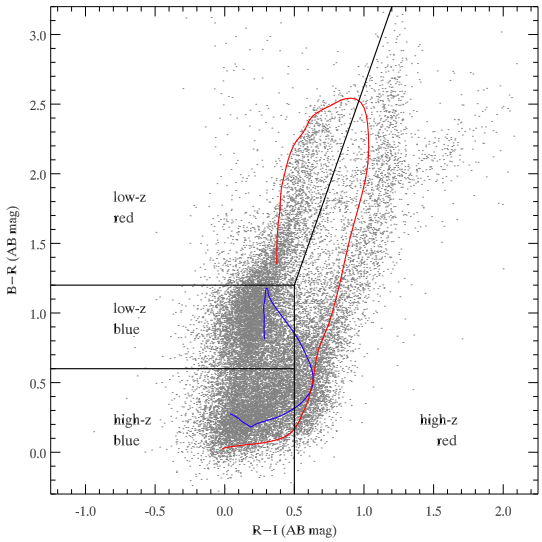

FIGURE 2.11: *BRI colour-colour plot showing the division into four regions designed to represent the indicated populations. The black points shown are galaxies in the deep GOODS-N survey, in which the looping features predicted by the model are clearly visible. The blue and red curves show the predicted* $0 < z < 3$ *redshift tracks for late- and early-type galaxies, respectively, based on PLE models. Here we use high-*z *to mean* $z > 0.5$.

al., 2004). The pixel units in the 870μm intensity map are normalised such that the *peak value* of the Gaussian represents the total flux, whereas the *Spitzer* MIPS 24μm and 70μm images have more traditional flux units, so here we integrate across the beam profile to find the total intensity, according to Eqn. 2.3.

$$I_{\rm tot} = \int_0^\infty I_o e^{-x^2/2\sigma^2} 2\pi x {\rm d}x = 2\pi I_0 \sigma^2 \tag{2.3}$$

where I_0 is the peak intensity of the Gaussian and σ^2 is its variance. When working with the submillimetre map, $I_{\rm tot} = I_0$ using this notation.

Table 2.3 shows that the high-z red galaxies are strongly detected at 870μm, at 5.9σ significance with $S_{870} = 142 \pm 24$ μJy. The low-z red galaxies also show a significant detection, at 4.7σ significance, while the blue galaxy populations are more weakly detected at $\sim 2\sigma$ significance (see Table 2.3). As we noted previously, however, it is only the high-z red galaxies which are detected at 24μm and 70μm, and therefore these galaxies stand out as being the only population which emit strongly throughout the FIR/sub-mm.

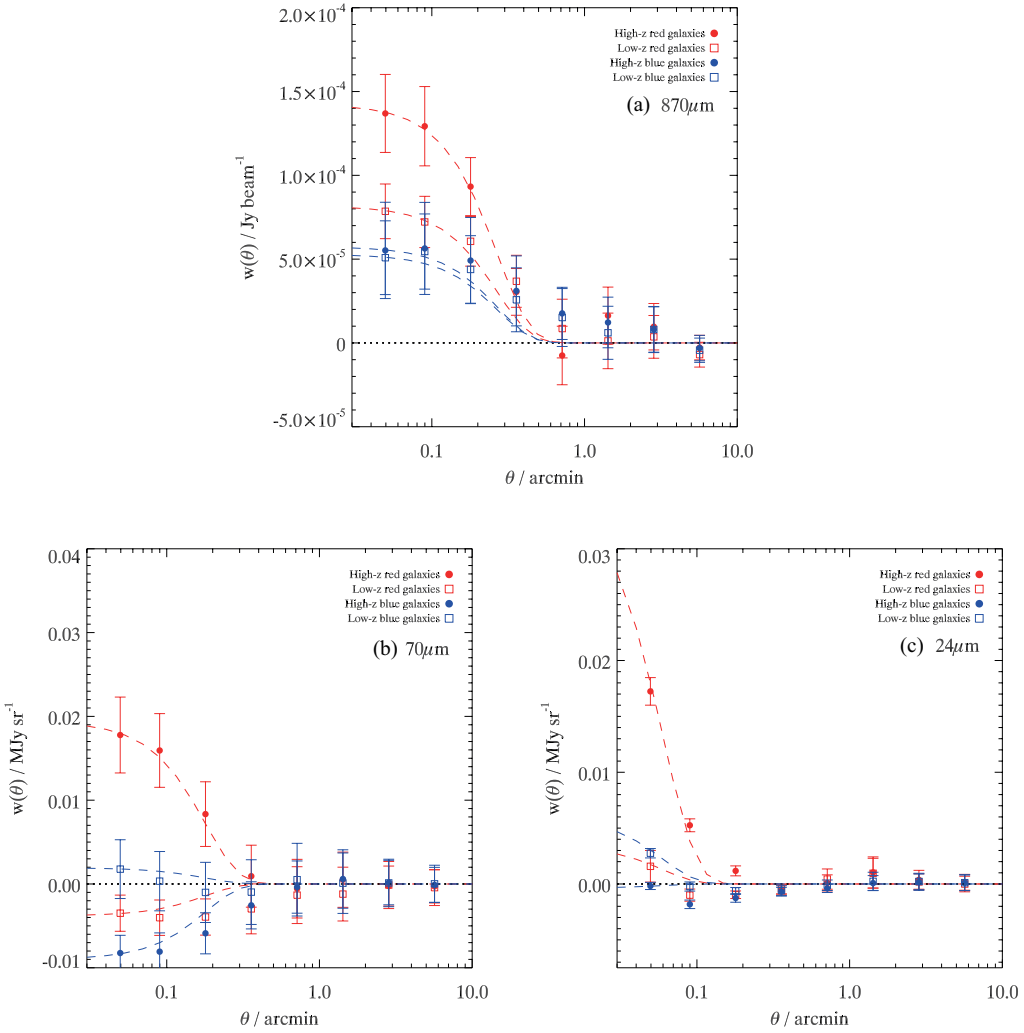

FIGURE 2.12: *Stacking analyses for our four optically-defined galaxy populations at* (a) *870μm,* (b) *70μm and* (c) *24μm. The high-z red galaxies have the brightest stacked flux in all three wavebands. The units of the vertical axes are the same as in the respective intensity maps: Jy beam^{-1} at 870μm and MJy sr^{-1} in the other bands. We convert to μJy in Table 2.3. For each correlation we show the beam profile of the detector, approximated by a Gaussian with* FWHM $= 27''$, $18''$ *and* $6''$ *for 870μm, 70μm and 24μm respectively.*

TABLE 2.3: *Average 870μm, 70μm and 24μm fluxes of different X-ray groups and optical galaxy populations, found by stacking the images. Positive detections at $> 3\sigma$ significance are indicated in bold.*

Population	870μm μJy	70μm μJy	24μm μJy
All X-ray sources	$\mathbf{477 \pm 28}$	$\mathbf{758 \pm 132}$	$\mathbf{126 \pm 11}$
Faint X-ray sources	$\mathbf{488 \pm 37}$	$\mathbf{759 \pm 115}$	$\mathbf{120 \pm 14}$
Bright X-ray sources	$\mathbf{430 \pm 97}$	$\mathbf{754 \pm 107}$	$\mathbf{212 \pm 30}$
High-z red galaxies	$\mathbf{142 \pm 24}$	$\mathbf{111 \pm 28}$	$\mathbf{23 \pm 3}$
Low-z red galaxies	$\mathbf{81 \pm 17}$	-22 ± 14	2 ± 2
High-z blue galaxies	57 ± 30	-51 ± 13	0 ± 0
Low-z blue galaxies	53 ± 23	11 ± 22	$\mathbf{4 \pm 1}$

2.5.2 Gravitational lensing

The results in Fig. 2.12*a* and Table 2.3 have suggested that high-z red optical galaxies emit strongly in the sub-mm. A similar result to this was found by Almaini et al. (2005). They presented evidence that bright sub-mm sources cross-correlate with $R < 23$ galaxies, with a median redshift of $z \approx 0.5$. Their results were consistent with $\approx 25\%$ of sub-mm sources being associated with comparatively low-z structure, however they argue that a more likely explanation for the correlation is gravitational lensing of high-z sub-mm sources by $z \approx 0.5$ galaxies. We therefore explore whether this hypothesis fits our results from the $z > 0.5$ red galaxies.

The ECDFS is known to be deficient in bright sub-mm sources, with the bright end of the number counts significantly lower than has been found in other fields (Weiß et al., 2009). Since gravitational lensing acts to increase the number of bright sources, it is unlikely that the ECDFS contains a significant number of lensed sub-mm galaxies. Nevertheless, we have repeated Almaini et al.'s (2005) analysis. They detect an overdensity of galaxies within 30″ of $S_{850} > 10$ mJy sub-mm source positions, but no significant overdensity around $S_{850} < 10$ mJy sources, and suggest that this is consistent with lensing models which predict a marked increase in the lensed fraction above this fiducial sub-mm flux. The ECDFS contains only 5 sources with $S_{850} > 10$ mJy and we measure no overdensity of high-z red galaxies within 30″ of these sub-mm sources. We therefore find

no indication that the correlation we measure between high-z red galaxies and LABOCA sources arises from gravitational lensing by foreground galaxies.

We suggest therefore that the cross-correlation we measure between $z > 0.5$ red galaxies and sub-mm sources is in fact due to sub-mm emission from these galaxies. These may be star-forming galaxies, however we note that obscured AGN models predict that Compton-thick AGN should make a significant contribution to the sub-mm population; our high-z red galaxies may include the hosts of these sources.

2.5.3 NIR–FIR colours of high-z red galaxies

In Figs. 2.13, 2.14 and 2.15[4] we compare the optical and NIR colours of the high-z red galaxies to those of the X-ray sources and find that the faint X-ray sources and the high-z red galaxies tend to occupy the same colour space, while the locus of the bright X-ray sources is elsewhere (Fig. 2.13). This raises the possibility that the high-z red galaxies and the faint X-ray sources, the two object classes seen to exhibit the strongest correlation with sub-mm sources, both sample the same population. The faint X-ray sources are expected to include the more absorbed AGN; the question, then, is whether the high-z red galaxies also host absorbed AGN, specifically Compton-thick AGN which are X-ray-undetected.

We have attempted to estimate the AGN fraction within the high-z red population using the *Spitzer* IRAC $[3.6]-[4.5]:[5.8]-[8.0]$ colour-colour plot, which is known to be a robust way of distinguishing AGN from other sources (Stern et al., 2005). However, IRAC observations are available only for the small, central field (SWIRE survey; Lonsdale et al., 2004) and the 8μm resolution is relatively poor, so only $\sim 1\%$ of our X-ray and optical populations are detected in all four IRAC bands. 70% of the faint X-ray sources and 3% of the high-z red galaxies which are detected in all four IRAC channels lie within or very close to the AGN wedge, but with such small samples it is hard to draw any firm conclusions here.

Looking at longer, mid/far-IR wavelengths, we can use the stacked 24μm, 70μm and 870μm fluxes given in Table 2.3 to characterise the average far-IR SEDs of the high-z red galaxies and the X-ray sources. These SEDs are shown in Fig. 2.16; the data have been shifted to the rest frame assuming the median redshift of the X-ray redshift sample, $z = 1.3$. We find that two temperature components are needed to fit the data for the X-

[4]In Figs. 2.14 and 2.15, which include K-band data, we use the MUSYC K-selected catalogue instead of the BVR-selected catalogue.

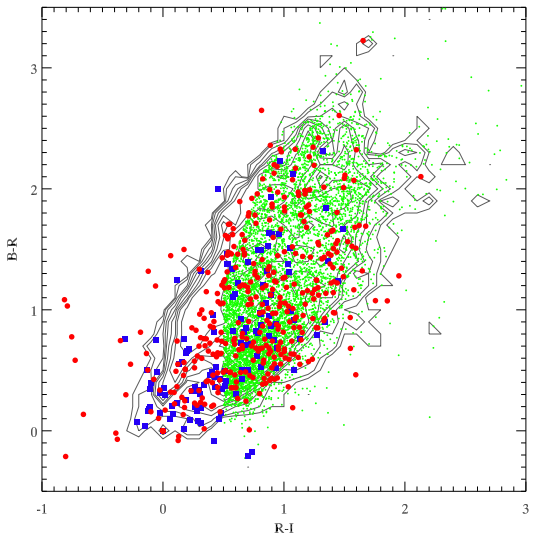

FIGURE 2.13: *BRI colour-colour plot for sources in the ECDFS. Faint and bright X-ray sources are marked as red circles and blue squares, respectively. Green points are objects selected as high-z red galaxies. The contours show the colour distribution of all optical sources in the ECDFS MUSYC catalogue.*

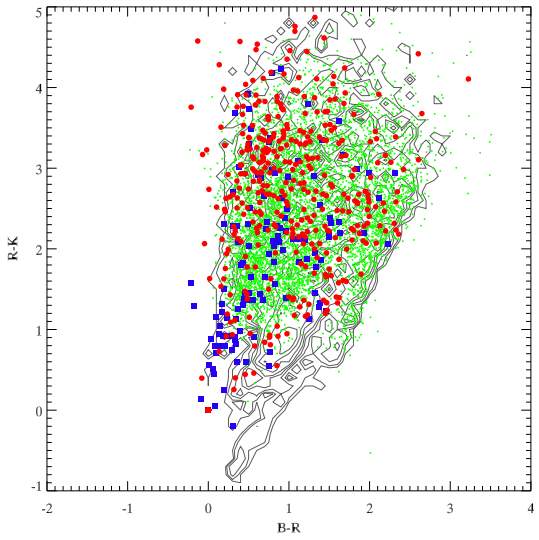

FIGURE 2.14: *BRK colour-colour plot for sources in the ECDFS. All points are as in figure 2.13.*

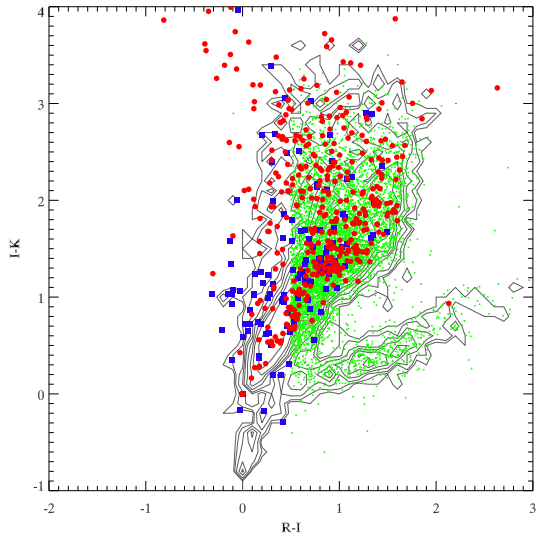

FIGURE 2.15: *RIK colour-colour plot for sources in the ECDFS. All points are as in figure 2.13.*

ray sources and the high-z red galaxies, with both populations well matched by a model with $T_1 = 35$ K, $T_2 = 145$ K and a ratio between the components of $L_2/L_1 = 0.37$, although this is by no means a unique solution. With only three datapoints constraining the fits, the derived temperatures cannot be taken too seriously, particularly as the 24μm, 70μm and 870μm fluxes may yet arise from different sources. Nevertheless, Fig. 2.16 does serve to illustrate that the FIR colours (and implied dust temperatures) of red galaxies and X-ray sources appear broadly consistent, as may be expected if the dust emission has a common AGN origin.

We conclude that $z > 0.5$ red galaxies appear to be the brightest class of optical galaxies in the FIR/sub-mm, and that there is no inconsistency in the optical/NIR/FIR colours of these high-z red galaxies and faint X-ray sources. These galaxies could therefore host a Compton-thick AGN population. We shall see in Chapter 3 that the sub-mm background associated with these red galaxies is also consistent with the predicted contribution from such AGN.

2.6 Discussion

We have found a strong correlation between X-ray sources and sub-mm sources, indicative of a significant AGN contribution to the sub-mm population. It is, however, not possible to conclude immediately that the AGN are the main source of the bolo-

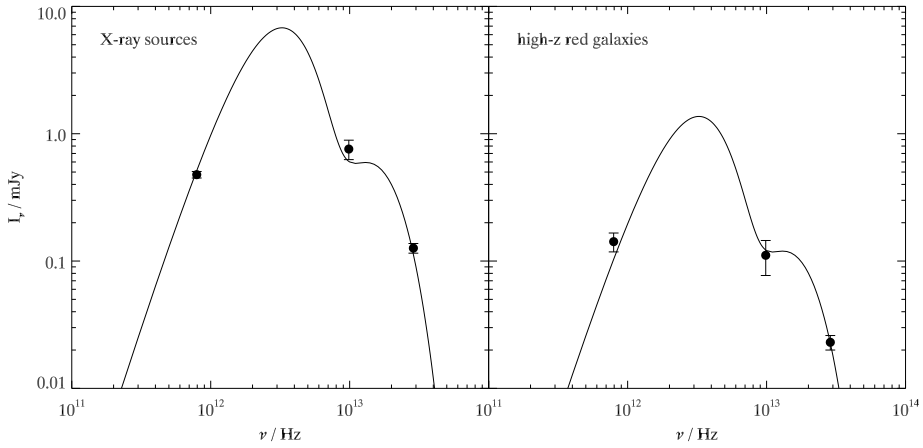

FIGURE 2.16: *Stacked 870μm, 70μm and 24μm fluxes for* (a) *X-ray sources and* (b) *high-z red galaxies in the ECDFS. In both cases the data are well fit by a two-blackbody dust model with $T_1 = 35$ K, $T_2 = 145$ K and a ratio between the two components of $L_2/L_1 = 0.37$. A redshift of $z = 1.3$, the median of the X-ray redshift sample, has been assumed. With only 3 points in each case these temperatures cannot be taken too literally, however it is clear there is no inconsistency here between the FIR colours of the two populations.*

metric output. Sub-mm galaxies typically show strong PAH features (Lutz et al., 2005; Menéndez-Delmestre et al., 2007; Pope et al., 2008; Coppin et al., 2010) and very high FIR luminosities (e.g. Alexander et al., 2005; Coppin et al., 2008b), thought to be fuelled by starbursts. These observations are generally taken to indicate that sub-mm galaxies are mostly dominated by star-formation rather than AGN activity. However, the question of whether AGN activity may be significant to the bolometric output of sub-mm sources is not entirely clear-cut, as we discuss in §3.4.

We have considered the separate sub-mm contribution of X-ray sources at bright and faint fluxes and low and high levels of absorption. We have found some indication of a difference between absorbed and unabsorbed AGN, with the former preferentially being more submillimetre-bright. This is in line with the findings of other studies and supports a non-unified AGN model.

In the typical non-unified AGN model (Fabian, 1999), absorbed QSOs represent an earlier evolutionary phase in which there is rapid growth in the host spheroid, accompanied by a major episode of star formation. Unabsorbed quasars are seen during the subsequent phase, in which the host galaxy is quiescent. This is brought about by the expulsion of cool gas and dust from the galaxy once the spheroid is fully formed, a pro-

cess which simultaneously quenches the star-formation, cuts off the sub-mm emission and renders the QSO unobscured.

While this model invokes a star-formation episode, it is interesting to consider whether the AGN might itself be responsible for the sub-mm emission. Sub-mm emission is associated with dust at temperatures of a few tens of kelvin, therefore if AGN are submillimetre-bright they must maintain a cold dust component. Various authors using dust tori models to fit AGN data (e.g. Granato & Danese, 1994; Andreani et al., 1999; Kuraszkiewicz et al., 2003) have shown that the dust surrounding the central nucleus in high-z AGN can reach outer radii of ~ 1 kpc, where the dust can be cold enough to produce sub-mm emission, with no requirement to invoke star-formation.

Modern approaches to the dust torus model tend to favour the idea of a 'clumpy' torus, consisting of many separate clouds of gas and dust. The clumpiness of the torus could vary among AGN, with the more absorbed AGN having denser, dustier tori with greater optical depth. This would result in a lower intensity of radiation in the outer reaches of the torus, and therefore the dust at large radii would be cooler in absorbed AGN than in unabsorbed AGN, providing a possible explanation for the different observed sub-mm fluxes.

2.7 Summary

We have used ECDFS data to test the contribution of AGN to the sub-mm number counts and background. We have mainly used statistical cross-correlation techniques which do not depend on the direct identification of any sub-mm source which is an advantage given the large beam size of the LABOCA sources. Our conclusions are as follows:

- We find a strong spatial correlation between 852 faint X-ray sources and 126 sub-mm sources. We interpret this as indicating a significant AGN contribution to the sub-mm population.

- There is some suggestion that this correlation may be stronger for sources with faint X-ray fluxes and/or hard spectra, which tend to be associated with absorbed AGN.

- We confirm that high luminosity X-ray sources show a stronger correlation with the sub-mm than low-luminosity X-ray sources (Lutz et al., 2010). Since these high-L_X

sources also typically have faint fluxes, we conclude that they are at high redshifts, as expected, but also suggest that X-ray absorption may compound this trend.

- We find evidence that $N_H > 10^{22}$ cm^{-2} sources are brighter in the sub-mm than $N_H < 10^{22}$ cm^{-2} sources.

- We find that the sub-mm sources also cross-correlate with $z > 0.5$ red galaxies, but not with bluer galaxy classes. These high-z red galaxies have optical/NIR/FIR colours consistent with those observed for X-ray sources.

These results, consistent with a significant AGN contribution to the sub-mm population, can provide important observational constraints on models of AGN in the sub-mm. In the next chapter, we compare directly the results found here to the predictions of such a model. We will show that the AGN model and the ECDFS observations are in excellent agreement.

III

Modelling obscured AGN in the submillimetre

3.1 Introduction

In Chapter 2 we investigated the contribution of AGN in the Extended *Chandra* Deep Field South (ECDFS) to the sub-mm population. We took all *Chandra* X-ray sources in the field as our sample of AGN, which is justified on the basis that the X-ray population is known to be heavily AGN-dominated to the $\approx 10^{-16}$ ergs s^{-1} cm^{-2} limit of the ECDFS survey. Additionally, our analysis (as well as previous results from Lutz et al., 2010) showed that low-luminosity X-ray sources are comparatively weak sub-mm emitters, further suggesting that any starburst component in the X-ray sample does not contribute strongly to the sub-mm correlation we detect.

The total AGN population, however, is expected to be much larger than just the X-ray detected sample. A significant fraction of AGN are obscured by gas, which reduces the apparent X-ray flux; a flux-limited X-ray survey will therefore not detect AGN above a certain level of obscuration. The most heavily absorbed X-ray sources are Compton-thick, having a hydrogen column density greater than the inverse of the Thomson cross-section, that is $N_{\rm H} \geq 1.5 \times 10^{24}$ cm^{-2}; the nuclear emission from these sources cannot be directly seen in X-rays at all, save for at very high energies ($E > 10$ keV). The most heavily Compton-thick sources ($N_{\rm H} \gtrsim 10^{25}$ cm^{-2}) can likely be detected only via a reflection spectrum, with the radiation only observed after having been scattered off surrounding interstellar material (Matt et al., 1996, 2000).

A significant fraction of AGN are therefore expected to be missing from our X-ray

population. The upshot of this is that the sub-mm flux associated with our X-ray-selected AGN sample in Chapter 2 is not expected to be a full quantification of the sub-mm emission from AGN, since we are missing the heavily absorbed (and certainly the Compton-thick) sources. We therefore make use of a model of obscured AGN to quantify the full AGN contribution to the sub-mm.

The relative size of this highly absorbed population is an important consideration. Considerable work has been done over the past decade in attempting to determine what fraction of AGN are highly absorbed. Several separate studies have indicated that $\approx 50\%$ of local Seyfert 2s are Compton-thick (Maiolino et al., 1998; Risaliti et al., 1999; Guainazzi, Matt & Perola, 2005; Malizia et al., 2010), suggesting that Compton-thick sources make up $\gtrsim 25\%$ of the entire local AGN population, since absorbed AGN in general (i.e. those with $N_{\rm H} > 10^{22}$ cm^{-2}) are suggested to comprise $\gtrsim 50\%$ of the total (Martínez-Sansigre et al., 2005, 2006, 2007; Ajello et al., 2008; Della Ceca et al., 2008). How the absorbed fraction varies with redshift remains unclear, with studies by La Franca et al. (2005) and Ballantyne et al. (2006) suggesting an increase with redshift but others (Ueda et al., 2003; Treister & Urry, 2005; Gilli, Comastri & Hasinger, 2007) finding no evidence of a redshift dependence. Some confusion also remains over whether the heavily obscured fraction varies with luminosity, although the observational evidence here increasingly suggests that such a dependence exists. The general trend appears to indicate that the absorbed AGN fraction decreases with increasing X-ray luminosity (Ueda et al., 2003; Treister & Urry, 2005; Akylas et al., 2006).

However, despite some remaining uncertainty in the size of the highly obscured population and its dependences, it is now at least clear that a significant population of heavily absorbed AGN does exist. These sources are vital to our understanding of the accretion history of the universe and the origins of the X-ray background (XRB). Compton-thick AGN are needed by population synthesis models in order to match the 30 keV peak of the XRB (e.g. Gunn, 1999; Gilli, Comastri & Hasinger, 2007). But these sources are also likely to make an important contribution in the mid-IR, far-IR and sub-mm (Georgantopoulos et al., 2009; Hill & Shanks, 2010b; Chapter 4), since the obscuring material must reradiate the absorbed energy. This will be the focus of this chapter, as we use a model to predict the sub-mm emission from obscured AGN and test these predictions against the results presented in Chapter 2.

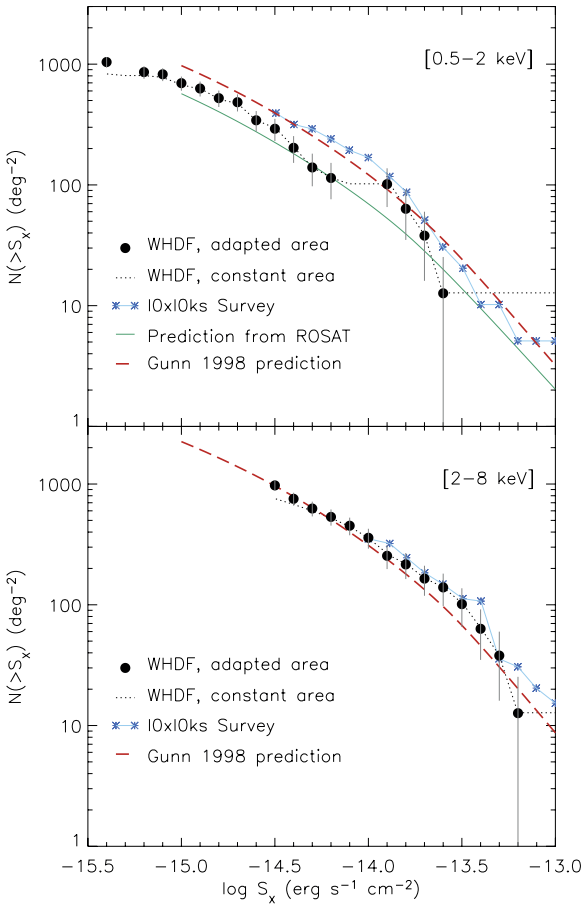

FIGURE 3.1: *X-ray source counts in the soft (upper panel) and hard (lower panel) energy bands, with observations compared to the prediction of our obscured AGN model. Figure: Vallbé-Mumbru (2004).*

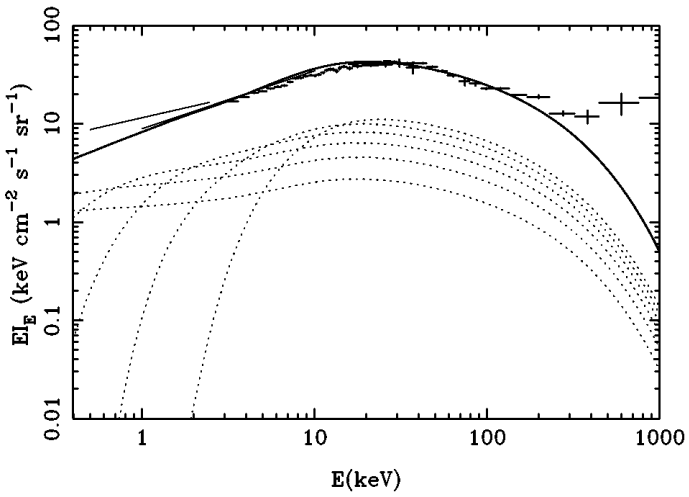

FIGURE 3.2: *The X-ray background, with the prediction of the obscured QSO model compared to observational data. Figure: Gunn (1999).*

3.2 Obscured AGN model

The model we employ is that of Gunn & Shanks (1999; see also Gunn, 1999). This model gives a good fit to both the X-ray background and X-ray number counts, as shown in Figs. 3.1 and 3.2. We review the model here, but refer the reader to Gunn (1999) for further detail.

The model assumes that AGN are drawn from an intrinsically flat column density distribution, having an absorbing neutral hydrogen column density of $\log(N_{\rm H}/{\rm cm}^2) = 19.5$, 20.5, 21.5, 22.5, 23.5, 24.5 or 25.5. In the X-ray energy range probed by the *Chandra* telescope, the lowest column density in this distribution will give an entirely unobscured source, while the highest, which is heavily Compton-thick, will be unobservable. The effect of the absorption on our canonical AGN X-ray spectrum is shown for different column densities in Fig. 3.3.

A fiducial column of $N_{\rm H} = 10^{22}$ cm^{-2} is typically used as the dividing line between absorbed and unabsorbed sources, therefore in our AGN model 4/7 or 57% of sources are absorbed and half of these (28% of the total) are Compton-thick – these proportions are consistent with the observations reviewed in the introduction to this chapter. The choice of a flat $N_{\rm H}$ distribution is supported by observations by La Franca et al. (2005) who, using a large sample of ≈ 500 X-ray detected AGN, showed that the measured column density distribution was consistent with an intrinsically flat distribution after selection effects were accounted for (a flux-limited X-ray survey will detect a greater fraction of low-column sources than high-column sources).

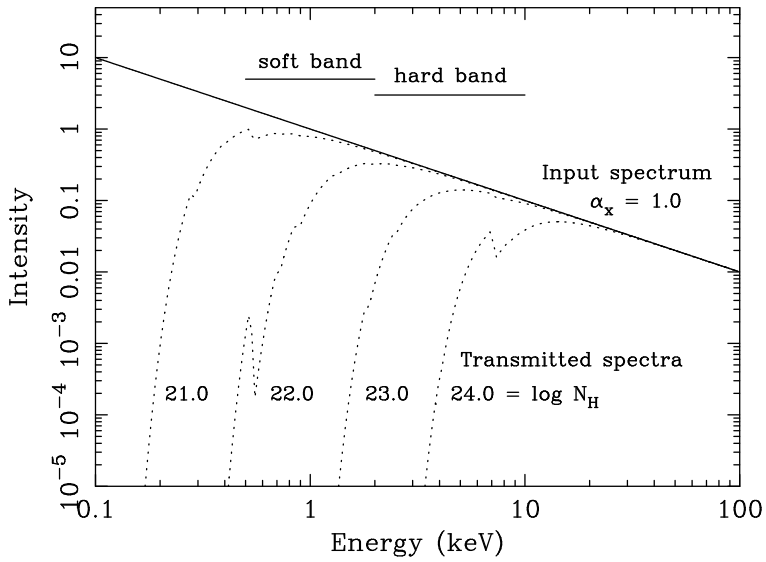

FIGURE 3.3: *The intrinsic X-ray spectrum assumed for AGN in our model (solid line), with the apparent spectrum shown for different absorbing column densities (dotted lines). Figure: Gunn (1999).*

The model as presented by Gunn & Shanks (1999) is non-unified: it assumes that the observed column density is directly a measure of the intrinsic amount of gas, not an apparent effect resulting from the viewing angle. It is important to emphasise that this assumption is of no consequence to the model's success in fitting the XRB, where the distribution of column densities is important, but the supposed physical origin of this distribution has no bearing on the fit.

The non-unified assumption, however, bears strongly on the predictions for the sub-mm, since dust masses in the model are calculated from a Galactic gas-to-dust ratio, so more heavily absorbed sources — which here are assumed to have a greater mass of neutral hydrogen — will consequently have greater dust masses and therefore make a greater sub-mm contribution. We make use of the model within this non-unified paradigm, but also later adapt it in order to explore the unified AGN scenario, in which different column densities arise due to orientation effects alone and do not reflect any intrinsic difference between AGN populations.

Dust absorption in the model is calculated using an empirical polynomial law based on Howarth (1983) and Seaton (1979), which accounts for departures from a basic 'dust screen' law (i.e., one where the absorbed flux at wavelength λ goes as $A_\lambda \propto 1/\lambda$) such as the 2200Å graphite feature. Gunn & Shanks note, however, that using the $1/\lambda$ law does not significantly affect the results.

We assume a dust temperature of 30K in the model. This is consistent with recent observations of sub-mm sources (Coppin et al., 2008b; Elbaz et al., 2010), as well as with the (albeit poorly constrained) temperature inferred from the stacked FIR/sub-mm fluxes of X-ray sources in the ECDFS in §2.5.3 (the warmer component makes a negligible contribution in the sub-mm). An opacity law is assumed in which the dust emissivity goes as $\kappa_{\rm d} \propto \lambda^{-\beta}$. In a perfect blackbody, the emissivity index takes a value of $\beta = 0$. Non-zero values of β alter the shape of the blackbody emission, creating instead a 'greybody', usually with $1 < \beta < 2$. Gunn & Shanks assumed $\beta = 2$, however we instead assume the more currently favoured value of $\beta = 1.5$ (Dunne & Eales, 2001; Coppin et al., 2008b).

3.3 Predictions for sub-mm number counts and extragalactic background

In Fig. 3.4 we show the predicted sub-mm number counts from our non-unified obscured AGN model. There is excellent agreement with the observed source counts at $S_{850} > 0.5$ mJy. At fainter 850μm fluxes, the AGN model begins to underpredict the counts, however we show in the figure the predicted contribution of normal spiral galaxies, which is significant at these faint fluxes (see also Busswell & Shanks, 2001). This galaxy model is described fully in Chapter 4, where we make similar predictions for galaxy number counts in the mid- and far-IR regimes.

The predicted density of submillimetre galaxies (SMGs; the class of sub-mm sources with $S_{850} > 4$ mJy) is 783 deg^{-2}, in very good agreement with the error-weighted mean of 768 ± 89 deg^{-2} for the observational data shown in Fig. 3.4.[1]

We can use this prediction for the sub-mm source counts in Fig. 3.4 to determine a corresponding prediction for the sub-mm extragalactic background light (EBL) arising from AGN. This is found using Eqn. 3.1:

$$I_{\rm EBL} = \int S \frac{{\rm d}N}{{\rm d}S} {\rm d}S = \sum_i S_i \frac{{\rm d}N_i}{{\rm d}S_i} {\rm d}S_i \tag{3.1}$$

where ${\rm d}N_i/{\rm d}S_i$ is the differential number count measured at flux S_i.

Using this formula we find that the predicted sub-mm background from the com-

[1]This error-weighted mean was calculated without the ECDFS counts (Weiß et al., 2009) as this field is known to contain an atypical underdensity of bright sub-mm sources (*ibid.*).

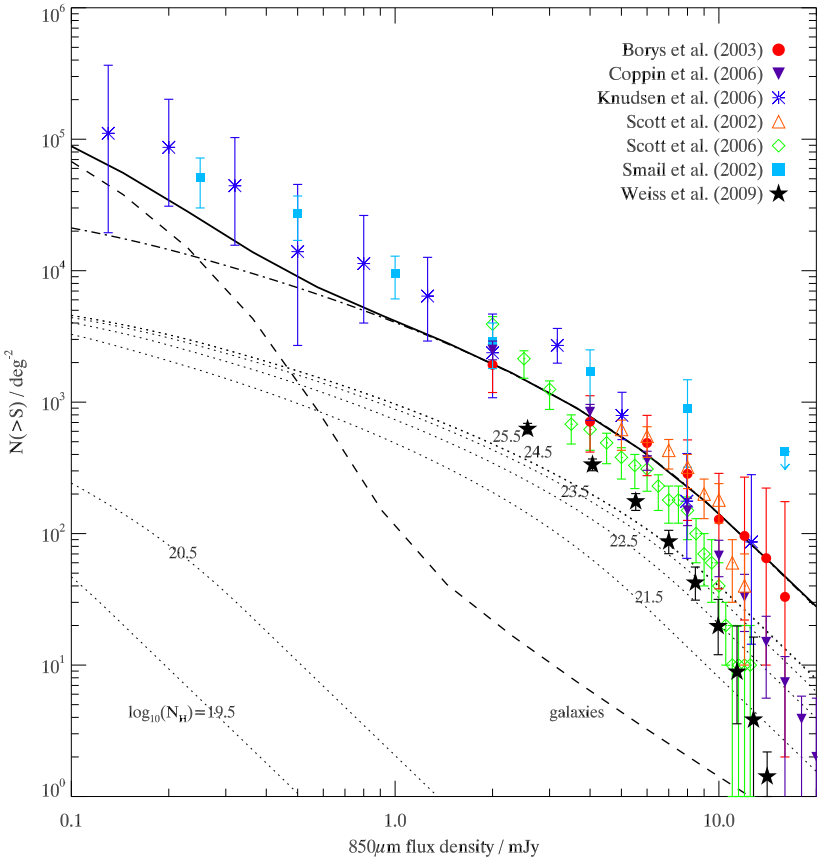

FIGURE 3.4: *Integral number counts at 850μm. We use the model of Gunn & Shanks (1999), which is known to fit the hard X-ray background, to generate predicted sub-mm number counts from a population of obscured AGN. The total AGN contribution is shown by the dash-dot line; dotted lines show individual contributions from AGN with different columns (labelled; note that the $N_{\rm H} = 10^{24.5}$ and $10^{25.5}$ cm^{-2} lines are indistinguishable); this is a non-unified AGN model where more absorbed AGN contribute more strongly to the sub-mm.*

TABLE 3.1: *Predicted contribution of AGN to the submillimetre extragalactic background, to different lower flux limits. At $S_{850} \gtrsim 1$ mJy the AGN are predicted to account for roughly the entire submillimetre background, but at fainter fluxes this falls off. In this model, AGN could account for some 40% of the whole submillimetre EBL.*

S_{850} limit mJy	Total observed EBL Jy deg^{-2}	Predicted EBL from AGN Jy deg^{-2}	Percentage
1.0	13.6 [a]	12.2	$\approx 90\%$
0.5	$\sim$30 [b]	14.5	$\approx 50\%$
0.0	$\sim$45 [c]	17.7	$\approx 40\%$

[a] based on the P(D) analysis of Weiß et al. (2009)

[b] Weiß et al. (2009)

[c] Puget et al. (1996), Fixsen et al. (1998)

bined AGN + galaxy model shown in Fig. 3.4 is 42.7 Jy deg^{-2}, in good agreement with current estimates of the total sub-mm background: based on *COBE FIRAS* measurements, this is estimated to be ~ 45 Jy deg^{-2} (Puget et al., 1996; Fixsen et al., 1998).

The model suggests that while AGN may make up the bright sub-mm population, the sub-mm background is dominated by normal galaxies, which are much fainter but far more numerous. Of the 42.7 Jy deg^{-2} predicted for the combined model, 17.7 Jy deg^{-2} comes from AGN and 25.0 Jy deg^{-2} is contributed by galaxies. Obscured AGN are therefore suggested to produce $\approx 40\%$ of the sub-mm EBL. This proportion increases as a function of limiting 850μm flux, as shown in Table 3.1.

In Chapter 2, we presented sub-mm stacking analyses for X-ray sources and high-z red galaxies (Table 2.3). We now use these analyses to quantify the contribution made by these populations to the sub-mm extragalactic background, by multiplying by the stacked average flux by the total number of sources and dividing by the area of the ECDFS, 0.25 deg^2 (Eqn. 3.2).

$$I_{\rm EBL} = \frac{N\bar{S}}{A} \tag{3.2}$$

For the high-z red galaxies this contribution is found to be 4.8 ± 1.2 Jy deg^{-2}, while for the X-ray sources it is 1.5 ± 0.1 Jy deg^{-2}. Therefore, the X-ray-detected AGN contribute

only $\approx 3\%$ of the total sub-mm background (~ 45 Jy deg^{-2}) and only $\approx 8.5\%$ of the sub-mm background component which comes from AGN (17.7 Jy deg^{-2}).

This now provides us with a crucial observational test of our AGN model. We can generate a prediction for the sub-mm EBL arising from just those AGN which would be detected in the ECDFS X-ray survey — i.e. those with X-ray fluxes of $S_{0.5-2.0} > 1.1 \times 10^{-16}$ ergs s^{-1} cm^{-2} — and compare this prediction to the measured value of 1.5 ± 0.1 Jy deg^{-2}.

3.3.1 Model predictions for ECDFS X-ray sources

Sub-mm contribution vs. X-ray flux

The prediction of our model for the sub-mm background associated with $S_{0.5-2.0} > 1.1 \times 10^{-16}$ ergs s^{-1} cm^{-2} sources is 2.3 Jy deg^{-2}, $\approx 50\%$ greater than the measured value of 1.5 ± 0.1 Jy deg^{-2}. This initially appears to indicate that our model is over-predicting the contribution which AGN make in the sub-mm. However, the bright sub-mm source counts in the ECDFS are known to be lower than in other fields, by as much as a factor of 2 (Weiß et al., 2009), and this deficiency of bright sub-mm sources in the ECDFS could explain why the total stacked sub-mm flux of our X-ray sources is lower than the model prediction.

Nevertheless, we can revise the model to bring the predicted sub-mm background from X-ray-detected AGN into line with the observations. We make this revision by altering the dust covering factor, which is the only remaining free parameter in the model after fixing the dust temperature at 30K and the emissivity index at $\beta = 1.5$. Gunn & Shanks assume a covering factor $f_{\rm cov} = 1.0$, which represents an isotropic distribution of dust. If we instead take $f_{\rm cov} = 0.65$, the predicted sub-mm background from X-ray-detected AGN falls to 1.5 Jy deg^{-2}, consistent with the observational value.

In this revised model, however, the total AGN contribution to the sub-mm sources counts is lower, as shown in Fig. 3.5. The model now accounts for only around half of bright sources, with the predicted number of SMGs falling from the 783 deg^{-2} quoted above to 367 deg^{-2}. However, while this value is lower than most of the observational data, it agrees very well with the observed SMG sky density of 335 ± 34 deg^{-2} for the ECDFS (Weiß et al., 2009).

This is significant, because it means that our non-unified AGN model simultaneously matches the total ECDFS 870μm number counts and the measured sub-mm background

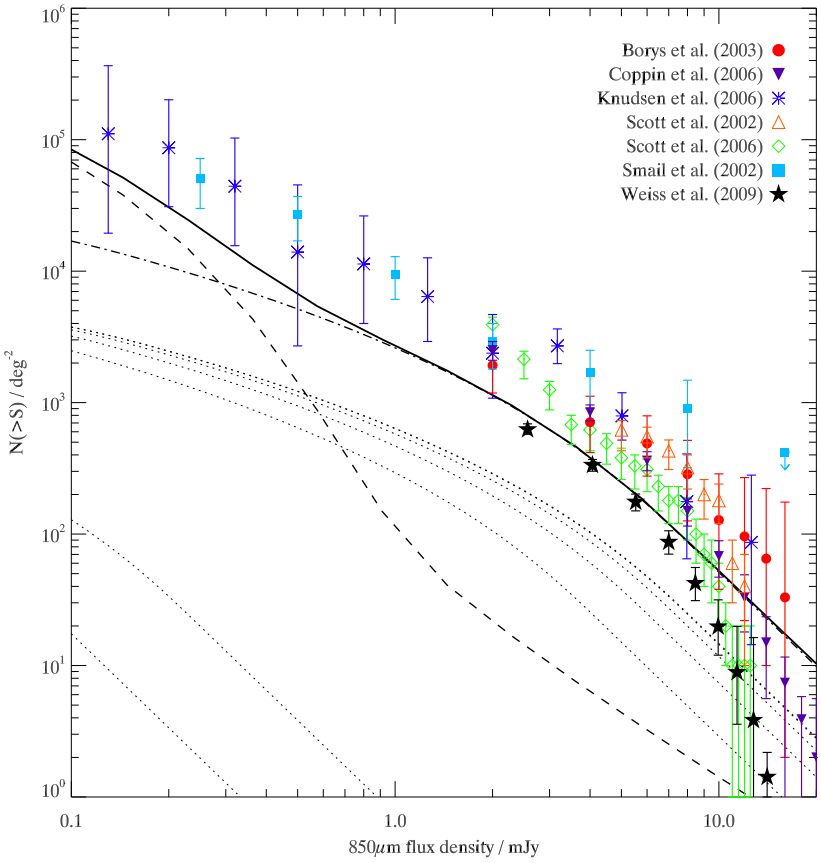

FIGURE 3.5: *Integral number counts at 850μm, as for Fig. 3.4 except now showing the prediction using the $f_{\rm cov} = 0.65$ model, which has been normalised to fit the observed sub-mm background from ECDFS X-ray sources. Although the prediction is a now factor of ≈ 2 lower than most of the counts, it is more in line with the counts for the ECDFS (black stars; Weiß et al., 2009).*

flux from the ECDFS X-ray sources. Therefore, our original model, which matches the total sub-mm source counts well and predicts a background contribution of 2.3 Jy deg^{-2} from $S_{0.5-2.0} \geq 1.1 \times 10^{-16}$ ergs s^{-1} cm^{-2} sources, may yet represent a valid description of the AGN contribution to the sub-mm population in other more typical fields.

Taking the model which matches the measured 1.5 ± 0.1 Jy deg^{-2} sub-mm flux from $S_{0.5-2.0} \geq 1.1 \times 10^{-16}$ ergs s^{-1} cm^{-2} X-ray sources, we can make further tests by predicting the expected sub-mm background contribution from X-ray sources in other X-ray flux ranges. This is shown in Fig. 3.6. We measure the actual sub-mm background associated with ECDFS sources to several X-ray flux limits and compare to the predictions. The figure indicates that the model is predicting the trend with flux generally very well. Since the data in Fig. 3.6 include those in Fig. 2.6*a*, this also shows that our AGN model fits the data in that figure.

Sub-mm contribution vs. L_X

We can also test the model's predictions against the result in Fig. 2.5, where we found that $L_X > 10^{44}$ ergs s^{-1} sources are brighter in the sub-mm. The AGN model naturally predicts such a luminosity dependence, since the amount of light that can be absorbed in the X-ray/optical (and subsequently reradiated in the sub-mm) is proportional to the intrinsic X-ray/optical luminosity. A simple test we can do with the model is to calculate the expected sub-mm background from AGN which are brighter or fainter than the characteristic luminosity L^*. This prediction should be consistent with the result from Fig. 2.5 since $L^* \approx 10^{44}$ ergs s^{-1} at the $z \approx 2$ redshift expected for sub-mm sources (Aird et al., 2010). Our model predicts a sub-mm background of 0.6 Jy deg^{-2} from $L > L^*$ ECDFS X-ray sources and 0.9 Jy deg^{-2} from $L < L^*$ sources (although high-luminosity sources are much brighter in the sub-mm, there are many more low-luminosity sources). Taking the stacked fluxes in Fig. 2.5 and scaling to account for the incompleteness of the redshift sample, we measure a sub-mm background contribution from $L_X > 10^{44}$ ergs s^{-1} sources of 0.6 ± 0.1 Jy deg^{-2} and for lower-luminosity sources of 0.9 ± 0.3 Jy deg^{-2}, in excellent agreement with the predictions.

Sub-mm contribution vs. $N_{\rm H}$

Finally, we test the model against the result in Fig. 2.9*b*, where we determined stacked fluxes for X-ray sources more or less absorbed than $N_{\rm H} = 10^{22}$ cm^{-2}. The model predicts

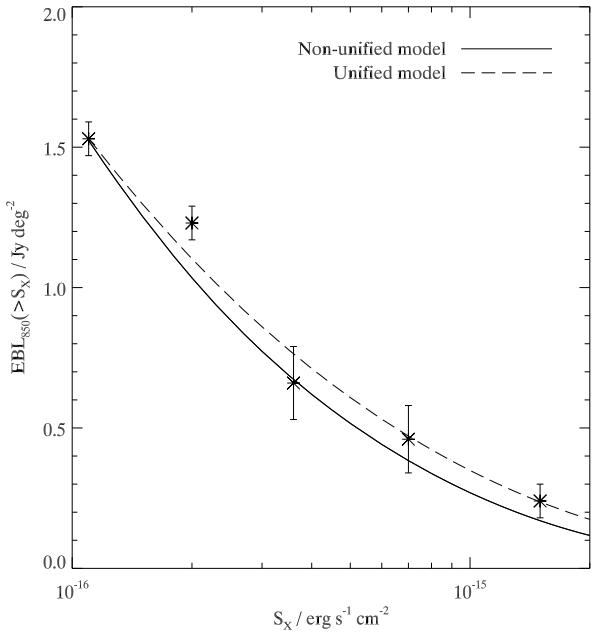

FIGURE 3.6: *The contribution of AGN to the sub-mm extragalactic background light (EBL) as a function of limiting AGN X-ray flux in the 0.5–2.0 keV band. Predictions from the obscured AGN model are shown for both the unified and non-unified cases. Datapoints show observational measurements from the ECDFS data.*

sub-mm background contributions of 1.0 Jy deg^{-2} and 0.5 Jy deg^{-2} for ECDFS X-ray sources with $N_{\rm H} > 10^{22}$ cm^{-2} and $N_{\rm H} < 10^{22}$ cm^{-2} respectively, agreeing well with the measured values from Fig. 2.9*b* of 1.2 ± 0.2 Jy deg^{-2} and 0.3 ± 0.1 Jy deg^{-2} respectively. We summarise all of the above tests in Table 3.2, where we also compare to predictions from the unified AGN model, which is described next.

3.3.2 Unified AGN model

In the unified case, we retain the same distribution of columns as before, since this is still important when considering the X-ray fluxes of the AGN, however the column density is no longer an indicator of the total absorbed luminosity and therefore no longer affects the sub-mm flux.

Having applied the observational constraint that the X-ray-detected AGN should contribute only 1.5 Jy deg^{-2} to the sub-mm background, this unified model underpredicts the sub-mm number counts by as much as an order of magnitude: the total predicted number of $S_{850} > 4$ mJy sources is 72 deg^{-2}, ≈ 5 times lower than the ECDFS

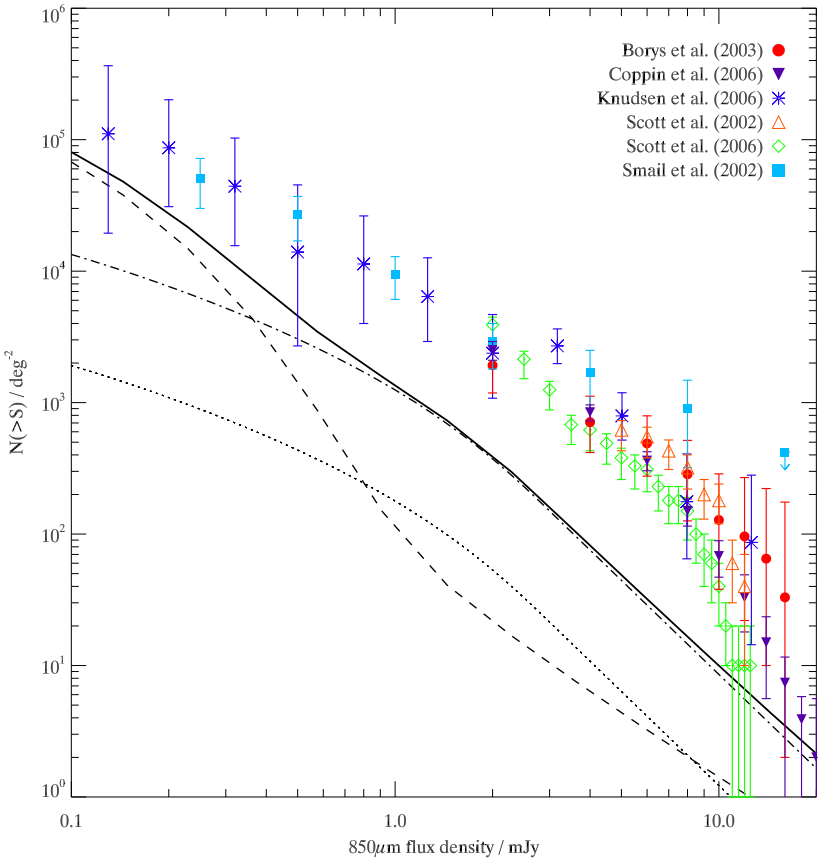

FIGURE 3.7: *Integral number counts at 850μm, as for Fig. 3.4 except now showing the prediction of the unified AGN model. In this case, there is no difference in the contribution made by each of the 7 populations with different column densities (dotted lines), as observed column density is solely a result of orientation effects in the unified model, which has no impact on sub-mm flux.*

TABLE 3.2: *Contributions to the sub-mm extragalactic background from ECDFS X-ray sources, divided by X-ray flux, X-ray luminosity and hydrogen column density. In each case we show the measured value for our stacking analyses, followed by the predictions of our AGN model in both the non-unified and unified cases. All sub-mm background contributions are given in Jy deg^{-2}; the X-ray fluxes are soft band ($0.5-2.0$ keV) fluxes in units of ergs s^{-1} cm^{-2}.*

		Model prediction	
Population	Observation	*Non-unified*	*Unified*
$S > 1.5 \times 10^{-15}$	0.2 ± 0.1	0.1	0.2
$S < 1.5 \times 10^{-15}$	1.3 ± 0.1	1.4	1.3
$L_X > L^*$	0.6 ± 0.1	0.6	0.8
$L_X < L^*$	0.9 ± 0.3	0.9	0.7
$N_{\rm H} > 10^{22}$ cm^{-2}	1.2 ± 0.2	1.0	0.4
$N_{\rm H} < 10^{22}$ cm^{-2}	0.3 ± 0.1	0.5	1.1

value and ≈ 10 times lower than the average of the other fields. This is shown in Fig. 3.7.

The significance of AGN to the sub-mm population is therefore considerably less within the framework of the unified AGN model than in the non-unified case. While we showed that in the non-unified model obscured AGN can make a dominant contribution, potentially even fully matching the source counts, in the unified model AGN account for only 10–20% of bright sub-mm sources.

We make the same tests of this model which were described previously for the non-unified case. The predictions are shown in Table 3.2 and Fig. 3.6 alongside those for the non-unified model and the observational measurements. We note that the predictions of the unified model for the flux and luminosity samples are in generally good agreement with the data. In these cases, the difference between the unified and non-unified cases are not great enough to say that the observations prefer one to the other. As expected, though, the unified and non-unified cases show a far more significant difference in the predicted contributions from more and less absorbed X-ray sources, and in this case it is the non-unified model which appears to better fit the observations.

3.3.3 Submillimetre background predictions

Having constrained the models based on the sub-mm background arising from X-ray-detected AGN, we can generate predictions for the total contribution from all AGN. As noted previously, the total sub-mm background, from observations with *COBE*, is estimated to be ≈ 45 Jy deg^{-2}. According to our non-unified model, the total sub-mm background from AGN is predicted to be 11.2 Jy deg^{-2} in the case with $f_{\rm cov} = 0.65$, or 17.7 Jy deg^{-2} with $f_{\rm cov} = 1.0$. The former value represents 25% of the entire background, while the latter reaches $\approx 40\%$ of the total.

We suggest, therefore, that assuming a non-unified AGN model, AGN are likely to account for at least 25% of the total sub-mm background. But since this value is based on a model normalised by the ECDFS observations, where sub-mm sources counts are much lower than the average, the total AGN contribution may in fact be as high as 40%.

Assuming instead a unified AGN model, the contribution is much smaller. In this case, the total predicted contribution from AGN is 5.9 Jy deg^{-2}, or $\approx 13\%$ of the total background. This provides an estimate of the lower limit on the AGN contribution to the EBL.

We note in passing that X-ray-undetected AGN in the ECDFS are predicted to contribute 9.7 Jy deg^{-2} to the sub-mm background. This is to be compared to the measured 4.8 ± 1.2 Jy deg^{-2} from the high-z red galaxies. Again there is no inconsistency here, particularly given that the optical survey is flux-limited.

3.4 Discussion: AGN or starburst dominance in sub-mm galaxies?

We have shown in this chapter that a model of obscured AGN can simultaneously give a good fit to the X-ray background and number counts and the sub-mm background and number counts, and have further shown that the model's predictions for X-ray-detected AGN agree well with the observational results for ECDFS X-ray sources. However, we have also noted in this thesis that an increasing consensus is developing around the idea that the bolometric output of sub-mm galaxies is dominated not by AGN but by starburst activity. In this Discussion we consider some of the evidence for this hypothesis.

One telltale sign of AGN activity is X-ray emission, therefore the X-ray properties of sub-mm galaxies are of particular interest. Alexander et al. (2005) found that SMGs show

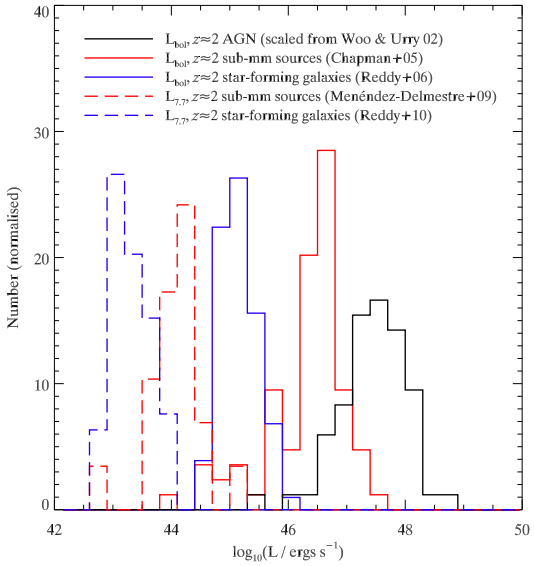

FIGURE 3.8: *Bolometric luminosity distributions for submillimetre galaxies, normal, star-forming Lyman-break galaxies and AGN (scaled to $z = 2$ from $z = 0.75$ assuming $(1 + z)^3$ evolution), and PAH 7.7μm luminosity distributions for the same SMG and LBG samples. All histograms have been normalised to the same area under the curve.*

much lower X-ray fluxes/luminosities than would be expected for AGN, with typical X-ray-to-FIR luminosity ratios of $L_{\rm X}/L_{\rm FIR} \approx 0.004$, compared to $L_{\rm X}/L_{\rm FIR} \approx 0.05$ expected for AGN. These authors therefore estimate an 8% AGN contribution to the bolometric luminosity of SMGs.

However, a key tenet of the non-unified model presented here is that the most sub-mm-luminous AGN are those with Compton-thick obscuration. In these cases, the only X-ray emission detectable with *Chandra* will be a greatly weakened reflected component (Matt et al., 1996, 2000), consisting of X-rays which are scattered off interstellar material in the host galaxy. In this context, significantly reduced $L_{\rm X}/L_{\rm FIR}$ ratios are not unexpected. Indeed, Alexander et al. (2005) note that the FIR luminosities seen in sub-mm galaxies are consistent with AGN origin if the dust covering factor is assumed to be large enough.

Perhaps the most significant result taken to indicate starburst-dominance in bright sub-mm sources is the detection in SMG spectra of bright polycyclic aromatic hydrocarbon features (PAHs; Leger & Puget, 1984; Allamandola, Tielens & Barker, 1985), known to be linked to starburst activity (Rigopoulou et al., 1999). However, PAHs are also ubiquitous in normal, non-starbursting galaxies (Helou et al., 2000; Draine et al., 2007) and

are strongly detected in the hosts of AGN (Clavel et al., 2000; Polletta et al., 2008; Gallimore et al., 2010). Spectroscopic studies have shown that unobscured AGN have very different mid-IR SEDs to starbursts and normal galaxies, with much brighter 7μm continua and relatively weaker PAH emission lines, but that obscured AGN have mid-IR SEDs very similar to those of normal galaxies and starbursts (Clavel et al., 2000; Peeters, Spoon & Tielens, 2004), as the increased obscuration of the central nucleus allows the host galaxy to dominate.

The simple presence of bright PAH features in SMGs does not therefore automatically indicate a major starburst. Indeed, Coppin et al. (2010) showed that these features were strongly detected in the spectra of confirmed AGN-dominated SMGs. The argument for starburst dominance in most SMGs is instead based on the *luminosity* of the PAH emission, in particular the 7.7μm band (e.g. Pope et al., 2008; Menéndez-Delmestre et al., 2009). In Fig. 3.8 we show how the bolometric luminosities and PAH luminosities compare for a sample of normal, star-forming galaxies (Reddy et al., 2006b, 2010) and a sample of SMGs (Chapman et al., 2005), both at $z \approx 2$.

The median $L_{\rm bol}$ of the SMGs is a factor of 25 times greater than that of the normal Lyman-break galaxies, and the two distributions show no real overlap. The median $L_{7.7}$, on the other hand, is only 6 times greater and there is some overlap between the two. Therefore, although the SMGs clearly do appear to have a higher level of star-formation than most galaxies at $z \approx 2$, it is not so great that another major contributor to the bolometric luminosity is ruled out. The figure also shows the $L_{\rm bol}$ distribution for AGN, which are at least as luminous as sub-mm galaxies and therefore provide a natural explanation for the extreme bolometric luminosities which are observed in SMGs but not seen in other $z \approx 2$ star-forming galaxies.

Menéndez-Delmestre et al. (2009) have suggested that the equivalent width of the 7.7μm line — that is, its strength relative to the continuum — is also a crucial indicator of starburst dominance in SMGs, since a substantial AGN component would yield a greatly enhanced underlying continuum. However, we have noted above that while this increased continuum is observed in unobscured, type-1 AGN, more heavily obscured AGN tend to have mid-IR spectra which are host-dominated and do not show a significantly enhanced continuum level (e.g. Peeters, Spoon & Tielens, 2004). Indeed, Martínez-Sansigre et al. (2008) have directly shown that the PAH line strengths in the hosts of type-2 AGN are consistent with those observed in sub-mm galaxies.

In summary, then, while it is clear that bright sub-mm sources do host significant

star-formation activity, it remains possible that this occurs in the host galaxies of AGN. The bolometric luminosities of SMGs are very significantly greater than is found in star-forming galaxies at similar redshift, being more comparable to quasar luminosities. The PAH luminosities of SMGs, on the other hand, are not quite so incomparable to normal galaxies. A significant AGN component is not ruled out, as long as the obscuration of the nucleus is great enough to curtail its contribution to the mid-IR continuum; a high level of obscuration is also required from X-ray observations, since this would explain the apparently low X-ray luminosities of sub-mm sources.

This scenario is very much in line with the model presented in this chapter, which predicts that only very obscured AGN may be bright sub-mm sources. Since we have shown that the predictions of this model also fit very well the sub-mm observations of ECDFS X-ray sources presented in Chapter 2, we conclude that it remains a significant possibility that the long-sought obscured AGN population may reside in sub-mm galaxies.

3.5 Summary

We have modelled the contribution of AGN to the sub-mm number counts and background, and have tested the predictions of the model against the ECDFS observations presented in Chapter 2. We summarise our findings below.

- We present a non-unified obscured AGN model which simultaneously matches the observed sub-mm background, the bright ECDFS sub-mm source counts and, significantly, the hard X-ray background.

- In this model, the fractional AGN contribution to the sub-mm background is at least 25%, and perhaps as high as $\approx 40\%$. The remaining component is suggested to come from faint star-forming galaxies.

- In a unified AGN model the AGN contribution would be only $\approx 13\%$. In this case the unidentified bright sub-mm sources may be identified with obscured starbursts rather than obscured AGN.

- We find that ECDFS X-ray sources to their flux limit make a contribution of 1.5 ± 0.1 Jy deg^{-2} to the sub-mm extragalactic background.

- We measure the sub-mm background arising from X-ray sources in different flux and luminosity ranges and find good agreement with the AGN model predictions in either the unified or non-unified case.

- The sub-mm background contributions from absorbed ($N_{\rm H} > 10^{22}$ cm^{-2}) and unabsorbed X-ray sources are also shown to agree well with the predictions of our non-unified AGN model. In this case, however, we find that the predictions of the unified AGN model are poorly matched to the data.

- The attraction of the non-unified model, therefore, is that it may simultaneously explain both the hard XRB and, at least, the bright sub-mm sources via a single obscured AGN population. Other models not only need to invoke a new population of obscured, ultraluminous star-forming galaxies to explain the bright sub-mm sources, but also a fainter population of obscured AGN to explain the hard X-ray background.

IV

Extending PLE models to the mid-IR, far-IR and sub-mm

4.1 Introduction

In studies of galaxy evolution there are, broadly, two ways to proceed. One is the *ab initio* approach, in which galaxy evolution is modelled using a chosen prescription for processes including the collapse and merging of dark matter halos, gas heating and cooling, star-formation and feedback (e.g. White & Frenk, 1991; Cole et al., 2000; Baugh et al., 2005; Bower et al., 2006). The other approach is more observationally led, beginning with a description of the local luminosity functions (LFs) and spectral energy distributions (SEDs) of galaxies and 'winding the clock back' to build up a picture of the high-redshift universe (Bruzual & Kron, 1980; Koo, 1981; Shanks et al., 1984; Pozzetti et al., 1998). These approaches are often called 'forward evolution' and 'backward evolution' respectively (for a review, see §5.2 of Hauser & Dwek, 2001). While forward evolution models can potentially offer greater insight into the physical processes that may be driving galaxy evolution, the advantage of backward evolution models is that they begin with a phenomenological description of the local universe, which is comparatively well understood and well constrained.

The semi-analytical models used to simulate structure formation in the ΛCDM cosmology employ a forward evolution, *ab initio* approach. In these models, galaxy formation is a hierarchical process, in which stellar mass is built up over extremely long timescales through the merging of smaller structures (Cole et al., 2000). However, hierarchical models have faced significant observational challenges. To summarise a wide

range of studies, the broad observational picture is that the most massive galaxies host old stellar populations (Franx et al., 2003; Cimatti et al., 2004; Glazebrook et al., 2004; Thomas et al., 2005; Bernardi et al., 2006) apparently indicating a high redshift of formation, and show little evolution in their number density since $z \approx 1$ (Wake et al., 2006; Brown et al., 2007; Cool et al., 2008), suggesting no significant dynamical evolution in the last several Gyr. These observations are contrary to the expectation from hierarchical evolution, where massive structures would be expected to have assembled since $z \approx 1$.

The observations are more in line with the predictions of passive evolution models, which assume that galaxies formed early and were in place at some high redshift, thereafter evolving to the present day only in terms of a decreasing star-formation rate. Instead of a hierarchical, merger-driven process of structure formation, passive evolution models assume galaxies formed from massive gas clouds in comparatively short-lived 'monolithic collapse' events.

In this chapter we use a model which employs the backward evolution approach and pure luminosity evolution, beginning with a local LF and evolving it to higher redshift using k- and/or $(k + e)$-corrections with no density evolution. We model galaxy evolution by simply assuming that star-formation declines at different rates in early- and late-type galaxies. This model has been used extensively in the past at optical and near-infrared (NIR) wavelengths (Metcalfe et al., 1995, 2001, 2006; McCracken et al., 2000) where, with modifications (see Metcalfe et al., 2006), it has been successful in matching observations from the U to the K band and out to $z \approx 4$. We now test the model's predictions against observations in the mid-IR, far-IR and sub-mm.

These long wavelength regimes are important to galaxy evolution studies. Observations with the *COBE* satellite in the 1990s confirmed the existence of a cosmic infrared background (CIB) which peaks in the far-IR at $\lambda \approx 100$–300μm (Puget et al., 1998; Fixsen et al., 1998; Hauser et al., 1998). It is now clear that the CIB, which arises from the re-emission by dust of absorbed radiation, has a total intensity roughly equal to that of the extragalactic background at optical wavelengths. Since infrared sources contribute only $\approx 30\%$ of the total energy output of the local universe (Soifer & Neugebauer, 1991), there is expected to be significant evolution in the populations which contribute to the infrared background. It is clear, then, that an understanding of the evolution of galaxies at long infrared wavelengths is important to studies of the star-formation and, since AGN may contribute to this background, accretion history of the universe.

Other authors have presented models which give a good fit to mid-IR, far-IR and sub-

mm observations, using both hierarchical forward evolution models (e.g. Granato et al., 2000; Lacey et al., 2008) and phenomenological backward evolution models (e.g. Chary & Elbaz, 2001; Rowan-Robinson, 2001, 2009; Lagache, Dole & Puget, 2003; Lagache et al., 2004).

Typically, these models are designed specifically to match infrared observations. The hierarchical ΛCDM model requires a top-heavy IMF to fit the FIR/sub-mm data (Baugh et al., 2005; Lacey et al., 2008), and the phenomenological models tend to employ a range of different spectral types, including luminous starbursts, or allow for strong evolution in the luminosity functions. Here our approach differs: all aspects of our model, including the modest amount of dust absorption, were defined in the optical bands. The surprise has been that this simple model continued to represent the data well as it was applied at high redshifts and to longer, near-IR wavelengths. We now extend this much further, out to the mid-IR, far-IR and sub-mm regimes, following Busswell & Shanks (2001). Determining where and how the model breaks down is instructive, since this may indicate a requirement for dynamical evolution or for another population to dominate the counts, e.g. AGN (Chapter 3).

For consistency with the work of Metcalfe et al., throughout this chapter we adopt a cosmology with $H_0 = 50$ km s^{-1} Mpc^{-1}, $\Omega_m = 0.3$ and $\Omega_\Lambda = 0.7$. A more standard cosmology with $H_0 = 70$ km s^{-1} Mpc^{-1} could be equally well adopted by scaling the M^* and τ values used in our model, as described by Metcalfe et al. (2006).

4.2 Data

To test our model predictions of colours at *Spitzer* IRAC wavelengths, we make use of data from the ≈ 200 arcmin^2 GOODS-North survey. This field is well suited since it has some of the deepest NIR and IRAC imaging available over a relatively wide area and has also been targetted in several spectroscopic follow-up surveys. For photometry we use the catalogue recently presented by Wang et al. (2010), who combine public *Spitzer* IRAC data (Dickinson et al., in prep.) with a new ultradeep K-band image, using the K positions as priors and detecting robust IRAC counterparts. We get redshifts for these sources by matching to redshift catalogues from Cohen et al. (2000), Cowie et al. (2004) and Wirth et al. (2004). We supplement this with the catalogue presented by Reddy et al. (2006), which includes spectroscopic redshifts and K-band and IRAC fluxes for 388 high-z galaxies in GOODS-N. Our total redshift sample includes 1,617 galaxies.

Numbers counts of galaxies in the *Spitzer* IRAC (3.6, 4.5, 5.8 and 8.0μm) and MIPS (24, 70 and 160μm) bands have been measured across a wide flux range by surveys which combine observations from several fields of differing width and depth in order to achieve good sampling of both the faint and bright end of the source counts. At IRAC wavelengths, we use the published counts of Magdis et al. (2008), whose survey combined 6 fields, and of Fazio et al. (2004), who provide counts from three regions ranging from an ultradeep $5' \times 10'$ field to the wide $3^\circ \times 3^\circ$ Boötes field. A similar selection of fields was used by Papovich et al. (2004) and Dole et al. (2004) in the MIPS bands, with the combination of deep and wide fields allowing them to determine number counts across 3 decades of flux. Marleau et al. (2004) provide 24μm counts in 3 fields ranging from 0.015 to 4.4 deg^2 in area. A more recent survey by Bethermin et al. (2010) took this approach further, combining MIPS observations across 9 fields of various depths covering ≈ 54 deg^2 in total. We use all of these datasets, as well as our own counts from public GOODS-N imaging in the IRAC bands (Dickinson et al., in prep.) and at 24μm (Chary et al., in prep.) using SExtractor (Bertin & Arnouts, 1996) on the image frames.

We also compare our model to observations at 60μm, where counts are available from wide-field IRAS surveys (Lonsdale et al., 1990; Rowan-Robinson et al., 1991; Gregorich et al., 1995), although these observations do not reach the same depth achieved by the more recent *Spitzer* surveys.

Finally, we use recent galaxy surveys in the sub-mm bands at 250, 350 and 500μm. These are the wavebands probed by the SPIRE detector on *Herschel* (Pilbratt et al., 2010) and by *Herschel's* balloon-borne forerunner, BLAST (Patanchon et al., 2009). We make use of BLAST number counts (Patanchon et al., 2009) and redshift distributions (Chapin et al., 2010; see also Dunlop et al., 2009) from observations covering ≈ 10 deg^2. We use SPIRE number counts from the HerMES survey, currently covering ≈ 20 deg^2, both as published by Oliver et al. (2010) and also as presented by Dunlop et al. (2010) and from the H-ATLAS survey, covering ≈ 14 deg^2 to date (Clements et al., 2010).

4.3 Model

Here we give a brief summary of the galaxy evolution model we employ, and we review some previous results from this model at optical/NIR wavelengths. For a more detailed description of the model we refer the reader to Metcalfe et al. (2006) and references therein.

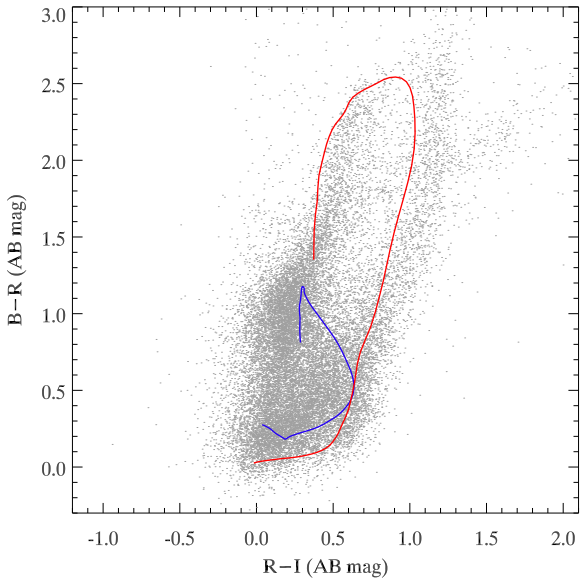

FIGURE 4.1: *A BRI colour-colour diagram showing the predicted redshift tracks for the $\tau = 9$ spirals (blue line) and the $\tau = 1$ ellipticals (red line). The data shown are $R < 25$ (AB) galaxies in the GOODS-N field. This plot clearly demonstrates the bimodality that exists in observations of galaxy populations, and our model is in excellent agreement with the data.*

4.3.1 Galaxy types

Our basic galaxy model assumes only two populations, broadly corresponding to early-types (old, red, passive systems) and late-types (young, blue, star-forming spirals). Both types are modelled with exponentially decreasing star formation rates (SFRs), i.e. $\mathrm{SFR}(t) \propto \mathrm{e}^{-t/\tau}$. The early- and late-type galaxies are distinguished by different characteristic e-folding times, τ: for early-types we use $\tau = 1$ Gyr, for late-types $\tau = 9$ Gyr. Based on this formula we use Bruzual & Charlot (2003; hereafter BC03) models to produce template spectral energy distributions (SEDs) for these two galaxy types, assuming a Chabrier (2003) IMF.

Assuming a bimodal galaxy population is clearly a simplification, but it is not without merit. Optical colour-magnitude diagrams have long shown evidence of a so-called 'red sequence' and 'blue cloud', the former consisting primarily of bulge-dominated galaxies with old stellar populations and the latter of young, disk-dominated, star-forming galaxies. Colour-colour diagrams also lend weight to a bimodal population — such plots can often be seen to show two curving tracks, and these are well matched by models us-

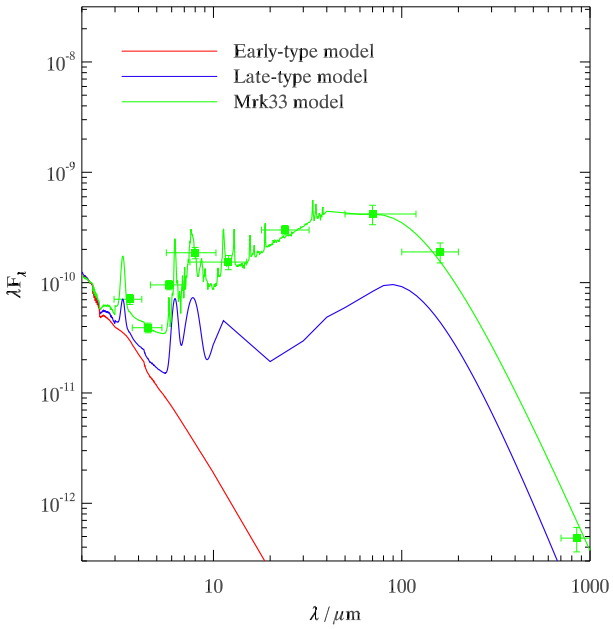

FIGURE 4.2: *Infrared SEDs for three galaxy templates. Our standard, bimodal models comprises the early- and late-type galaxies (red and blue); the early-types are dustless so we see only the long-wavelength tail of the stellar emission, while the late-types include dust with a schematic representation of the PAH features (see text). Also shown is an SED based on the starburst galaxy Mrk33 (green), which we introduce at $\lambda \geq 24\mu$m in place of a fairly small fraction of the normal late-types. The PAH spectrum for Mrk33 comes from IRS observations and the green datapoints show broadband photometry for Mrk33. All models and data are normalised to be equal at 2μm; the y-axis is in arbitrary units of λF_λ.*

ing a $\tau = 1$ and a $\tau = 9$ population; this is clear from Fig. 4.1.

4.3.2 Dust spectrum

In order to apply this model at infrared wavelengths, a prescription for dust absorption and re-radiation is required. We apply a $1/\lambda$ extinction law normalised at 4500Å in the B band with some normalisation A_B. That is, the flux at a given wavelength after absorption, F_λ, relates to the unabsorbed flux $F_{\lambda,0}$ according to Eqn. 4.1.

$$F_\lambda = 10^{-0.4 \times A_B \times \frac{4500}{\lambda}} F_{\lambda,0} \tag{4.1}$$

The absorbed radiation is re-emitted by the dust in the infrared. The primary com-

ponent of this emission is a modified Planck function, which has some given dust temperature and opacity. As with the model in Chapter 3, we apply an opacity law with the standard form $\kappa \propto \lambda^{-\beta}$ with $\beta = 1.5$ (Dunne & Eales, 2001).

Emission from polycyclic aromatic hydrocarbons (PAHs) is an important spectral feature between 3 and 13μm. In our spiral galaxy model we include a fairly schematic representation of the PAH features, designed to broadly resemble the spectra of galaxies observed in the Spitzer Infrared Nearby Galaxies Survey (SINGS; Kennicutt et al., 2003), presented by Draine et al. (2007). We show the IR spectra of our early- and late-types in Fig. 4.2. While the modelling of the PAH features in the late-types is somewhat rudimentary, we find it is sufficient to reproduce the observed colours and sources counts of galaxies which sample this part of the spectrum, so we consider it sufficient for the purposes of this work.

Fig. 4.2 also includes a third SED, which represents a starburst component modelled on Markarian 33 (Mrk33). This is an additional spectral type which we introduce when dealing with observations at $\lambda \geq 24\mu$m (see §4.5.2); the motivation for including this component is discussed in that section of the chapter.

We use a dust temperature of 30K, which is found to be a typical temperature of interstellar dust in star-forming galaxies (Farrah et al., 2003; Pope et al., 2006; Coppin et al., 2008b; Elbaz et al., 2010). We take $A_B = 0.3$ magnitudes for the normalisation of the $1/\lambda$ dust absorption law; this is the value determined by Metcalfe et al. (2001) when using this model at optical wavelengths, and is a fairly conservative amount of extinction. Note that we only include this dust extinction (and subsequent re-radiation) in the spiral galaxy population; the ellipticals are assumed to be dustless. The total integrated flux of the dust emission, in the form of both the PAH features and the blackbody, is normalised to be equal to the total absorbed flux.

4.3.3 Initial mass function and luminosity function

For each galaxy type, we begin with a K-band luminosity function, initially defined in the B band but shifted to K using modelled $B - K$ colours. The parameters for this LF are given in Table 4.1. The LF is then corrected it into the mid-IR/far-IR/sub-mm band we wish to investigate using the appropriate rest-frame $z = 0$ colour from Table 4.2. Then using $k + e$ corrections determined by the BC03 evolution code, the LF is evolved back from the present day. This model is a simplification of the model of Metcalfe et al. (2001, 2006) since rather than 5 independent colours, one for each type, we use only two,

TABLE 4.1: *Luminosity function parameters. These are the same as those used by Metcalfe et al. except for the magnitudes, which we calculate by taking their R band LF and subtracting the $R-K$ colours from our BC03 models. When shifting the LF to another band in this way we use two colours, one for early-types (E/S0 and Sab) and one for late-types (Sbc, Scd and Sdm).*

Population	Type	Φ^*/Mpc^{-3}	α	$M^*_{K,Vega}$
Early types	E/S0	9.27×10^{-4}	-0.7	-24.92
	Sab	4.63×10^{-4}	-0.7	-24.78
Late types	Sbc	6.20×10^{-4}	-1.1	-24.83
	Scd	2.73×10^{-4}	-1.5	-24.34
	Sdm	1.36×10^{-4}	-1.5	-23.71

TABLE 4.2: *$z=0$ colours between the K band and all the mid-IR, far-IR and sub-mm wavebands used in this work. For consistency with Metcalfe et al. we use Vega colours where possible; at 60μm and above this is infeasible and we instead use AB colours. Colours are given for our two main galaxy types as well as for the starburst population which we make use of at 24μm and above.*

	Vega colour $K-[x]$				
Population	[3.6]	[4.5]	[5.8]	[8.0]	[24]
Early types	0.16	0.18	0.25	0.35	0.44
Late types	0.46	0.44	1.66	2.98	5.36
Starburst	–	–	–	–	8.09

	AB colour $K-[x]$						
Population	[60]	[70]	[160]	[250]	[350]	[500]	[850]
Early types	–	–	–	–	–	–	–
Late types	3.13	3.47	3.67	2.67	1.74	0.73	-0.38
Starburst	5.13	5.29	5.15	4.24	3.42	2.55	0.99

TABLE 4.3: *Characteristic magnitudes, M^*, for the luminosity function of our galaxy types in all of the mid-IR, far-IR and sub-mm wavebands used in this chapter. Since the ellipticals are dustless in our model their contribution falls essentially to zero in the FIR/sub-mm, therefore these colours are omitted. As described later in the chapter, at 24μm and above we replace the Scd population with a population based on the starburst galaxy Mrk33. Note that for consistency with Metcalfe et al. we use Vega colours out to 24μm. At 60μm and above this is infeasible, so the magnitudes given for these bands are in the AB system.*

Type	$M^*_{3.6}$	$M^*_{4.5}$	$M^*_{5.8}$	$M^*_{8.0}$	M^*_{24}	M^*_{60}	M^*_{70}	M^*_{160}	M^*_{250}	M^*_{350}	M^*_{500}	M^*_{850}
E/S0	-25.08	-25.10	-25.17	-25.27	-25.36	–	–	–	–	–	–	–
Sab	-24.94	-24.96	-25.03	-25.13	-25.22	–	–	–	–	–	–	–
Sbc	-25.29	-25.27	-26.49	-27.81	-30.19	-26.07	-26.41	-26.61	-25.61	-24.68	-23.67	-22.56
Scd	-24.80	-24.78	-26.00	-27.32	–	–	–	–	–	–	–	–
Starburst	–	–	–	–	-32.92	-27.58	-27.74	-27.60	-26.69	-25.87	-25.00	-23.44
Sdm	-24.17	-24.15	-25.37	-26.69	-29.07	-24.95	-25.29	-25.49	-24.49	-23.56	-22.55	-21.44

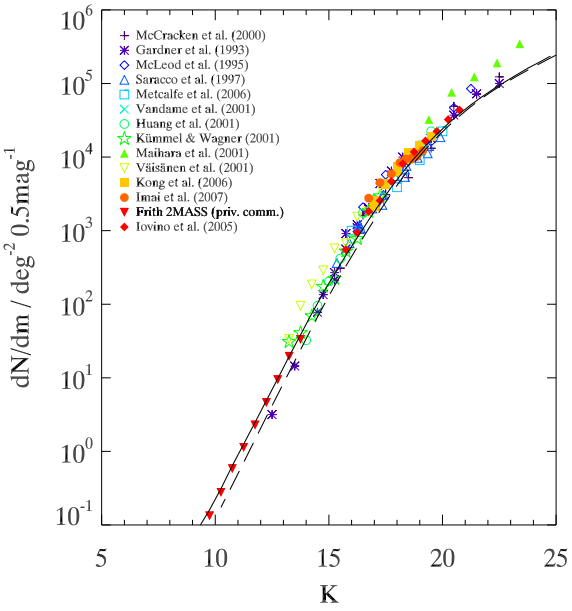

FIGURE 4.3: *Differential number counts in the K band. The solid line is the prediction of the model used in this work; the dashed line shows the model of Metcalfe et al. (2006) who use an $x = 3$ IMF for early-types as described in the main text.*

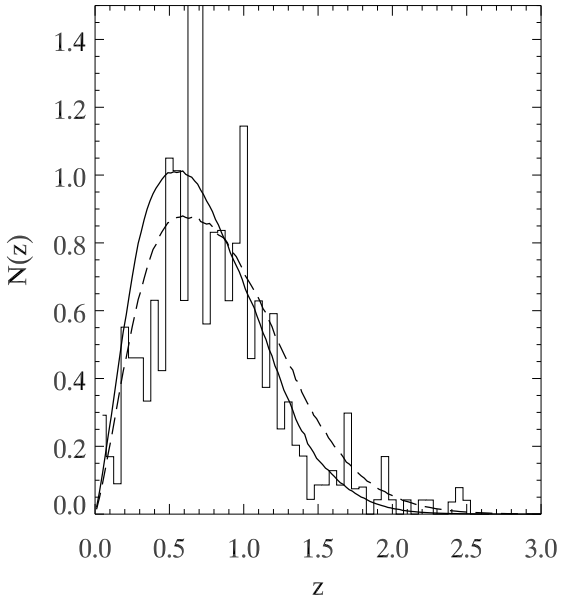

FIGURE 4.4: *The redshift distribution of sources in the K band. The histogram shows observational data from the K20 survey (Cimatti et al., 2002) down to a magnitude limit of $K = 20$. The solid and dashed lines are as in Fig. 4.3*

one for all of the early-types (E/S0 and Sab) and one for all of the late-types (Sbc, Scd and Sdm). This is justified on the basis that the band-band colour differences in the NIR are smaller than in the optical. The $z = 0$ colours are taken from the BC03 model predictions. Table 4.3 shows the values of M^* after shifting into MIR/FIR/sub-mm bands. On this basis, we determine predictions for the observed galaxy number counts and colours.

Metcalfe et al. (2001, 2006) used a Salpeter IMF (Salpeter, 1955; $x = 1.35$) for the $k + e$ corrections of spirals but used an $x = 3$ IMF, cut at $M > 0.5$ M$_\odot$, for the $k + e$ corrections of early-types. This was to reduce the passive evolution in the K band to almost the level of the K band k-correction to prevent too many $z > 1$ galaxies being predicted at $K < 20$, which would be the case for the Salpeter IMF. For the BC03 models we are using the Chabrier IMF (Chabier, 2003; $x = 1.3$ at $M > 1M_\odot$) with an SFR e-folding time of $\tau = 9$ Gyr for the spirals; this produces $k + e$ corrections very similar to the Salpeter with $\tau = 9$ Gyr. For the early-type galaxies, no $x = 3$ (or Scalo, 1986) IMF was easily available from BC03 and so here for predicting number counts and $n(z)$ in the K band and redward, we have simply assumed the k-correction from the Chabrier IMF, with $\tau = 1$ Gyr rather than $\tau = 2.5$ Gyr to account for the degeneracy between IMF slope and SFR in the $k + e$ predictions (Metcalfe et al., 2001). We have checked that these are good approximations to the $x = 3$ predictions in the near-/mid-IR bands. Ultimately, the choice of IMF and SFR for early-types has little impact on our results since the early-types are taken to be dustless, and their contribution is therefore negligible in most of the mid-IR, far-IR and sub-mm wavebands which are the focus of this chapter.

In Fig. 4.3 we show the model predictions for the K band number counts generated in this way and we note the model fits the counts very well across the full range of magnitudes. We also see that the model agrees well with the $x = 3$ model of Metcalfe et al. In Fig. 4.4 we show the K band redshift distribution compared to the data from the K20 survey (Cimatti et al., 2002) where again there is excellent agreement between the model and the data, with the fit being comparable to that found with the $x = 3$ model.

4.4 Galaxy colours

In Fig. 4.5 we present our model predictions for colour-redshift tracks in near-/mid-IR bands. The predictions are compared to observed colours of $K < 22.5$ galaxies in the GOODS-N catalogue of Wang et al. (2010), described in §4.2. Overall, the agreement between the data and our model in Fig. 4.5 is very good, suggesting that a simple optically-

defined PLE galaxy model can match colours in the mid-IR out to at least $\lambda = 8\mu$m and $z = 2.5$. The predicted spiral galaxy tracks in Fig. 4.5 show a 'bump' in $K-[3.6]$ at $z \approx 0.1$ and in $K-[4.5]$ at $z \approx 0.5$. These arise from the PAH emission feature at $\lambda = 3.3\mu$m passing through the 3.6 and 4.5 micron bands, respectively. In the $K-[4.5]:z$ plot there is clear evidence of this bump in the data, well matched by the model, however the corresponding bump is not as clearly seen in the $K-[3.6]:z$ plot. This PAH line is also responsible for the significant peak seen in the $[3.6]-[4.5]$ colour at $z \approx 0.4$, which again is replicated by the data.

The difference between the early- and late-type models is most pronounced in the $[5.8]-[8.0]$ colour (Fig. 4.5 lower-right panel), because the 5.8μm and 8.0μm bands sample the region of the spectrum where the contribution from dust is important relative to that from starlight. Since our early-types are modelled without dust it is the predicted colours of the late-types which give a better fit to most of the data here.

In Fig. 4.6 we show colour-colour plots in the IRAC bands and in each case it is clear that the models are successful in matching the data, which again comes from Wang et al. (2010) and is cut to $K < 21$. Figs. 4.5 and 4.6 indicate that by taking simple empirical spectra and evolving them back to higher z it is possible to get a reasonably accurate prediction for the average mid-IR colours of galaxies at a given redshift. Using colours to select galaxies in a specified redshift range has become a powerful tool, for example in the selection of Lyman-break galaxies (LBGs; e.g. Steidel et al., 2003; Adelberger et al., 2004, Bielby et al., 2010), distant red galaxies (DRGs; Franx et al., 2003), extremely red objects (EROs; e.g. Roche et al., 2002), pBzK and sBzK galaxies (Daddi et al., 2004), and "BM/BX" galaxies (Steidel et al., 2004). Our PLE models may provide a simple underlying framework in which these colour selections can be better understood.

The $[3.6]-[4.5]:[5.8]-[8.0]$ colour-colour plot (Fig. 4.6*c*) has been used widely to select populations at different redshifts (Stern et al., 2005; Yun et al., 2008; Dey et al., 2008; Devlin et al., 2009). The data in this plot visibly separate into two 'tiers' with the upper tier, redder in [3.6]–[4.5], hosting higher-z objects. Our models predict that the upper and lower tiers should divide galaxies above and below $z = 1.3$; this is consistent with the finding of Devlin et al. (2009) that it cut galaxies at $z \approx 1.2$, especially given that they found $\approx 15\%$ contamination of higher-z sources in the lower tier and lower-z sources in the upper tier. Stern et al. (2005) identified an 'AGN wedge' in the upper tier, a region they suggest is populated by active galactic nuclei. For reference we have marked this region in Fig. 4.6*c*; it is located redward of the high-z end of our galaxy models in

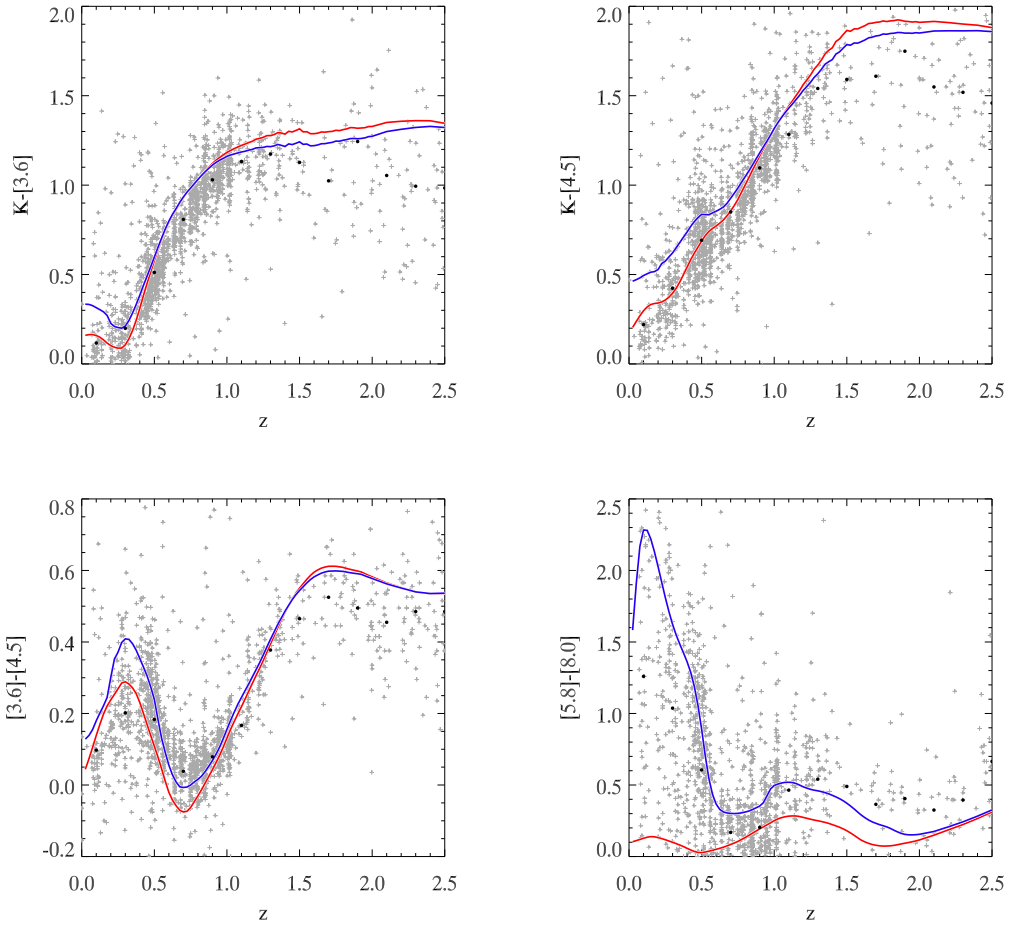

FIGURE 4.5: *Colour-redshift plots showing how our models compare to observational data from GOODS-N spectroscopic surveys. Red and blue lines are PLE redshift tracks for our early-type and late-type models respectively. Black circles indicate the median of the data in* $\Delta z = 0.2$ *bins. Overall there is a good agreement between the data and the model predictions.*

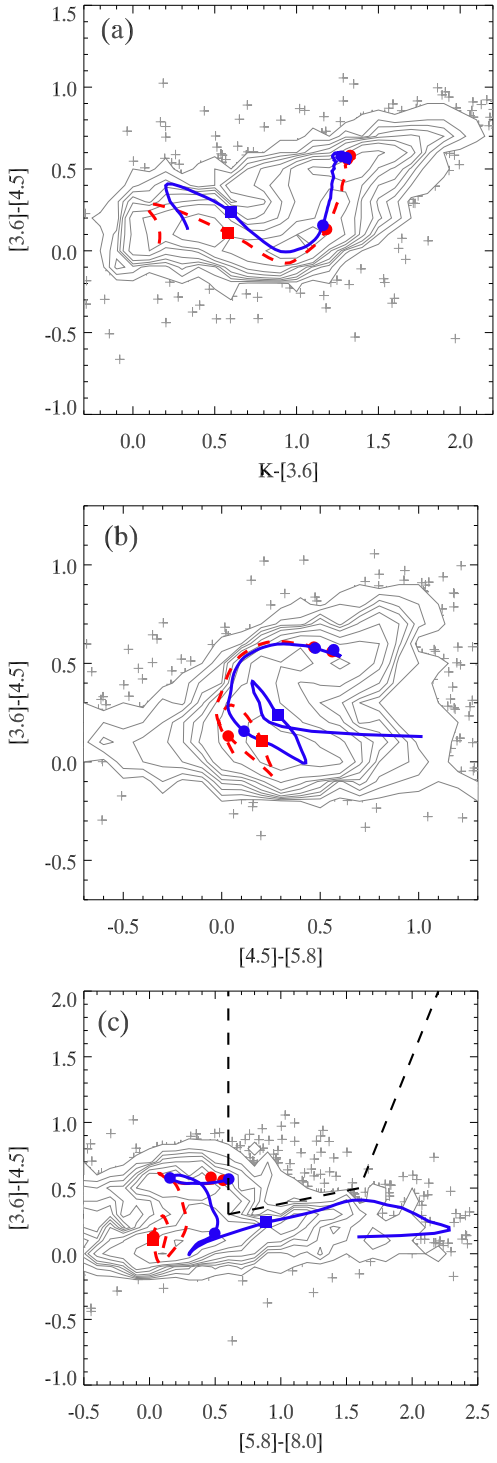

FIGURE 4.6: *Colour-colour plots comparing our models to $K < 21$ GOODS-N data. The lowest contour indicates 2 objects in a 0.1×0.1 magnitude bin – below this galaxies are shown as individual crosses. Our early-type (red) and late-type (blue) models are plotted, with a square marker at $z = 0.5$ and circles further along marking $z = 1$, 2 and 3. For reference, panel* (c) *also shows the 'AGN wedge' (dashed line; Stern et al., 2005).*

[5.8]–[8.0].

Essentially, simple colour-redshift tracks present a viable way for observers to select galaxies in a given z-range. Importantly, we find that sources which lie on the upper ($z > 1.3$) tier of the $[3.6]-[4.5]:[5.8]-[8.0]$ plot also lie around the $1.3 < z < 3$ track in, for example, a $B-R:R-I$ or $R-I:I-K$ plot, so we emphasise that colour selection techniques in the context of PLE models or otherwise can be used successfully and consistently all the way through the optical, near-IR and out to mid-IR wavelengths.

In summary, we have demonstrated that mid-IR colour-redshift data show no contradiction or inconsistency with the predictions of optically-defined galaxy evolution models with $\tau = 1$ Gyr for early-types and $\tau = 9$ Gyr for late-types.

4.5 Mid-IR number counts

4.5.1 IRAC bands

Fig. 4.7 shows the number counts of galaxies at 3.6, 4.5, 5.8 and 8.0μm. The predictions of our model are compared to data from Fazio et al. (2004) and Magdis et al. (2004), in observed fields ranging from an ultradeep $5' \times 10'$ field to the wide $3^\circ \times 3^\circ$ Boötes field, providing good sampling of both the faint and bright end of the counts. We also compare to counts of GOODS-N sources by using SExtractor on the public *Spitzer* imaging of the that field (Dickinson et al., in prep.), which agree well with the published data. In both datasets stars have been excluded.

For each band we show a second panel displaying the Euclidean normalised source counts, calculated as $\log(\mathrm{d}N/\mathrm{d}m) - 0.6(m-10)$; this removes the Euclidean slope from the counts (Fazio et al., 2004). Plotting number counts in this way enables a better comparison of models and data.

At 3.6μm and 4.5μm, the agreement between the model and the data is generally good. Although the model appears to overpredict the counts at the faint end, the data here suffer from confusion. The fit at 5.8μm is poorer than in the other bands, possibly due to our somewhat unsophisticated modelling of the PAH features, which may have a more noticeable effect at 5.8μm than elsewhere. While a more refined model of these features may improve the prediction, we do not consider this adaptation to be necessary for the purposes of this chapter. Indeed, we note that the fit to the 5.8μm data is very similar to that achieved by the ΛCDM hierarchical formation models presented by Lacey et al. (2008). At 8μm the fit is improved relative to 5.8μm due to a significant

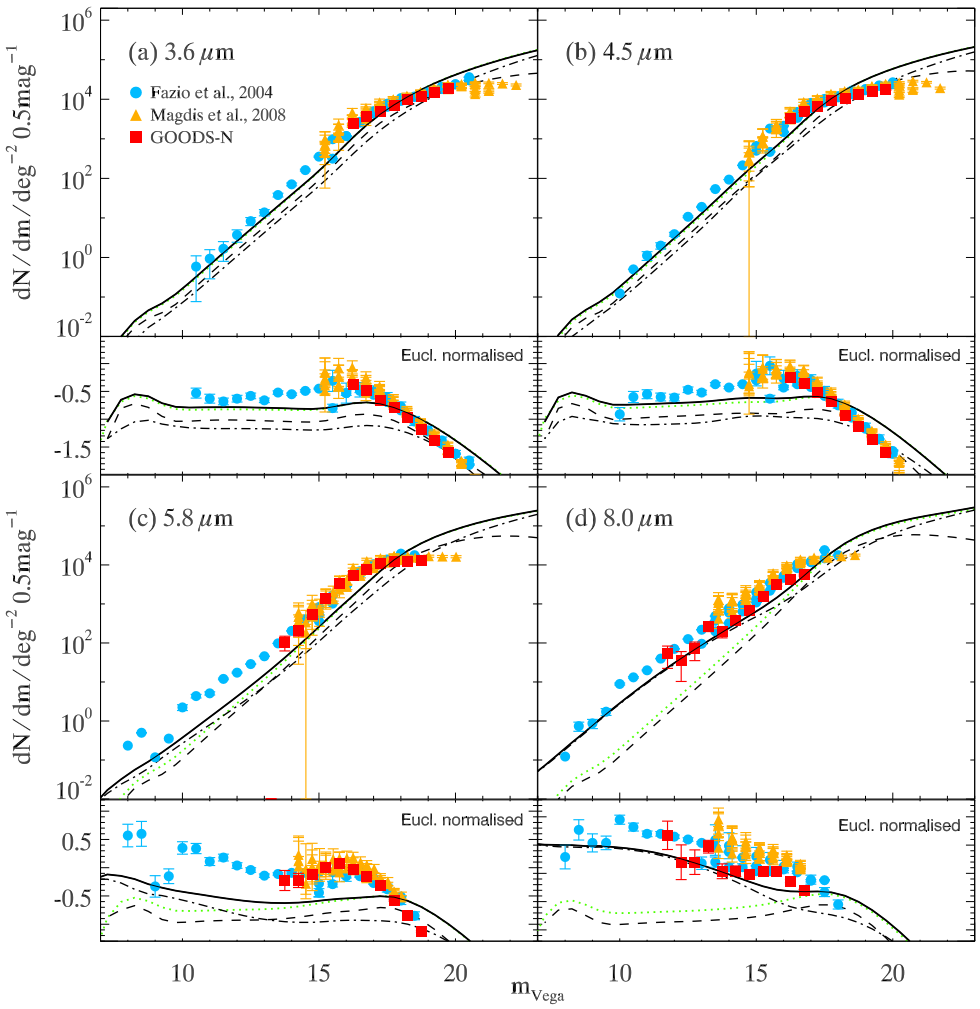

FIGURE 4.7: *Differential number counts in IRAC's 4 channels:* (a) *3.6μm,* (b) *4.5μm,* (c) *5.8μm and* (d) *8.0μm. In each case, the Euclidean-normalised counts are shown in a separate panel; the y-axis for these counts is* $\log(\mathrm{d}N/\mathrm{d}m) - 0.6(m - 10)$. *The solid black line shows the prediction of our model; dot-dashed and dashed black lines indicate the contributions from late- and early-type galaxies, respectively. The green dotted line shows the combined contribution made by all galaxies from stellar light only, i.e. without the emission from dust. As indicated, data are shown from Fazio et al. (2004), Magdis et al. (2008) and our own counts from our GOODS-N catalogue.*

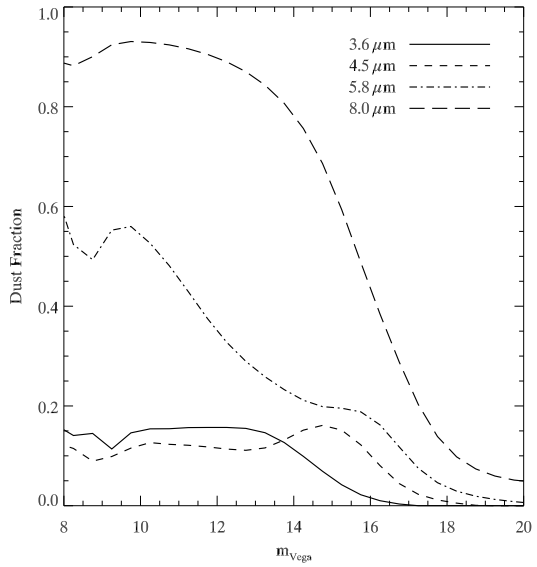

FIGURE 4.8: *The fraction of the galaxy number counts accounted for by dust emission, rather than stellar light, in each of the IRAC channels, based on the models in Fig. 4.7. The shift from starlight-dominated to dust-dominated emission appears to occur around* $\lambda \approx 5$–$6\mu m$.

dust contribution, although the model does still underpredict the data. There is much greater variation in the observed counts here, however, so the success or failure of the fit is harder to ascertain.

The plots also show the contribution made in each band by stellar light only (as opposed to dust). At 3.6μm and 4.5μm the stellar component accounts for the almost all of the counts, while in the longer wavelength bands it yields an underprediction. In Fig. 4.8 we show the fraction of the total predicted counts arising from dust emission in each of the IRAC bands, clearly demonstrating the transition from starlight-dominated to dust-dominated galaxy counts as we move from the near- to the mid-infrared.

In each band the very faintest source counts remain starlight-dominated, even at 8μm. The model suggests that direct stellar emission accounts for only $\approx 10\%$ of the 8μm number counts at magnitudes brighter than $m = 13$ (a flux of $S_{8\mu\mathrm{m}} \gtrsim 0.4$ mJy), but makes up the dominant fraction ($> 90\%$) of 8μm sources fainter than $m = 18$ ($S_{8\mu\mathrm{m}} \lesssim 4$ μJy).

Overall, we have shown that a basic PLE model, originally designed to match optical B-band counts, continues to provide a reasonably good description of the observed source counts out to the mid-IR wavelength regime at 8μm if a modest amount of dust absorption and re-emission for spiral galaxies is included.

4.5.2 24 microns

In Fig. 4.9 we show 24μm number counts, with data from Papovich et al. (2004), Marleau et al. (2004) and our own source counts from public GOODS-N 24μm data (Chary et al., in prep.). We find that our model of normal galaxies, using the same dust parameters which had reasonable success at $3.6 < \lambda < 8.0$ μm underpredicts the number counts by a factor of 4–5 (dashed line in Fig. 4.9), accounting for only 22% of $F_{24} > 30$ μJy sources. This, then, is the wavelength regime where our basic model first breaks down.

However, we find that a relatively simple alteration to the model addresses this problem somewhat. We introduce a subset of our spiral galaxies, modelled on the dust features of Mrk33, as presented in the SINGS spectroscopic survey of local galaxies. In the SINGS survey, two-component dust models are used to match observed mid-IR SEDs of local galaxies (Draine et al., 2007). In most cases the dust emission is dominated by dust in the diffuse ISM, but some galaxies' dust emission is dominated by a warmer component, attributable primarily to photo-dissociative regions (PDRs), where the dust is exposed to a stronger intensity of radiation. These sources are found to have typically higher star-formation rates.

The PDR dust is hotter and thus its emission peaks at shorter wavelength (see Fig. 4.2). As a result of this strong PDR contribution, therefore, these galaxies exhibit a significant excess in flux in the mid-infrared. We find that they can make a significant contribution in the $\lambda \geq 24\mu$m regime, without adversely affecting the fit of the model at shorter optical to mid-IR wavelengths.

18% of the 65 SINGS galaxies discussed in Draine et al. (2007) are of this type; these include Mrk33, NGC2798, NGC3049 and Tol89. We modelled an SED with such an infrared excess, based on the starburst galaxy Mrk33. Our SED is based on the observed mid-IR spectrum[1] of Mrk33 from SINGS observations with IRS, as well as broadband photometry from Dale et al. (2005) to constrain the dust blackbody at longer wavelength. This SED and the broadband data appear in Fig. 4.2. We substituted this SED for a comparable fraction (16%) of the dusty late-type galaxies in our model by replacing the Scd galaxies (see Tables 4.1–4.3) with this starburst population. This component is shown as the dash-dot line in Fig. 4.9.

We find that including these sources in our PLE model yields a significant improvement in the fit to the counts, particularly at the bright end, suggesting that at 24μm the

[1] available for download at http://sings.stsci.edu/

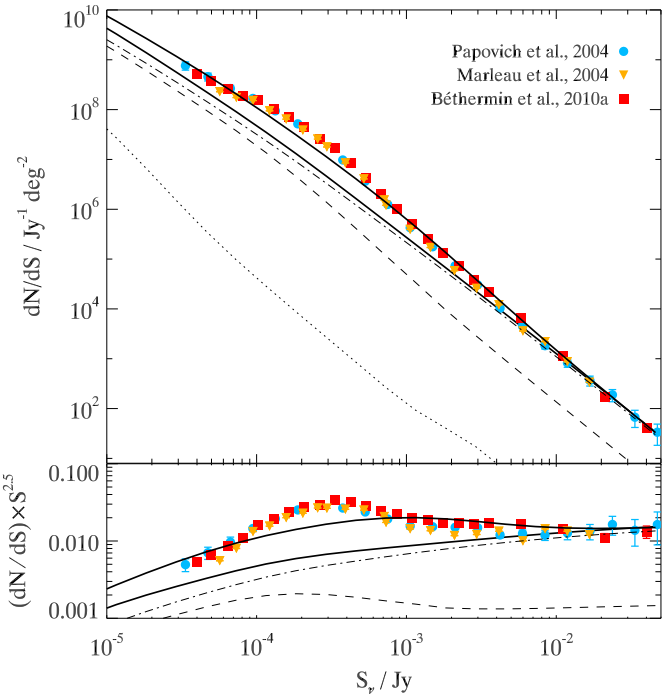

FIGURE 4.9: *Differential number counts at 24μm, with Euclidean normalised counts shown in the bottom panel. In each panel, the lower of the two solid lines is the prediction of our normal model, with contributions from normal spirals (dashed line), Mrk33 starbursts (dot-dashed) and early-types (dotted); the latter contribution is negligible. Mrk33 galaxies clearly dominate the counts. The bright end is extremely well matched, but at the faint end the model is deficient by a factor of a few. We show also the prediction of the model where the Mrk33 component is replaced by an SED with the bright-end ($z = 0$) normalisation of Mrk33 but the $k + e$ evolution of the normal spirals: this is the upper solid line.*

counts are dominated by sources with warmer dust and higher SFRs – primarily starburst galaxies.

While the bright end of the number counts are extremely well matched, at $S_{24\mu\mathrm{m}} < 0.5$ mJy the counts are still underpredicted by a factor of a few. This suggests that our model is deficient in the number of predicted 24μm sources at high redshift, and comparing the predicted redshift distribution of the model to the observed $n(z)$ (Perez-Gonzalez et al., 2005) confirms that this is the case.

Babbedge et al. (2006) suggest that while the galaxy luminosity functions at IRAC wavelengths show relatively little evolution, there is strong evolution in the 24μm LF, particularly out to $z \approx 1$. Including our Mrk33 component brings our model in line with local observations and in doing so enables us to match the bright-flux, low-redshift end

of the counts. Allowing this warm-dust, high-SFR component to evolve more strongly could make it possible to accurately fit the 24μm counts across the full range of flux; this would be in line with the approach taken in previous analyses such as that of Babbedge et al. (2006) and Rowan-Robinson (2001; 2009). However, we explore here the alternative possibility that the counts can be matched by exploiting the negative 24μm k-correction, combined with the moderate PLE which was successful at IRAC wavelengths, instead of invoking much stronger evolution.

This is motivated initially by the finding that the shape of the predicted source counts for the normal spirals matches reasonably well the shape of the data, showing an upturn around 0.5–1.0 mJy where the counts briefly increase at a super-Euclidean rate (Fig. 4.9). The Mrk33 model, although matching the bright end normalisation well, has a much flatter shape with no increase at the faint end.

The faint-end increase in the spiral model arises from a strong negative k-correction, whereas in the Mrk33 SED the k-correction is positive. As the SEDs are redshifted, the PAH region moves into the 24μm band. As this happens, the cool-dust spiral model becomes brighter (giving a negative k-correction) but the Mrk33 model, which has a warm dust component, becomes fainter overall. (See Fig. 4.2).

Therefore, where we previously used the Mrk33 component, we now use instead a population with the same $z = 0$ LF as the Mrk33 population (i.e. the same $K - [24]$ colour), providing the good fit to the bright end counts, but with the $k + e$ evolution of our normal spiral galaxies. We find this gives a much improved fit to the data at faint fluxes (Fig. 4.9). We are essentially using a hypothetical SED which has the same shape as the rest of our spiral galaxies but a redder $K - [24]$ colour and a greater total IR luminosity.

Using the appropriate bright end normalisation, then, PLE yields a reasonably good fit across 3 decades of 24μm flux. Since there is a decoupling of the stellar and dust emissions, this arbitrary normalisation is not unphysical, however unlike our initial inclusion of the Mrk33 component it is not observationally motivated.

We conclude that the 24μm band is the first regime where our simple bimodal PLE model begins to break down. Even with the Mrk33 galaxies included, the model does not have the sufficient ingredients to match the faint-flux, high-redshift counts. However, we have shown that these data can be well matched if one component of our spiral galaxies is altered to be much redder in $K - [24]$, although the data can alternatively be matched by allowing for much stronger evolution, above the level found in our PLE model.

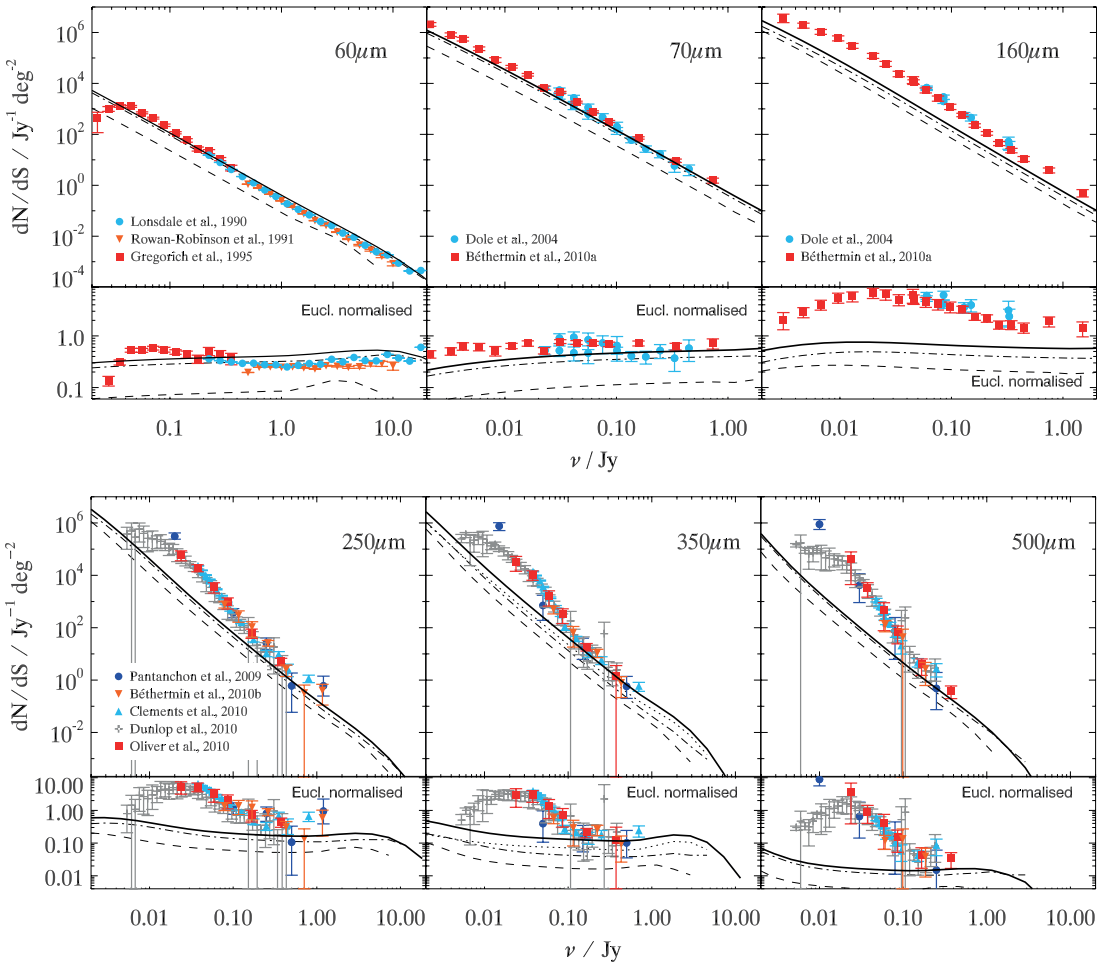

FIGURE 4.10: *Differential number counts at 60–500 microns compared to galaxy model predictions. The total prediction of our galaxy model is given by the solid line; this model comprises the normal spirals (dashed) and the Mrk33 component (dot-dashed). This model gives a reasonable fit to the bright-end data but underpredicts the faint end marginally at 70μmand substantially at 160μm.*

4.6 Far-IR/sub-mm number counts

In Fig. 4.10 we show number counts in 6 wavebands in the far-IR and sub-mm regimes. Counts at 60μm are from wide-field IRAS surveys (Lonsdale et al., 1990; Rowan-Robinson et al., 1991; Gregorich et al., 1995), 70μm and 160μm data come from more recent deep *Spitzer* surveys (Dole et al., 2004; Béthermin et al., 2010) and counts at 250–500μm come from BLAST (Patanchon et al., 2009) and *Herschel* (Clements et al., 2010; Dunlop et al., 2010; Oliver et al., 2010) observations.

4.6.1 Galaxy model predictions

In the far-IR (upper three panels) there appears to be a continuation of the result we found at 24μm: the galaxy model (solid black line), which continues to be dominated by the Mrk33 starburst component (dot-dashed black line), matches the bright end of the counts well, but perhaps begins to underpredict the faint end – this can be seen in the faintest 70μm counts. Our result at 60μm is consistent with that of Busswell & Shanks (2001), who also achieved a good fit to the 60μm counts using a similar model.

While the fit to the 60–70μm counts is, overall, reasonable, the model does very poorly at matching 160μm counts. Moving to submillimetre wavelengths (lower three panels), although the bright end appears to match well, at faint fluxes the model underpredicts the data by as much as 1–2 orders of magnitude. Therefore, normal galaxies which dominate observations at optical to mid-infrared wavelengths account for only a few percent of sources seen in the sub-mm.

4.6.2 Obscured AGN model predictions

The conventional view of the submillimetre-bright galaxy population observed at 850μm is that they are high-z ULIRGs with very high levels of star-formation fuelling their extreme bolometric luminosities (Smail et al., 1997; Barger et al, 1998; Alexander et al., 2005) however, as discussed in §3.4, the possibility remains that obscured AGN make a major contribution. In Chapter 3 we demonstrated that a model of obscured AGN could give a good fit to the observed 850μm source counts and extragalactic background and showed that the predictions of this model for the sub-mm contribution made by X-ray-detected AGN were in line with our measurements for X-ray sources in the ECDFS (Chapter 2).

We now apply the same obscured AGN model described in Chapter 3 to the FIR/sub-mm bands being considered here. Fig. 4.11 shows the predictions of the AGN model for

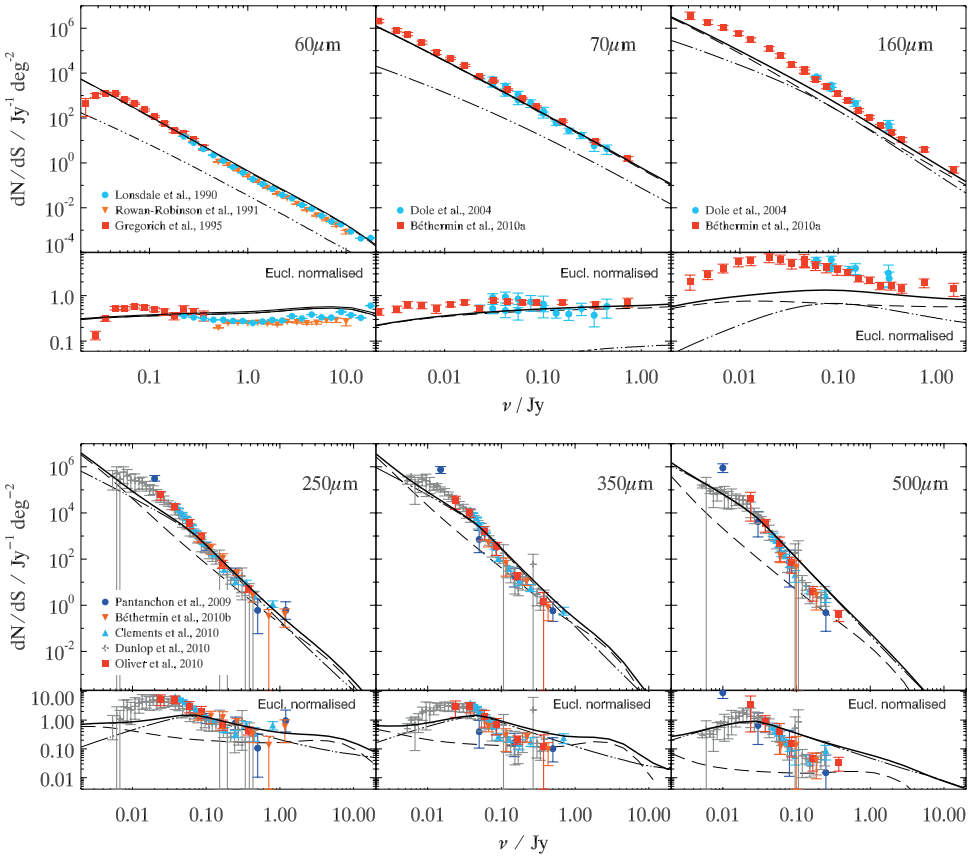

FIGURE 4.11: *Differential number counts at 60–500 microns compared to the prediction of our galaxy + AGN model. The total prediction is given by the solid line, with the galaxy (long dashed) and AGN (dot-dot-dashed) components shown separately. The AGN component is negligible at 60μm and 70μm. At sub-mm wavelengths, the fit is improved relative to the galaxy-only model (Fig. 4.10).*

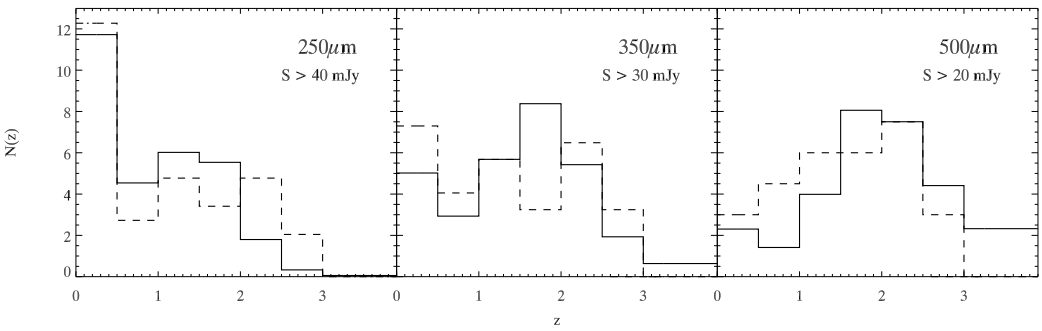

FIGURE 4.12: *Redshift distributions at 250μm, 350μm and 500μm, showing our model prediction (for galaxies and obscured AGN combined; solid line) against the observed distributions published by Chapin et al. (2010; dashed line). The histograms have been normalised to the same total number of sources. In all three bands there is good agreement between the model and the data.*

the same bands as in Fig. 4.10. The galaxy model prediction, as presented in Fig. 4.10, is also shown, as is the total prediction of the combined AGN + galaxy model.

At 60μm and 70μm, the AGN contribution is entirely negligible across the full flux range, since the dust in this model is at 30 K. At 160μm, the AGN contribution roughly equals that of the galaxies, however the combined galaxy-AGN model still falls short of the number counts. The poor fit here may suggest that an additional population is needed to explain the counts; this may be a population of starburst galaxies not associated with AGN (e.g. Wilman et al., 2010).

At 250–500μm, we find that the AGN model can dramatically improve the fit to the data. At 250μm and 350μm, the prediction at faint fluxes ($S < 30$ mJy) is still lower than the data, but sources here are beyond the confusion limit (Nguyen et al., 2010) and so the data must be treated somewhat cautiously. At 500μm, the bright end is somewhat overpredicted by the AGN model. Overall, though, we suggest that the model fits the sub-mm data with reasonable success, and we emphasise that no aspect of the model has been altered to fit these source counts. As noted by Clements et al. (2010; see their figure 1), almost all galaxy evolution models have been unable to match the steep upturn seen in the SPIRE counts.

In Fig. 4.12 we show predicted sub-mm redshift distributions compared to data from a BLAST survey (Chapin et al., 2010). The agreement between the model and the data is generally very good. Dunlop et al. (2009) show that the 250μm $n(z)$ is bimodal, with the population divided broadly into low-z spirals and high-z submillimetre galaxies. This

is replicated in our model – the low-redshift peak arises from our spiral galaxies and the $z > 0.5$ sources are made up of the obscured AGN.

In summary, our PLE galaxy model continues to perform reasonably well out to $\lambda \approx 70\mu$m, but is unable to match source counts at longer wavelengths. At this point we invoke the PLE model of obscured AGN which we have previously shown to match 850μm data, and find that it also gives a reasonable fit at 250–500μm.

4.7 Discussion

We have shown that our basic PLE galaxy model can give a good description of galaxy populations out to 8μm, with starlight dominating the counts out to $\approx 6\mu$m and dust emission dominating after that out to 8 microns. With a starburst component included in line with local observations, the model can continue to match observations out to $\approx 70\mu$m with reasonable success. A caveat is that the 24–70μm counts have been fitted here with a k-correction that comes from a hybrid galaxy template, formed from a stellar blackbody and a PAH component in a ratio not found in local galaxies; others have interpreted data at these wavelengths as requiring strong evolution and this remains a viable alternative interpretation. Either way, the success of the PLE model in fitting data at these long wavelengths is still impressive, given that PLE represents the simplest approximation other than no-evolution models.

There is an increasing consensus surrounding the hierarchical galaxy evolution scenario, in which galaxies form at late times through a gradual build-up of stellar mass via the merging of smaller systems. This motivates the question as to whether PLE models should be treated simply as a convenient phenomenological description of galaxy populations, which can match – and, more valuably, predict – observations, or whether they may in fact have a real, physical basis. In the latter case, the implication would be that galaxies form at high-z in a monolithic collapse event, and passively evolve thereafter. But if these models represent a phenomenological description only, then it must be that hierarchical galaxy evolution is able to present the appearance of generally passive evolution.

The detection of massive galaxy populations at $z > 2$ has proven a challenge for hierarchical models (Baugh et al., 1998; Somerville, Primack & Faber, 2001; Bower et al., 2006) since hierarchical formation should intuitively produce few massive structures at high-redshift given that the process of formation is one of gradual build-up. However,

it has been shown that massive galaxies at $z \gtrsim 2$ can be explained by invoking AGN feedback (e.g. Bower et al., 2006) and/or cold gas accretion (Dekel et al., 2009; Kang et al., 2010). At lower redshift, $z < 1$, hierarchical models predict a rapid evolution in the number of massive ($M > 10^{11} M_{\odot}$) galaxies between $z = 1$ and the present (Baugh et al., 2003). Observations, on the other hand, have shown no evidence for density evolution of massive $\sim L^*$ ellipticals out to $z = 0.9$ (Wake et al., 2006; Brown et al., 2007; Cool et al., 2008). However, it has been possible to reconcile the slow evolution of observed early-type galaxies with the hierarchical model by use of a suitable halo occupation distribution (HOD).

PLE models are entirely consistent with the presence of massive galaxies at high-z and the small amount of evolution $z < 1$, however these models have had only mixed success in matching the clustering of massive galaxies. Wake et al. (2008) suggest that the evolution in the clustering of luminous red galaxies (LRGs) between $z = 0.6$ and $z = 0.2$ rules out passive evolution, particularly at small scales, finding that a hierarchical model with a low merger rate provides a better fit. However, Sawangwit et al. (2009) show that a passive model, with no change in comoving source density, is fully compatible with their clustering measurements in a much larger LRG sample. Thus PLE has not only been found to be an excellent phenomenological fit to the data, it is still possible that it may even represent a good physical model as well.

At wavelengths of 160μm and longer our galaxy PLE model finally fails. We then invoked the non-unified, obscured AGN model of Gunn & Shanks (1999) which, when combined with the galaxy model, fits the 870μm source counts (Chapter 3). We showed that this model also fits the *Herschel* counts at 250, 350 and 500μm. Given that this could remove the need for high luminosity, massive starbursts to fit the sub-mm counts, then this AGN model could be said to ease the problem that such massive galaxies at high redshifts represent for the standard ΛCDM cosmological model. There would be for example no need to invoke a top heavy IMF to explain such sources (Baugh et al., 2005). It would only remain to check whether the model could accommodate the galaxy PLE phenomenology at shorter wavelengths ($\lambda < 160\mu$m).

The AGN model we use is non-unified, with absorbed AGN having brighter sub-mm fluxes than unabsorbed AGN. In Chapter 3 we suggested that if a unified rather than non-unified AGN model was applied, the AGN contribution to the sub-mm would drop dramatically and another component would be required to fit the sub-mm source counts. Conventionally, this is taken to be a population of highly evolved starburst galaxies with

the bolometric luminosities of QSOs. We now consider this alternative possibility in the context of a PLE model where these sources are modelled as dust-obscured early-type progenitors. We have therefore modelled a population of early-types that evolve according to a $\tau = 1$ Gyr model with a Chabrier IMF and dust absorption in the range $A_B = 0.3$–1 mag, which re-radiates optical light into the FIR assuming the usual 30K dust temperature. Although this model produces a K band evolution of 2–3 mag at $z \approx 2$–6 relative to the $x = 3$ IMF model or the k-correction, we found the contribution to the sub-mm counts to be negligible.

In addition, the Chabrier IMF produces strong evolution at $z \approx 1$ and would need a dust absorption of $A_B \approx 2$ mag to avoid over-predicting the high-z tail of the $K < 20$ redshift distribution. This level of extinction would destroy the viability of the PLE models to fit galaxy colour and count distributions through the optical and NIR bands. Appealing to a top-heavy IMF might still enable the sub-mm counts to be fitted, but such an IMF could not be allowed to apply at $z \approx 1$–2 because the problem of overpredicting the $K < 20$ $n(z)$ would be exacerbated. Somewhat paradoxically, although the semi-analytic model that invokes a top-heavy IMF (Baugh et al., 2005; Lacey et al., 2008) fits well the sub-mm counts, it appears to seriously *underpredict* the average $K < 20$ redshift (Gonzalez-Perez et al., 2009). These authors also show that the model of Bower et al. appears to fit the K $n(z)$ better, but fails to fit the sub-mm counts.

Certainly in the context of our PLE model there is greater observational motivation for a dwarf-dominated IMF than a top-heavy IMF: the top-heavy IMF is not required since sub-mm counts are matched by the AGN population, and the dwarf-dominated IMF can therefore provide an explanation for the absence of a detectable initial burst of star-formation from early-type galaxies at very high redshift – this burst may be absent due to a lack of bright stars in the IMF of early-types. Arguments against such a model include the apparently prompt enrichment of early type galaxies evidenced by their α-element enhancement (Tinsley, 1979; Trager et al., 2000). But the excellence of the fits of our simple galaxy count models from the UV through the K band to the sub-mm means that this alternative idea for the origin of early-types is still worthy of serious consideration.

4.8 Summary

In this work we have explored how successfully the phenomenology of galaxy populations at mid-IR, far-IR and sub-mm wavelengths can be described by a PLE galaxy model known to fit observations in the optical/NIR. We employed the simple bimodal model developed by Metcalfe et al. (1995, 2001, 2006; see also McCracken et al., 2006), which includes spiral galaxies with a very modest amount of dust ($A_B = 0.3$ mag) and early-type galaxies with no dust absorption. Our conclusions are as follows:

- This simple model continues to provide a reasonable description of galaxy populations out to 8μm. At 6–8μm the bright source counts move from being starlight dominated to dust emission dominated. At 8μm, stellar light makes a $\lesssim 15\%$ contribution at bright fluxes (> 400 μJy) but a $> 90\%$ contribution at very faint fluxes (< 4 μJy).

- Colour-redshift tracks from the model are well matched to galaxy colours out to at least $\lambda = 8\mu$m and $z = 2.5$.

- At 24–70μm, our basic model no longer matches observed source counts, accounting for only $\approx 20\%$ of 24μm sources. By replacing 16% of our spirals with warmer-dust, higher-SFR galaxies, consistent with local observations, we match the bright counts very well, but there remains an underprediction of the faint-end counts. If we instead use a population of spirals which have our standard late-type SED but the $z = 0$ $K - [24]$ colour of Mrk33 (essentially, the normal spiral SED normalised to brighter flux), we fit the counts across the full flux range.

- At sub-mm wavelengths ($\lambda = 250$, 350, 500μm) the galaxy model fails – we find that normal galaxies account for only a few percent of sources here. However, we show that a PLE model of obscured AGN, which we have previously shown to give a good fit to observations at 850μm (Chapter 3; Hill & Shanks, 2010a), can again give a good fit to the counts and redshift distributions in these bands.

V

A sub-mm survey of the William Herschel Deep Field

5.1 Introduction

There is increasing observational evidence for a significant AGN contribution to the sub-mm population. Obscured AGN in particular appear to show high sub-mm fluxes. These results come both from statistical techniques (e.g. Chapter 2; Hill & Shanks, 2010a; Lutz et al., 2010) and from targetted sub-mm observations of known QSOs (e.g. Coppin et al., 2008a; Martínez-Sansigre et al., 2009).

Our work so far has focussed on the former, employing statistical cross-correlation and stacking methods (as well as phenomenological models) to ascertain the contribution made by AGN at sub-mm wavelengths. However, in addition to this we have undertaken a survey designed to measure 870μm fluxes for a sample of known quasars; this is being done in the ultradeep William Herschel Deep Field[1] (WHDF; e.g. Metcalfe et al., 1995, 2001, 2006). The WHDF is especially suitable for this survey thanks to a significant sample of spectroscopically confirmed quasars within a small, easily observable area, which includes both unobscured and heavily absorbed sources matched in redshift and luminosity (Vallbé-Mumbru, 2004).

As described in §1.3, determining robust counterparts for sub-mm sources requires radio (or mid-IR) observations, in order to achieve positional accuracy. We have there-

[1] so-named because the initial optical observations were carried out using the William Herschel Telescope in La Palma

FIGURE 5.1: *A true colour image of the William Herschel Deep Field from the U, B and R band frames. Image credit: N. Metcalfe.*

fore surveyed the WHDF at 8.4 GHz in addition to our sub-mm observations. However, these data are still at the reduction stage and therefore a search for robust counterparts to the sub-mm sources has yet to be undertaken.

This chapter therefore presents initial results from the sub-mm survey, focussing again on statistical analyses which will complement the analyses in Chapter 2. An analysis including the radio-detected counterparts will be presented in a future paper.

5.2 The William Herschel Deep Field

The William Herschel Deep Field is a $\approx 7' \times 7'$ area centred at around $00^h20^m +00^\circ$ (J2000) which has a wealth of multiwavelength data and has been extensively studied over the past 15 years (Metcalfe et al., 1995, 2001, 2006; McCracken et al., 2000a, 2000b). A true colour image of the WHDF is shown in Fig. 5.1.

The field has ultradeep, ground-based optical $UBRIZ$ imaging from the William Herschel Telescope in La Palma (reaching $B < 27.9$) as well as near-infrared H and K imaging from Calar Alto and the UK Infrared Telescope and deep, high-resolution I-band imaging from the *Hubble Space Telescope*'s Advanced Camera for Surveys.

In addition to this comprehensive optical/NIR coverage, the WHDF also has *Chandra* X-ray coverage, reaching a depth of $\approx 10^{-15}$ ergs s^{-1} cm^{-2} over the whole area with a total integration time of ≈ 70 ksec. These observations were undertaken between

November 2000 and January 2001. 170 X-ray sources were detected at $\geq 2\sigma$ significance, of which 69 were at $\geq 3\sigma$ and 36 at $\geq 5\sigma$. Spectroscopic follow-up of some of these X-ray sources was subsequently done — these observations are described in §5.5.1 below.

The most recent additions to the WHDF data are (*a*) an 870μm sub-mm survey, which we undertook between 2008 and 2009 and which is described in this chapter, and (*b*) radio observations at 8.4 GHz ($\lambda = 3.6$cm) acquired with the Expanded Very Large Array (EVLA) in New Mexico in 2010.

The EVLA survey will complement very well the sub-mm observations. The well established FIR-radio correlation (Condon, 1992) means that radio data are frequently employed to determine more precise positions for sub-mm sources (e.g. Ivison et al, 2002), since the beamsize of sub-mm instruments is very large ($\sim 20''$). It is assumed that where a radio source lies within the error box of a sub-mm source position, it can reliably be taken to be the counterpart of the sub-mm source. Radio interferometers like the EVLA are able to determine source positions with far greater precision than the $\pm 10''$ accuracy of the sub-mm data. To this end, therefore, we have acquired 35 hours of EVLA X-band observations, expected to reach an rms noise level of ≈ 2 μJy, sufficient to detect our sub-mm sources. The reduction of these data is underway.

5.3 Sub-mm observations and data reduction

5.3.1 Observations

We have acquired 21 hours of observations of the WHDF with the Large Apex Bolometer Camera (LABOCA; Siringo et al., 2009) on the 12m APEX telescope (Güsten et al., 2006). The LABOCA instrument comprises 295 semiconducting composite bolometers arranged in a series of concentric hexagons. The detectors themselves are germanium 'thermistors', which can detect the rise in temperature that occurs due to incident radiation and thereby measure a photon flux. LABOCA is sensitive to radiation in a passband centred at 870μm, with a FWHM of $\approx 150\mu$m.

The LABOCA beam has a FWHM of 18.6$''$and the total field of view (FoV) of the detector is 11.4$'$. The WHDF covers a region of $\approx 7' \times 7'$, as noted above, so this field fits well into the FoV of LABOCA. The LABOCA detectors do not form a contiguous array, however, so to achieve full sampling of the field we carried out our observations using a standard spiral raster map pattern. In this process, the centre of the array is moved around in a spiral pattern and also shifted side-to-side and up-and-down in a raster

configuration, in order that every part of the field will be sampled by the bolometer.

Our observations were carried out in two separate observing runs[2], the first in August 2008 and the second in May 2009, in generally very good conditions.

5.3.2 Data reduction

Initial data reduction was performed by J. Geach using the standard BoA pipeline software (Schuller et al., in prep.). Counts from the detector are first converted into an output voltage, which can then be converted into a flux density, in standard units of Jy beam^{-1}, via a voltage-flux relation determined empirically during LABOCA's commissioning. A further correction is then applied to account for the zenith opacity at the time of observing. This zenith opacity, τ_z, is a measure of how much incoming radiation is absorbed by the atmosphere and is determined by 'skydip' observations (calibration exposures of the sky). Flux calibration is performed using observations of primary and secondary calibrators. Uranus and Neptune were used as primary calibration sources during our observing run. The result of this process is a series of exposure maps for each scan of the target field. BoA then co-adds these maps, weighting the signal from each by $1/\sigma^2$. The final output is a combined intensity (flux) map, as well as corresponding rms noise and signal-to-noise (SNR) maps.

This data reduction process was carried out separately for the data from each of the two observing runs. As a final stage in the reduction process, therefore, we combined the maps, weighting them by the noise. The final intensity map was produced according to Eqn. 5.1 and the final noise map according to Eqn. 5.2.

$$I = \left(\frac{I_1}{\sigma_1^2} + \frac{I_2}{\sigma_2^2}\right) \Bigg/ \left(\frac{1}{\sigma_1^2} + \frac{1}{\sigma_1^2}\right) \tag{5.1}$$

$$\sigma = 1 \Bigg/ \sqrt{\frac{1}{\sigma_1^2} + \frac{1}{\sigma_1^2}} \tag{5.2}$$

where I is intensity, σ is rms noise and subscripts 1 and 2 indicate the first and second observing runs. A signal-to-noise map was produced by taking the ratio of the two, and each of the maps was then Gaussian-smoothed.

[2]ESO programme IDs 381.A-0897(A) and 083.A-0707(A)

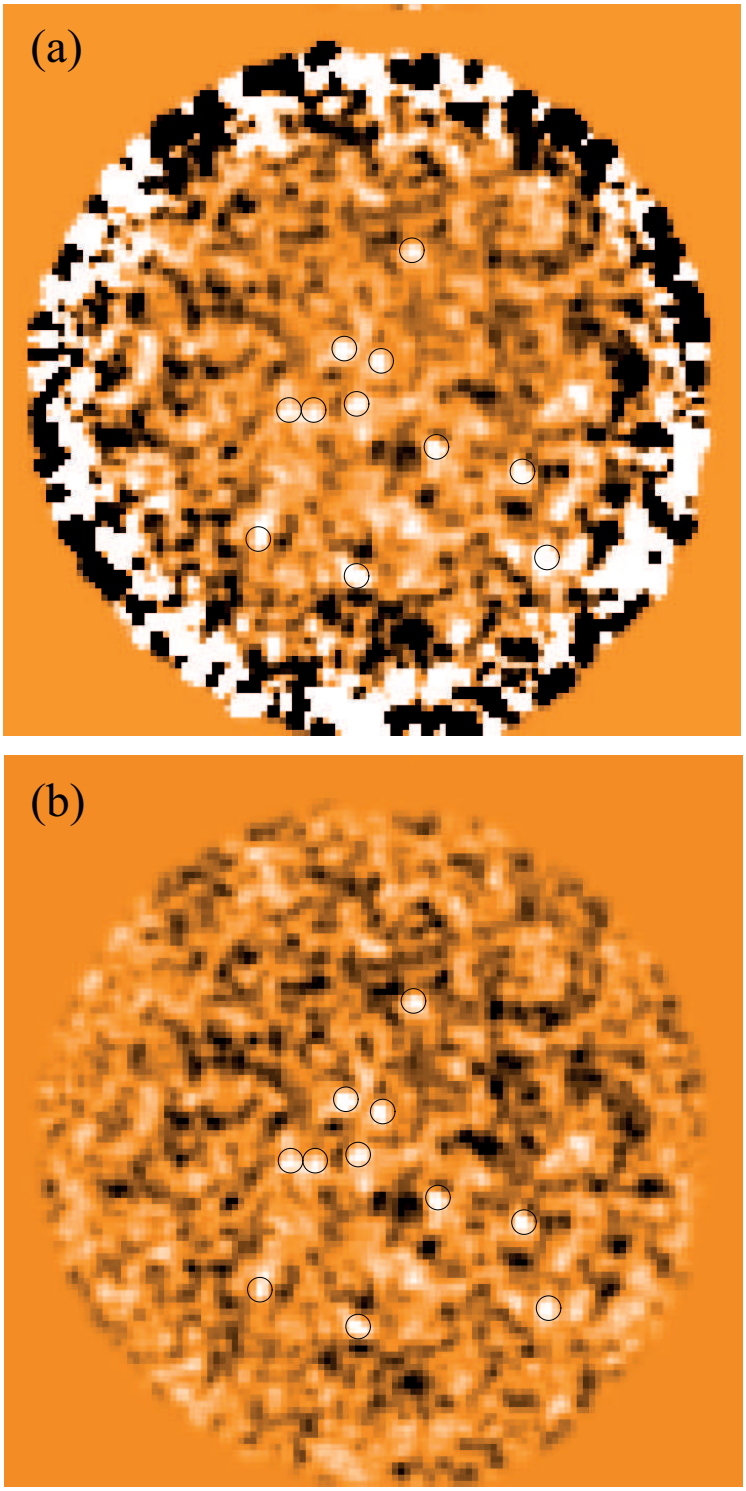

FIGURE 5.2: (a) *LABOCA 870μm intensity map of the WHDF, with 11 sources detected at $\geq 3.2\sigma$ marked. The reduced off-axis sensitivity of LABOCA produces the increase in noise at the edges of the frame.* (b) *LABOCA signal-to-noise map of the WHDF, with the same 11 sources marked,*

5.4 LABOCA data

The final intensity and SNR maps are shown in Fig. 5.2. It is clear from Fig. 5.2*a* that the noise increases substantially at large off-axis angles; in the SNR map (panel *b*), this increase in the noise manifests itself as a dearth of sources around the edges of the frame. In the central area, the maps are very similar, with points of bright intensity having corresponding peaks in the SNR map, an indication that the noise level is relatively uniform across the field centre.

5.4.1 Noise level

We find that across the central region of the field the data reach an rms noise level of ≈ 1 mJy beam^{-1}, making the WHDF one of the deepest sub-mm fields observed to date (*cf.* figure 6 of Weiß et al., 2009).

To check the reliability of the pipeline-reduced noise map we have produced a 'standard deviation map', by measuring the standard deviation of the intensity map in a series of annuli from the field centre, having masked out the bright sources. If the pipeline has worked successfully, this standard deviation map should be comparable to the BoA-produced noise map.

In Figs. 5.3 and 5.4, we compare the contours and radial profiles, respectively, of the two maps. For the pipeline-reduced map, the noise profile shown in Fig. 5.4 is the median of 120 profiles measured radially at 3° intervals. The agreement between the two noise maps is very good — this is particularly clear from Fig. 5.4 — suggesting that the noise has been reliably estimated for our field and that our quoted depth of ≈ 1 mJy beam^{-1} is robust.

5.4.2 LABOCA sources

The field contains 11 significant sub-mm sources, circled in Fig. 5.2. We select the sources from the SNR map, with a criterion of $S/N \geq 3.2$. This significance was chosen by comparing the map to its inverse: there are no negative spikes in the SNR map with a magnitude of 3.2σ. This is illustrated in Fig. 5.5, which shows a pixel value histogram for the SNR map. The map shows a strong positive excess while the negative side of the distribution follows the Gaussian curve well, supporting our choice of $S/N \geq 3.2\sigma$ as a source detection threshold.

The positions of the 11 sources are indicated on Fig. 5.3 and their fluxes are shown

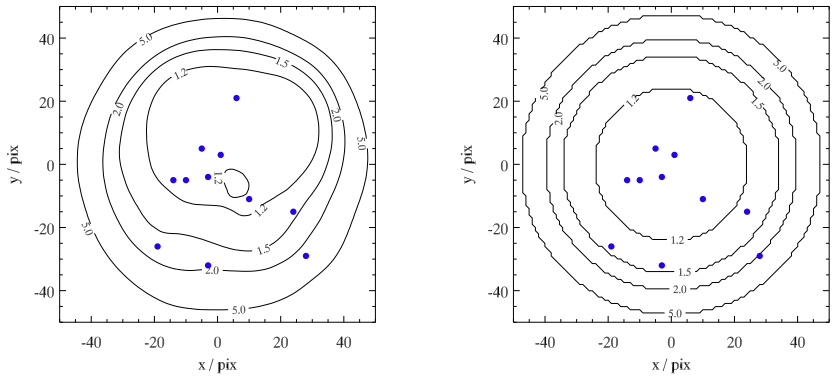

FIGURE 5.3: *Noise contour maps of the WHDF, with the rms noise level marked at 1.2, 1.5, 2.0 and 5.0 mJy beam^{-1}, using* (a) *the pipeline-reduced noise map and* (b) *the standard deviation of the background flux measured in radial annuli.* 3.2σ *LABOCA sources are marked as blue circles. The maps generally agree well (see also Fig. 5.4). Most of our LABOCA sources are detected within the central region where the noise is lowest.*

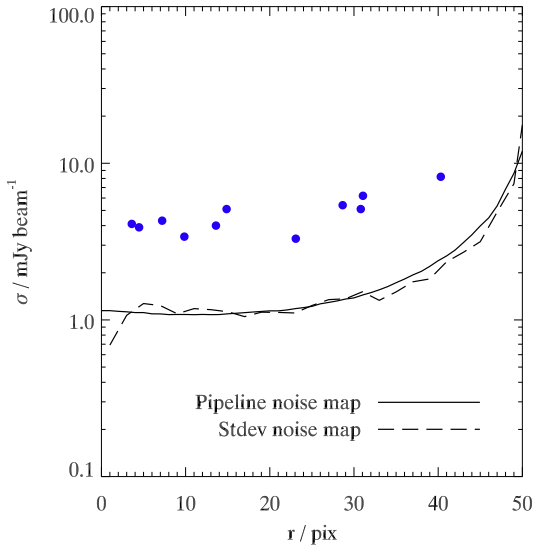

FIGURE 5.4: *Radial noise profile of the WHDF showing the rms noise level as a function of radius from the centre (in pixels;* 1 *pix* $\approx 9''$*), for both the pipeline-reduced and standard deviation noise maps, described in the main text.* 3.2σ *LABOCA sources are marked (blue circles) at their respective source flux and radial separation.*

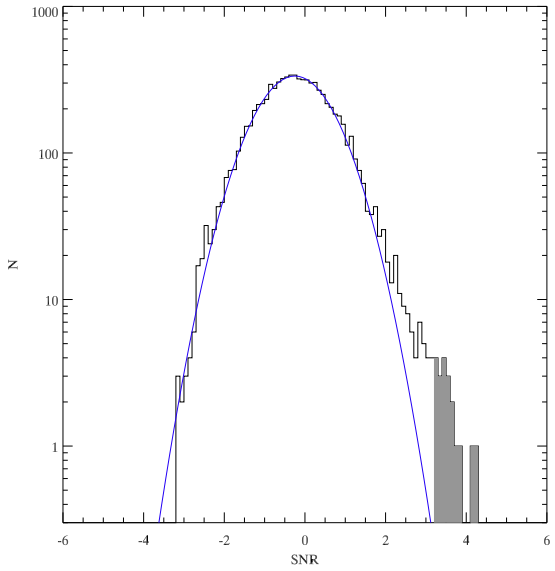

FIGURE 5.5: *A histogram of pixel values from the SNR map. A Gaussian has been empirically fit to the profile — most of the pixels lie within this distribution, however a significant positive excess appears due to the presence of sources. The shaded region indicates those pixels lying above the* 3.2σ *threshold we have set for source detection.*

in comparison to the background noise in Fig. 5.4. Most of the sources lie within the low-noise central area of the field, with 7/11 located within the $\sigma \leq 1.2$ mJy contour. The positions, SNRs and fluxes of the 11 sources are summarised in Table 5.1.

5.5 Sub-mm observations of WHDF quasars

5.5.1 Absorbed and unabsorbed quasar samples

In §5.2 we briefly summarised the *Chandra* observations of the WHDF, which yielded detections of 170 X-ray sources. In 2001 and 2002, 36 of these WHDF X-ray sources were targetted in 10 hours of spectroscopic follow-up with the LDSS2 multi-object spectrograph on the 6.5m Magellan-1 (Walter Baade) telescope at the Las Campanas Observatory in Chile. These were optical observations, using a grism centred at $\lambda \approx 5500$Å.

A stated aim of this observing run was to investigate non-quasar X-ray sources, so the principal targets for spectroscopic follow-up were X-ray sources whose optical counterparts did not appear especially point-like (Vallbé-Mumbru, 2004). Nevertheless, 15 of the targets were spectroscopically confirmed as QSOs, and a further 2 were classified as being either QSOs or narrow emission line galaxies (NELGs). In this section we take the

TABLE 5.1: *WHDF LABOCA 870 micron sources detected at* $\geq 3.2\sigma$.

ID	RA	Dec	SNR	S_{850} / mJy
WHDF-LAB-01	00:22:37.55	+00:19:16.8	4.3	5.1
WHDF-LAB-02	00:22:28.44	+00:21:42.6	4.2	4.3
WHDF-LAB-03	00:22:46.06	+00:18:40.3	3.8	5.4
WHDF-LAB-04	00:22:29.66	+00:20:20.5	3.7	4.1
WHDF-LAB-05	00:22:22.97	+00:20:11.4	3.6	4.0
WHDF-LAB-06	00:22:32.09	+00:21:24.3	3.6	3.9
WHDF-LAB-07	00:22:48.49	+00:16:32.8	3.5	8.2
WHDF-LAB-08	00:22:29.66	+00:16:05.4	3.4	6.2
WHDF-LAB-09	00:22:19.90	+00:17:00.1	3.2	5.1
WHDF-LAB-10	00:22:35.16	+00:24:08.3	3.2	3.3
WHDF-LAB-11	00:22:25.40	+00:20:11.4	3.2	3.4

15 confirmed QSOs as our sample of WHDF quasars; details of these sources are given in Table 5.2.

The QSO classification was made by Vallbé-Mumbru (2004) on the basis of both X-ray luminosity ($L_{\rm X} > 10^{44}$ ergs s^{-1}) and optical emission lines. Most of the sources classed as QSOs showed broad emission lines, including NeV λ1240, SiIV λ1400, NIV λ1486, HeII λ1640, OIII] λ1663 and/or NIII λ1750, all of which are AGN indicators. If broad lines were detected the source was classified as a type 1 quasar. One source was classified as a type 2 quasar on the basis of strongly detected narrow emission lines (WHDFCH008); its spectrum is shown in Fig. 5.6.

The X-ray hardness ratios (defined in §2.4.3) of the QSOs can give an indication of the level of obscuration. Fig. 5.7 shows hardness ratio against redshift for our quasar sample, compared to the predicted tracks for quasars at different absorbing column densities (an intrinsic photon index of $\Gamma = 2$ is assumed).

The locus of the quasars is at $HR \approx -0.5$, consistent with the model which predicts $HR = -0.5$ for essentially all unabsorbed QSOs. Only four of the 15 QSOs are harder than $HR = -0.4$; these 4 sources — WHDFCH007, -008, -044 and -099 — are expected to be highly obscured. WHDFCH007 and WHDFCH044 have extremely hard spectra with $HR \geq 0.6$, corresponding to an apparent photon index of $\Gamma \approx -1$; such sources are rare, with, for example, none being detected in the ≈ 2 deg^2 *XMM-Newton* COSMOS survey

TABLE 5.2: *Spectroscopically confirmed quasars in the WHDF. The positions, 0.5–10 keV fluxes (in ergs s^{-1} cm^{-2}), X-ray hardness ratios and spectroscopic redshifts are given. Absorbed quasars are indicated in bold.*

ID[a]	RA[b]	Dec[b]	$S_{0.5-10}$	HR	z
WHDFCH005	00:22:35.963	00:18:50.04	5.62×10^{-14}	-0.60 ± 0.04	0.52
WHDFCH007	00:22:24.821	00:20:10.94	1.17×10^{-14}	0.82 ± 0.11	1.32
WHDFCH008	00:22:22.884	00:20:13.24	3.62×10^{-15}	-0.20 ± 0.24	2.11
WHDFCH016	00:22:45.164	00:18:22.64	1.44×10^{-14}	-0.43 ± 0.10	1.73
WHDFCH017	00:22:44.468	00:18:25.64	3.22×10^{-13}	-0.55 ± 0.02	0.40
WHDFCH020	00:22:36.142	00:24:33.84	1.09×10^{-14}	-0.55 ± 0.10	0.95
WHDFCH036	00:22:31.734	00:25:38.84	6.26×10^{-14}	-0.48 ± 0.05	0.83
WHDFCH044	00:22:55.092	00:20:55.74	2.66×10^{-14}	0.60 ± 0.11	0.79
WHDFCH048	00:22:41.297	00:25:33.34	2.15×10^{-14}	-0.43 ± 0.09	1.52
WHDFCH055	00:22:11.862	00:19:50.44	2.17×10^{-14}	-0.23 ± 0.10	0.74
WHDFCH090	00:22:48.795	00:15:18.74	4.83×10^{-14}	-0.41 ± 0.06	1.32
WHDFCH099	00:22:11.187	00:24:04.13	8.84×10^{-15}	0.11 ± 0.18	0.82
WHDFCH109	00:22:09.917	00:16:28.94	6.69×10^{-14}	-0.55 ± 0.04	0.57
WHDFCH110	00:22:07.433	00:23:07.74	2.20×10^{-14}	-0.43 ± 0.09	0.82
WHDFCH113	00:23:01.247	00:19:18.01	5.99×10^{-15}	-0.44 ± 0.16	2.55

[a] as in Vallbé-Mumbru (2004)

[b] J2000

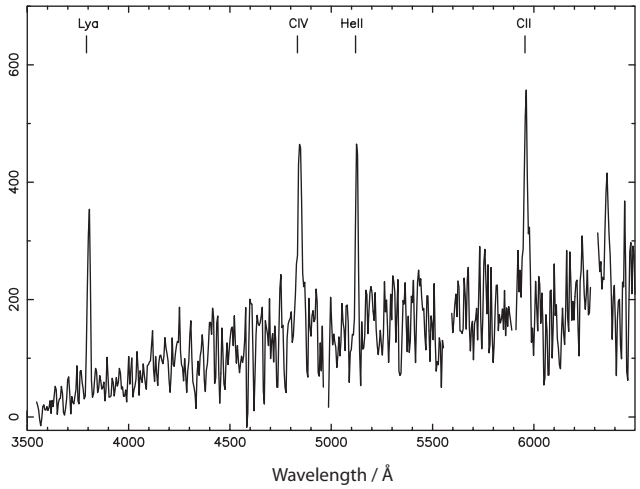

FIGURE 5.6: *Optical spectrum of* WHDFCH008 *acquired with LDSS2 on the Magellan telescope. With only narrow emission lines detected (labelled in the figure) this source was classified as a type 2 QSO. Figure adapted from Vallbé-Mumbru (2004).*

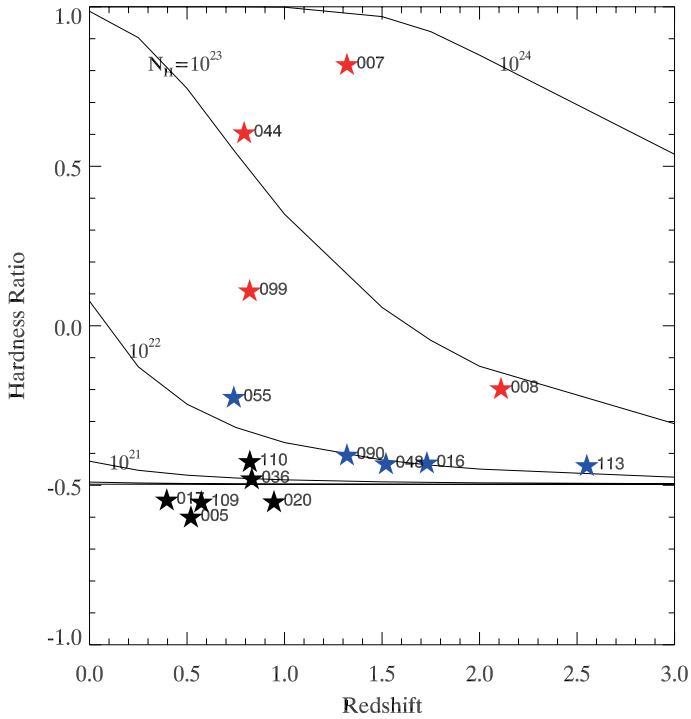

FIGURE 5.7: *Hardness ratio versus redshift. The curves show predicted tracks for obscured QSOs at different column densities, which are indicated on the figure (in units of* cm^{-2}*). An intrinsic* $\Gamma = 2$ *power-law spectrum is assumed. Below* $N_{\rm H} = 10^{21}$ cm^{-2} *the lines become indistinguishable. WHDF X-ray QSOs are marked; each is labelled with its ID (with the* WHDFCH *prefix omitted). On the basis of this figure we classify the QSOs into 3 categories: heavily absorbed (*$N_{\rm H} > 10^{22}$ cm^{-2}*; red), mildly absorbed (*$N_{\rm H} \approx 10^{22}$ cm^{-2}*; blue) and unabsorbed (*$N_{\rm H} < 10^{22}$ cm^{-2}*; black).*

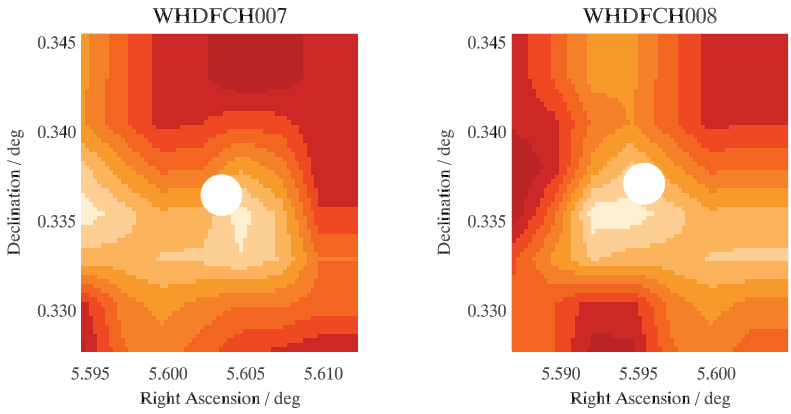

FIGURE 5.8: *Thumbnail images of the LABOCA 870μm intensity map at the positions of the highly absorbed QSOs* WHDFCH007 *and* WHDFCH008. *In each case the X-ray source position is marked by a white circle. Both sources are apparently strongly detected in the sub-mm.*

(Mainieri et al., 2007).

Based on Fig. 5.7 we divide the WHDF quasar sample into three groups: heavily absorbed ($N_{\rm H} > 10^{22}$ cm^{-2}), mildly absorbed ($N_{\rm H} \approx 10^{22}$ cm^{-2}) and unabsorbed ($N_{\rm H} < 10^{22}$ cm^{-2}); these are marked in the figure in red, blue and black respectively.

5.5.2 LABOCA detections

Possible counterparts

With our quasar sample defined, we first check to see whether any of the 15 QSOs are coincident with a bright sub-mm source detected in our $\geq 3.2\sigma$ catalogue (Table 5.1). We find that two of the quasars have possible LABOCA counterparts: WHDFCH007 (coincident with WHDF-LAB-11) and WHDFCH008 (coincident with WHDF-LAB-05). Fig. 5.8 shows thumbnail images of the LABOCA flux map at the positions of these X-ray sources, and a bright source is clearly visible in both cases.

Notably, these two QSOs are in our highly absorbed sample. The other two highly absorbed quasars, WHDFCH044 and -099, lie near the edges of the map where no 3.2σ sources are detected due to the high noise. It is interesting, therefore, that of the two highly absorbed WHDF QSOs which lie in the central, low-noise area of the field, both appear to have bright sub-mm counterparts.

In Figs. 5.9 and 5.10, we show thumbnail images for three $N_{\rm H} \approx 10^{22}$ cm^{-2} QSOs and four unabsorbed QSOs, respectively. The full samples have 6 and 8 sources respectively,

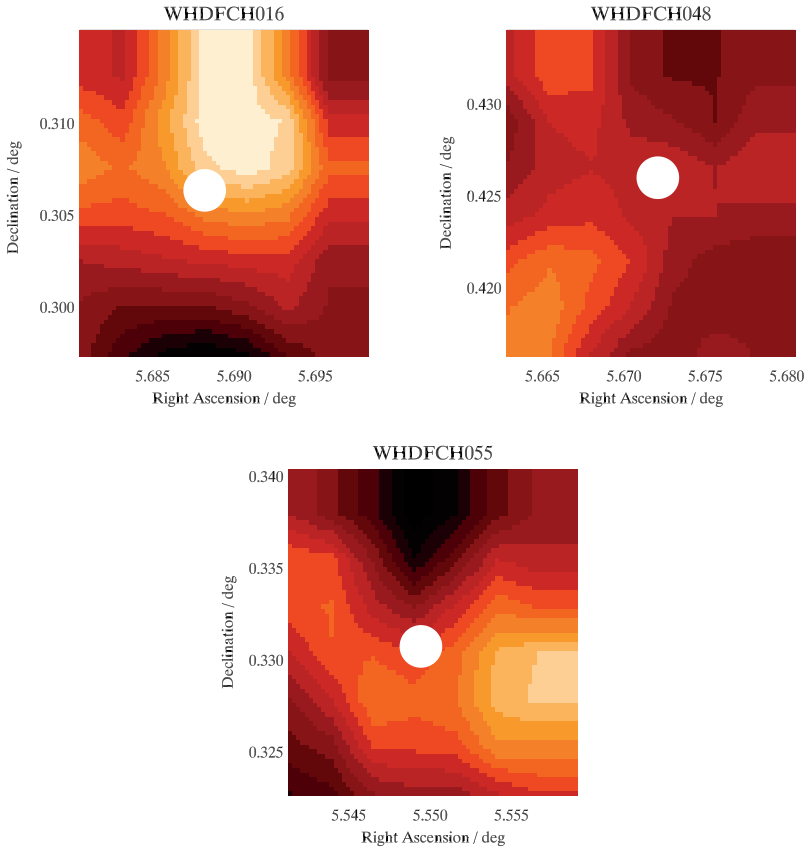

FIGURE 5.9: *As in Fig. 5.8, but for sources characterised as mildly obscured with* $N_{\rm H} \approx 10^{22}\ cm^{-2}$.

however we have excluded those sources which lie close to the edge where the map is dominated by noise.

Some of the sources in these figures appear to lie close to bright areas, e.g. WHDFCH016 in Fig. 5.9 or WHDFCH017 in Fig. 5.10, however, none of these QSOs could be said to be *coincident* with a peak in the map as was the case for WHDFCH007 and -008.

Stacking

To get an overall picture of the sub-mm flux associated with our highly absorbed, mildly absorbed and unabsorbed quasar populations, we stack the flux map for each of the populations.

To ensure that the noisy fringe sources do not dominate the stacked flux there are two ways to proceed — either to exclude the sources near the edge and stack the remaining sources linearly (exploiting the relatively uniform noise across the centre), or to perform a noise-weighted stack which mitigates the effect of the noisy objects. Having performed

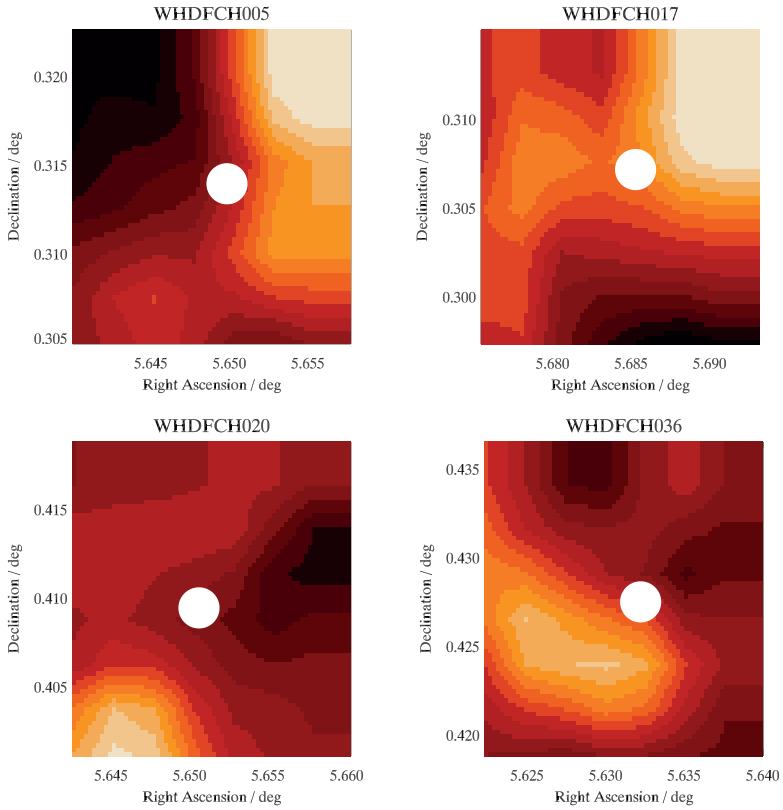

FIGURE 5.10: *As in Fig. 5.8, but for sources characterised as unabsorbed with* $N_{\rm H} \approx 10^{22}$ cm^{-2}.

both analyses, we find the results are not affected by the choice of method.

The stacked flux images for the three QSO populations are shown in Fig. 5.11. The highly absorbed quasars are the only sources to be strongly submm-bright. Although the samples used here are small, these results are consistent with a model in which sub-mm emission arises preferentially from more absorbed AGN, in agreement with our analyses in Chapter 2 which showed a similar result.

5.6 Discussion and Summary

Whether WHDF-LAB-11 and WHDF-LAB-05 are actually counterparts for the highly absorbed QSOs WHDFCH007 and WHDFCH008 is something we hope to confirm once the WHDF radio observations become available. Until then, we can use simple statistical arguments to determine the likelihood of the apparent counterparts coinciding by chance.

The beam size of the smoothed LABOCA map is 27″, which at a pixel scale of ≈ 9 arcsec/pixel corresponds to 3 pixels in diameter. Therefore, any object lying within ± 1

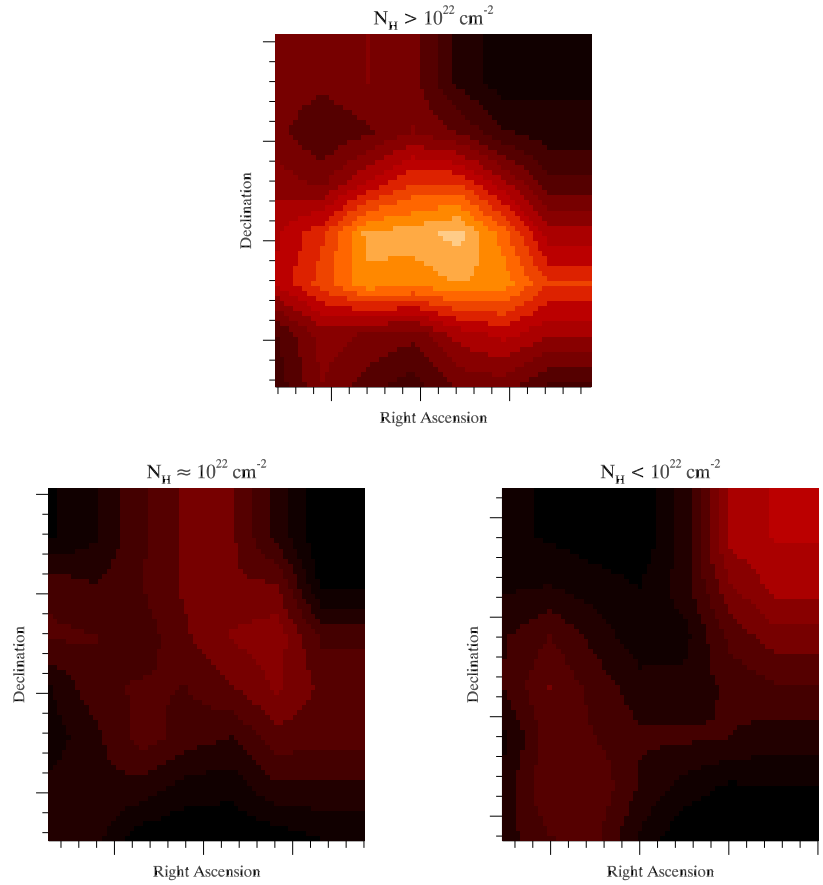

FIGURE 5.11: *Noise-weighted stacked intensity maps for the three populations with* $N_{\rm H} > 10^{22}$ *cm*$^{-2}$, $N_{\rm H} \approx 10^{22}$ *cm*$^{-2}$ *and* $N_{\rm H} < 10^{22}$ *cm*$^{-2}$. *Only the most highly absorbed QSOs show any stacked sub-mm emission.*

pixel of a LABOCA source can be said to coincide with it. There are 9,160 pixels in the LABOCA SNR map and 11 discrete peaks at $\geq 3.2\sigma$, giving 99 pixels which lie within ≤ 1 pixel of a 3.2σ peak. The odds of any given QSO coinciding with a LABOCA source is thus $^{99}/_{9160} = 1.1\%$.

So each of our QSOs has roughly a 1% chance of lining up with a LABOCA source. Until the radio data are available to better constrain the LABOCA positions, therefore, the conclusion that these heavily absorbed QSOs have sub-mm counterparts remains somewhat tentative. Nevertheless, it is notable that only the most obscured AGN have possible 870μm detections.

In addition to the radio data which have been acquired, we are seeking *Herschel* observations at 250, 350 and 500μm, which will constrain the SED and allow dust temperatures to be measured for the detected sources. If the unabsorbed QSOs are found to be detected in these shorter-wavelength bands, it could reveal whether any temper-

ature difference exists between obscured and unobscured quasars, as was hypothesised in §2.6. This is therefore an ongoing program in which considerable future work can be done. This chapter has presented initial results from the sub-mm survey so far, which are summarised below.

Summary

- We present an 870μm survey of the well-studied William Herschel Deep Field, reaching a depth of 1 mJy. 11 sources are detected at $\geq 3.2\sigma$.
- 2 of these 11 sources may be counterparts of X-ray-selected WHDF quasars: WHDFCH007, an extremely hard QSO with $\Gamma \approx -1$ and WHDFCH008, a type 2 QSO with only narrow optical emission lines, both consistent with being heavily obscured.
- We divide a sample of 15 WHDF quasars into three subsets, having $N_{\rm H} < 10^{22}$, $N_{\rm H} \approx 10^{22}$ and $N_{\rm H} > 10^{22}$ cm^{-2}, and find that only the most absorbed population shows any significant stacked 870μm flux.
- Our findings, alongside those presented in Chapters 2 and 3, are supportive of a model in which obscured AGN are sub-mm bright and unobscured AGN are not.
- Upcoming radio data, as well as proposed observations in other bands, will enable further investigation of the sub-mm properties of absorbed and unabsorbed AGN in the WHDF in the future.

VI

A survey of Lyman break galaxies at $z \approx 3$

6.1 Introduction

As noted in the Introduction to this thesis, one of the most important discoveries in recent years in the field of galaxy evolution was that of the existence of a large population of normal star-forming galaxies at high redshift, $z \approx 3$, when the universe was only around one sixth its current age (Steidel et al., 1996, 1999, 2003; Adelberger et al., 2003; Franx et al., 2003). These sources, called Lyman break galaxies (LBGs), allowed astronomers for the first time to make observational estimates of the star-formation history of the universe out to high redshifts (Madau et al., 1996; Steidel et al., 1999).

The identification of the LBG population resulted from of the use of broadband colour selection to identify the presence of the 912Å Lyman break at optical wavelengths. This strong break in the ultraviolet spectrum of star-forming galaxies is shifted into the U band at $z \approx 3$, causing a significant reddening of the, e.g., $U - B$ or $U - G$ colour (Steidel & Hamilton, 1993; Steidel, Pettini & Hamilton, 1995).

With the possible exception of observations made at sub-mm/mm wavelengths, where a strong negative k-correction results in a redshift distribution dominated by high-z sources (Ivison et al., 2002; Smail et al., 2002; Chapman et al., 2005), this use of broadband colour criteria to preselect high-z galaxy candidates is the most effective tool astronomers have for surveying the galaxy population at high redshift (Steidel et al., 2003).

Importantly, too, whereas sub-mm-selected sources are unusual, ultraluminous objects (Chapman et al., 2005) with relatively low densities, LBGs represent a much larger

population of comparatively 'normal' galaxies. For example, their luminosities, star-formation rates and level of obscuration are found to be in line with those of local star-forming galaxies (Steidel et al., 1996, 1999; Lowenthal et al., 1997; Pettini et al., 2001; Magdis et al., 2010).

Over the last 5 years we have undertaken a large survey of $z \approx 3$ LBGs (see Bielby et al., 2010), a key goal of which is to better constrain the interactions between high-redshift galaxies and the IGM. Work in this area is described in Chapter 7, however in this chapter we first provide details of the survey strategy, data reduction, spectroscopic analysis and LBG sample.

6.2 Survey overview

The observations described herein form part of a larger survey, the first part of which was presented by Bielby et al. (2010). In order to facilitate an investigation of how $z \approx 3$ galaxies interact with gas in the intergalactic medium (IGM), the survey comprises observations of several target fields centred on bright $z > 3$ quasars, since features in the QSO spectra can provide information on the local IGM (Chapter 7).

Bielby et al. presented the first 5 fields of the survey, centred on the following quasars: Q0042–2627 ($z = 3.29$), J0124+0044 ($z = 3.84$), HE0940–1050 ($z = 3.05$), J1201+0116 ($z = 3.23$) and PKS2126–158 ($z = 3.28$), hereafter referred to by only the first component of these names. A spectroscopic survey of each of these quasar fields was carried out with the Visible Multiobject Spectrograph (VIMOS) on the European Southern Observatory's Very Large Telescope (VLT) in Chile. Each field consisted of four subfields (individual pointings with the VLT spectrograph), except for HE0940 where only three subfields were available at the time of their publication. A VIMOS pointing has a field of view of $16' \times 18'$ (see §6.5.1), therefore each quasar field covered $\approx 32' \times 36'$, or ≈ 0.32 deg^2, except for HE0940 which with 3 subfields covered ≈ 0.24 deg^2.

Building on this initial dataset, we present here a further 6 subfields of HE0940, tripling its previous area, as well as observations of 4 new fields, around the quasars Q2359+0653 ($z = 3.23$), Q0302–0035 ($z = 3.23$), Q2231+0015 ($z = 3.02$) and Q2348-011 ($z = 3.02$), with 4, 4, 3 and 9 subfields respectively. Table 6.1 gives a summary of all the fields making up the LBG survey. This includes those presented by Bielby et al., covering 1.52 deg^2, and those presented here, which take the total observed area to 3.6 deg^2, more than doubling the previous size.

TABLE 6.1: *A summary of the fields making up our $z \approx 3$ LBG survey. The table gives the name, coordinates and redshift of the QSO on which the fields are roughly centred, as well as the number of subfields (individual VLT VIMOS pointings) with spectroscopic data. The first block of fields were presented by Bielby et al. (2010), the second block are presented in this thesis.*

Field	RA[a]	Dec[a]	z [b]	Subfields	Reference
Q0042–2627	00:44:33.9	–26:11:21	3.29	4	Bielby et al. (2010)
J0124+0044	01:24:03.8	+00:44:33	3.84	4	Bielby et al. (2010)
HE0940–1050	09:42:53.4	–11:04:25	3.05	3	Bielby et al. (2010)
J1201+0116	12:01:44.4	+01:16:12	3.23	4	Bielby et al. (2010)
PKS2126–158	21:29:12.2	–15:38:41	3.28	4	Bielby et al. (2010)
				19	
Q2359+0653	00:01:40.6	+07:09:54	3.23	4	This work
Q0302–0035	03:03:41.0	–00:23:22	3.23	4	This work
Q2231+0015	22:34:09.0	+00:00:02	3.02	3	This work
HE0940–1050	09:42:53.4	–11:04:25	3.05	6	This work
Q2348-011	23:50:57.9	-00:52:10	3.02	9	This work
				26	

[a] J2000 coordinates of QSO; not necessarily the exact centre of the observed field.

[b] redshift of the central quasar

6.3 Imaging

6.3.1 Observations and data reduction

The selection of $z \approx 3$ LBG candidates was performed using photometry from optical broadband imaging. The imaging data for Q2359 and Q0302 were acquired with the Mosaic wide-field imager on the 4m Mayall telescope at Kitt Peak National Observatory (KPNO) by N. Metcalfe and J. da Ângela in September 2005. The Q2231 data are from the Wide Field Camera on the 2.5m Isaac Newton Telescope (INT) on La Palma, and were observed in August 2005. All of these observations were carried out in the U, B and R bands.

The HE0940 and Q2348 data were acquired with the MegaCam imager on the 3.6m CFHT in April 2004 by P. Petitjean. These data are in the u, g and r rather than the U, B and R bands. Table 6.2 gives full details of all the imaging data. The instruments, filters and data reduction processes are described below.

KPNO Mosaic

The Mosaic-1 imager at KPNO consists of 8 2k×4k CCDs arranged into an 8k×8k square. With a plate scale of 0.26″/pixel, this gives a field of view of 36′×36′. There are 0.5–0.7mm gaps between the chips, corresponding to gaps of 9–13″ on-sky, so a dithering pattern was used during the observations to provide complete field coverage. U, Harris B and Harris R filters were used, centred at 3552Å, 4298Å and 6380Å respectively.

The Mosaic image data were reduced by R. Bielby using the `mscred` package in IRAF. The reduction process is described by Bielby et al. (2010), however we briefly outline the procedure here. Initially a master bias frame is produced for each night's observing. The dome flats and sky flats are then processed using the `ccdproc` and `mcspupil` routines, subtracting the bias and eliminating the faint 2600-pixel pupil image artefact which appears in all Mosaic observations. The object frames were processed similarly, subtracting the bias and pupil image, and then were flat-fielded using the dome and sky flats. Bad pixels and cosmic rays were masked out of the science frames using the `crreject`, `crplusbpmask` and `fixpix` procedures. Finally, the SWARP software package (Bertin et al., 2002) was used to resample and co-add the frames, producing a final science image.

TABLE 6.2: *Details of imaging observations for the LBG target fields presented in this thesis.*

Field	RA[a]	Dec[a]	Instrument	Band	Exposure[b]	Seeing	Dates
Q2359	00:01:44.85	+07:11:56.0	Mosaic (KPNO)	U	19.2	1.46″	29–30 Sep 2005
				B	7.2	1.45″	
				R	6.0	1.15″	
Q0302	03:03:45.27	–00:21:34.2	Mosaic (KPNO)	U	19.2	1.34″	29–30 Sep 2005
				B	6.4	1.28″	
				R	4.8	1.19″	
Q2231	22:34:28.00	+00:00:02.0	WFCam (INT)	U	54.0	1.23″	30 Aug 2005
				B	13.2	1.01″	
				R	19.2	1.01″	
HE0940	09:42:53.06	–11:02:56.9	MegaCam (CFHT)	u	6.8	0.99″	14, 21–27 Apr 2004
				g	3.1	0.86″	
				r	3.7	0.85″	
Q2348	23:50:57.90	–00:52:09.9	MegaCam (CFHT)	u	9.9	0.78″	19–20 Aug, 7–10 Nov, 15 Dec 2004
				g	5.5	0.79″	
				r	4.4	0.75″	

[a] J2000 coordinates of imaging field centre

[b] exposure time in kiloseconds

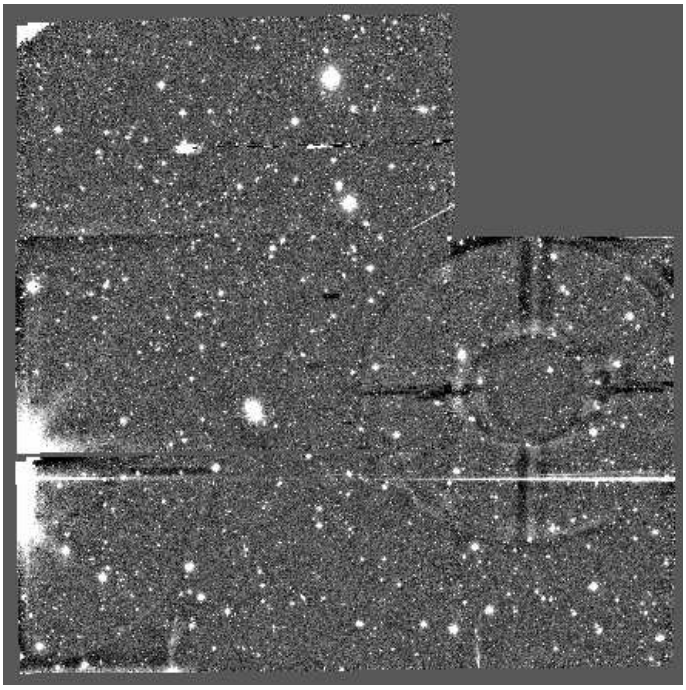

FIGURE 6.1: *WFCam B band image of field Q2231, showing the shape of the WFCam field of view. 3 of the rectangular CCDs are tiled one above another, orientated horizontally. The fourth, orientated vertically, is positioned beside them, aligned to the bottom of the field. This leaves a 2k×2k-pixel gap in the field of view in the upper right corner. The circular artefact is the result of the reflections in the optics due to a bright star just off the side of the field (η Aquarii).*

INT WFCam

The Wide Field Camera (WFCam) on the INT comprises 4 2k×4k CCDs. These are arranged into a 6k×6k block with a 2k×2k square missing (see Fig. 6.1). With $\approx 1'$ gaps between chips and a pixel scale of 0.33″/pixel, WFCam has a total FoV of $\approx 34' \times 34'$ (0.32 deg^2); however, accounting for the incomplete coverage of the field, the total observing area is reduced to 0.28 deg^2.

The WFCam observations of Q2231 were made using the RGO U, Harris B and Harris R filters. The RGO U filter has a central wavelength of 3581Å and a FWHM of 638Å, making it very similar to the U band filter used at KPNO (centre 3552Å, FWHM 631Å). The B and R band filters were the same as at KPNO. Therefore, given that the filters are so similar, we will use the same UBR selection criteria when identifying LBG candidates in either the Mosaic or WFCam datasets.

Initial data reduction, including bias removal, flat-fielding and photometric calibration, was performed by the Cambridge Astronomical Survey Unit (CASU). Astrometry

calibration and exposure stacking was done by R. Bielby, using the SCAMP and SWARP packages.

CFHT MegaCam

MegaCam is a considerably larger instrument than Mosaic or WFCam, with 36 2k×4.6k CCDs arranged into a 18k×18k grid. With a high resolution of 0.187″/pixel this gives a 1°×1° FoV. The observations of HE0940 and Q2348 were carried out using the u*, g′ and r′ filters (referred to in this thesis as u, g and r for convenience), with respective central wavelengths of 3743Å, 4872Å and 6282Å. The u and r filters are very similar to the U and R filters described previously, but as expected the g filter differs markedly from Harris B in its wavelength range. We will therefore construct alternative LBG selection criteria for the MegaCam datasets.

6.3.2 Photometry

Photometric zeropoints for the imaging fields were determined from standard star observations carried out as part of each of the imaging runs. The standard star fields were reduced in the same way as the science frames to ensure consistency. Source detection in the science images was performed with SExtractor (Bertin & Arnouts, 1996), using a 1.2σ detection threshold and a 5-pixel minimum size.

The U, B and R band number counts in each of the 5 LBG fields are shown in Figs. 6.2, 6.3 and 6.4. Also plotted are data from the William Herschel Deep Field (WHDF; see §5.2) presented by Metcalfe et al., which reach deeper limiting magnitudes than our data and can therefore give an impression of the completeness of our fields. In the lower panel of each figure we show the counts from the LBG fields divided by a polynomial fit to the Metcalfe et al. counts, which allows a more direct estimation of completeness.

In the U and B bands, the data reach the 50% completeness level at reasonably bright magnitudes, ≈ 23.5. The R band data are more complete, reaching 50% at $R \approx 24.5$ in the Q2359, Q0302, Q2231 and Q2348 fields, and at $R \approx 26$ in HE0940. The HE0940 data appear to reach greater depths in all 3 bands.

Our LBG selection does not include a stellarity criterion, since LBGs are expected to appear as unresolved point sources in the 0.8–1.5″ seeing in which the imaging data was observed, and therefore we have also made no attempt to remove stars from the data in Figs. 6.2–6.4. This is likely to explain the > 1 completeness at bright magnitudes, which

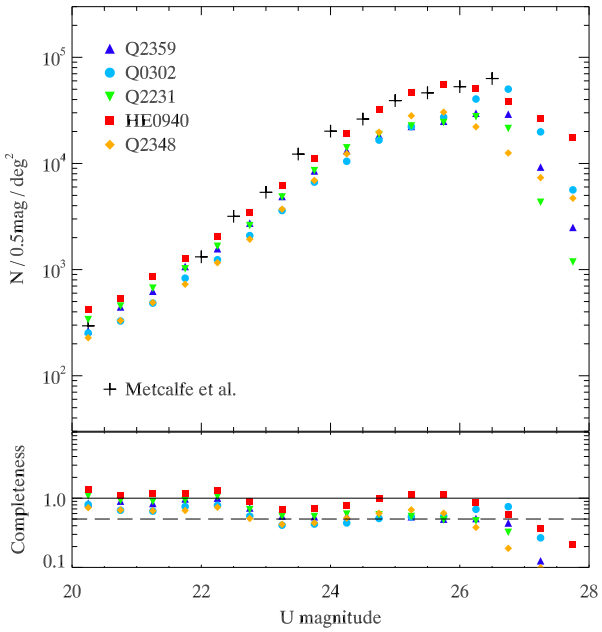

FIGURE 6.2: Upper panel: *Source counts in the U band for the 5 LBG fields, compared to deeper counts from Metcalfe et al.* Lower panel: *An estimate of the completeness of each of the fields, measured by dividing the number counts by a polynomial fit to the Metcalfe et al. data. The dashed line marks a completeness of 0.5; the solid line is at unity.*

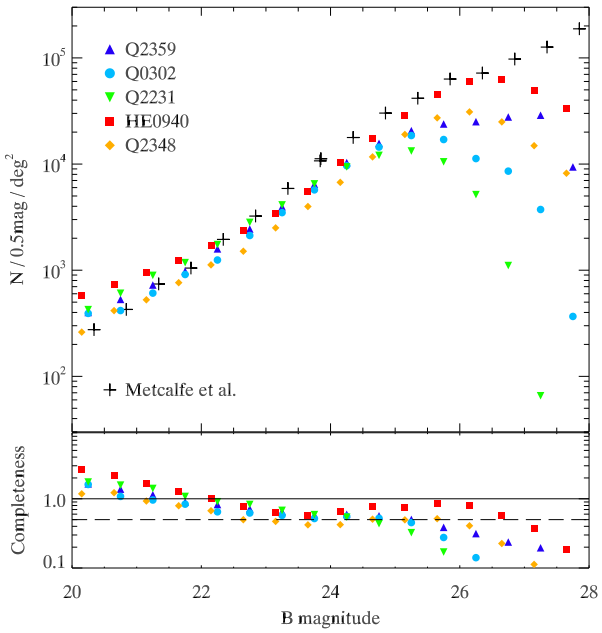

FIGURE 6.3: *As in Fig. 6.2, but for the B band. Note that the HE0940 and Q2348 data are actually g band counts and have been shifted +0.9 mag along the x-axis to allow comparison with the other fields.*

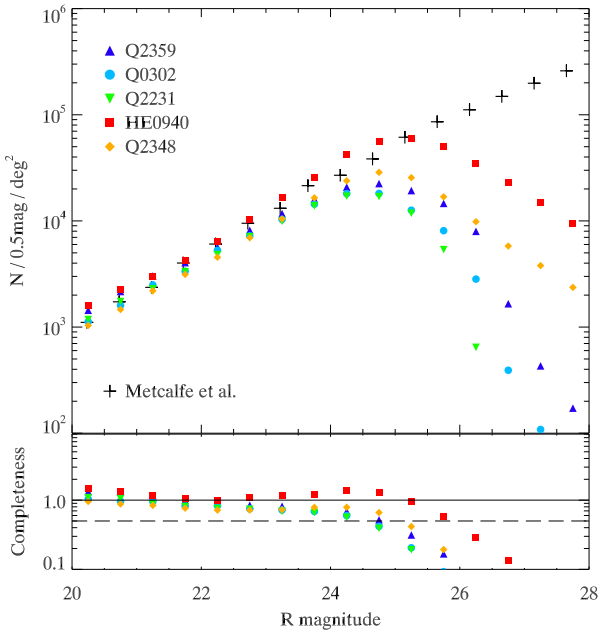

FIGURE 6.4: *As in Fig. 6.2, but for the R band.*

is particularly prevalent in the B band counts. In any case, our LBGs are all selected at $R > 23$, so the presence of stars at bright magnitudes is not important for our purposes.

Importantly, we note that in Fig. 6.3 the abscissae of the HE0940 and Q2348 counts have been shifted by +0.9 mag, to account for the fact that these are g band source counts while all the other data are B band counts.

6.4 Candidate selection

6.4.1 UBR selection

In the Q2359, Q0302 and Q2231 fields, we select LBG candidates based on their U, B and R photometry. The criteria we use are the same as those used by Bielby et al. (2010), which are based on those of Steidel et al. (2003). There are 4 groups to the selection, designated LBG_PRI1, LBG_PRI2, LBG_PRI3 and LBG_DROP and defined as follows:

LBG_PRI1

- $23 < R < 25.5$
- $0.5 < (U - B) < 4.0$
- $(B - R) < 0.8(U - B) + 0.6$

- $(B - R) < 2.2$

LBG_PRI2

- $23 < R < 25.5$
- $(U - B) > 0.0$
- $(B - R) < 0.8(U - B) + 0.8$
- $-1 < (B - R) < 2.7$
- $\notin$ LBG_PRI1

LBG_PRI3

- $23 < R < 25.5$
- $-0.5 < (U - B) < 0.0$
- $-1.0 < (B - R) < 0.8(U - B) + 0.6$
- $\notin \{$LBG_PRI1,LBG_PRI2$\}$

LBG_DROP

- $23 < R < 25.5$
- $0.5 < (B - R) < 2.2$
- No detection in U

The first 3 groups represent an order of priority — that is, LBG_PRI1 candidates are considered more likely to be $z \approx 3$ LBGs than e.g. LBG_PRI3 candidates. This is because whereas LBG_PRI1 tends to select outliers in the UBR colour–colour plot, the lower priority groups select objects increasingly close to the main body of sources, and therefore suffer from increased contamination from lower-redshift interlopers.

The fourth group is somewhat separate, being for galaxies which are not detected in the U band at all. Such sources may be excellent LBG candidates, since it may be that the presence of the Lyman limit in the U band has made the galaxy extremely faint in this band, such that it 'drops out' below the magnitude limit. However, the LBG_DROP population is also likely to suffer from contamination, in this case because objects with no counterpart in 1 of the 3 bands have a higher chance of being spurious sources.

Figs. 6.5, 6.6 and 6.7 show UBR colour–colour plots for Q2359, Q0302 and Q2231, respectively. In each plot, the LBG_PRI1, LBG_PRI2, LBG_PRI3 and LBG_DROP candidates

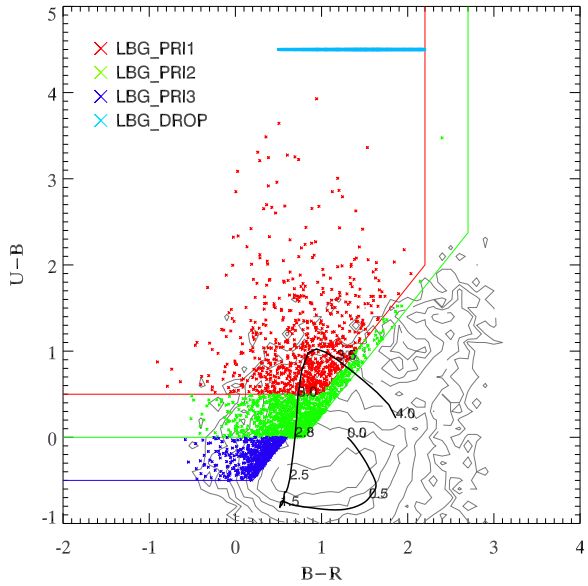

FIGURE 6.5: *UBR colour-colour plot showing candidate selection in Q2359. Objects selected as* LBG_PRI1, LBG_PRI2, LBG_PRI3 *and* LBG_DROP *candidates are shown in different colours as indicated by the legend. The* LBG_DROP *candidates have been placed at $U - B = 4.5$. The contours show the colour distribution of the rest of the objects in the field.*

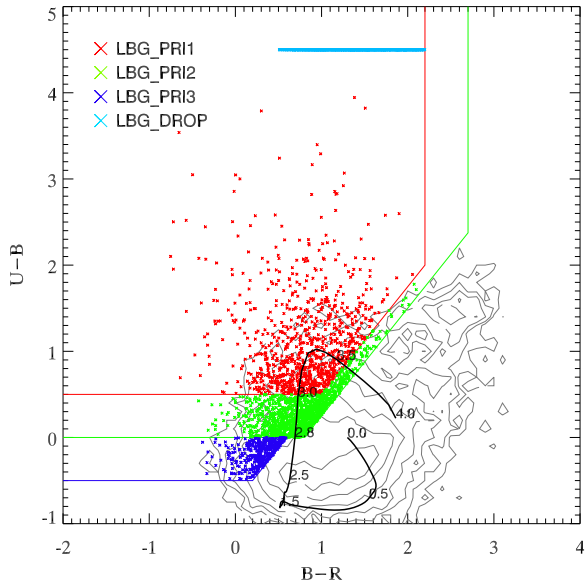

FIGURE 6.6: *As for Fig. 6.5, but for Q0302.*

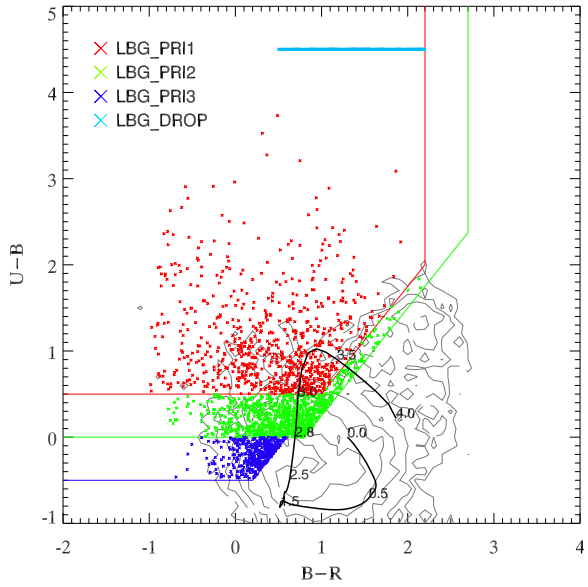

FIGURE 6.7: *As for Fig. 6.5, but for Q2231.*

are indicated. A model colour–redshift track is also plotted, showing the expected evolutionary path of a star-forming galaxy from $z = 0$ to $z = 4$. This was produced using the Bruzual & Charlot (2003) model, assuming a Chabrier IMF and an exponential SFR with e-folding time $\tau = 9$ Gyr (as in §4.3). The model indicates that our selection criteria (across all the priority groups) should find galaxies in the range $\approx 2.5 < z < 3.8$. It also suggests that, of the sources which are confirmed as high-redshift LBGs, the LBG_PRI3s should typically be at a lower redshift than the LBG_PRI2s, which in turn should be at lower redshift than the LBG_PRI1s. Bielby et al. (2010) noted that this trend was detected in their LBG sample.

6.4.2 ugr selection

In HE0940 and Q2348, LBG candidates are selected based on ugr photometry. We therefore adapt the criteria outlined above to account for the different colour bands. Again we select candidates as either LBG_PRI1, LBG_PRI2, LBG_PRI3 or LBG_DROP, defined as follows:

LBG_PRI1

- $23 < r < 25$
- $1.4 < (u - g) < 4.0$

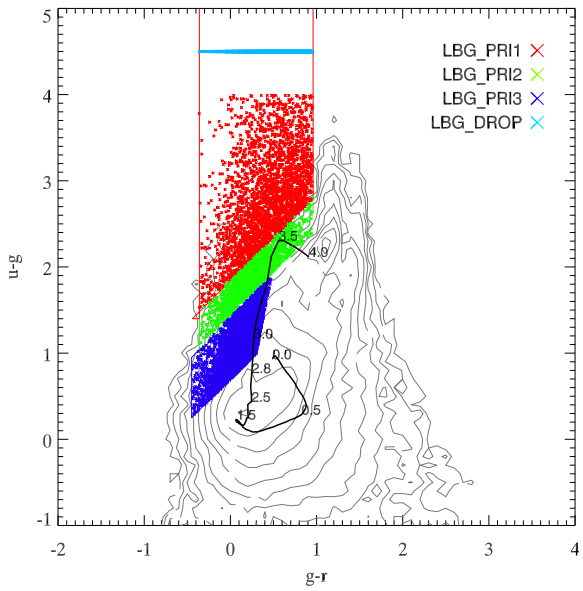

FIGURE 6.8: *A ugr colour-colour plot showing the selection of candidates in HE0940. Symbols are as in Fig. 6.5.*

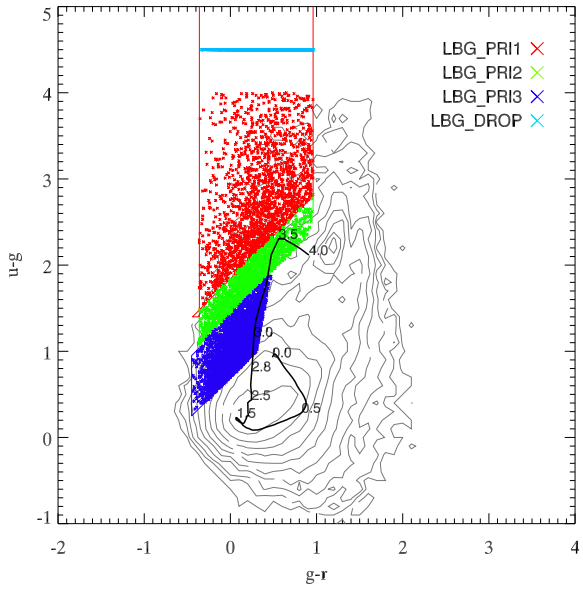

FIGURE 6.9: *As for Fig. 6.8, but for Q2348.*

- $-0.36 < (g - r) < 0.96$
- $(g - r) < (u - g) - 1.88$

LBG_PRI2

- $23 < r < 25$
- $(u - g) > 1.0$
- $-0.36 < (g - r) < 0.96$
- $(g - r) < (u - g) - 1.44$
- $\notin$ LBG_PRI1

LBG_PRI3

- $23 < r < 25$
- $(g - r) < (u - g) - 0.7$
- $-0.45 < (g - r) < 0.2(u - g) + 0.1$
- $\notin \{$LBG_PRI1,LBG_PRI2$\}$

LBG_DROP

- $23 < r < 25$
- $-0.36 < (g - r) < 0.96$
- No detection in u

Figs. 6.8 and 6.9 show the resulting candidates on ugr colour-colour plots, and Table 6.3 gives the numbers and sky densities of candidates in all 5 LBG fields. The density of our primary targets (LBG_PRI1) is relatively constant across all 5 fields at ≈ 0.65 arcmin^{-2}. The selection of LBG_PRI2 and LBG_PRI3 candidates yields consistent results for the 3 UBR-selected fields and the 2 ugr-selected fields separately, but the two are very different to each other, reflecting the different selection method. The number of dropouts shows variation across all 5 fields.

6.5 Spectroscopy

6.5.1 Observations

The LBG candidates were targetted in spectroscopic follow-up observations with the VLT VIMOS spectrograph between September 2008 and December 2009, with programme

TABLE 6.3: *Numbers and sky densities of $z \approx 3$ LBG candidates in each of the fields. For each priority class, the first column shows the total number of candidates selected and the second, italicised column shows the density in arcmin^{-2}. The last two columns show the figures for all $z \approx 3$ LBG candidates.*

Field	LBG_PRI1		LBG_PRI2		LBG_PRI3		LBG_DROP		All	
Q2359	795	*0.61*	1,130	*0.87*	549	*0.42*	2,235	*1.72*	4,709	*3.63*
Q0302	891	*0.69*	1,227	*0.95*	433	*0.33*	1,014	*0.78*	3,565	*2.75*
Q2231	748	*0.65*	948	*0.82*	424	*0.37*	514	*0.45*	2,634	*2.29*
HE0940	2,808	*0.78*	1,494	*0.42*	4,347	*1.21*	6,146	*1.71*	14,795	*4.11*
Q2348	1,843	*0.51*	1,624	*0.45*	4,808	*1.34*	1,850	*0.51*	14,795	*2.81*

IDs 081.A-0418(B) (Q2231), 081.A-0418(D) (Q2359), 081.A-0418(F) (Q0302), 082.A-0494(B) (HE0940) and 082.A-0494(D) (Q2348). The observations were done during dark time in generally good conditions with a typical seeing of $\approx 1''$ and an airmass of 1.0–1.3. Table 6.4 gives details of all the fields observed.

The VIMOS instrument (Le Fevre et al., 2003) comprises four separate CCDs, each with a field of view of $7' \times 8'$. These four arms are arranged in a 2×2 grid with a $\approx 2''$ gap between each CCD, giving a total $16' \times 18'$ FoV as quoted previously. Of this 288 arcmin^2 field, 224 arcmin^2 is covered by the detector.

To perform multi-object spectroscopy, masks are designed for each quadrant, with slits placed at target source positions. A grism then disperses the light from target objects onto the CCD. Our observations utilise the low resolution blue (LR_Blue) grism and the order sorting blue (OS_Blue) filter, resulting in a wavelength range of 3700Å–6700Å, blazing at ≈4000Å. This wavelength range is ideal for our survey, detecting the Lyα line at $2.0 < z < 4.5$. The resolving power of the spectrograph in this configuration is $R = 180$ assuming a $1''$ slit (as used in these observations), which gives a resolution element of $\Delta\lambda \approx 22$Å at the blaze wavelength. The spectral dispersion is 5.3Å/pixel.

The slit masks were designed using the VMMPS software which is standard for VIMOS observations. The aims during mask design are (a) to maximise the number of observed targets, (b) to favour higher-priority targets and (c) to ensure slits are of sufficient size to allow a robust sky subtraction. Since these aims are frequently in conflict with one another, the mask design process is one of attempting to optimise the observa-

TABLE 6.4: *Details of spectroscopic observations for the LBG target fields presented in this thesis.*

Field	Subfield	RA[a]	Dec[a]	Exposure[b]	Airmass	Seeing	Dates
Q2359	f1	00:01:09.94	+07:03:26.8	10	$1.1 - 1.2$	$0.6 - 1.7''$	23–25 Sep 2008
Q2359	f2	00:01:12.92	+07:16:39.2	10	$1.1 - 1.3$	$0.6 - 1.3''$	3, 20–21 Oct 2008
Q2359	f3	00:02:11.50	+07:15:33.9	10	$1.2 - 1.4$	$0.6 - 1.3''$	3, 21–25 Nov 2008
Q2359	f4	00:02:12.89	+07:02:19.1	10	$1.2 - 1.3$	$0.5 - 1.1''$	26–30 Nov 2008
Q2231	f1	22:34:28.19	–00:06:03.3	10	$1.1 - 1.2$	$0.5 - 1.0''$	23, 28 Oct 2008
Q2231	f2	22:34:28.55	+00:06:13.2	10	$1.1 - 1.2$	$0.4 - 0.9''$	21–22 Oct 2008
Q2231	f3	22:33:39.51	–00:06:10.8	10	$1.1 - 1.2$	$0.5 - 1.0''$	3 Aug; 27 Jul 2008
Q0302	f1	03:04:20.12	–00:14:28.8	12	$1.1 - 1.3$	$0.7 - 1.2''$	23, 31 Oct 2008
Q0302	f2	03:03:10.27	–00:16:18.7	12	$1.1 - 1.2$	$0.7 - 1.5''$	21–23 Nov 2008
Q0302	f3	03:03:15.41	–00:30:40.0	12	$1.1 - 1.2$	$0.7 - 1.5''$	25–26 Nov 2008
Q0302	f4	03:04:15.56	–00:28:59.1	12	$1.1 - 1.2$	$0.7 - 1.2''$	24 Sep; 1, 7 Oct 2008

Continued overleaf...

Table 6.4 — continued.

HE0940	f4	09:42:10.00	–10:54:30.3	11.2	$1.0 - 1.3$	$0.8 - 1.5''$	1 Feb 2009
HE0940	f5	09:43:07.47	–11:24:50.3	11.2	$1.0 - 1.3$	$0.7 - 1.4''$	3 Feb 2009
HE0940	f6	09:41:59.99	–11:24:50.4	11.2	$1.0 - 1.2$	$0.5 - 1.2''$	20–21 Feb 2009
HE0940	f7	09:44:14.99	–11:24:49.9	11.2	$1.0 - 1.2$	$0.5 - 1.3''$	22, 24 Feb 2009
HE0940	f8	09:43:21.49	–10:41:00.5	11.2	$1.0 - 1.2$	$0.5 - 1.0''$	26–27 Feb 2009
HE0940	f9	09:42:09.99	–10:40:59.8	11.2	$1.0 - 1.3$	$0.5 - 1.2''$	2 Feb 2009
Q2348	f1	23:51:50.08	–00:54:21.9	11.5	$1.1 - 1.2$	$0.5 - 1.7''$	23–25 Jul 2009
Q2348	f2	23:50:45.09	–00:54:22.2	11.5	$1.0 - 1.1$	$0.5 - 1.0''$	19–20 Jul 2009
Q2348	f3	23:49:40.07	–00:54:22.6	11.5	$1.0 - 1.2$	$0.4 - 0.8''$	27 Jul 2009
Q2348	f4	23:51:50.12	–00:37:31.6	11.5	$1.1 - 1.2$	$0.5 - 1.5''$	20–21 Aug 2009
Q2348	f5	23:50:45.05	–00:37:31.5	11.5	$1.0 - 1.2$	$0.7 - 1.4''$	16–20 Sep 2009
Q2348	f6	23:49:40.00	–00:37:32.0	11.5	$1.1 - 1.2$	$0.8 - 1.3''$	24–25 Sep 2009
Q2348	f7	23:51:50.12	–01:07:31.4	11.5	$1.1 - 1.2$	$0.7 - 1.0''$	12, 20 Oct 2009
Q2348	f8	23:50:45.00	–01:07:32.0	11.5	$1.1 - 1.3$	$0.7 - 1.3''$	22 Nov, 10 Dec 2009
Q2348	f9	23:49:40.00	–01:07:32.0	11.5	$1.1 - 1.3$	$0.8 - 1.5''$	15–22 Nov 2009

[a] J2000 coordinates of subfield centre

[b] in kiloseconds

tions to satisfy all three as well as possible. Point (c) is addressed by setting a minimum slit length of 8″ (40 pixels given the pixel scale of 0.205″/pixel), which given ≈ 1″ seeing leaves ≈ 7″ (34 pixels) of sky observations which can be used for subtraction. Slit length was increased as much as possible where such an increase would not prevent the observation of an additional target — that is, where it did not conflict with point (a).

With the LR_Blue grism, each spectrum spans 640 pixels along the dispersion axis. Assuming a 40 pixel slit width as specified above, this would allow for a possible total of over 300 slits on the full 4k×2k detector. This is however not practically achievable given the density of LBG candidates, and is hampered further by the need to select high-priority candidates (point b), which have a lower sky density still. Our final slit masks therefore typically contain some 50–70 slits per quadrant.

6.5.2 Data reduction

We make use of pipeline-reduced data products produced with the VIMOS Esorex reduction package. Using bias frames, flat fields and arc lamp exposures taken for each mask during each observing run, the pipeline generates bias-subtracted, flat-fielded, wavelength-calibrated science frames consisting of a series of 2D spectra. One such science frame is produced for each separate observing block for each quadrant of each subfield.

Following Bielby et al. we use the `imcombine` procedure in IRAF to combine the reduced frames from each observing block, generating a master science frame for each quadrant of each field. When combining the frames we use the `crreject` mode, designed to remove cosmic rays by rejecting pixels with significant positive spikes. We have also used the `avsigclip` rejection mode with a rejection threshold of 3σ, and find that our results are not significantly affected, suggesting that our results do not depend strongly on the parameters used to combine the science frames at this stage.

We extract 1D spectra from the reduced, combined 2D spectra using the IDL routine `specplot` prepared by R. Bielby. The `vmmosobsstare` procedure of the VIMOS Esorex pipeline provides the location of the target object in each slit, however the object's position in the slit shifts as one moves along the dispersion axis. Therefore, `specplot` uses the provided location as an initial starting point and then traces the object along the dispersion axis by fitting Gaussian functions across the slit, measuring the shifts in the Gaussian peak location, and fitting these positions with a 4th order polynomial.

An aperture, which is typically 6 pixels (or 1.2″) wide, is then laid over the object.

Sky apertures are placed either side of the object, covering as large an area as is usable, which may be limited by either the size of the slit or the presence of defects, which can sometimes be avoided by reducing the size of the sky aperture. One-dimensional object and sky spectra are then found by averaging across the respective apertures, and the sky spectrum is then subtracted from the object spectrum to give a final spectrum for the object.

In some cases there remain significant sources of contamination in the final object spectrum. These can arise from bad pixels, either in the object or sky aperture, or more frequently from the bright sky emission lines [OI] 5577Å, [NaI] 5990Å and [OI] 6300Å; in either case, the resulting contamination may manifest itself as either a positive or a negative spike in the spectrum. Such artefacts are, however, easily spotted during a routine inspection of the 2D spectrum.

6.6 Identification of targets

Every source targetted for spectroscopic observation is inspected visually, in both the 2D and 1D spectra, to determine where possible a redshift and classification. Sources are classified as either $z \approx 3$ Lyman-break galaxies, low-redshift galaxies, QSOs or Galactic stars. The LBGs are divided into those showing Lyα emission (designated LBe) and those showing Lyα absorption (LBa). The low-z galaxies are classed as either emission line galaxies (ELGs) or luminous red galaxies (LRGs), although the distinction is not important for the purposes of this work. QSOs are determined by the presence of broad emission features. Stars are classified by comparison to template spectra: in particular we check for A, F, G, K and M stars.

In determining the redshift and classification the spectral feature primarily used in the case of LBGs is the Lyα emission/absorption line at 1216Å; for lower redshift galaxies it is the [OIII] emission line at 3727Å. In addition to these, some of the following features are used:

For $z \approx 3$ LBGs:

- 912Å Lyman limit
- 1026Å Lyβ emission/absorption
- 1035Å OVI emission
- 1260Å SiII absorption

- 1302Å OI absorption
- 1336Å CII absorption
- 1393Å, 1403Å SiIV absorption doublet
- 1554Å CIV absorption

For low-z galaxies:

- 3833Å CN absorption
- 3869Å [NeIII] emission
- 3934Å K-band absorption
- 4000Å HK break
- 4102Å Hδ emission
- 4861Å Hβ emission/absorption
- 4959Å [OIII] emission
- 5007Å [OIII] emission

The presence of the HK break and the nearby [OIII] 3727Å emission causes these interlopers to appear fairly frequently in our spectroscopic samples, since these features mimic the Lyα emission and associated break which our selection is designed to detect. The ISM absorption features listed above for LBGs are therefore of considerable importance in identifying genuine $z \approx 3$ galaxies. For every target which is identified, we assign a quality parameter to the redshift determined, in the range $0 \leq Q \leq 1$. A quality of $Q \leq 0.3$ indicates that a possible redshift has been determined, but is not considered a robust measurement. Above this, for LBGs, the quality parameters indicate that the redshift is based on the following features:

- $Q = 0.4$ — a spectral break with some weak Lyα emission and low-SNR ISM absorption features, or strong Lyα emission but with no detected continuum
- $Q = 0.5$ — a spectral break with high-SNR Lyα emission plus low-SNR ISM absorption features
- $Q = 0.6$ — a spectral break with high-SNR Lyα emission plus unambiguous, high-SNR ISM absorption features
- $Q \geq 0.7$ — a spectral break with high-SNR Lyα emission plus high-SNR absorption and emission lines

TABLE 6.5: *Numbers of objects in each target field spectroscopically identified as either high-z LBGs, $z < 2$ galaxies, QSOs or stars.*

Field	$z \approx 3$ LBGs	$z < 2$ galaxies	QSOs	Stars
Q2359	185 (0.21 arcmin^{-2})	127	3	8
Q0302	192 (0.21 arcmin^{-2})	131	10	13
Q2231	122 (0.18 arcmin^{-2})	128	6	18
HE0940	317 (0.24 arcmin^{-2})	260	3	48
Q2348	334 (0.17 arcmin^{-2})	183	8	48
Total	1,150 (0.20 arcmin^{-2})	829	30	135

All LBGs with $Q \geq 0.4$ are included in our final sample. We note that although Bielby et al. (2010) employed a similar quality parameter, the criteria they used were different and therefore they included only $Q \geq 0.5$ LBGs in their subsequent analyses.

6.7 LBG sample

6.7.1 Sky densities and redshift distributions

We have identified 1,150 LBGs in the range $2 < z < 4$ within an area of 5,824 arcmin^2, yielding a sky density of 0.20 arcmin^{-2}. This is to be compared to the previous fields from this survey presented by Bielby et al. (2010), where 1,020 LBGs were identified in 4,256 arcmin^2 giving a density of 0.24 arcmin^{-2}. The comparability of these figures suggests broad consistency between the two separately reduced datasets. The total $z \approx 3$ LBG survey therefore now includes 2,170 LBGs in 10,080 arcmin^2 (a density of 0.22 arcmin^{-2}). The total numbers of sources identified in each of the 5 fields presented here are given in Table 6.5.

Fig. 6.10 shows the $n(z)$ distributions of all sources with measured redshifts in each of the 5 LBG fields. The figure shows that LBGs in HE0940 and Q2348, where LBGs were selected in ugr, have higher average redshifts than in the UBR-selected fields, suggesting that the ugr criteria bias the selection toward higher z. It is also notable from Table 6.5 that the ugr selection appears to include more Galactic stars. Future ugr-selected LBG surveys may wish to alter our colour criteria to better avoid stellar interlopers.

Fig. 6.10 also shows the $n(z)$ for the subsets of sources with $Q \geq 0.5$ and $Q \geq 0.6$. We

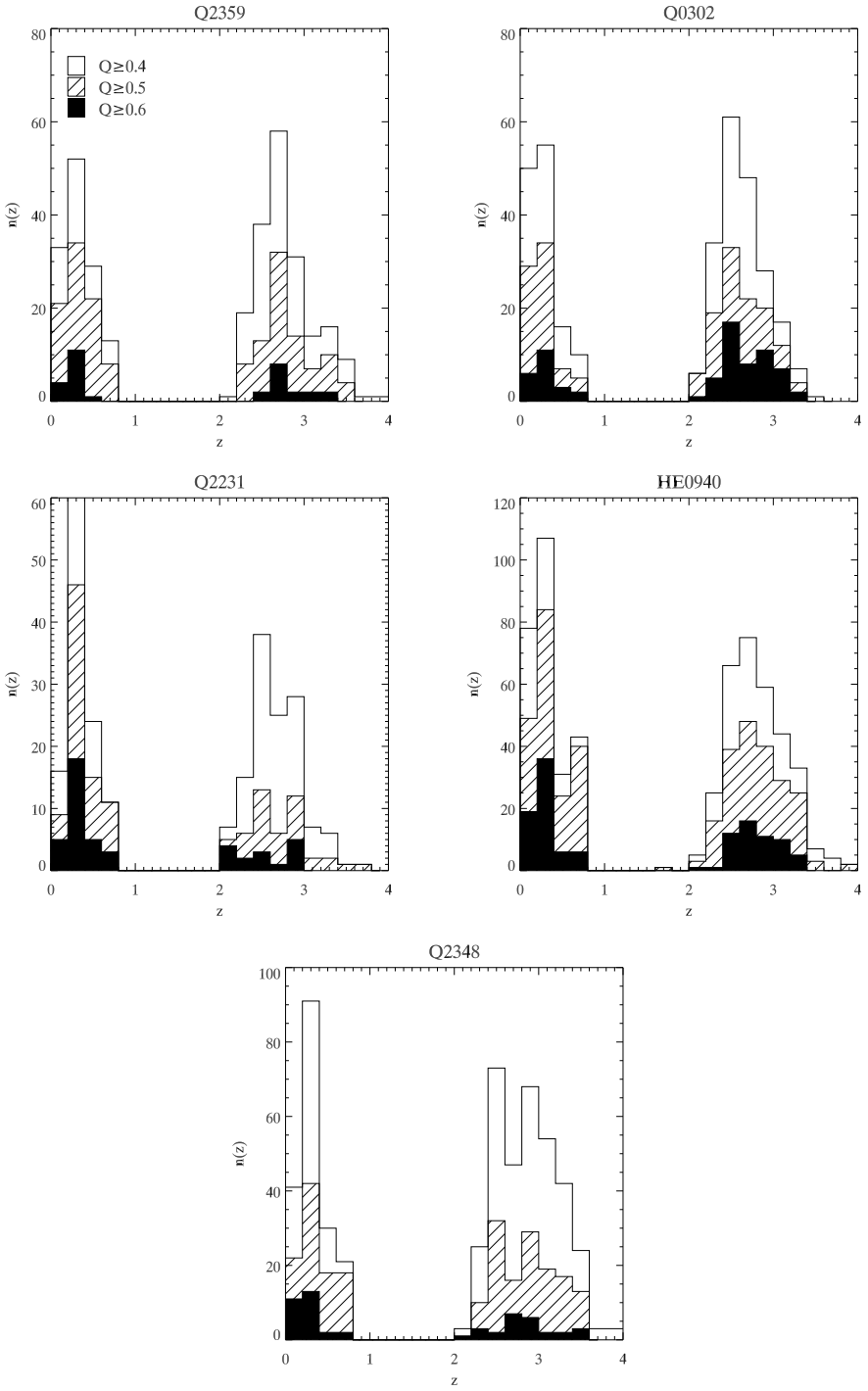

FIGURE 6.10: *Redshift distributions of identified sources in each of the target fields. In each panel we show the distribution for the full sample ($Q \geq 0.4$), as well as for the $Q \geq 0.5$ (hashed) and $Q \geq 0.6$ (filled) subsets, where Q is the redshift quality parameter.*

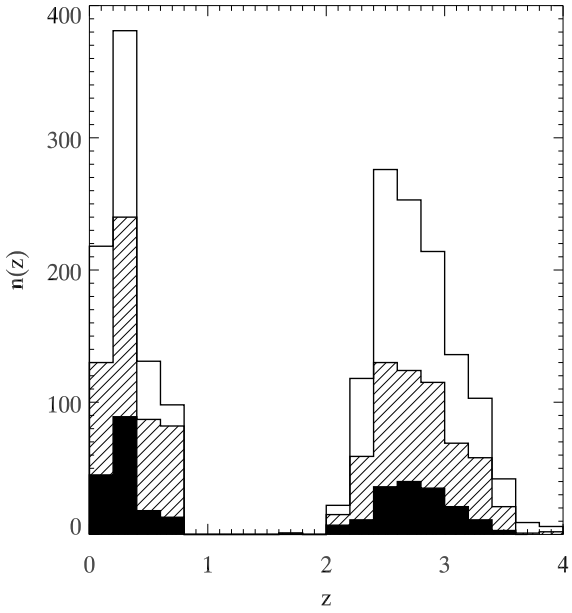

FIGURE 6.11: *Redshift distribution of all identified sources in our 5 target fields. The distribution is shown for the full sample (i.e., sources with $Q \geq 0.4$; unfilled), as well as for the $Q \geq 0.5$ (hashed) and $Q \geq 0.6$ (filled) subsets, where Q is the redshift quality parameter.*

TABLE 6.6: *Redshift distribution statistics for spectroscopically confirmed, $Q \geq 0.4$ LBGs in the 5 observed fields. In each case the mean redshift $\bar{z}$ (with standard error), median redshift $\tilde{z}$ and standard deviation σ of the distribution is given.*

Field	$\bar{z}$	$\tilde{z}$	σ
Q2359	2.77 ± 0.02	2.72	0.33
Q0302	2.64 ± 0.02	2.61	0.28
Q2231	2.65 ± 0.03	2.62	0.29
HE0940	2.81 ± 0.02	2.77	0.33
Q2348	2.87 ± 0.02	2.87	0.36
Total	2.78 ± 0.01	2.74	0.34

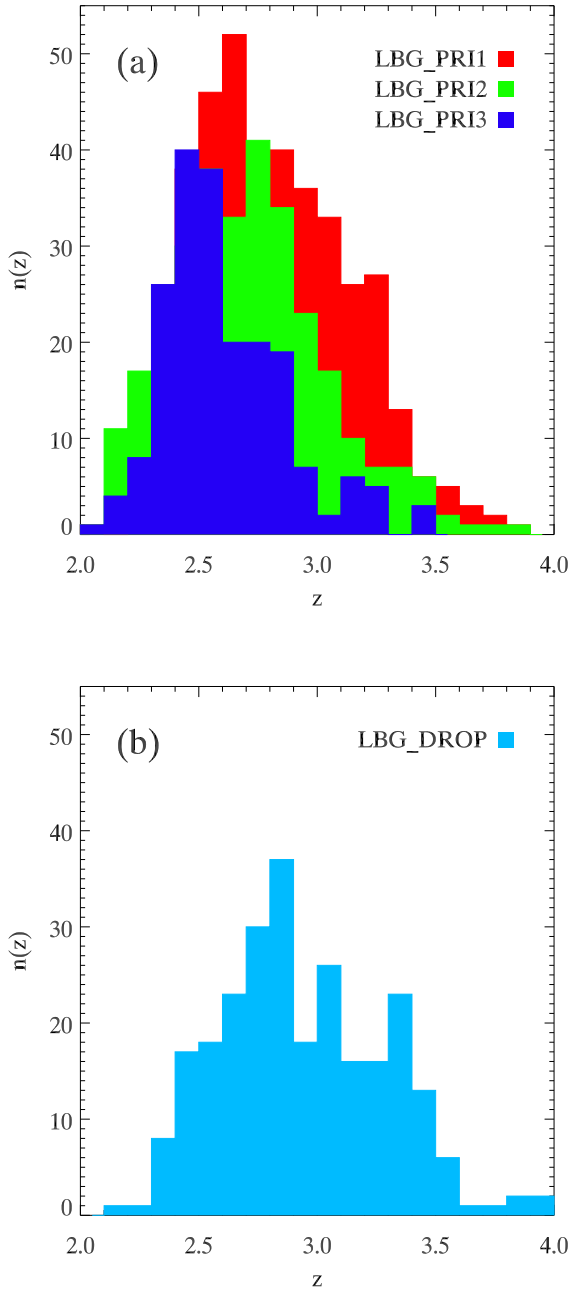

FIGURE 6.12: *Redshift distribution of all identified sources our 5 target fields, separated by initial candidate priority. Panel* (a) *shows the* LBG_PRI1, LBG_PRI2 *and* LBG_PRI3 *classes, while the* LBG_DROPs *are shown separately in panel* (b) *for clarity. Colours are as in Figs. 6.5–6.8.*

note that in any given field, the *distributions* of sources at $Q \geq 0.4$, $Q \geq 0.5$ or $Q \geq 0.6$ are roughly the same — the LBGs with higher ID qualities are not skewed to lower or higher redshift, for example — suggesting that the redshift distributions shown are fairly robust. The average redshifts and standard deviations are given in Table 6.6. The redshift distribution of the full LBG sample[1] has a mean redshift of 2.78 ± 0.01 and a standard deviation of 0.34, and is shown in Fig. 6.11.

A prediction made during the selection of candidates (§6.4) was that the candidates selected as LBG_PRI1 would lie at higher redshift than the LBG_PRI2 candidates, which would in turn be at higher redshift than LBG_PRI3s. Fig. 6.12 shows how the redshift distribution of our full LBG sample is divided by candidate selection priority, and it is clear that this prediction has been realised by the data. Quantitatively, we find that the LBG_PRI1s have a mean redshift of $\bar{z} = 2.83 \pm 0.02$, the LBG_PRI2s have $\bar{z} = 2.71 \pm 0.02$ and the LBG_PRI3s have $\bar{z} = 2.61 \pm 0.02$. The LBG_DROP candidates are shown in a separate panel for clarity, and have the highest mean redshift of all the groups, with $\bar{z} = 2.93 \pm 0.02$; Bielby et al. also found that the LBG_DROPs had the highest average redshift, confirming that the selection of U-band dropouts is a powerful tool in identifying $z \approx 3$ galaxies.

There is a notable difference between the surveyed fields presented here and by Bielby et al. (2010) in the numbers of low-redshift galaxies. Bielby et al. typically identified ~ 0.2 times as many $z < 2$ galaxies as $z \approx 3$ LBGs, whereas in our fields the number of low-z galaxies is $\sim 0.8\times$ that of LBGs (Table 6.5). Since we have noted that the density of LBGs detected here is comparable to that in Bielby et al.'s study, this does not indicate that more $z < 2$ galaxies have been observed at the expense of LBGs, but rather that the identification of low-z sources has been done with slightly greater completeness. At any rate, our science analyses shall focus only on the high-redshift sources, so any difference here is largely inconsequential.

6.7.2 Spectra

$z \approx 3$ Lyman break galaxies

We have identified 1,150 LBGs at $z \approx 3$, of which 875 show Lyα in emission and the other 275 show Lyα in absorption. In Figs. 6.13 and 6.14 we show stacked spectra for the

[1] "Full sample" here refers to the 1,150 LBGs from the 5 fields presented in this chapter, not the 2,170 LBGs from the total LBG survey including the fields of Bielby et al. (2010)

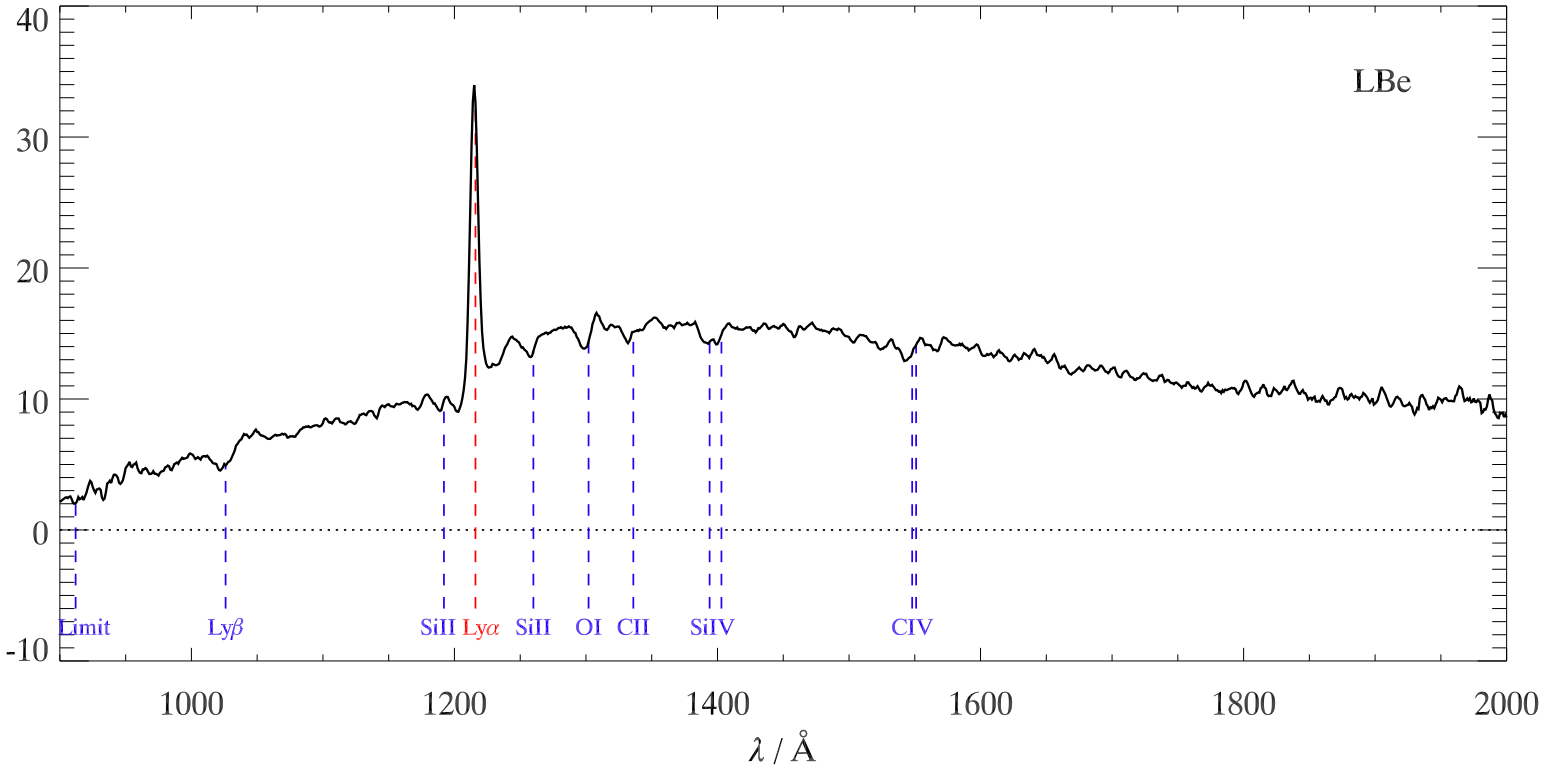

FIGURE 6.13: *Composite spectra for all LBGs showing Lyα in emission, with ISM absorption lines clearly detected.*

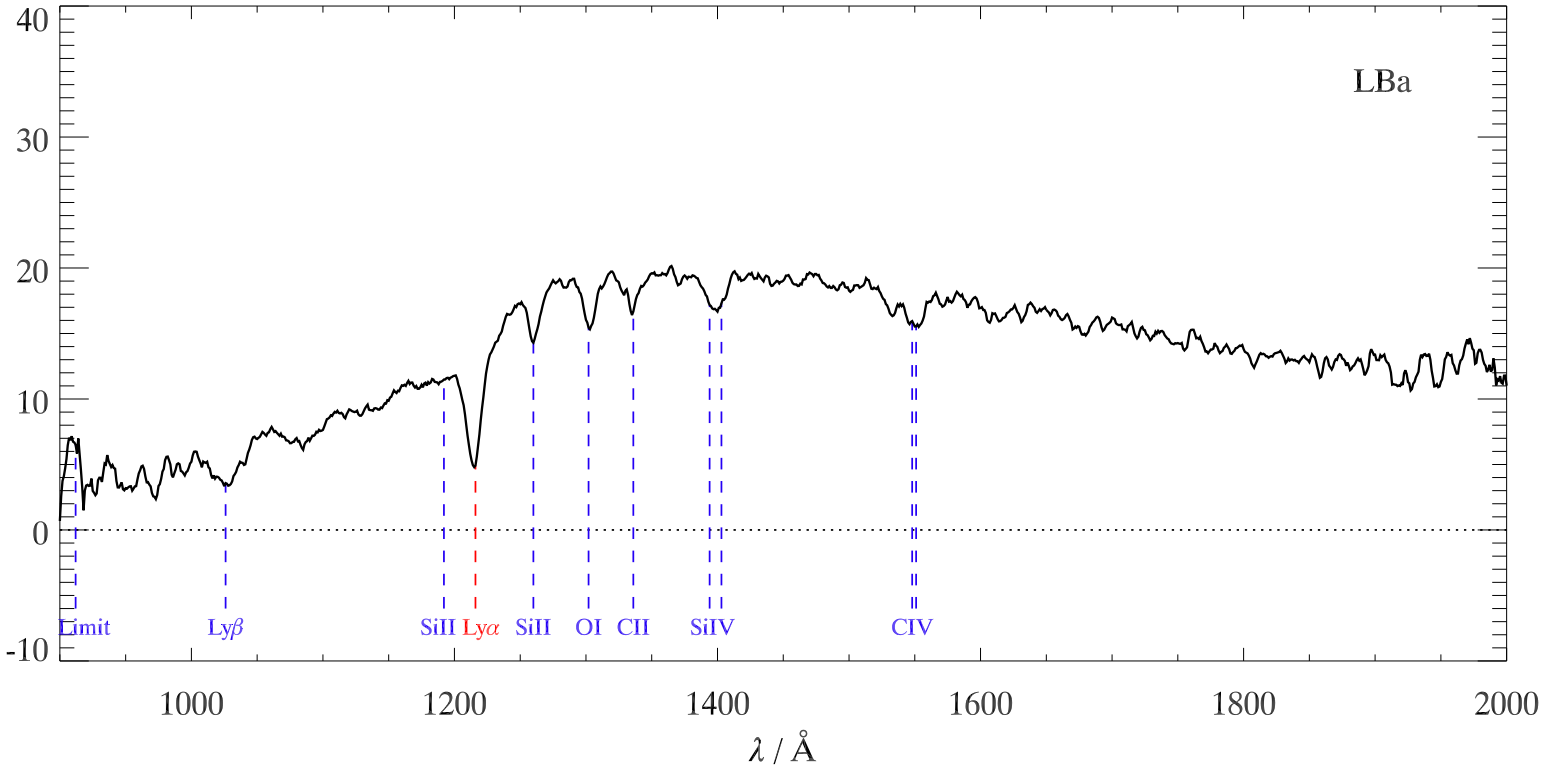

FIGURE 6.14: *Composite spectra for all LBGs showing Lyα in absorption, with ISM absorption lines clearly detected.*

LBGs, separated into the LBe and LBa classes. These composite spectra were generated by averaging over the entire samples, having masked out all major artefacts from the individual spectra.

These stacked spectra show the average ultraviolet SED of a $z \approx 3$ LBG with excellent signal-to-noise, and the quality of these spectra provide an indication of the robustness of our LBG identifications. In Fig. 6.15, we show 3 separate composite spectra for sources classed as LBe's with quality IDs of $Q = 0.4$, $Q = 0.5$ and $Q \geq 0.6$. These spectra reflect the quality criteria set out in §6.6 well, with increasing quality spectra clearly showing increasingly high signal-to-noise in both Lyα emission and ISM absorption features. The absorption features are only weakly detected in $Q = 0.4$ LBGs.

In the composite spectra comprised of the full LBG samples (Figs. 6.13 and 6.14), many absorption and emission features are clearly identifiable — in particular the silicon, oxygen and carbon ISM absorption lines. For the LBe's (Fig. 6.13), it is clear that the ISM features are offset relative to Lyα (and therefore also relative to the marked line positions, since the spectrum has been shifted to the rest frame using the redshift of Lyα).

This result is expected, since the Lyα emission and the ISM absorption features arise from separate parts of the galaxy. The ISM absorption features occur chiefly in the cool outflowing material, driven from the star-forming regions of the galaxy by stellar winds (Tenorio-Tagle et al., 1999; Adelberger et al., 2003); we therefore typically see these features blueshifted relative to the galaxy itself, since we tend to observe the closer front of the effluxing gas. Lyα emission, on the other hand, originates in the star-forming hydrogen clouds of the galaxy, giving it a systematically higher redshift than the absorption features; additionally, resonant scattering of the Lyα photons increases the path length taken by these photons and therefore increases the Lyα redshift further still (Adelberger et al., 2003).

The result is that the 'true' redshift of the galaxy lies somewhere between the apparent redshifts of the Lyα emission line and the ISM absorption lines. The difference between these two redshifts is generally characterised as a velocity difference, according to Eqn. 6.1:

$$\Delta v = v_{\mathrm{Ly}\alpha} - v_{\mathrm{ISM}} = \frac{c(z_{\mathrm{Ly}\alpha} - z_{\mathrm{ISM}})}{1 + (z_{\mathrm{Ly}\alpha} + z_{\mathrm{ISM}})/2} \tag{6.1}$$

Adelberger et al. (2003) found a mean value of $\langle \Delta v \rangle = 614 \pm 316$ km s^{-1}, Shapley

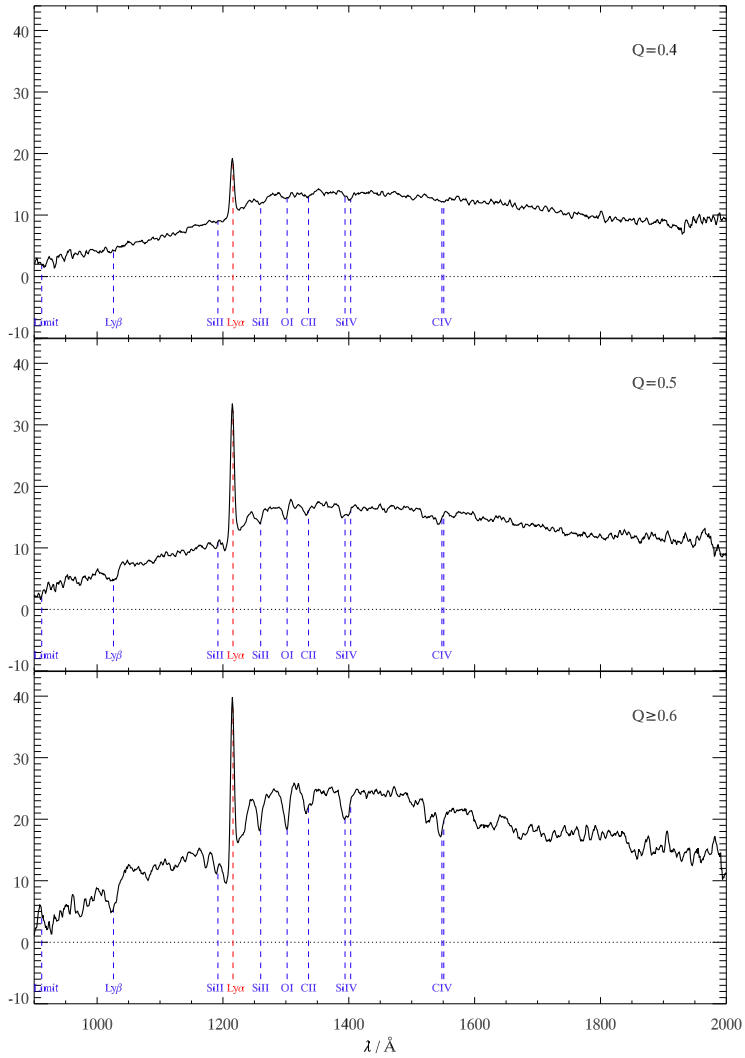

FIGURE 6.15: *Composite spectra for galaxies classified as LBe's, separated by ID quality parameter Q. Those with $Q = 0.4$ (upper panel) show comparatively weak Lyα emission and marginal detections of ISM absorption lines. Moving to higher quality values, the strength of the Lyα line increases and we also see high-SNR absorption features.*

et al. (2003) measured $\langle \Delta v \rangle = 650$ km s^{-1} and, using the first half of the data from this LBG survey, Bielby et al. (2010) found $\langle \Delta v \rangle = 625 \pm 510$ km s^{-1}. In this study we have also determined separate values for $z_{\mathrm{Ly}\alpha}$ and z_{ISM} wherever possible, and from these measurements we find $\langle \Delta v \rangle = 615 \pm 584$ km s^{-1} for those LBGs with $Q \geq 0.5$ (we impose this limit since the ISM features in $Q = 0.4$ LBGs are less securely identified), consistent with previous measurements.

It is evident from Fig. 6.14 that in our LBa sample (LBGs showing Lyα absorption) there is no offset between the Lyα redshift and the ISM redshift, indicating that broad Lyα absorption arises from the same outflowing material as produces the ISM absorption lines. For this reason, the LBa galaxies are not included in the calculation of $\langle \Delta v \rangle$ above.

Quasars

We have identified 30 $z > 2$ QSOs, in our spectroscopic sample, identified as such by the presence of a broad emission lines. Their spectra are shown in Fig. 6.16. All of the QSOs show broad Lyα emission and most (at least $3/4$) also show broad CIV λ1549, a high-ionisation emission line often used to constrain the dynamics and size of the broad-line region in QSOs as well as the virial mass of the black hole (Fine et al., 2010 and references therein). Many of the QSOs also show broad OVI λ1035 and NV λ1241, the latter usually being blended with Lyα. These emission lines are indicated in each panel of Fig. 6.16.

Several other emission lines are detected in some of the QSO spectra but are not marked in the figure. Lyβ λ1026 is clearly seen in panel (d), where it may be asymmetrically broadened to longer wavelengths by the presence of relatively weak OVI λ1035. Panel (n) shows an emission line peaking at 1029Å, likely suggesting a blend between Lyβ and OVI.

Panels (i) and (p) both show very broad emission at ≈ 1500Å. These emission features cover the expected wavelength range of an FeIII multiplet, however they considerably brighter than would be expected for these FeIII lines (Vestergaard & Wilkes, 2001; Sigut, Pradhan & Nahar, 2004), therefore the origin of these emission lines is unclear.

OI λ1304 emission appears in panels (g), (t) and (s) (but is difficult to see in the figure), however in all 3 cases the peak of the emission appears at slightly longer wavelength than the nominal 1304Å. This may indicate a blend with SiII λ1308, but is more likely due to the low-ionisation lines (which include OI) arising from a separate part of the broad line region to the high-ionisation lines and thus having a marginally higher redshift (Constantin et al., 2002). Finally, panels (a), (c), (l), (m), (o), (r), (s) and (t) all

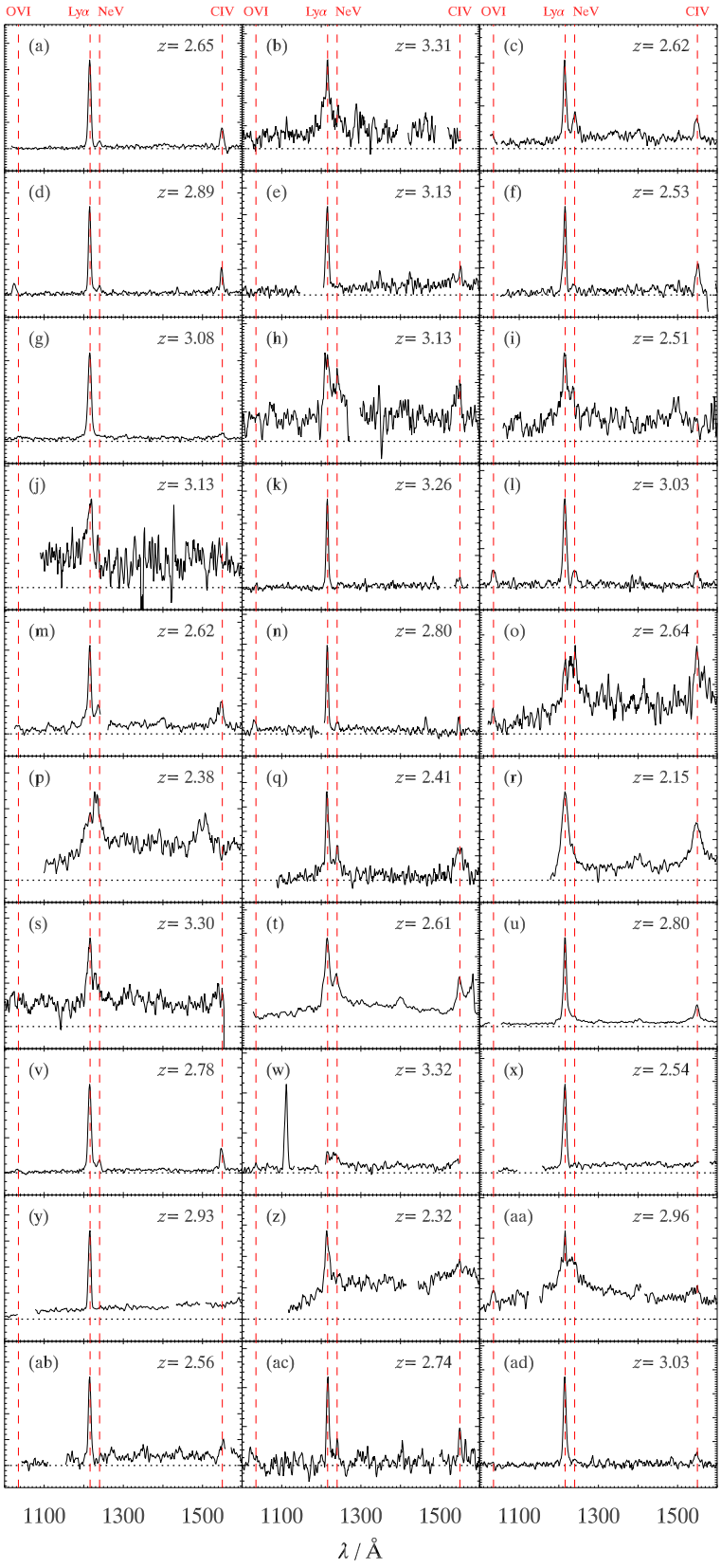

FIGURE 6.16: *Rest-frame VIMOS spectra for the QSOs detected in the 5 fields presented. The y-axis scales differ from panel to panel, but the dotted line marks zero flux in each case. Dashed red lines indicate the wavelength of* OVI, *Ly*α, NeV *and* CIV *emission. Gaps in the spectra indicate that an artefact has been masked out.*

show clear emission at ≈ 1400Å, arising from a blend of the SiIV λ1396 and OVI] λ1402 transitions.

6.8 Summary

This chapter has presented a survey of $z \approx 3$ LBGs in 26 new VLT VIMOS pointings, covering ≈ 6000 arcmin^2. We summarise the chapter below.

- Both the imaging and spectroscopic observations of our LBG fields, including the selection criteria used to identify LBG candidates, have been described.
- A sample of 1,150 LBGs is presented, with a mean redshift of $\bar{z} = 2.78$. We also detect 30 QSOs, 829 low-redshift galaxies and 135 Galactic stars.
- The mean LBG redshift decreases with decreasing candidate priority, as expected from colour-redshift tracks.
- The stacked LBG spectra show strong emission and absorption features. In galaxies which show Lyα in emission, there is an offset between the Lyα redshift and the redshift of the ISM absorption lines, with $\Delta v = 615 \pm 584$ km s^{-1}. In LBGs showing Lyα in absorption, no offset exists.

Our sample can now be combined with the 1,020 LBGs detected in the first half of the survey, presented by Bielby et al. (2010). In the next chapter, we will use this combined sample to measure LBG clustering and the interactions of LBGs with the intergalactic medium.

VII

Galaxy clustering and feedback at $z \approx 3$

7.1 Introduction

The majority of the baryons in the universe are not contained in luminous stellar structures but are more sparsely distributed through the intervening space, including both the interstellar and intergalactic media. Interstellar gas provides the reservoir from which the star-formation process is fuelled, but once this process is underway, winds from stars and supernovae begin to drive the interstellar gas outward (Heckman et al., 1990; Lehnert & Heckman, 1996; Wilman et al., 2005). The supernovae in particular may produce high-velocity winds which are able to act on large scales, driving gas and metals out of the galaxy and into the intergalactic medium, where $\approx 80\%$ of baryons reside (Bi & Davidsen, 1997).

The significance of galaxy feedback to current evolution models was highlghted in §1.2.2. The outflows heat and enrich the IGM and reduce the available gas in the galaxy for star-formation. A similar feedback process is expected to occur as a result of AGN activity, driven by powerful jets. Simulations have indicated that these outflows may play a crucial role in galaxy evolution (Springel & Hernquist, 2003; Springel, Di Matteo & Hernquist, 2005; Bower et al., 2006; Oppenheimer & Davé, 2006).

In §6.7.2 we observed that the redshift offset between the observed Lyα emission and ISM absorption lines revealed the presence of outflows from LBGs. In this Chapter we use cross-correlation techniques to investigate the effect of these outflows on the IGM over megaparsec scales.

Initially, however, we measure the clustering of the $z \approx 3$ LBG population. Since hierarchical galaxy evolution models predict the formation of galaxies through the coming together of smaller structures, the clustering of galaxies at high-redshift can provide an important constraint (Springel et al., 2005; Orsi et al., 2008). Measurements of the clustering amplitude of $z \approx 3$ LBGs have shown some variation, from $r_0 = 3.67 \pm 0.24$ h^{-1} Mpc (Bielby et al., 2010) to $r_0 = 5.9 \pm 0.5$ h^{-1} Mpc (Foucaud et al., 2003), however most measurements are consistent with $r_0 = 4.0$–4.5 h^{-1} Mpc (Adelberger et al., 2003; da Ângela et al., 2005; Hildebrandt et al., 2007; Bielby et al., 2010). Further measurements of this amplitude are therefore extremely important to better constrain galaxy clustering at $z \approx 3$.

7.2 Clustering of $z \approx 3$ LBGs

7.2.1 Autocorrelation function

We measure the clustering of LBGs with the redshift-space correlation function, $\xi(s)$. This is related to the angular correlation function, $w(\theta)$, employed in Chapter 2, but incorporates the redshift of each source as well as its position on the sky. The redshift-space distance, s, between two sources is given by $s = \sqrt{\sigma^2 + \pi^2}$, where σ is the angular separation of the sources (equivalent to θ in $w(\theta)$) and π is the difference between the comoving luminosity distances to their respective redshifts.

We use a simple estimator of $\xi(s)$ which is identical to the $w(\theta)$ estimator described in §2.3; that is, we count the number of data-data (DD) and data-random (DR) pairs and then find the correlation function according to Eqn. 7.1.

$$\xi(s) = \frac{\mathrm{DD}(s)}{\mathrm{DR}(s)} - 1 \tag{7.1}$$

We construct random catalogues covering the same areas of sky as were observed in our spectroscopic survey, accounting for the geometry of the VIMOS detector with gaps between the four quadrants, with $50\times$ as many random sources as detected LBGs. Random right ascensions and declinations are assigned within these regions, then for each object a redshift is assigned such that the redshift distribution of the random sources replicates that of the observed LBGs. A separate catalogue is constructed for each subfield (VIMOS pointing) of each field, to reflect the different numbers of detected LBGs and the different redshift distributions found in each subfield.

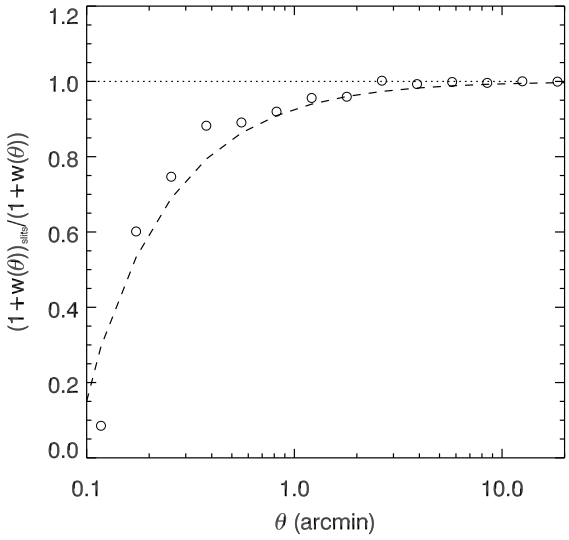

FIGURE 7.1: *The effect of 'slit collisions', showing the reduction in the measured clustering at small scales due to the preclusion of observing close LBG pairs with a multi-object spectrograph. Figure: Bielby et al. (2010)*

We correct $\xi(s)$ for the effect of 'slit collisions', following Bielby et al. (2010). Any LBG observed with VIMOS takes up an area on the detector of at least 40×640 pixels (§6.5.1), corresponding to $8'' \times 130''$ on-sky. Other LBG candidates lying within this area can therefore not be observed, and as a result pairs of LBGs at small separations are systematically missed by our survey.

This will reduce the measured LBG autocorrelation at small separations. Bielby et al. (2010) quantify this effect by comparing the angular autocorrelation of photometrically selected LBG candidates and spectroscopically observed LBGs; the result is shown in Fig. 7.1. We correct for this effect in our LBG survey by weighting DD pairs at $\theta < 2'$ according to the weighting factor given in Eqn. 7.2, based on Fig. 7.1.

$$W(\theta) = \frac{1}{1 - (0.0738 \times \theta^{-1.052})} \tag{7.2}$$

7.2.2 Galaxy redshifts

As discussed in §1.2.2 and shown in §6.7.2, the observed Lyα line is redshifted relative to the intrinsic galaxy redshift, while the interstellar absorption lines are blueshifted. In order to accurately measure the LBG redshift-space autocorrelation function, therefore, we must account for these offsets.

We do this using one of following 3 expressions, following the method of Adelberger

et al. (2005).

$$z' = \bar{z} + 0.070\Delta z - 0.0010(\bar{z} - 2.7) \tag{7.3}$$

$$z' = z_{\rm em} - 0.0033 - 0.0050(z_{\rm em} - 2.7) \tag{7.4}$$

$$z' = z_{\rm abs} - 0.0022 - 0.0015(z_{\rm abs} - 2.7) \tag{7.5}$$

where z' is the intrinsic galaxy redshift, $z_{\rm em}$ is the redshift of the Lyα emission line, $z_{\rm abs}$ is the redshift of the ISM absorption lines, $\bar{z} = (z_{\rm em} + z_{\rm abs})/2$ and $\Delta z = z_{\rm em} - z_{\rm abs}$.

Eqn. 7.3 relies upon having a reasonably robust measurement of both the Lyα emission and the ISM features; we therefore use it only for those LBGs with high-quality redshift IDs ($Q \geq 0.5$ for the new sample, $Q \geq 0.6$ for Bileby et al.'s sample), as Fig. 6.15 shows that the ISM features are only weakly detected in the lower-quality LBGs. For the low-Q sources we instead use Eqn. 7.4, which determines an intrinsic redshift based on the Lyα emission line alone.

Finally, Fig. 6.14 shows that in those LBGs where Lyα is in absorption, the Lyα redshift is the same as the ISM redshift, therefore for these LBGs we find the intrinsic redshift using Eqn. 7.5, with $z_{\rm abs} = z_{{\rm Ly}\alpha} = z_{\rm ISM}$.

7.2.3 Clustering results

Fig. 7.2 shows the measured $\xi(s)$ for our $z \approx 3$ LBG sample. Panel (a) shows the separate measurements for the first half of the LBG survey presented by Bielby et al. (2010) and the second half presented in Chapter 6, and serves to show that the two separately reduced datasets yield consistent clustering results. At $s < 2\ h^{-1}$ Mpc and $s > 6\ h^{-1}$ Mpc there is excellent agreement between the two samples, as well as with the $r_0 = 4.2\ h^{-1}$ Mpc, $\gamma = 1.8$ power-law model (dotted line); this is given by Bielby et al. (2010) as the best fitting model to da Ângela et al.'s (2005) analysis of Steidel et al.'s (2003) $z \approx 3$ LBG sample. At $2 < s < 6\ h^{-1}$ Mpc, the measured $\xi(s)$ is deficient relative to the power-law model — this is especially true in the Bielby et al. sample, but a less prominent deficiency is also detected in the sample presented here.

In panel (b), we show the measured $\xi(s)$ for the full, combined LBG sample, consisting of 2,170 spectroscopically identified LBGs. We again show the $r_0 = 4.2\ h^{-1}$ Mpc,

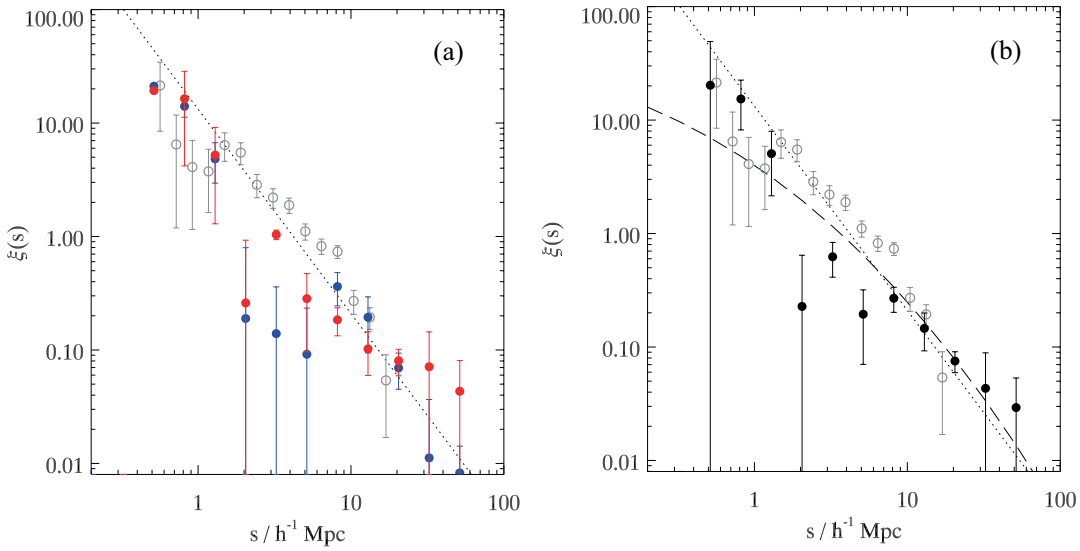

FIGURE 7.2: *Autocorrelation of LBGs in our survey.* (a) *A comparison of the $\xi(s)$ result measured for the first half of the survey presented by Bielby et al. (filled blue circles), the second half presented in this work (filled red circles) and the previous result by da Ângela et al. (open grey circles).* (b) *The combined result for our full LBG survey (filled black circles) compared to that of da Ângela et al. (open grey circles). The dotted line shows the best-fit result for the da Ângela sample, a power-law with $\gamma = 1.8$ and $r_0 = 4.2\ h^{-1}$ Mpc; the long-dashed line shows this same power-law model including the effect of a 510 km s^{-1} LBG velocity dispersion.*

$\gamma = 1.8$ power-law model (dotted line), but also show here the predicted $\xi(s)$ assuming this same intrinsic level of clustering but including the effects of the LBG velocity dispersion (dashed line). This dispersion is taken to be $\Delta v = 510$ km s^{-1}, comprising 450 km s^{-1} for the LBG redshift measurement error, 200 km s^{-1} outflow velocity error and 140 km s^{-1} intrinsic velocity dispersion. The first two errors are estimated by Bielby et al. (2010) and the latter value comes from simulations by Tummuangpak et al. (in prep.). These errors combine in quadrature to give the total $\Delta v = 510$ km s^{-1} dispersion.

Fig. 7.2 shows that redshift errors reduce the measured amplitude as the clustering signal is smoothed out. It is clear from the figure that this is expected to be particularly significant at $s \lesssim 2\ h^{-1}$ Mpc, and including this effect in the model yields a better fit to both our data and da Ângela et al.'s result at these small separations.

However, the model does not appear to account for the reduced clustering strength we measure at $2 < s < 6\ h^{-1}$ Mpc. Bielby et al. showed that even with extremely large assumed redshift errors ($\Delta v = 1000$ km s^{-1}) and a broken power-law model, these low $\xi(s)$ values at intermediate separations are difficult to explain, and suggest that statistical

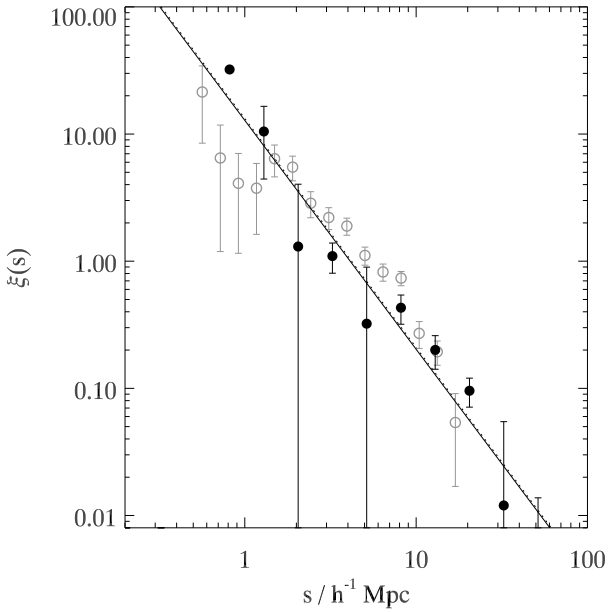

FIGURE 7.3: *Autocorrelation of LBGs with high redshift quality parameters. Symbols are as in Fig. 7.2. The dotted line shows the best fit to da Ângela et al.'s result, a power-law with* $\gamma = 1.8$ *and* $r_0 = 4.2\ h^{-1}$ *Mpc; the solid line shows the best fit to our data, a power-law with* $\gamma = 1.8$ *and* $r_0 = 4.12\ h^{-1}$ *Mpc.*

fluctuations in LBG clustering may be responsible, with their LBG sample potentially having a lower-than-average clustering amplitude.

However, LBG redshift errors are likely to be the largest cause of error in our $\xi(s)$ and may yet be the cause of the discrepant clustering measurement at $2 < s < 6\ h^{-1}$ Mpc. We can investigate this hypothesis here by measuring $\xi(s)$ for only those LBGs with high ID quality parameters, since these sources are expected to have lower redshift measurement errors (§6.6). This is a more feasible approach now than it was for Bielby et al., since the sample is now twice as large.

Fig. 7.3 shows $\xi(s)$ calculated using only the sources with $Q \geq 0.5$ for the sample presented in this thesis or $Q \geq 0.6$ for the sample presented by Bielby et al. Given the differently defined quality parameters, these two criteria are broadly consistent with one another: in each case they reduce the LBG sample size by approximately half. The figure shows that using these high-quality LBGs only, the measured $\xi(s)$ is in excellent agreement with the previous measurement of da Ângela et al.

A chi-square analysis of the result from our high-quality sample in Fig. 7.3 yields a clustering amplitude of $r_0 = 4.12 \pm 0.31\ h^{-1}$ Mpc, assuming a power-law with $\gamma =$

1.8. This model fits the data well, with $\chi^2_{\rm reduced} = 1.11$. This amplitude is in excellent agreement with the value of $4.20^{+0.14}_{-0.15}\ h^{-1}$ Mpc, given by Bielby et al. (2010) as the best-fit to the $\xi(s)$ measured by da Ângela et al. (2005), and also agrees with the values of $r_0 = 4.48^{+0.09}_{-0.14}\ h^{-1}$ Mpc, $\gamma = 1.76^{+0.08}_{-0.09}$ found by da Ângela et al. (2005), and $r_0 = 3.96 \pm 0.15$ h^{-1} Mpc, $\gamma = 1.55 \pm 0.29$ found by Adelberger et al. (2003).

We have therefore found that the LBGs in our survey with the most robust redshifts confirm previous measurements of the $z \approx 3$ LBG clustering amplitude, but we have also found an indication that the LBG sample as a whole may suffer from large redshift errors at low ID qualities. In the next section, we explore this directly to better constrain the redshift errors.

7.3 Redshift errors

Uncertainties in our measured LBG redshifts may be the primary source of errors in our clustering measurements. Bielby et al. (2010) suggest that the largest component of the redshift error comes from uncertainty in fitting the Lyα emission line. From a series of mock spectra with Gaussian random noise, they estimate that this measurement error is typically 450 km s^{-1}.

Here, we extend the investigation into the redshift errors in our survey by using duplicate redshift measurements. The fields presented in Chapter 6, particularly Q2348, were designed with overlapping regions and consequently there are some LBG candidates which were observed in more than one mask. In cases where these duplicated targets are confirmed as LBGs, this provides two independent redshift measurements for the same LBG, and thus a direct observational test of the redshift measurement accuracy.

Fig. 7.4 shows the Δz distribution for the LBGs with duplicate observations, where $\Delta z = |z_1 - z_2|$ is the difference between the two redshift measurements. 20 objects were classified as LBGs in two separate observations; of these, Fig. 7.4 indicates that 16 had fairly small errors of $\Delta z < 0.02$ (of which 13 had very small errors of $\Delta z < 0.005$), while 4 had considerably larger errors. In addition to these 20 objects, we have also searched a region of our Q0302 field which overlaps with Steidel et al.'s (2003) survey for any LBGs which were identified in both surveys: we find 3 such objects, and the redshift differences for these galaxies are also indicated in Fig. 7.4.

The standard deviation of the 20 Δz values measured for duplicate observations in

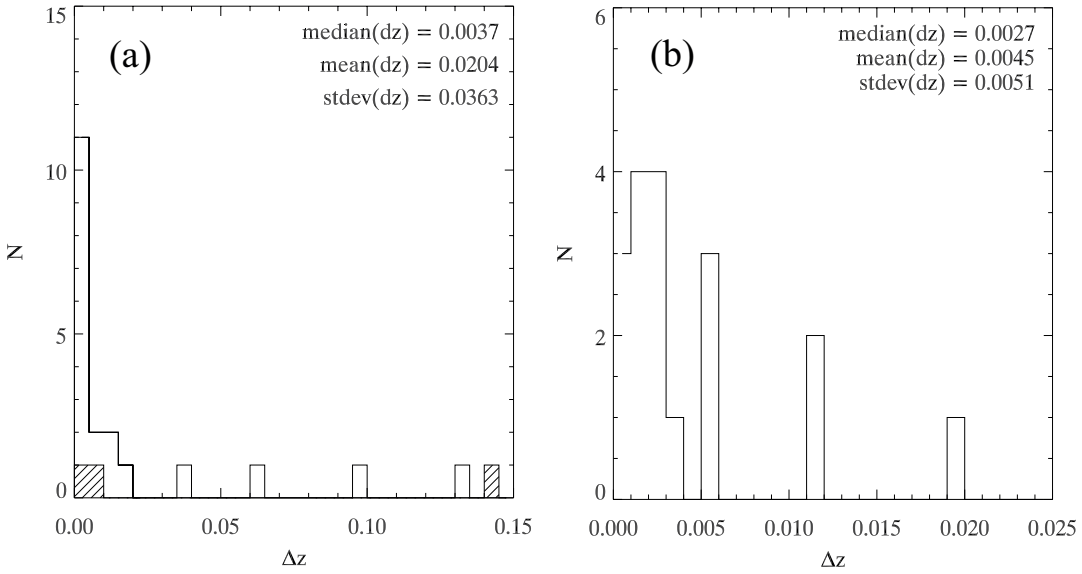

FIGURE 7.4: *The distribution of redshift measurement errors, Δz, calculated using the LBGs which were observed twice in our survey and therefore have two independent redshift measurements. In panel* (a) *we show the full distribution, in panel* (b) *a close-up of the distribution at $z < 0.025$. Overplotted as a hashed histogram in panel* (a) *are the Δz values for 3 sources in our survey which had a redshift in the survey of Steidel et al. (2003).*

our survey is $\sigma = 0.036$, corresponding to a velocity error of ≈2,800 km s^{-1} assuming a redshift of $z = 2.8$, the sample mean. However, this misrepresents the true error in our redshift measurements, since it is skewed by the 4 sources with very high Δz. These 4 values do not represent redshift *measurement* errors. The measurement error is the uncertainty associated with locating the exact peak of the Lyα line due to noise in the spectrum. In the cases where we find large Δz values, the error does not arise due to uncertainty in the peak wavelength, but in uncertainty over which spectral feature is actually Lyα. In these cases, different spectral features have been identified as Lyα, leading to large Δz. These are therefore better characterised as *identification* errors, in that two different solutions have been reached in the two observations.

For the 16 duplicated targets shown in Fig. 7.4*b*, the same feature has been identified as Lyα and therefore the Δz for these objects gives an indication of the measurement error. The standard deviation for these objects is $\sigma = 0.005$, corresponding to $\Delta v = 400$ km s^{-1}, comparable to the value of 450 km s^{-1} estimated by Bielby et al. (2010).

The suggestion, therefore, is that ≈80% of our LBGs have redshift measurement errors of $\Delta v \leq 400$ km s^{-1}, while the other 20% may have larger errors. This problem, however, disproportionately affects sources with an ID quality parameter $Q = 0.4$: of

the four sources with large Δz, one was given a quality factor of 0.4 for both redshift measurements, while the other 3 have one measurement with $Q = 0.4$ and another with $Q = 0.5$; in the latter cases the $Q = 0.5$ measurement is fairly robust while the $Q = 0.4$ measurement is less reliable. Therefore, the LBGs which may suffer from large errors can be excluded by removing the $Q = 0.4$[1] LBGs from the sample. We have seen previously that this yields a significant improvement in the measured LBG autocorrelation.

7.4 Galaxy feedback

7.4.1 QSO sightlines

QSO sightlines are a powerful probe of the IGM, primarily due to the Lyman alpha forest. Clouds of neutral hydrogen along the line-of-sight to a distant quasar cause Lyα absorption in the QSO spectrum. This occurs at 1216Å in the rest-frame of the hydrogen cloud. Since the cloud is necessarily at lower redshift than the quasar itself, the absorption appears shortward of 1216Å in the QSO's rest frame. Therefore the combination of many Lyα absorption systems at many different redshifts along the sightline produces a series of absorption lines in the spectrum shortward of the QSO's Lyα λ1216 emission: this is called the Lyα forest.

The Lyα forest therefore provides a map of the intergalactic medium between the quasar and the Earth, with each individual Lyα absorption line revealing the location of a hydrogen cloud by its redshift. More than this, the strength of the absorption line (its equivalent width) reveals the amount of neutral hydrogen present — where the IGM hosts a large amount of gas, the Lyα line will have a high equivalent width.

This is best expressed in terms of the Lyα *transmissivity*, defined according to Eqn. 7.6:

$$T = \frac{f}{f_{\rm c}} \tag{7.6}$$

where f is the measured flux level and $f_{\rm c}$ is the continuum flux level (i.e., the flux which would be observed if no absorption were present) at that wavelength. Where the Lyα transmissivity is high, the IGM contains little neutral hydrogen; where it is low, a high density exists.

[1] we reiterate that in Bielby et al.'s fields this is equivalent to $Q = 0.5$

Calculating T across the Lyα forest requires a measure of $f_{\rm c}$, the quasar continuum. Our method here follows that of Young et al. (1979) and Carswell et al. (1982). The QSO spectrum is first divided into wavelength intervals, in which the mean and standard deviation of the observed flux are calculated. A sigma-clipping process is then employed to iteratively reject the most aberrant pixels, until the remaining pixels show a roughly Gaussian distribution; the mean flux of these pixels is then taken to be the continuum level in that wavelength bin. Finally, a cubic spline interpolation across the bins gives a continuum level for the entire spectrum. This continuum fitting procedure was performed by N. Crighton.

We use two sets of quasar spectra in our analysis: a high-resolution sample and a low-resolution sample. The observations and data reduction for these QSOs are described by Crighton et al. (2010). The low-resolution spectra were acquired with the AAOmega spectrograph on the Anglo-Australian telescope and have a resolution of ≈ 130 km s^{-1}, while the high-resolution spectra come from the Keck telescope and reach 6–8 km s^{-1} resolution (Crighton et al., 2010). In Fig. 7.5 we show examples of both high- and low-resolution spectra, illustrating well the difference in resolution between the two. The spectra in Fig. 7.5 also clearly show both the nature of the Lyα forest and the results of the continuum fitting method we employ.

Damped Lyα absorbers (DLAs), systems with hydrogen column densities $> 10^{20}$ cm^{-2}, produce Lyα absorption lines with highly broadened wings. It is therefore important to mask DLA absorption features out of the spectra, since the broad wings would introduce a significant error when inferring the neutral hydrogen distribution along the sightline from the measured Lyα transmissivity.

We note also that we only use the quasar spectral range between Lyβ and Lyα, since shortward of Lyβ it is impossible to isolate the Lyα forest from the Lyβ forest, and therefore to determine the redshift of a given absorption line.

Using the method outlined here, we are therefore able to use our sample of QSO spectra to infer the gas density of the intergalactic medium along the quasar sightlines. By cross-correlating this information with the positions of our LBG sample, we can attempt to measure the interactions between galaxies and the IGM at high redshift.

7.4.2 Lyα–LBG cross-correlation method

We cross-correlate our LBGs with the IGM Lyα transmissivity by measuring the mean transmissivity of the Lyα forest as a function of separation s from the LBG positions. In

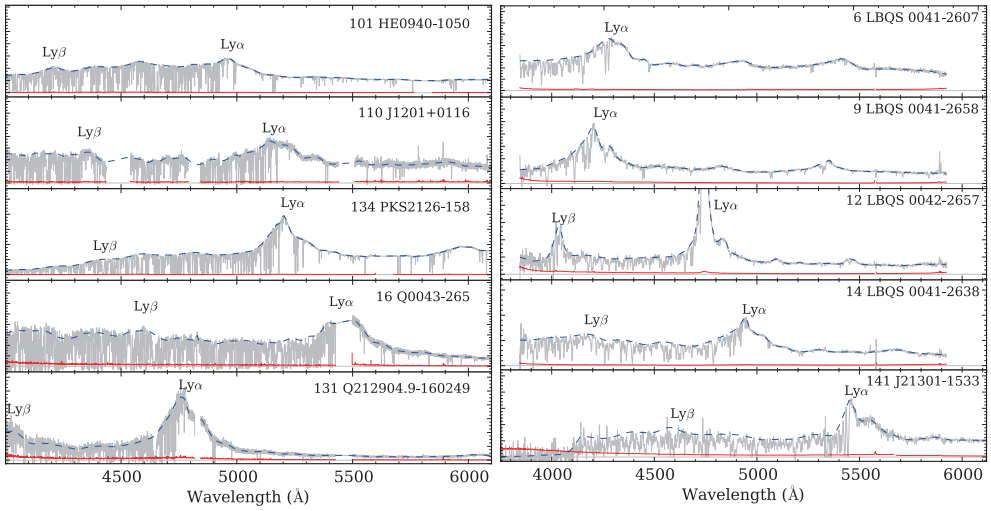

FIGURE 7.5: *Examples of quasar spectra used to measure the Lyα forest. The left column shows high-resolution Keck spectra; the right, low-resolution AAOmega spectra. The Lyα forest is the series of closely packed absorption lines at wavelengths shortward of the QSO's Lyα emission; these features are far better resolved in the Keck spectra. The blue dashed line shows the continuum fitted as described in the text, the red line shows the 1σ error per pixel. Blank regions have been masked out due to artefacts or the presence of DLAs. Figure adapted from Crighton et al. (2010)*

practice this is done by defining a bin size Δs and calculating the average transmissivity in concentric spherical shells enclosed by radii s and $s + \Delta s$; we use $\Delta s = 0.5\ h^{-1}$ Mpc, following Adelberger et al. (2003, 2005) and Crighton et al. (2010).

We normalise the resulting correlation function for each quasar such that the mean measured transmissivity between 10 and 20 h^{-1} Mpc is $\bar{T} = 0.76$. This is the global mean transmissivity at $z \approx 3$ as measured by Adelberger et al. (2003, 2005); we use the transmissivity at $10 < s < 20\ h^{-1}$ Mpc because the LBGs are unlikely to affect the ISM at such large separations and therefore we can expect that $\bar{T}$ here should be equal to the global $\bar{T}$ value.

By normalising the result for each quasar in this way we counteract some of the uncertainty in the continuum fitting process. Absorption lines in Lyα forest have some width, and therefore two lines very close to each another may overlap a little the observed spectrum. This can give the impression of an overall lower continuum, which produces an error in the measured transmissivity. Scaling the Lyα–LBG cross-correlation for each QSO is equivalent to correcting the continuum level up or down, such that it fits the expected $\bar{T}$ over large scales. The drawback is that we are not accounting for the

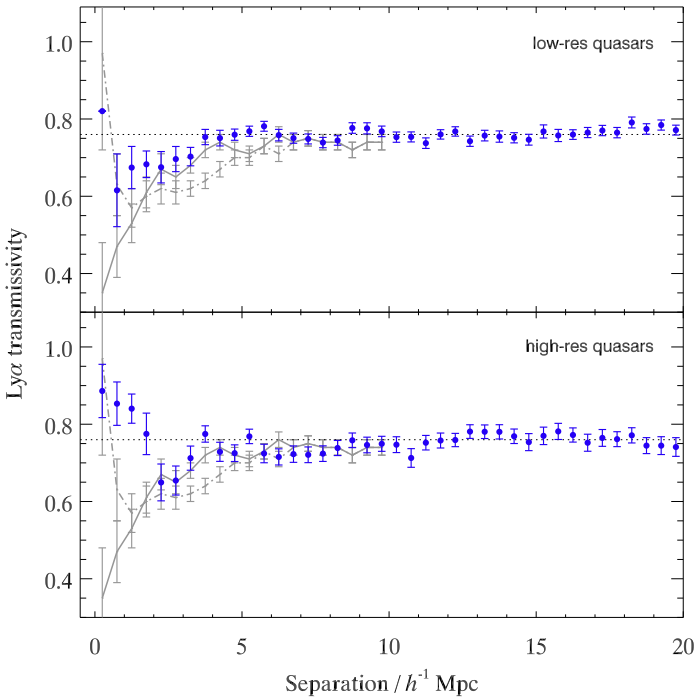

FIGURE 7.6: *Lyα–LBG cross-correlation showing the Lyα transmissivity of the IGM at a given separation s from LBG positions. Blue circles show our results, with LBG–LBG error bars. Previous results from Adelberger et al. (2003; dash-dot grey line) and Adelberger et al. (2005; solid grey line) are also shown. The dotted horizontal line marks the global mean transmissivity, $\bar{T} = 0.76$. The upper panel shows the results using low-resolution quasars, the lower panel high-resolution quasars.*

redshift evolution of the mean ISM transmissivity across the redshift range probed by each QSO's Lyα forest (e.g. McDonald et al., 2000), which we estimate could introduce an error of $\approx 10\%$ on our cross-correlation measurements.

Finally, we combine the scaled cross-correlation results from each QSO in order to give a combined Lyα–LBG cross-correlation for the full sample. We measure LBG–LBG errors for each bin, given by the standard error on the different measurements for all LBGs contributing to that bin.

7.4.3 Results

Fig. 7.6 shows the results of our cross-correlation for both the high-resolution and low-resolution quasars. The results are compared to those of Adelberger et al. (2003, 2005). Adelberger et al. (2003) measured a significant reduction in the transmissivity at $s < 5$ h^{-1} Mpc, but with an apparent upturn at ≈ 0.5 h^{-1} Mpc. Adelberger et al. (2005) also

found that the transmissivity decreases within 5 h^{-1} Mpc, but measured no small-scale increase.

Our result from the low-resolution QSOs is generally in good agreement with the previous findings. We detect a significant reduction in transmissivity within 4 h^{-1} Mpc of Lyman-break galaxies. The transmissivity here is not found to be as low as was measured by Adelberger et al. (2003), but is broadly consistent with Adelberger et al.'s (2005) result. In common with Adelberger et al. (2003), however, we do measure an increase in T at 0.5 h^{-1} Mpc, however since this point is based on a single LBG (and hence has no LBG–LBG error in the figure), it cannot be regarded as significant.

The cross-correlation with the high-resolution quasars is somewhat different. At $2 < s < 5\ h^{-1}$ Mpc, we measure a strong decrease in T in excellent agreement with Adelberger et al.'s (2005) measurement, however at $s < 2\,h^{-1}$ Mpc we find a progressive increase in Lyα transmissivity. The first 4 bins, where this increase is measured, have respectively 2, 6, 8 and 11 LBG–Lyα pairs, so the measurement of a small-scale increase here is more robust than the single point in the low-resolution result.

The effect of redshift errors

As before, LBG redshift errors are a possible cause of error in the Fig. 7.6 results. We have repeated the analyses using only the high-quality LBG sample and find no significant change to our results here. However, we can quantify the effect of redshift errors using mock LBG catalogues.

We take the full LBG catalogue used in our cross-correlation and apply Gaussian noise to the LBG redshifts. Following our findings in §7.3, we use two Gaussian distributions, the first representing the redshift measurement error, the second what we called the 'identification error'. For each LBG, a measurement error Δz is drawn from a Gaussian with $\sigma_z = 0.0051$, corresponding to $\Delta v \simeq 400$ km s^{-1}. For a randomly selected $1/5$ of LBGs, an additional identification error is assumed: this is drawn from a Gaussian with $\sigma_z = 0.0402$, the standard deviation measured for the 4 LBGs with identification errors in Fig. 7.4.

The resulting Δz distribution is shown in Fig. 7.7*a* (*cf.* Fig. 7.4*a*). These Δz values are added to the measured LBG redshifts to construct the mock catalogue, which has a redshift distribution as shown in Fig. 7.7*b*.

We use this method to generate 50 different mock catalogues, each of which we cross-correlate with the Lyα transmissivity. The standard deviation of these 50 results provides

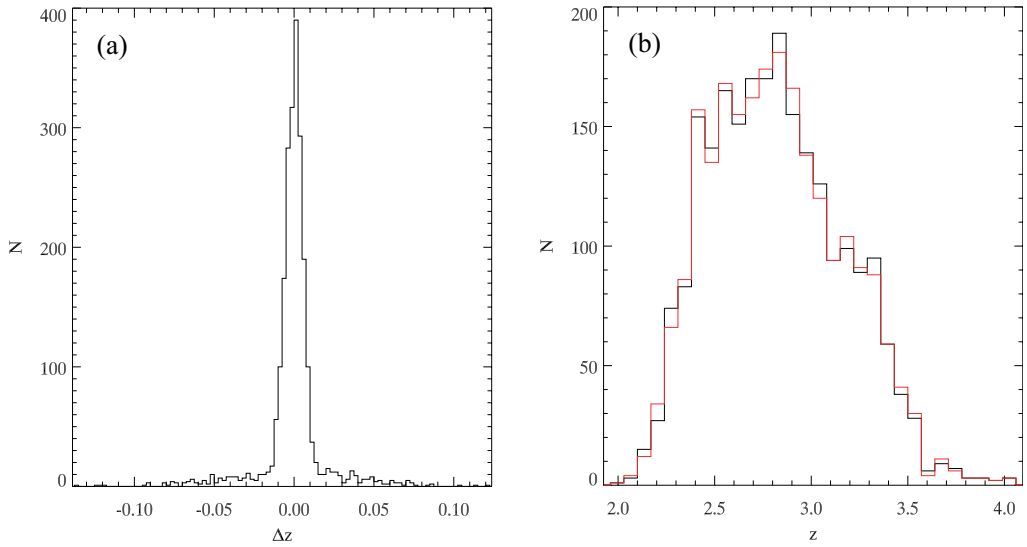

FIGURE 7.7: *Redshift errors used to generate mock LBG catalogues.* (a) *The distribution of Δz values added to LBG redshifts, drawn from a double-Gaussian distribution as described in the text.* (b) *The resulting redshift distribution of the mock catalogue (red) compared to that of the actual data (black).*

an estimate of the uncertainty on the cross-correlation measurement in Fig. 7.6 arising due to redshift errors. In Fig. 7.8 we show our results again, this time with the redshift-error uncertainties.

Fig. 7.8 shows that, as expected, the high transmissivity measured at $s = 0.5\ h^{-1}$ Mpc with the low-resolution quasars is not significant. Since this point is based on just one LBG–Lyα pair, the redshift error on this single LBG can result in a very large range of transmissivities. However the rest of the correlation function, where ≥ 10 LBGs contribute to each bin, is fairly robust to redshift errors. In the high-resolution result, the uncertainty has increased quite significantly on all of the first 4 bins, such that they now appear consistent with the global mean transmissivity, but these points nevertheless remain different to Adelberger et al.'s (2005) result at $\gtrsim 3\sigma$ significance.

Transmissivity models

The result of Adelberger et al. (2005) is found to be well described by a power-law model in which the transmissivity goes as $T = 0.77 - (0.3/s)$, where the separation s is in units of h^{-1} Mpc. In Fig. 7.9 we show this model compared to the observational data out to 10 h^{-1} Mpc. However, the redshift measurement errors as well as the intrinsic velocity dispersion of the LBGs will smooth this power-law out, particularly at low separations.

We therefore also show in Fig. 7.9 the predicted cross-correlation once this velocity

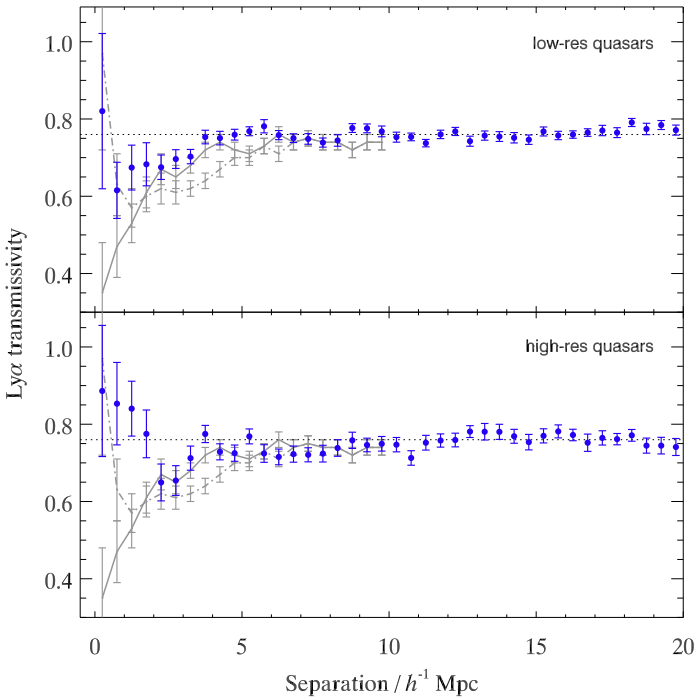

FIGURE 7.8: *As for Fig. 7.6, but now showing uncertainties on the cross-correlation due to LBG redshift errors.*

dispersion is included in the $T = 0.77-(0.3/s)$ model. We have again assumed $\Delta v = 510$ km s^{-1}, as described previously.

Adelberger et al. (2003) suggested that the upturn in the correlation function that they detected at $s < 1\ h^{-1}$ Mpc could indicate a region of high transmissivity around LBGs. We therefore show 2 additional models in Fig. 7.9, which include not only the 510 km s^{-1} velocity dispersion but also the effect of a region with $T = 1$ around each LBG. The dashed red line shows the prediction when this region extends to 0.5 h^{-1} Mpc, the solid red line 1.5 h^{-1} Mpc.

The cross-correlation we measure for low-resolution quasars agrees very well with the expectation of the model which does not include any transmissivity spike (but does include the velocity dispersion effects), but neither of the models with such a spike are rejected. The figure shows that a $T = 1$ spike of size 0.5 h^{-1} Mpc produces a negligible difference from the model without it, and could never be conclusively detected with errors as large as ours or Adelberger et al.'s. A larger 1.5 h^{-1} Mpc transmissivity spike is predicted to produce a more significantly different correlation function, but is still not ruled out by our low-resolution measurement.

In our high-resolution result, the 1.5 h^{-1} Mpc transmissivity spike model is the favoured

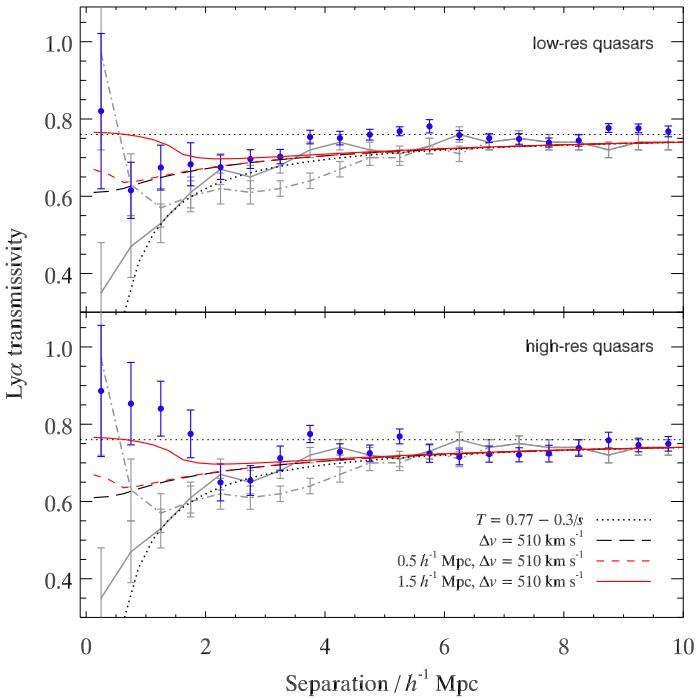

FIGURE 7.9: *Lyα–LBG cross correlation compared to transmissivity models. Blue points and grey lines are as for Fig. 7.6. Four models are shown, as indicated in the figure legend.*

solution, showing a fairly good fit to our data. We note that assuming a velocity dispersion smaller than 510 km s^{-1} would improve the fit further, since there would be less smoothing out of the correlation signal and thus the predicted transmissivity would be higher. However, the model with no $T = 1$ spike is only rejected at the $\approx 2\sigma$ level, and our high-resolution result is based on only 7 QSOs (compared to 35 low-resolution quasars), so any conclusion here is tentative.

In Fig. 7.10 we show the correlation measured for the combined quasar sample, i.e. both the low- and high-resolution sources. As in the case of the high-resolution sample alone, the basic model with no transmissivity spike is not formally rejected, but nevertheless the best fit is clearly found for the model with a 1.5 h^{-1} Mpc spike.

The biggest problem with the 1.5 h^{-1} Mpc spike model is that it is rejected by Adelberger et al.'s (2005) result at $\approx 3\sigma$ significance. Crighton et al. (2010) show that both the Adelberger et al. (2003) and the Adelberger et al. (2005) measurements are consistent with a $T = 0.77 - (0.3/s)$ model convolved with a velocity dispersion of 150 km s^{-1}, smaller than the Δv assumed for our sample by virtue of the improved resolution of the Keck telescope (which was used for their LBG observations) relative to the VLT. Since our observations are consistent (within 2σ) with the same intrinsic model convolved with a

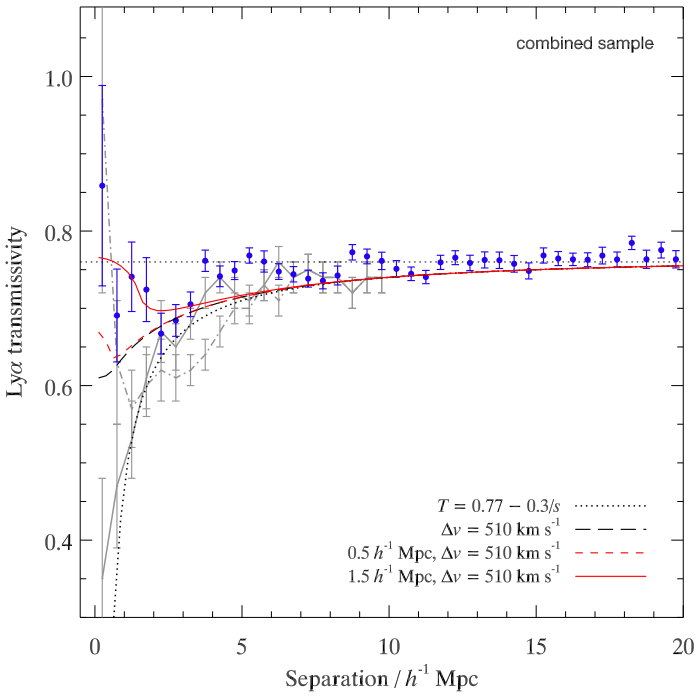

FIGURE 7.10: *As for Fig. 7.9, but for the combined sample of both low- and high-resolution quasas.*

larger 510 km s^{-1} dispersion, this may provide the best simultaneous explanation for all the datasets presented in Fig. 7.9, but the favoured model for our data remains the 1.5 h^{-1} Mpc transmissivity spike.

7.5 Discussion

The interaction between galaxies and the IGM on scales $< 2\ h^{-1}$ Mpc remains uncertain, with our high-resolution QSO result suggestive of a large region of high transmissivity around LBGs, Adelberger et al.'s (2005) result suggesting increasingly low transmissivity toward LBG positions, and our low-resolution result not rejecting either of these hypotheses.

If a Lyα transmission spike were to exist at small separations from LBGs, this would indicate that the neutral hydrogen which naturally falls into the overdense regions where galaxies form is being ionised, or else is being expelled from the galaxies' immediate environment, over $\sim 1\ h^{-1}$ Mpc scales. The most likely explanation for this would be high-velocity, supernova-driven galactic winds. An observational detection of this phenomenon in high-z star-forming galaxies would be extremely significant, as these super-

winds are thought to be the mechanism by which the IGM is heated and enriched with metals (§1.2.2).

As it stands, the observations presented here are unable to give an unambiguous indication as to whether this process is occurring. Two key improvements would make a conclusive result more possible. The first is a increase in the number of LBGs lying very close to QSO sightlines. In our low-resolution quasar sample only one LBG (of > 2000) lay in our smallest separation bin; in the high-resolution sample, there were 2. As a result, even small errors in the LBG redshift can affect the result dramatically (Fig. 7.8), and even if no such error existed, it is not clear that a result based on just a few LBGs would be representative of the galaxy population as a whole.

We are embarking on a large program of observations to increase the number of spectroscopically confirmed LBGs in our sample by a factor of 10. This is primarily aimed at measuring baryon acoustic oscilliations at $z \approx 3$ via LBG clustering, however by observing QSOs in the fields we will also significantly increase the number of LBGs close to quasar sightlines and therefore improve the statistics in our cross-correlation.

The second key improvement would come from an increase in redshift measurement accuracy. The smoothing effect of large redshift errors on the cross-correlation is significant, and makes it hard to distinguish between different models. A possible way to achieve this would be to move from identifying LBGs by eye to an automated template-fitting procedure; indeed, if a large survey to identify $\sim 10^4$ LBGs is to be undertaken, this may be essential. Improved errors could make it easier to confirm or reject the 1.5 h^{-1} Mpc transmissivity spike model, but Crighton et al. (2010) show that even a small velocity dispersion of $\Delta v \simeq 150$ km s^{-1} can hamper the measurement of a 0.5 h^{-1} Mpc spike.

7.6 Summary

Using the sample of $z \approx 3$ LBGs from the survey described in Chapter 6 (combined with the sample previously presented by Bielby et al.) we have investigated the clustering and feedback of galaxies at $z \approx 3$. Our conclusions follow.

- Using our high-quality LBG sample, which has the most robust redshifts, we measure an LBG clustering amplitude of $r_0 = 4.12 \pm 0.31$ h^{-1} Mpc, assuming a power-law with $\gamma = 1.8$, in excellent agreement with previous measurements.

- The redshift measurement error on our LBGs is $\Delta z = 0.005$, corresponding to $\Delta v = 400$ km s^{-1} at $z = 2.8$, the mean redshift of our sample. In $\approx 20\%$ of sources (specifically in those with low ID quality parameters), a larger error may arise due to misidentification of the Lyα feature.

- We find evidence for a drop in Lyα transmissivity within 4 h^{-1} Mpc of our Lyman-break galaxies, indicating an increase in the amount of neutral hydrogen in the IGM around high-z galaxies. This is expected given that galaxies form in over-dense regions of the universe. Our results here are broadly in line with previous measurements by Adelberger et al. (2003, 2005).

- At smaller scales, below 1–2 h^{-1} Mpc, our results suggest an increase in Lyα transmissivity, suggestive of an envelope in which the LBG has ionised or expelled intergalactic material, likely due to superwinds. However, our results here are also statistically consistent with no such increase.

- An increase in the number of LBGs detected close to QSO sightlines and an improvement in redshift measurement errors may elucidate the question of whether $z \approx 3$ LBGs show evidence for this large-scale feedback.

VIII

Conclusions

This thesis has explored contemporary issues in studies of galaxy evolution, addressing in particular the role played by AGN in the high-redshift universe, the extent to which simple luminosity evolution may explain our observations of galaxies, and the interactions of high-redshift galaxies with their environment. In this final chapter, we review and summarise our findings.

8.1 Galaxies and AGN in the FIR and sub-mm

In Chapter 4 we investigated the predictions of simple galaxy evolution models in the mid-IR, far-IR and sub-mm. We considered a pure luminosity evolution model, in which galaxy evolution is driven only by a decreasing star-formation rate rather than a hierarchical process of merging. Our model, though simplistic, has been used with considerable success to model the number counts, redshift distributions and colours of galaxies throughout the optical and near-IR bands (Metcalfe et al., 1995, 2001, 2006; McCracken et al., 2006).

In the mid-IR, where dust emission takes over from star-formation as the primary source of flux (a change which we find occurs at $\lambda \approx 5$–6 μm), our model showed broadly good agreement with observations, even with a fairly schematic prescription for the dust spectrum. A population of galaxies with a mid-IR excess due to warm dust, likely residing in PDR regions, was found to be a necessary component at $\geq 24\mu$m, but this population was included only at the level seen in local galaxies (Draine et al., 2007), and therefore the inclusion of this component remains true to our backward-evolution approach.

At sub-mm wavelengths ($\lambda \geq 250\mu$m), our PLE model accounts for only a few per

cent of sources. The principal sub-mm bands are at 250, 350, 500 and 850μm, and in all of these wavebands the number counts are steep, suggesting strong evolution (Scott et al., 2006; Coppin et al., 2006; Pantanchon et al., 2009; Weiß et al., 2009; Béthermin et al., 2010b; Clements et al., 2010; Oliver et al., 2010). One explanation for this is a strongly evolving starburst population, which can be modelled by appealing to a top-heavy IMF (Baugh et al., 2005; Lacey et al., 2008), but we have shown that a viable alternative is to include a population of obscured AGN.

Using the Gunn & Shanks (1999) model of obscured AGN, we showed in Chapter 4 that AGN can give a reasonable fit to number counts and a good fit to redshift distributions (matching the observed bimodality) across the 250–500μm range. This result built upon our findings in Chapters 2–3, which focussed on the 870μm band.

In Chapter 2 we used deep, wide-field observations of the ECDFS at both X-ray and sub-mm wavelengths to make observational measurements of the AGN contribution to the sub-mm. We presented the most significant detection to date of a cross-correlation between X-ray AGN and 870μm LABOCA sources. Measuring the sub-mm background associated with AGN at different X-ray fluxes, luminosities and column densities, we determined key observational constraints for an AGN model.

In Chapter 3, therefore, we compared the predictions of our obscured AGN model to the measurements made in Chapter 2. We found that the model, constrained to match the 1.5 ± 0.1 Jy deg^{-2} sub-mm background measured for X-ray-detected AGN, simultaneously matched the full 870μm number counts. An important caveat here is that our model assumes a non-unified scenario, in which more obscured AGN are brighter in the sub-mm than less obscured AGN. The strongest contribution to the sub-mm population, therefore, comes from those AGN which are Compton-thick and thus absent from our X-ray sample.

The unified AGN model (Antonucci, 1993) provides an extremely elegant description of the various classes of active galaxy observed in the universe, and remains the standard model for AGN. However, sub-mm observations in particular have offered increasing observational evidence in favour of a non-unified paradigm in which obscured AGN are preferentially brighter in the sub-mm (Page et al., 2004; Priddey et al., 2007; Martínez-Sansigre et al., 2009; Rigopoulou et al., 2009). In Chapters 2 and 5 we performed stacking analyses of AGN at different levels of obscuration, in the ECDFS and WHDF respectively. In both cases, we found evidence for a stronger contribution from the more obscured AGN, with neutral hydrogen column densities of $N_{\rm H} > 10^{22}$ cm^{-2}. In

Chapter 3 we showed that the ECDFS measurements were in excellent agreement with the non-unified model prediction. If it is the Compton-thick AGN which are brightest in the sub-mm, this can also explain the apparently low X-ray fluxes of sub-mm galaxies, as well as the observation that their mid-IR spectra show PAH features comparable with starburst galaxies, since heavily obscured AGN are known to have PAH spectra resembling starbursts (Clavel et al., 2000; Pieters, Spoon & Tielens, 2004).

Therefore, our results show that the combination of a simple galaxy model and an obscured AGN model, both extrapolated back to high redshift from observations of the local universe assuming pure luminosity evolution, provides a relatively good fit to observations all the way from the X-ray to the submillimetre (covering more than 5 decades in wavelength), and out to at least $z \sim 3$, providing a model for the sub-mm-bright sources which avoids the need to introduce a population of ultraluminous starbursts. In the context of a ΛCDM cosmology, this removes the need to invoke a top-heavy IMF for high-redshift starburst galaxies (see §8.3 below).

8.2 The interaction of galaxies and the IGM at high redshift

In Chapter 6 we presented a survey of Lyman-break galaxies at $z \approx 3$, covering the imaging, candidate selection and spectroscopic follow-up of targets. We contrasted the separate selection methods used for fields with UBR and ugr photometry, noting that our ugr-selected LBGs were found to come closer to the nominal $z = 3$ target of the survey, but also that the ugr selection suffered from greater contamination from Galactic stars. We produced composite LBG spectra, for the galaxies showing Lyα both in emission and in absorption. For LBGs where Lyα was found in emission, we measured a 615 ± 584 km s^{-1} offset between the redshift measured for Lyα and that measured for the ISM absorption lines.

This offset, consistent with previous measurements, reveals the presence of galactic outflows, with a shell of material effluxing from the galaxy giving rise to different redshifts for different lines (§1.2.2). In Chapter 7 we used our LBG sample to investigate whether galactic outflows may affect the intergalactic medium on megaparsec scales.

The distribution of hydrogen in the IGM was determined using the Lyα forest in the spectra of high-redshift quasars. This 'forest' is a series of Lyα absorption lines in the QSO spectrum, the wavelengths of which can be used to determine where along the quasar line-of-sight a significant amount of neutral hydrogen exists. We cross-correlated

the inferred neutral hydrogen densities with the location of known LBGs, to measure the effect galaxies have on the IGM around them.

We find clear evidence for an increase in the amount of neutral hydrogen within 4 h^{-1} Mpc of LBGs, manifested by a drop in the Lyα transmissivity. Since galaxies form where the dark matter distribution is overdense, it makes sense to expect that the IGM will also show increased density around galaxies, as the gas is drawn gravitationally into the deep potential wells at these points. We find that our results are consistent, given the velocity dispersion on our LBG redshifts, with a Lyα transmissivity which goes as $T = 0.77 - (0.3/s)$, where s is the separation in h^{-1} Mpc between the LBG and the quasar sightline. The results of Adelberger et al. (2003, 2005) and Crighton et al. (2010) also show agreement with this model, and the shape of this power-law may therefore provide a key observational test for hydrodynamical simulations of galaxy evoltion.

Our results have also indicated the presence of a megaparsec-scale spike in the Lyα transmissivity around LBGs. This suggests significant feedback from these galaxies, creating an envelope around them in which the neutral hydrogen has been ionised or swept away, presumably due to supernova-driven winds. This would be an important result for our understanding of supernova feedback and its relationship to galaxy evolution. We presented results using both a high-resolution and a low-resolution quasar sample, and while the low-resolution QSOs produced an inconclusive result regarding this small-scale effect, the high-resolution quasars (and the combined sample) appeared to favour the presence of a transmissivity spike of radius 1.5 h^{-1} Mpc. On the other hand, Adelberger et al.'s (2005) result heavily disfavours this model.

Improvements in the LBG redshift accuracy, potentially through template fitting, and in the number of LBG–sightline pairs will be important to providing more precise constraints on LBG–IGM interactions. We are therefore embarking on a significant extension to our survey LBGs and QSOs; this should enable us to further address this topic in the future.

8.3 Coda

The standard model of cosmology holds that $\approx 70\%$ of the mass-energy density of the universe is comprised of an as yet undetected 'dark energy'. The other $\approx 30\%$ is matter, the majority of which consists of cold dark matter — massive particles which are thought to be ubiquitous throughout the universe but do not reflect light. Only 4% of the total

mass-energy consists of baryonic matter, though this makes up the entirety of the visible universe. Simulations within this standard ΛCDM cosmology have shown that the dark matter collapses into halos of different masses, which then grow by merging. Baryons interact gravitationally with the dark matter, and so are drawn to the centre of halos. As the halos merge, galaxies grow hierarchically and this drives their evolution.

At several points in this thesis we have discussed some of the issues faced by this model, especially those relating to how a hierarchical model can account for large populations of massive galaxies at high redshifts, but we have noted also that at least partial solutions to many of these problems have been found. To explain the presence of sub-mm galaxies, which many observers have suggested are a population of very massive, ultraluminous starbursts, at high redshifts, some authors (e.g. Baugh et al., 2005; Lacey et al., 2008) have appealed to a top-heavy IMF for starburst galaxies. However, while this provides a good fit in the FIR and sub-mm, it fails to match observations at lower redshift in the K band.

Our results have shown that the bright sub-mm sources may be a population of obscured AGN rather than ultraluminous starburst galaxies. Crucially, this can remove the need for the top-heavy IMF to be invoked in hierarchical evolution models, avoiding the problems that this IMF introduces in the optical/NIR.

At shorter IR wavelengths we have found a very good fit for our PLE galaxy model, which incorporates none of the hierarchical evolution fundamental to ΛCDM, and this must still be explained, but here feedback processes may be significant in reproducing through hierarchical evolution some of the observations which appear to indicate more passive evolution.

Simulations have indicated that feedback from galaxies and AGN is essential to regulate star-formation in order to match observations of the evolution of galaxies and the IGM. Without these feedback process, star-formation rates are significantly over-predicted at hgh-z. Here again our results can be seen as offering key observational support for the standard model. We find evidence to suggest that the IGM is ionised or underdense within 1.5 h^{-1} Mpc of LBGs, indicative of the galactic superwinds thought to drive the feedback process.

In closing, we suggest that some of the results presented in this thesis may help to address some of the issues and challenges that currently exist in the standard ΛCDM model for the universe.

Bibliography

Abel T., Bryan G. L., Norman M. L., 2002, Sci, 295, 93

Adelberger K. L., Steidel C. C., 2000, ApJ, 544, 218

Adelberger K. L., Steidel C. C., Shapley A. E., Pettini M., 2003, ApJ, 584, 45

Adelberger K. L., Steidel C. C., Shapley A. E., Hunt M. P., Erb D. K., Reddy N. A., Pettini M., 2004, ApJ, 607, 226

Adelberger K. L., Shapley A. E., Steidel C. C., Pettini M., Erb D. K., Reddy N. A., 2005, ApJ, 629, 636

Aird J., Nandra K., Laird E. S., et al., 2010, MNRAS, 401, 2531

Ajello M., Rau A., Greiner J., et al., 2008, ApJ, 673, 96

Akylas A., Georgantopoulos I., Georgakakis A., Kitsionas S., Hatziminaoglou E., 2006, A&A, 459, 693

Alexander D. M., Bauer F. E., Chapman S. C., Smail I., Blain A. W., Brandt W. N., Ivison R. J., 2005, ApJ, 632, 736

Allamandola L. J., Tielens A. G. G. M., Barker J. R., 1985, ApJ, 290, L25

Almaini O., Scott S. E., Dunlop J. S., et al., 2003, MNRAS, 338, 303

Almaini O., Dunlop J. S., Willott C. J., Alexander D. M., Bauer F. E., Liu C. T., 2005, MNRAS, 358, 875

Andreani P., La Franca F., Cristiani S., 1993, MNRAS, 261, L35

Andreani P., Franceschini A., Granato G., 1999, MNRAS, 306, 161

Antonucci R., 1993, ARA&A, 31, 473

Arimoto N., Yoshii Y., 1987, A&A, 173, 23

Arnouts S., Vandame B., Benoist C., et al., 2001, A&A, 379, 740

Babbedge T. S. R., Rowan-Robinson M., Vaccari M., et al., 2006, MNRAS, 370, 1159

Ballantyne D. R., Shi Y., Rieke G. H., Donley J. L., Papovich C., Rigby J. R., 2006, ApJ, 653, 1070

Barger A. J., Cowie L. L., Sanders D. B., Fulton E., Taniguchi Y., Sato Y., Kawara K., Okuda H., 1998, Nature, 394, 248

Barger A. J., Cowie L. L., Steffen A. T., Hornschemeier A. E., Brandt W. N., Garmire G. P., 2001, ApJ, 560, L23

Bauer F. E., Alexander D. M., Brandt W. N., Schneider D. P., Treister E., Hornschemeier A. E., Garmire G. P., 2004, AJ, 128, 2048

Baugh C. M., Cole S., Frenk C. S., Lacey C. G., 1998, ApJ, 498, 504

Baugh C. M., Benson A. J., Cole S., Frenk C. S., Lacey C., 2003, astro-ph/0203051

Baugh C. M., Lacey C. G., Frenk C. S., Granato G. L S. L., Bressan A., Benson A. J., Cole S., 2005, MNRAS, 356, 1191

Baskin A., Laor A., 2005, MNRAS, 358, 1043

Bernardi M., Nichol R. C., Sheth R. K., Miller C. J., Brinkmann J., 2006, AJ, 131, 1288

Bertin E., Arnouts S., 1996, A&AS, 117, 393

Bertin E., Dennefeld M., 1997, A&A, 317, 43

Bethe H., 1939, PhRv, 55, 434

Béthermin M., Dole H., Cousin M., Bavouzet N., 2010a, A&A, 516, 43

Béthermin M., Dole H., Beelen A., Aussel H., 2010b, A&A, 512, 78

Bi H., Davidsen A. F., 1997, ApJ, 479, 523

Bielby R., Shanks T., Weilbacher P. M., et al., 2010, arXiv:1005.3028

Blain A. W., Smail I., Ivison R. J., Kneib J.-P., Frayer D. T., 2002, PhR, 369, 111

Borys C., Chapman S., Halpern M., Scott D., 2003, MNRAS, 344, 385

Borys, C., Scott, D., Chapman, S., Halpern, M., Nandra, K., Pope, A., 2004, MNRAS, 355, 485

Bower R. G., 1991, MNRAS, 248, 332

Bower R. G., Benson A. J., Malbon R., Helly J. C., Frenk, C. S., Baugh C. M., Cole S., Lacey C., 2006, MNRAS, 370, 645

Brown M. J. I., Dey A., Jannuzi B. T., Brand K., Benson A. J., Brodwin M., Croton D. J., Eisenhardt P. R., 2007, ApJ, 654, 85

Bruzual G., 1983, ApJ, 273, 105

Bruzual G., Kron R. G., 1980, ApJ, 241, 25

Bruzual G., Charlot S., 1993, ApJ, 405, 538

Bruzual G., Charlot S., 2003, MNRAS, 344, 1000

Burgarella D., Pérez-González P. G., Tyler K. D., et al., 2006, A&A, 450, 69

Busswell G. S., Shanks T., 2001, MNRAS, 323, 67

Butcher H. R., Oemler Jr. A., 1985, ApJS, 57, 665

Capak P., Cowie L. L., Hu E. M., et al., 2004, AJ, 127, 180

Carswell R. F., Whelan J. A. J., Smith M. G., Boksenberg A., Tytler D., 1982, MNRAS, 198, 91

Chabrier G., 2003, PASP, 115, 763

Chambers K. C., Miley G. K., van Breugel W. J. M., 1990, ApJ, 363, 21

Chapin E. L., Chapman S. C., Coppin K. E., et al., 2010, arXiv:1003.2647

Chapman S. C., Blain A. W., Smail I., Ivison R. J., 2005, ApJ, 622, 772

Chary R., Elbaz D., 2001, ApJ, 556, 562

Chini R., Krügel E., 1994, A&A, 288, L33

Cimatti A., Pozzetti L., Mignoli, M., et al., 2002, A&A, 391, 1

Cimatti A., Daddi E., Renzini A., et al., 2004, Nature, 430, 184

Clavel J., Schulz B., Altieri B., et al., 2000, A&A, 357, 839

Clements D. L., Rigby E., Maddox S., et al., 2010, A&A, 518, 8

Cohen J. G., Hogg D. W., Blandford R., Cowie L. L., Hu E., Songaila A., Shopbell P., Richberg K., 2000, ApJ, 538, 29

Cole S., 1991, ApJ, 367, 45

Cole S., Aragon-Salamanca A., Frenk C. S., Navarro J. F., Zepf S. E., 1994, MNRAS, 271, 781

Cole S., Lacey C. G., Baugh C. M., Frenk C. S., 2000, MNRAS, 319, 168

Comastri A., 2004, in "Supermassive Black Holes in the Distant Universe", vol. 308 of Astrophysics and Space Science Library, p. 245

Condon J. J., 1992, ARA&A, 30, 575

Constantin A., Shields J. C., Hamann F., Foltz C. B., Chaffee F. H., 2002, ApJ, 565, 50

Cool R. J., Eisenstein D. J., Fan X., et al., 2008, ApJ, 682, 919

Coppin K., Chapin E. L., Mortier A. M. J., et al., 2006, MNRAS, 372, 1621

Coppin K. E. K., Swinbank A. M., Neri R., et al., 2008a, MNRAS, 389, 45

Coppin K., Halpern M., Scott D., et al., 2008b, MNRAS, 384, 1597

Coppin K., Pope A., Menéndez-Delmestre K., et al., 2010, arXiv:1003.0447

Cowie L. L., Songaila A., Hu E. M., 1991, Nature, 354, 460

Cowie L. L., Barger A. J., Hu E. M., Capak P., Songaila A., 2004, AJ, 127, 3137

Crenshaw D. M., Kraemer S. B., Hutchings J. B., et al., 2000, AJ, 120, 1731

Crighton N. H. M., Bielby R., Shanks T., et al., 2010, arXiv:1006.4385

Curtis H., 1921, Bull. Nat. Res. Coun., 2, 194

da Ângela J., Outram P. J., Shanks T., Boyle B. J., Croom S. M., Loaring N. S., Miller L., Smith R. J., 2005, MNRAS, 360, 1040

Daddi E., Cimatti A., Renzini A., Fontana A., Mignoli M., Pozzetti L., Tozzi P., Zamorani G., 2004, ApJ, 617, 746

Dale D. A., Bendo G. J., Engelbracht C. W., et al., 2005, ApJ, 633, 857

Davé R., Cen R., Ostriker J. P., et al., 2001, ApJ, 552, 473

Davis M., Wilkinson D. T., 1974, ApJ, 192, 251

Davis M., Efstathiou G., Frenk C. S., White, S. D. M., 1985, ApJ, 292, 371

Dekel A., Birnboim Y., Engel G., et al., 2009, Nature, 457, 451

Della Ceca R., Caccianiga A., Severgnini P., et al., 2008, A&A, 487, 119

De Lucia G., Springel V., White S. D. M., Croton D., Kauffmann G., 2006, MNRAS, 366, 499

Devlin M. J., Ade P. A. R., Aretxaga I., et al., 2009, Nature, 458, 737

Dickinson M. & the FIDEL team, 2007, BAAS, 39, 822

Dietrich M., Wagner S. J., Courvoisier T. J.-L., Bock H., North P., 1999, A&A, 351, 31

Dole H., Lagache G., Puget J.-L., et al., 2006, A&A, 451, 417

Draine B. T., Lee H. M., 1984, ApJ, 285, 89

Draine B. T., Dale D. A., Bendo, G., et al., 2007, ApJ, 663, 866

Dressler A., Gunn J. E., 1982, ApJS, 78, 1

Dube R. R., Wickes W. C., Wilkinson D. T., 1979, ApJ, 232, 333

Dunlop J. S., Ade P. A. R., Bock J. J., et al., 2009, arXiv:0910.3642

Dunlop J. S., 2010, in Proc. Recontres de Moriond (March 2010), in prep.

Dunne L., Eales S., 2001, MNRAS, 327, 697

Eggen O. J., Lynden-Bell D., Sandage A. R., 1962, ApJ, 136, 748

Elbaz D., Hwang H. S., Magnelli B., et al., 2010, arXiv:1005.2859

Ellison S. L., Songaila A., Schaye J., Pettini M., 2000, AJ, 120, 1175

Erb D. K., Shapley A. E., Pettini M., Steidel C. C., Reddy N. A., Adelberger K. L., 2006, ApJ, 644, 813

Fabian A. C., 1999, MNRAS, 308, 39

Fabian A. C., George I. M., Miyoshi S., Rees, M. J., 1990, MNRAS, 242, 14

Farrah D., Afonso J., Efstathiou A., Rowan-Robinson M., Fox M., Clements D., 2003, MNRAS, 343, 585

Ferland G. J., Peterson B. M., 1989, ApJ, 347, 656

Ferland G. J., Peterson B. M., Horne K., Welsh W. F., Nahar S. N., 1992, ApJ, 387, 95

Fine S., Croom S. M., Bland-Hawthorn J., Pimbblet K. A., Ross N. P., Schneider D. P., Shanks T., 2010, arXiv:1005.5287

Fixsen D. J., Dwek E., Mather J. C., Bennett C. L., Shafer R. A., 1998, ApJ, 508, 123

Foucaud S., McCracken H. J., Le Févre O., Arnouts S., Brodwin M., Lilly S. J., Crampton D., Mellier Y., 2003, A&A, 409, 835

Franx M., Labbé I., Rudnick G., et al., 2003, ApJ, 587, 79

Frenk C. S., White S. D. M., Efstathiou G., Davis M., 1990, ApJ, 351, 10

Fukugita M., Nakamura O., Turner E. L., Helmboldt J., Nichol R. C., 2004, ApJ, 601, L127

Gallimore J. F., Yzaguirre A., Jakoboski J., et al., 2010, ApJS, 187, 172

Gardner J. P., Cowie L. L., Wainscoat R. J., 1993, ApJ, 415, L9

Gawiser E., van Dokkum P. G., Gronwall C., et al., 2006, ApJ 642, L13

Gebhardt K., Bender R., Bower G., et al., 2000, ApJ, 539, 13

Georgantopoulos I., Akylas A., Georgakakis A., Rowan-Robinson M., 2009, A&A, 507, 747

Giacconi R., Zirm A., Wang J.-X., et al., 2002, ApJS, 139, 369

Giavalisco M., 2002, ARA&A, 40, 579

Gilli R., Comastri A., Hasinger G., 2007, A&A, 463, 79

Glazebrook. K., Abraham R. G., McCarthy P. J., et al., 2004, Nature, 430, 181

Gonzalez-Perez V., Baugh C. M., Lacey C. G., Almeida C., 2009, MNRAS, 398, 497

Goto T., Nichol R. C., Okamura S., et al., 2003, PASJ, 55, 771

Granato G. L., Danese L., 1994, MNRAS, 268, 235

Granato G. L., Lacey C. G., Silva L., Bressan A., Baugh C. M., Cole S., Frenk C. S., 2000, ApJ, 542, 710

Gray A. G., Moore A. W., Nichol R. C., Connolly A. J., Genovese C., Wasserman, L., 2004, ASPC, 314, 249

Gregorich D. T., Neugebauer G., Soifer B. T., Gunn J. E., Herter T. L., 1995, AJ, 110, 259

Greve T. R., Bertoldi F., Smail I., et al., 2005, MNRAS, 359, 1165

Guainazzi M., Matt G., Perola G. C., 2005, A&A, 444, 119

Gunn K. F., 1999, PhD thesis, Univ. Durham

Gunn K. F., Shanks T., 1999, astro-ph/9909089

Güsten R., Nyman L. Å., Schilke P., Meuten K., Cesarsky C., Booth R., 2006, A&A, 454, L13

Guth A., 1981, PhRvD, 23, 347

Haardt F., Maraschi L., 1991, ApJ, 380, 51

Haardt F., Maraschi L., 1993, ApJ, 413, 507

Hauser M. G., Dwek, E., 2001, ARA&A, 39, 249

Hauser M. G., Arendt R. G., Kelsall T., et al., 1998, ApJ, 508, 25

Heckman T. M., 2000, RSPTA, 358, 2077

Heckman T. M., Armus L., Miley G. K., 1990, ApJS, 74, 833

Heckman T. M., Lehnert M. D., Strickland D. K., Armus L., 2000, ApJS, 129, 493

Helou G., Lu N. Y., Werner M. W., Malhotra S., Silbermann N., 2000, ApJ, 532, L21

Hertzsprung E., 1911, Publ. Astrophys. Obs. Potsdam, 22, 1

Heydon-Dumbleton N. H., Collins C. A., MacGillivray H. T., 1989, MNRAS, 238, 379

Hildebrandt H., Pielorz J., Erben T., Schneider P., Eifler T., Simon P., Dietrich J. P., 2007, A&A, 462, 865

Hill M. D., Shanks T., 2010a, arXiv:1007.1659

Hill M. D., Shanks T., 2010b, arXiv:1007.3126

Holland W. S., Robson E. I., Rawlings S., et al., 1999, MNRAS, 303, 659

Holt J., Tadhunter C. N., Morganti R., 2003, MNRAS, 342, 227

Huang J.-S., Thompson D., Kümmel M. W., et al., 2001, A&A, 368, 787

Hubble E., 1926, ApJ, 63, 236

Huchra J., Burg R., 1992, ApJ, 393, 90

Hughes D. H., Dunlop J. S., Gear W. K., 1997, MNRAS, 289, 766

Hughes D. H., Serjeant S., Dunlop J., et al., 1998, Nature, 394, 241

Iovino A., McCracken H. J., Garilli B., et al., 2005, A&A, 442, 423

Imai K., Matsuhara H., Oyabu S., Wada T., Takagi T., Fujishiro N., Hanami H., Pearson C. P., 2007, AJ, 133, 2418

Ivison R. J., Greve T. R., Smail I., et al., 2002, MNRAS, 337, 1

Jarvis J. F., Tyson J. A., 1981, AJ, 86, 476

Kaiser M. E., Bradley L. D. II, Hutchings J. B., et al., 1999, Ap&SS, 269, 431

Kang X., Lin W. P., Skibba R., Chen D. N., 2010, ApJ, 713, 1301

Kennicutt R. C., Armus L., Bendo, G., et al., 2003, PASP, 115, 928

Khachikian E. Y., Weedman D. W., 1974, ApJ, 192, 581

Kirshner R. P., Oemler Jr. A., Schechter P. L., 1978, AJ, 83, 1549

Knudsen K. K., Barnard V. E., van der Werf P. P., et al., 2006, MNRAS, 368, 487

Kong X., Daddi E., Arimoto, N., et al., 2006, ApJ, 638, 72

Koo D. C., 1981, PhD thesis, Univ. California Berkeley

Koo D. C., 1986, ApJ, 311, 651

Koo D. C., Kron R. T., 1980, PASP, 92, 537

Koo D. C., Kron R. G., 1987, in Proc. IAU Symp. 124: Observational Cosmology (August 1986), p. 383

Kormendy J., Richstone D., 1995, ARA&A, 33, 581

Kornei K. A., Shapley A. E., Erb D. K., Steidel C. C., Reddy N. A., Pettini M., Bogosavljević, M., 2010, ApJ, 711, 693

Koski A. T., 1978, ApJ, 223, 56

Kron R. G., 1980, ApJS, 43, 305

Kümmel M. W., Wagner S. J., 2001, A&A, 370, 384

Kuraszkiewicz J. K., Wilkes B. J., Hooper E. J., et al., 2003, ApJ, 590, 128

Lacey C., Guiderdoni B., Rocca-Volmerange B., Silk J., 1993, ApJ, 402, 15

Lacey C. G., Baugh C. M., Frenk C. S., Silva L., Granato G. L., Bressan A., 2008, MNRAS, 385, 1155

Lacey C. G., Baugh C. M., Frenk C. S., Benson A. J., 2010, arXiv:1004.3545

La Franca F., Fiore F., Comastri A., et al., 2005, ApJ, 635, 864

Lagache G., Dole H., Puget J.-L., 2003, MNRAS, 338, 555

Lagache G., Dole H., Puget J.-L., et al., 2004, ApJS, 154, 112

Lai K., Huang J.-S., Fazio G., et al., 2008 ApJ, 674, 70

Le Févre O., Saisse M., Mancini D., et al., 2003, in Proc. SPIE, vol. 4841, p. 1670

Leger A., Puget J. L., 1984, A&A, 137, L5

Lehmer B. D., Brandt W. N., Alexander D. M., et al., 2005, ApJS, 161, 21

Lehnert M. D., Heckman T. M., 1996, ApJ, 462, 651

Lilly S. J., 1988, ApJ, 333, 161

Lilly S. J., Cowie L. L., Gardner J. P., 1991, ApJ, 369, 79

Linde A. D., 1982, PhLB, 108, 389

Liu H., Wang J., Mao Y., Wei J., 2010, ApJ, 715, 113

Lonsdale C. J., Hacking P. B., Conrow T. P., Rowan-Robinson M., 1990, ApJ, 358, 60

Lonsdale C., Polletta M., Surace J., et al. 2004, ApJS, 154, 54

Lowenthal J. D., Koo D. C., Guzman R., et al., 1997, ApJ, 481, 673

Lutz D., Valiante E., Sturm E., Genzel R., Tacconi L. J., Lehnert M. D., Sternberg A., Baker A.J., 2005, ApJ, 625, L83

Lutz D., Mainieri V., Hasinger G., et al., 2010, ApJ, 712, 1287

McCarthy P. J., 1993, ARA&A, 31, 639

McCracken H. J., Metcalfe N., Shanks T., Campos A., Gardner J. P., Fong, R., 2000, MNRAS, 311, 707

McCracken H. J., Radovich M., Bertin, E., et al., 2003, A&A, 410, 17

McDonald P., Miralda-Escudé J., Rauch M., Sargent W. L. W., Barlow T. A., Cen R., Ostriker J. P., 2000, ApJ, 543, 1

McLeod B. A., Bernstein G. M., Rieke M. J., Tollestrup E. V., Fazio G. G., 1995, ApJS, 96, 117

McMahon R. G., Omont A., Bergeron J., Kreysa E., Haslam C. G. T., 1994, MNRAS, 276, L9

Madau P., 1995, ApJ, 441, 18

Madau P., 1997, in Proc. AIP Conf. 393: Star formation, near and far (October 1996), p. 481

Madau P., Ferguson H. C., Dickinson M. E., Giavalisco M., Steidel C. C., Fruchter A., 1996, MNRAS, 283, 1388

Maddox S. J., Sutherland W. J., Efstathiou G., Loveday J., Peterson, B. A., 1990, MNRAS, 247, 1

Magdis G. E., Rigopoulou D., Huang J.-S., Fazio G. G., Willner S. P., Ashby M. L. N., 2008, MNRAS, 386, 11

Magdis G. E., Elbaz D., Daddi E., Morrison G. E., Dickinson M., Rigopoulou D., Gobat R., Hwang H. S., 2010, ApJ, 714, 1740

Magorrian J., Tremaine S., Richstone, D., et al., 1998, AJ, 115, 2285

Maihara T., Iwamuro F., Tanabe H., et al., 2001, PASJ, 53, 25

Mainieri V., Hasinger G., Cappelluti N., et al., 2007, ApJS, 172, 368

Maiolino R., Salvati M., Bassani L., Dadina M., della Ceca R., Matt G., Risaliti G., Zamorani, G., 1998, A&A, 338, 781

Malizia A., Stephen J. B., Bassani L., Bird A. J., Panessa F., Ubertini, P., 2010, arXiv:1002.4712

Marleau F. R., Fadda D., Storrie-Lombardi L. J., et al., 2004, ApJS, 154, 66

Martínez-Sansigre A., Rawlings S., Lacy M., Fadda D., Jarvis M. J., Marleau F. R., Simpson C., Willott C. J., 2006, MNRAS, 370, 1479

Martínez-Sansigre A., Rawlings S., Boneld D. G., et al., 2007, MNRAS, 379, L6

Martínez-Sansigre A., Karim A., Schinnerer E., et al., 2009, ApJ, 706, 184

Matt G., Fiore F., Perola G. C., Piro L., Fink H. H., Grandi P., Matsuoka M., Oliva E., Salvati M., 1996, MNRAS, 281, 69

Matt G., Fabian A. C., Guainazzi M., Iwasawa K., Bassani L., Malaguti G., 2000, MNRAS, 318, 173

Meier D. L., 1976, ApJ, 207, 343

Menéndez-Delmestre K., Blain A. W., Alexander D. M., et al., 2007, ApJ, 655, 65

Menéndez-Delmestre K., Blain A. W., Smail I., et al., 2009, ApJ, 699, 667

Metcalfe N., Fong R., Shanks T., Kilkenny D., 1989, MNRAS, 236, 207

Metcalfe N., Shanks T., Fong R., Jones L. R., 1991 MNRAS, 249, 498

Metcalfe N., Shanks T., Fong, R., 1995, MNRAS, 274, 769

Metcalfe N., Shanks T., Campos A., McCracken H. J., Fong, R., 2001, MNRAS, 323, 795

Metcalfe N., Shanks T., Weilbacher, P. M., McCracken H. J., Fong, R., 2006, MNRAS, 370, 1257

Nguyen H. T., Schulz B., Levenson L., et al., 2010, A&A, 518, 5

Oliver S. J., Wang L., Smith A. J., et al., 2010, A&A, 518, L21

Omont A., McMahon R. G., Cox P., Kreysa E., Bergeron J., Pajot F., Storrie-Lombardi L. J., 1996, A&A, 315, 1

Omont A., Cox P., Bertoldi F., McMahon R. G., Carilli C., Isaak K. G., 2001, A&A, 374, 371

Omont A., Beelen A., Bertoldi F., Cox P., Carilli C. L., Priddey R. S., McMahon R. G., Isaak K. G., 2003, A&A, 398, 857

Oppenheimer B. D., Davé R., 2006, MNRAS, 373, 1265

Orsi A., Lacey C. G., Baugh C. M., Infante L., 2008, MNRAS, 391, 1589

Page M. J., Stevens J. A., Mittaz J. P. D., Carrera F. J., 2001, Science, 294, 2516

Page M. J., Stevens J. A., Ivison R. J., Carrera F. J., 2004, ApJ, 611, L85

Partridge R. B., 1974, ApJ, 192, 241

Patanchon G., Ade P. A. R., Bock J. J., et al., 2009, ApJ, 707, 1750

Peeters E., Spoon H. W. W., Tielens A. G. G. M., 2004, ApJ, 613, 986

Pentericci L., Grazian A., Scarlata C., Fontana A., Castellano M., Giallongo E., Vanzella E., 2010, A&A, 514, 64

Pérez-González P. G., Rieke G. H., Egami E., et al., 2005, ApJ, 630, 82

Peterson B. M., Wandel A., 1999, ApJ, 521, 95

Peterson B. A., Ellis R. S., Efstathiou G., Shanks T., Bean A. J., Fong R., Zen-Long Z., 1986, MNRAS, 221, 223

Pettini M., Shapley A. E., Steidel C. C., Cuby J.-G., Dickinson M., Moorwood A. F. M., Adelberger K. L., Giavalisco M., 2001, ApJ, 554, 981

Pettini M., Madau P., Bolte M., Prochaska J. X., Ellison S. L., Fan X., 2003, ApJ, 594, 695

Petric A. O., Carilli C. L., Bertoldi F., Beelen A., Cox P., Omont A., 2006, AJ, 132, 1307

Pilbratt G. L., Riedinger J. R., Passvogel T., et al., 2010, A&A, 518, L1

Pieri M. M., Schaye J., Aguirre A., 2006, ApJ, 638, 45

Polletta M., Tajer M., Maraschi L., et al., 2007, ApJ, 663, 81

Polletta M., Omont A., Berta S., et al., 2008, A&A, 492, 81

Pope A., Scott D., Dickinson M., et al., 2006, MNRAS, 370, 1185

Pope A., Chary R.-R., Alexander D. M., et al., 2008, ApJ, 675, 1171

Pozzetti L., Madau P., Zamorani G., et al., 1998, MNRAS, 298, 1133

Priddey, R. S., McMahon R. G., 2001, MNRAS, 324, L17

Priddey R. S., Isaak K. G., McMahon R. G., Omont A., 2003, MNRAS, 339, 1183

Priddey R. S., Gallagher S. C., Isaak K. G., Sharp R. G., McMahon R. G., Butner H. M., 2007, MNRAS, 374, 867

Pritchet C. J., 1994, PASP, 106, 1052

Puget J. L., Abergel A., Bernard J. P., Boulanger F., Burton W. B., Desert F. X., Hartmann, D., 1996, A&A, 308, 5

Quinn P. J., Salmon J. K., Zurek W. H., 1986, Nature, 322, 329

Rawlings S., Eales S., Warren S., 1990, MNRAS, 243, 14

Rawlings S., Willott C. J., Hill G. J., Archibald E. N., Dunlop J. S., Hughes D. H., 2004, MNRAS, 351, 676

Reddy N. A., Steidel C. C., Fadda D., Yan L., Pettini M., Shapley A. E., Erb D. K., Adelberger K. L., 2006a, ApJ, 644, 792

Reddy N. A., Steidel C. C., Erb D. K., Shapley A. E., Pettini M., 2006b, ApJ, 653, 1004

Rieke G. H., Young E. T., Engelbracht C. W., et al., 2004, ApJS, 154 25

Rigopoulou D., Mainieri V., Almaini O., et al., 2009, MNRAS, 400, 1199

Rigopoulou D., Spoon H. W. W., Genzel R., Lutz D., Moorwood A. F. M., Tran Q. D., 1999, AJ, 118, 2625

Risaliti G., Maiolino R., Salvati M., 1999, ApJ, 522, 157

Roche N. D., Almaini O., Dunlop J., Ivison R. J., Willott C. J., 2002, MNRAS, 337, 1282

Rosse W. P., the Earl of, 1850, RSLPT, 140, 499

Rowan-Robinson M., 1999, Ap&SS, 266, 291

Rowan-Robinson M., 2001, ApJ, 549, 745

Rowan-Robinson M., 2009, MNRAS, 394, 117

Rowan-Robinson M., Saunders W., Lawrence A., Leech K., 1991, MNRAS, 253, 485

Russell H. N., 1913, Obs., 36, 32

Salpeter E., 1955, ApJ, 121, 161

Sandage A., 1961, ApJ, 134, 916

Sanders D. M., Mirabel I. F., 1996, ARA&A, 34, 749

Santini P., Maiolino R., Magnelli B., et al., 2010, A&A, 518, L154

Saracco P., Iovino A., Garilli B., Maccagni D., Chincarini G., 1997, AJ, 114, 887

Sargsyan L. A., Weedman D. W., 2009, ApJ, 701, 1398

Sawangwit U., Shanks T., Abdalla F. B., Cannon R. D., Croom S. M., Edge A. C., Ross N. P., Wake D. A., 2009, arXiv:0912.0511

Scalo J., 1986, Fund. Cosmic Phys., 11, 1

Schmidt M., 1965, ApJ, 141, 1295

Scott S. E., Fox M. J., Dunlop J. S., et al., 2002, MNRAS, 331, 817

Scott S. E., Dunlop J. S., Serjeant S., 2006, MNRAS, 370, 1057

Schaye J., Theuns T., Rauch M., Efstathiou G., Sargent W. L. W., 2000, MNRAS, 318, 817

Seyfert C. K., 1943, ApJ, 97, 28

Shakura N. I., Sunyaev R. A., 1973, A&A, 24, 337

Shanks T., Stevenson P. R. F., Fong R., MacGillivray H. T., 1984, MNRAS, 206, 767

Shapley H., 1921, Bull. Nat. Res. Coun., 2, 171

Shapley A. E., Steidel C. C., Adelberger K. L., Dickinson M., Giavalisco M., Pettini M., 2001, ApJ, 562, 95

Shapley A. E., Steidel C. C., Adelberger K. L., Pettini M., 2003, ApJ, 588, 65

Sigut T. A. A., Pradhan A. K., Nahar S. N., 2004, ApJ, 611, 81

Siringo G., Kreysa E., Kovács A., et al., 2009, A&A, 397, 945

Smail I., Ivison R. J., Blain A. W., 1997, ApJ, 490, L5

Smail I., Ivison R. J., Blain A. W., Kneib J.-P., 2002, MNRAS, 331, 495

Soifer B. T., Neugebauer G., 1991, AJ, 101, 354

Somerville R. S., Primack, J. R., Faber S. M., 2001, MNRAS, 320, 504

Songaila A., 2001, ApJ, 561, L153

Songaila A., Cowie L. L., 1996, AJ, 112, 335

Spinrad H., 1982, PASP, 94, 397

Springel V., Hernquist L., 2003, MNRAS, 339, 312

Springel V., Di Matteo T., Hernquist L., 2005, MNRAS, 361, 776

Springel V., White S. D. M., Jenkins A., et al., 2005, Nature, 435, 629

Stalin C. S., Petitjean P., Srianand R., Fox A. J., Coppolani F., Schwope A., 2010, MNRAS, 401, 294

Steidel C. C., Hamilton D., 1993, AJ, 105, 2017

Steidel C. C., Pettini M., Hamilton D. 1995, AJ, 110, 2519

Steidel C. C., Giavalisco M., Pettini M., Dickinson M., Adelberger K. L., 1996, ApJ, 462, 17

Steidel C. C., Adelberger K. L., Giavalisco M., Dickinson M., Pettini M., 1999, ApJ, 519, 1

Steidel C. C., Adelberger K. L., Shapley A. E., Pettini M., Dickinson M., Giavalisco M., 2003, ApJ, 592, 728

Steidel C. C., Shapley A. E., Pettini M., Adelberger K. L., Erb D. K., Reddy N. A., Hunt, M. P., 2004, ApJ, 604, 534

Stein W. A., Soifer B. T., 1983, ARA&A, 21, 177

Stern D., Eisenhardt P., Gorjian V., et al., 2005, ApJ, 631, 163

Strateva I., Ivezić Ž., Knapp G. R., et al., 2001, AJ, 122, 1861

Strömgren B., 1933, ZA, 7, 222

Tadhunter C., Wills K., Morganti R., Oosterloo T., Dickson, R., 2001, MNRAS, 327, 227

Tajer M., Polletta M., Chiappetti L., et al., 2007, A&A, 467, 73

Tenorio-Tagle G., Silich S. A., Kunth D., Terlevich E., Terlevich R., 1999, MNRAS, 309, 332

Thomas D., Maraston C., Bender R., de Oliveira C. M., 2005, ApJ, 621, 673

Tinsley B. M., 1968, ApJ, 151, 547

Tinsley B. M., 1978, ApJ, 222, 14

Tinsley B. M., 1979, ApJ, 229, 1046

Tozzi P., Gilli R., Mainieri V., et al., 2006, A&A, 451, 457

Trager S. C., Faber S. M., Worthey G., González J. J., 2000, AJ, 120 165

Treister E., Urry C. M., 2005, ApJ, 621, 115

Treister E., Virani S., Gawiser E., et al., 2009, ApJ, 693, 1713

Tremonti C. A., Heckman T. M., Kauffmann G., et al., 2004, ApJ, 613, 898

Turner T. J., Miller L., 2009, A&ARv, 17, 47

Tyson J. A., 1988, AJ, 96, 1

Ueda Y., Akiyama M., Ohta K., Miyaji T., 2003, ApJ, 598, 886

Urry C. M., Padovani P., 1995, PASP, 107, 803

Väisänen P., Tollestrup E. V., Willner S. P., Cohen M., 2001, ApJ, 540, 593

Vallbé-Mumbru M., 2004, PhD thesis, Univ. Durham

Vandame B., Olsen L. F., Jorgensen H. E., et al., 2001, astro-ph/0102300

Vestergaard M., Wilkes B. J., 2001, ApJS, 134, 1

Wake D. A., Nichol R. C., Eisenstein D. J., et al., 2006, MNRAS, 372, 537

Wake D. A., Sheth R. K., Nichol R. C., et al., 2008, MNRAS, 387, 1045

Wardlow J. L., Smail I., Coppin K. E. K., et al., 2010, arXiv:1006.2137

Weiß A., Kovacs A., Coppin K., et al., 2009, ApJ, 707, 1201

White S. D. M., Rees M. J., 1978, MNRAS, 183, 341

White, S. D. M., Frenk C. S., 1991, ApJ, 379, 52

Wilman, R. J., Gerssen, J., Bower R. G., Morris S. L., Bacon R., de Zeeuw P. T., Davies R. L., 2005, Nature, 436, 227

Wilman, R. J., Jarvis M. J., Mauch T., Rawlings S., Hickey S., 2010, MNRAS, 405, 447

Wirth G. D., Willmer C. N. A., Amico P., et al., 2004, AJ, 127, 3121

Woo J.-H., Urry C. M., 2002, ApJ, 579, 530

Wolf C., Meisenheimer K., Kleinheinrich M., et al., 2004, A&A, 421, 913

Worsley M. A., Fabian A. C., Bauer F. E., et al., 2005, MNRAS, 357, 1281

Yasuda N., Fukugita M., Narayanan V., et al., 2001, AJ, 122, 1104

Young P. J., Sargent W. L. W., Boksenberg A., Carswell R. F., Whelan J. A. J., 1979, ApJ, 229, 891

Yüksel H., Kistler M. D., Beacom J. F., Hopkins A. M., 2008, ApJ, 683, 5

Yun M. S., Aretxaga I., Ashby M. L. N., et al., 2008, MNRAS, 389, 333